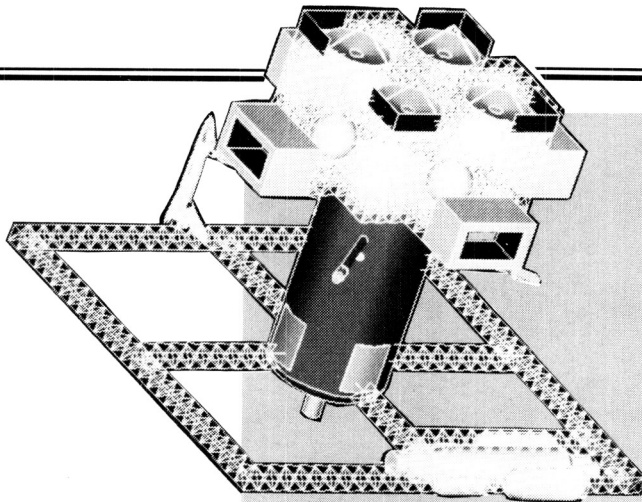
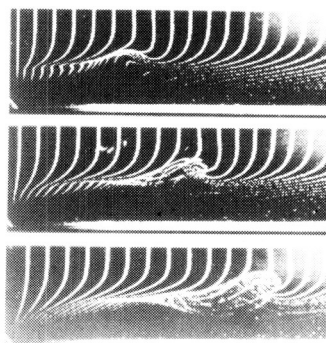


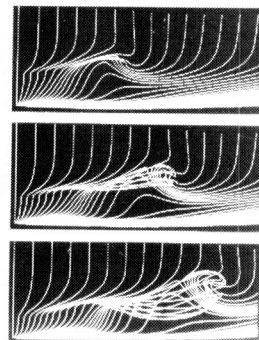
# Research and Technology 1987



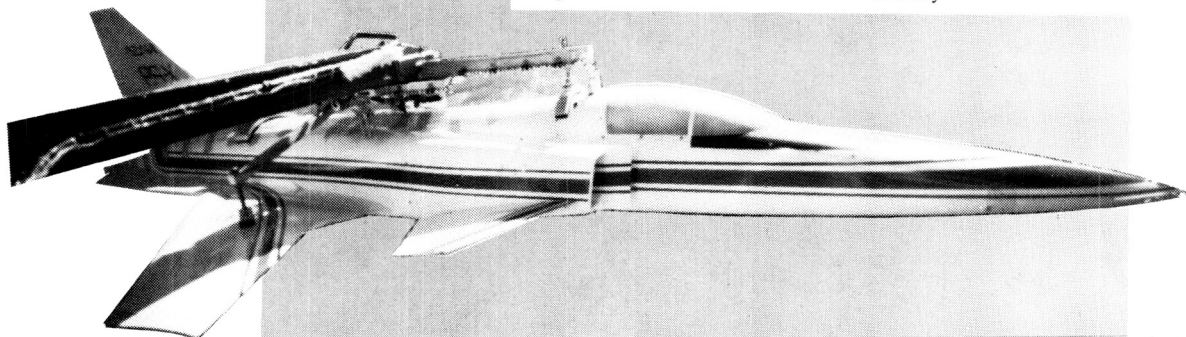
Annual Report of the  
Langley Research Center



Experiment



Theory



(NASA-TM-4021) RESEARCH AND TECHNOLOGY 1987  
Annual Report (NASA) 154 p CSCI 05D

N88-17577

Unclas  
H1/99 0103603

# Research and Technology 1987

---

Annual Report of the  
Langley Research Center



National Aeronautics and  
Space Administration

**Langley Research Center**  
Hampton, Virginia 23665-5225

NASA Technical Memorandum 4021



# Foreword

---

The mission of the NASA Langley Research Center is to increase the knowledge and capability of the United States in a full range of aeronautics disciplines and in selected space disciplines. This mission will be accomplished by performing innovative research relevant to national needs and Agency goals, transferring technology to users in a timely manner, and providing development support to other United States Government agencies, industry, and other NASA centers. This report contains highlights of the major accomplishments and applications that have been made during the past year. The highlights illustrate both the broad range of the research and technology activities at NASA Langley Research Center and the contributions of this work toward maintaining United States leadership in aeronautics and space research. For further information about the report, contact Dr. Richard W. Barnwell, Chief Scientist, Mail Stop 105-A, NASA Langley Research Center, Hampton, Virginia 23665, (804) 865-3316.



Richard H. Petersen  
Director

PRECEDING PAGE BLANK NOT FILMED

# Availability Information

---

The NASA program office and the corresponding Agency-wide Research and Technology Objectives and Plans (RTOP) work breakdown structure are listed in the Contents for each research and technology accomplishment. OAST designates the Office of Aeronautics and Space Technology; OSSA designates the Office of Space Science and Applications; AA designates the Associate Administrator; OCE designates the Office of the Chief Engineer; OCP designates the Office of Commercial Programs; OSF designates the Office of Space Flight; and OSS designates the Office of the Space Station.

For additional information on any summary, contact the individual identified with the highlight. This individual is generally either a member or a leader of the research group submitting the highlight. Commercial telephone users may dial the listed extension preceded by (804) 865. Telephone users with access to the Federal Telecommunications System (FTS) may dial the extension preceded by 928.

# Contents

---

Foreword . . . . .	iii
Availability Information . . . . .	iv

## Aeronautics Directorate

Aeronautics Directorate . . . . .	1
Numerical Method for Computing Transonic Flow Over Wings in Wind Tunnel . . . . . (OAST 505-60-01)	1
Multiple-Module Scramjet Inlet Analysis . . . . . (OAST 505-60-01)	2
Vortex Breakdown Simulation by Direct Method . . . . . (OAST 505-60-11)	3
X-29 Computational Support . . . . . (OAST 505-60-21)	3
Three-Dimensional Design Method for Transonic Wings . . . . . (OAST 505-60-21)	4
F-14A VSTFE Wing Glove Design . . . . . (OAST 505-60-21)	5
Wind Tunnel Wall Effects on Delta-Wing Flow Fields . . . . . (OAST 505-60-21)	6
Airfoil Designed for High-Altitude, Long-Endurance Remotely Piloted Vehicle . . . . . (OAST 505-60-21)	6
Experimental Calibration of Incompressible and Compressible Stability Theory . . . . . (OAST 505-60-21)	7
Unsteady Flow Simulations About an Airfoil: Application to Model Helicopter Blade With Active Control . . . . . (OAST 505-60-21)	8
Novel Approach to Detection of Laminar Separation and Reattachment . . . . . (OAST 505-60-31)	9
Wall Interference Assessment/Correction of Transonic Airfoil Data From Adaptive Wall Tunnel . . . . . (OAST 505-61-01)	9
Laminar Breakdown of Boundary Layers . . . . . (OAST 505-61-31)	10
Liquid Crystals of Boundary-Layer Flow Visualization . . . . . (OAST 505-61-41)	11
Design of Natural Laminar-Flow Fuselages . . . . . (OAST 505-61-41)	12
Full-Scale Semispan Tests of Natural Laminar-Flow Airfoil . . . . . (OAST 505-61-41)	13
Light Airplane Spin Resistance . . . . . (OAST 505-61-41)	14
Study of Leaside Flows Over Conically Cambered Delta Wings at Supersonic Speeds . . . . . (OAST 505-61-71)	14

Investigation of Separated Flows Over Forebody-Cambered Strake at Mach 1.80 . . . . .	15
(OAST 505-61-71)	
Passive Venting System for Reducing Cavity Drag . . . . .	16
(OAST 505-61-71)	
Equivalent Forebody Concept for Supersonic Speeds . . . . .	17
(OAST 505-61-71)	
Wing Tip Vortex Turbine for Transport Aircraft . . . . .	18
(OAST 505-61-71)	
Dynamic Stall Effects on Aircraft Configurations . . . . .	18
(OAST 505-61-71)	
High-Angle-of-Attack Drop Model Research on X-29 . . . . .	19
(OAST 505-61-71)	
Navier-Stokes Predictions of Multifunction Nozzle Flows . . . . .	20
(OAST 505-62-91)	
Nozzle Post-Exit Vanes for Multiaxis Thrust Vectoring . . . . .	21
(OAST 505-62-91)	
Storm Hazards Program . . . . .	22
(OAST 505-68-01)	
High-Speed Civil Transport Study . . . . .	22
(OAST 505-69-61)	

#### Electronics Directorate

Electronics Directorate . . . . .	25
Process for Making Highly Active Noble Metal-on-Metal Oxide Catalyst . . . . .	25
(OSSA 146-74-06)	
Radio Frequency Strain Monitor . . . . .	26
(AA 307-51-07)	
Ultrasonic Testing of Space Shuttle SRM Bond Lines . . . . .	26
(OCE 323-51-66)	
Surface Wave Nondestructive Evaluation of Space Shuttle Solid Rocket Motor Field Joint . . . . .	27
(OCE 323-51-66)	
Three-Component Laser Velocimeter Used to Measure Vortex Flow Field Above YF-17 Model . . . . .	28
(OAST 505-61-01)	
Flexible Thermal Mapping Surface Sensor . . . . .	29
(OAST 505-61-01)	
Advancements in Instrumentation for Magnetic Suspension and Balance System . . . . .	30
(OAST 505-61-01)	
CARS Measurements in Supersonic Combustion Flow . . . . .	31
(OAST 505-62-81)	
Dual-Block Grid Generation and Euler Flow Calculations About Fighter Aircraft Configurations . . . . .	32
(OAST 505-90-21)	

Ultrasonic Harmonic Generation to Determine Crack Opening in Compact Tension Specimens . . . . .	33
(OAST 506-43-11)	
Remote Noncontacting Heat Transfer Measurements for Detection of Boundary-Layer Transition in Wind Tunnel Tests . . . . .	34
(OAST 506-43-11)	
Ultrasonic Measurement of Nonlinear Elastic Properties of Graphite/Epoxy Composites . . . . .	34
(OAST 506-43-11)	
Ultrasonic Measurements for Identification of Superconductivity in High-Temperature Superconductor . . . . .	35
(OAST 506-43-11)	
Oxygen Monitoring and Control System for Langley 8-Foot High-Temperature Tunnel . . .	36
(OAST 506-43-81)	
Spaceborne Optical Disk Controller Development . . . . .	36
(OAST 506-44-11)	
Diode Laser Injection Control of Titanium-Doped Sapphire Lasers . . . . .	38
(OAST 506-45-31)	
High-Temperature Superconducting Materials . . . . .	38
(OAST 506-45-31)	
MOPA Performance of $\text{Ti:Al}_2\text{O}_3$ . . . . .	39
(OAST 506-45-31)	
Crystal Fiber Technology for Evaluation of Solid-State Laser Materials . . . . .	40
(OAST 506-45-31)	
Flow Visualization Using Laser Light Sheets . . . . .	41
(OAST 533-02-01)	

### Flight Systems Directorate

Flight Systems Directorate . . . . .	43
Assessment of Computer Interface Device for Voice Control of Remote TV Cameras . . .	43
(OSS 482-58-13)	
Attitude Control Stability Analysis for Evolving Space Station . . . . .	44
(OSS 483-32-33)	
Comparison of In-Flight and Ground-Based Simulator-Derived Flying Qualities and Pilot Performance . . . . .	44
(OAST 505-66-01)	
Parameter Estimation Applied to X-29 Drop Model . . . . .	45
(OAST 505-66-01)	
Restructurable Flight Control System . . . . .	46
(OAST 505-66-01)	
Algorithm for Optimally Trimming Airplanes Equipped With Multiple Control Effectors . . . . .	47
(OAST 505-66-01)	
Completion of High-Level Graphics Language for Flight Displays . . . . .	47
(OAST 505-66-11)	

Rotatable Antialiased Character Set for All-Raster Flight Displays . . . . .	48
(OAST 505-66-11)	
Interactive Editor for Definition of Touch Sensitive Zones . . . . .	49
(OAST 505-66-11)	
Defect-Free High-Resolution Electroluminescent Display Achieved . . . . .	50
(OAST 505-66-11)	
Flight Demonstration for Failure Detection and Isolation of Redundant Inertial Sensors . . . . .	51
(OAST 505-66-21)	
Estimating the Distribution of Fault Latency in Digital Processors . . . . .	51
(OAST 505-66-21)	
Development of Confidence Limits for Estimating Software Reliability . . . . .	53
(OAST 505-66-21)	
Wideband Electric Field Measurement System . . . . .	54
(OAST 505-66-21)	
Assessed Fuel Penalties and Time Flexibility of 4-D Flight Profiles in Mismodeled Wind . . . . .	55
(OAST 505-66-41)	
Effect of Motion Cues During Complex Curved Approach and Landing Tasks . . . . .	55
(OAST 505-66-41)	
Evaluation of Concept for Data Link Air Traffic Control Message Exchange . . . . .	56
(OAST 505-66-41)	
Takeoff Performance Monitoring System . . . . .	57
(OAST 505-66-41)	
Stochastic Optimal Feedforward/Output Feedback Controls Design Methodology . . . . .	57
(OAST 505-66-41)	
Effects of Combining Vertical and Horizontal Information Into Primary Flight Display . . . . .	58
(OAST 505-67-41)	
Validated Wind Shear Model Through Comparison With Dallas-Fort Worth/Delta Airlines Microburst Event . . . . .	59
(OAST 505-67-41)	
Identification of Wind Shear Hazard Index for Design of Alert and Warning Systems . . . . .	60
(OAST 505-67-41)	
Developed Prototype Onboard Fault-Monitoring and Diagnosis Expert System . . . . .	60
(OAST 505-67-41)	
Controls/Structures/Electromagnetics Interaction Space Technology for Large Space Antennas . . . . .	61
(OAST 506-44-21 and 505-43-51)	
Optimal Open Multistep Discretization Formulas for Real-Time Simulation . . . . .	62
(OAST 506-46-21)	
Control of Multiple Robot Arms . . . . .	63
(OAST 549-01-51)	
Space Truss Assembly Using Teleoperated Manipulators . . . . .	63
(OAST 549-01-51)	
Microgravity Crystal Growth on Mission 61A . . . . .	64
(OSSA 694-80-70)	
Identification of Fundamental National Aero-Space Plane Stability and Control Issue . . . . .	64
(OAST 763-01-51)	



---



---

## Space Directorate

Space Directorate . . . . .	67
Comparison of Climate Model Simulations With Satellite Observations . . . . .	67
(OSSA 146-74-04)	
Laboratory Measurements of Ozone Infrared Spectrum . . . . .	68
(OSSA 147-23-11)	
Stratospheric Remote Sensing Using Emission Far-Infrared Spectroscopy . . . . .	69
(OSSA 147-44-02)	
Infrared Measurements of Atmospheric Gases Above South Pole . . . . .	70
(OSSA 147-44-02)	
Amazon Boundary-Layer Experiment . . . . .	70
(OSSA 176-20-09)	
Airborne Lidar Measurements of Ozone and Aerosols Over Amazon Basin During Wet Season . . . . .	71
(OSSA 176-40-04)	
Modeling Space Radiation Effects . . . . .	72
(OSSA 199-22-76)	
Analysis of Vegetation Growth/Carbon Cycling at Continental-Sized Geographic Scales . . . . .	73
(OSSA 199-30-86)	
Microbial Activity, Atmospheric Gases, and Life on Mars . . . . .	74
(OSSA 199-52-26)	
Atomic Oxygen Beam Generator . . . . .	75
(AA 307-51-07)	
Simulation of Real-Gas Effects on Aeroassist Flight Experiment Vehicle . . . . .	75
(OAST 506-40-11)	
Experimental Investigation of Space Shuttle Orbiter Ascent Separation . . . . .	76
(OAST 506-40-11)	
Reaction Control System Plume and Flow Field Interaction . . . . .	77
(OAST 506-40-11)	
Aerodynamic Characteristics of Transatmospheric Vehicle Concept Over Wide Speed Range . . . . .	78
(OAST 506-40-11)	
Space Shuttle Orbiter Stability and Control Characteristics at High Angles of Attack . . . . .	79
(OAST 506-40-11)	
Crew Emergency Rescue Vehicle . . . . .	79
(OAST 506-40-11)	
Calculation of Three-Dimensional Nonequilibrium Viscous Flow Over Space Shuttle Windward Surface . . . . .	80
(OAST 506-40-11)	
Near-Wake Flow Field Over Aeroassist Flight Experiment Vehicle . . . . .	81
(OAST 506-40-11)	
Aerothermodynamic Study of Slender Conical Vehicles . . . . .	82
(OAST 506-40-11)	

In Situ Upper-Altitude Density Measurement From Space Shuttle	
Orbiter Accelerometry . . . . .	82
(OAST 506-40-11)	
Q-Switched Solar-Pumped Iodine Lasers . . . . .	83
(OAST 506-41-41)	
Engine Selection for Advanced Earth-to-Orbit Vehicles . . . . .	84
(OAST 506-49-11)	
Solid Modeling Aerospace Research Tool . . . . .	85
(OAST 506-49-11)	
Transportation Base Space Station for Year 2025 . . . . .	85
(OAST 506-49-31)	
Concept for Low-Gravity Research Facility . . . . .	86
(OAST 506-49-31)	
Advanced Satellite-Servicing Facility . . . . .	87
(OAST 506-49-31)	
Space Station On-Orbit Operation Model . . . . .	88
(OAST 506-49-31)	
Global-Scale Distribution of Carbon Monoxide as Measured From	
Space Shuttle Platform . . . . .	89
(OSSA 618-22-31)	
Satellite Measurements of Stratospheric Polar Aerosols . . . . .	90
(OSSA 665-10-40)	
Polar Stratospheric Clouds and Antarctic Ozone Hole . . . . .	91
(OSSA 665-10-40)	
Evaluation of Optical Disk System for Archiving Data From Earth	
Radiation Budget Experiment . . . . .	91
(OSSA 665-45-20)	
Surface Radiation Measurements for Satellite Algorithm Studies . . . . .	92
(OSSA 672-22-20)	
Infrared Radiation Studies From Nimbus Satellite Data Sets . . . . .	92
(OSSA 672-40-05)	
Clouds, Radiation, and Atmospheric Energy . . . . .	93
(OSSA 672-40-05)	
Detection of Ozone Depletion Via Solar Lyman Alpha Radiation . . . . .	94
(OSSA 673-41-07)	
Electronic Data Base for Stratospheric Trace Gases . . . . .	95
(OSSA 673-56-02)	
Middle Atmosphere Modeling Dynamics and Transport Processes . . . . .	95
(OSSA 673-64-02)	
Validation of Stratospheric Satellite Wind Analyses . . . . .	96
(OSSA 673-64-02)	
Launch Vehicle Architecture Study . . . . .	96
(OSF 906-65-01)	

---



---

## Structures Directorate

Structures Directorate . . . . .	99
Thermally Induced Twist in Composite Tubes . . . . .	99
(OSS 481-33-13)	
Impact Response of Composite Fuselage Frames . . . . .	100
(OAST 505-42-23)	
Structural Response of Redesigned SRM Joint Nearly Insensitive to Pressure Distribution . . . . .	101
(OAST 505-43-41 and 505-63-11)	
Acoustic Effects on Airfoil Drag . . . . .	102
(OAST 505-60-31)	
F-15 Aft End Acoustics . . . . .	103
(OAST 505-61-11)	
Changes in RSRA/X-Wing Stopped-Rotor Stability Characteristics Due to Static Aeroelastic Deformation . . . . .	103
(OAST 505-61-51)	
Shape Optimization of Bolted SRB Field Joint Alternative . . . . .	105
(OAST 505-63-11)	
Reduction of Blade-Vortex Interaction Noise . . . . .	106
(OAST 505-61-51)	
Alleviation of Cavitation in Superplastically Formed 7475 Aluminum Alloy Using Post-Forming Pressure . . . . .	107
(OAST 505-63-01)	
Method of Predicting Energy-Absorption Capability of Composite Subfloor Beams . . . .	107
(OAST 505-63-01)	
Use of B <sub>4</sub> C Particulates to Improve Properties in Aluminum Matrix Composites . . . .	108
(OAST 505-63-01)	
Three-Dimensional Analysis of Fatigue Crack Closure . . . . .	109
(OAST 505-63-01)	
Inexpensive Method for Calculating Strain-Energy Release Rate . . . . .	109
(OAST 505-63-01)	
Improved Processibility of LARC-TPI Composites by Matrix Resin Blending . . . . .	110
(OAST 505-63-01)	
General Compressive Strength Theory for Composite Laminates . . . . .	110
(OAST 505-63-11)	
Parallel Method for Solving Eigenvalue Problems . . . . .	111
(OAST 505-63-11)	
Response of Buckled Plates to Acoustic Force . . . . .	112
(OAST 505-63-11)	
Aeroservoelastic Analysis Validated by Wind Tunnel Tests . . . . .	113
(OAST 505-63-21)	
Development of Transonic Aeroelasticity Code for Realistic Aircraft Configurations . . .	114
(OAST 505-63-21)	
2-D Global/Local Analysis Using Computational Structural Mechanics Test Bed . . . .	115
(OAST 505-63-31)	

Fluorinated Polyimide Films for Thermal Control Coatings . . . . .	116
(OAST 505-63-91)	
Augmented Heating Rate Measurements by Shock Impingement on Cylindrical	
Leading Edge . . . . .	116
(OAST 506-40-21)	
Improved Processibility of Polyimides Through Use of Diamic Acid Additives . . . . .	117
(OAST 506-43-11)	
Comparison of Simulated Low-Earth and Geosynchronous Orbit Exposure on	
Composite Materials . . . . .	118
(OAST 506-43-21)	
New Direct Solution for Thermal Stresses in Spherical Nose Cap Under Arbitrary	
Temperature Distribution . . . . .	119
(OAST 506-43-31)	
Optimization Procedure to Control Spacing of Vibration Frequencies for Flexible	
Space Structures . . . . .	119
(OAST 506-43-41)	
Shape Control of Large Space Antenna Reflectors Based on Electromagnetic	
Performance . . . . .	120
(OAST 506-43-41)	
Tapered Ends for Space Shuttle Solid Rocket Booster/External Tank Attachment	
Ring . . . . .	121
(OAST 506-43-41)	
Weight Efficient In-Line Bolted Joint for Space Shuttle Solid Rocket Motor Case	
Segments . . . . .	121
(OAST 506-43-41)	
New Developments in Model Parameter Determination for System Identification . . . . .	122
(OAST 506-43-51)	
Feasibility of Scaled Models for Dynamic Tests of Erectable Space Station . . . . .	123
(OAST 506-43-51)	
Test Methodology for Carbon-Carbon Composites . . . . .	124
(OAST 506-43-71)	
Active Control of 3-D Acoustic Environments . . . . .	125
(OAST 535-03-11)	
Deployable and Foldable Beam/Truss for Space Applications . . . . .	125
(OAST 542-03-15)	
Cornering and Wear Behavior of Space Shuttle Orbiter Main Tire . . . . .	126
(OSF 551-15-01)	
Improved Performance of Titanium-Aluminides by Use of Thermal Control Coatings . . . . .	127
(OAST 763-01-41)	

#### Systems Engineering and Operations Directorate

Systems Engineering and Operations Directorate . . . . .	129
Coupled Bending-Torsion Steady-State Response of Pretwisted Nonuniform Rotating	
Beams Using Transfer-Matrix Method . . . . .	129
(AA 023-08-00)	

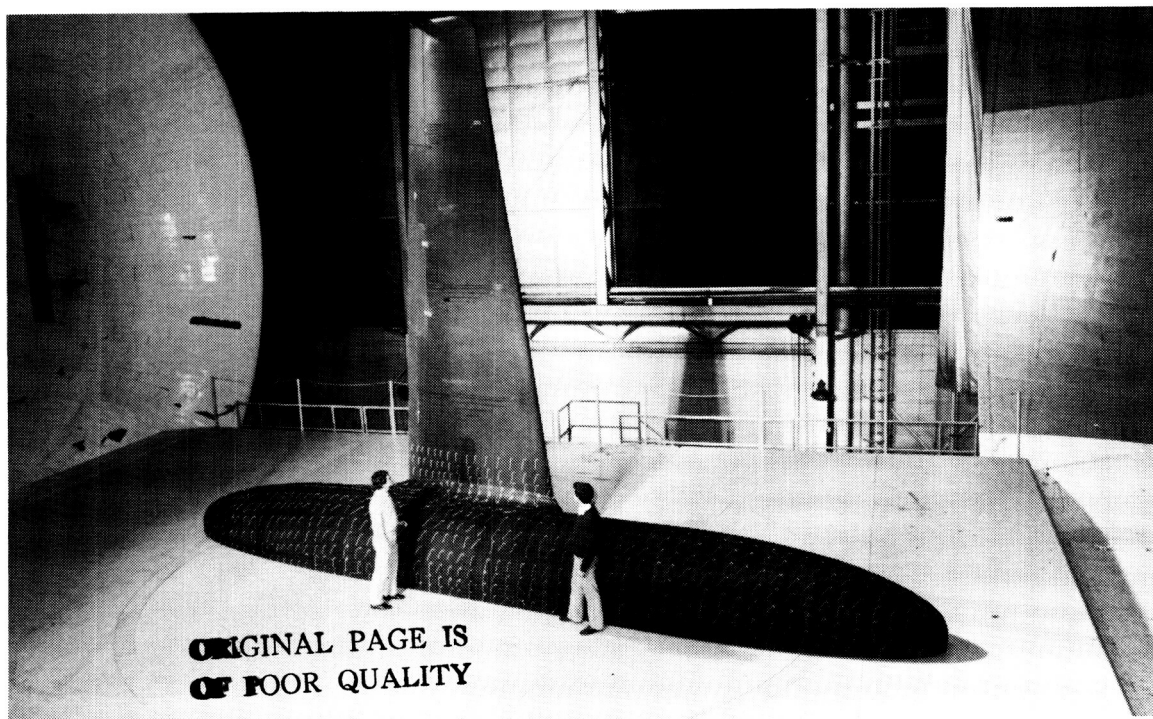
Foam Fiberglass Used for Radio-Controlled Spin Model . . . . .	130
(OAST 505-61-41)	
Radiographic Technique for Wooden Structures . . . . .	130
(AA 023-08-00)	
Pultrusion Process Development for Fabrication of High-Performance Thermoplastic/Graphite Composites . . . . .	131
(AA 307-51-07)	
Plume Dispersion of Exhaust From Cryogenic Wind Tunnel . . . . .	131
(OAST 505-61-01)	
FAVOR Model Carry-Through Fixture Test and Analysis Results . . . . .	132
(OAST 505-61-01)	
Numerical Model of Unsteady, Subsonic Aeroelastic Behavior . . . . .	133
(OAST 505-61-01)	
Use of Advanced Composites in Research Aircraft Models . . . . .	133
(OAST 505-62-14)	
Rotary Actuator for COFS Mini-Mast . . . . .	134
(OAST 506-01-11)	
Pitot-Static/Flow Direction Survey Probes . . . . .	134
(OAST 506-40-11)	
Concept for Solid Rocket Booster In-Line Bolted Joint . . . . .	135
(OAST 506-43-41)	
Alternate Design of Partial Solid Rocket Booster External Tank Attachment Ring for Space Transportation System . . . . .	135
(OAST 506-43-41)	
Low-Weight, High-Stiffness, Thermally Stable Equipment for High-Precision Optical Measurements . . . . .	136
(OSSA 618-32-33)	

#### Technology Utilization Program

Technology Utilization Program . . . . .	139
Stress in Railcar Wheels . . . . .	139
(OCP 141-20-10)	
Burn Depth Measurement System . . . . .	139
(OCP 141-20-40)	
Dialysis Chamber . . . . .	140
(OCP 141-20-40)	

# Aeronautics Directorate

---





The Aeronautics Directorate is composed of approximately 300 scientists and engineers engaged in basic and applied research in the various aeronautics disciplines. The directorate is organized into four research divisions and a program office, which conduct aeronautical research to advance the state of the art throughout the complete aerodynamic speed range.

The Hypersonic Technology Office coordinates broad-scope hypersonic vehicle research and technology programs including those involving the National Aero-Space Plane.

The Advanced Vehicles Division conducts multidisciplinary advanced aeronautical vehicle studies to assess the benefits of discipline research advances and to identify potential new research thrusts. In particular, the vehicle classes of long-haul subsonic and supersonic transports, advanced military aircraft, and general-aviation and commuter aircraft are addressed. The primary emphasis is on high-risk, far-term application of integrated research results from primary aeronautical disciplines.

The Low-Speed Aerodynamics Division conducts research in the areas of basic fluid mechanics, low-speed aerodynamics, flight dynamics and flight management, aircraft operations, aviation safety, laminar-flow control, and improved test methods. The division develops and validates theoretical aerodynamic methods for subsonic conditions and design methodology required to improve subsonic aerodynamic performance, stall/spin behavior, handling qualities, and takeoff and landing performance.

The Transonic Aerodynamics Division conducts research to advance the state of the art of transonic aircraft technology in the areas of fundamental aerodynamics, with particular emphasis on Reynolds number effects, laminar-flow concepts, stability and control, performance analysis, configuration concepts, and related aerodynamic phenomena. Particular areas of emphasis include improving the efficiency and reducing the fuel consumption of conventional jet transports, developing the technology for advanced military combat aircraft, developing theoretical and analytical methods for predicting aerodynamic characteristics in separated and transonic flows, developing advanced airfoils for low-speed and transonic aircraft and helicopters, and developing advanced experimental techniques, including advanced wall concepts, for transonic wind tunnels, cryogenic wind

tunnel technology, and magnetic suspension and balance systems.

The High-Speed Aerodynamics Division conducts research to advance the state of the art for supersonic aircraft, hypersonic aircraft, and missiles and to support the development of high-performance military aircraft, advanced cruise and tactical missiles, the Space Shuttle, and follow-on advanced space transportation systems. New analytical methods for design and analysis are derived and applied to advanced high-speed aircraft and missile concepts. Key experiments are conducted to validate the analytical methods, explore the potential of advanced concepts, and provide a data base for use by industry design teams.

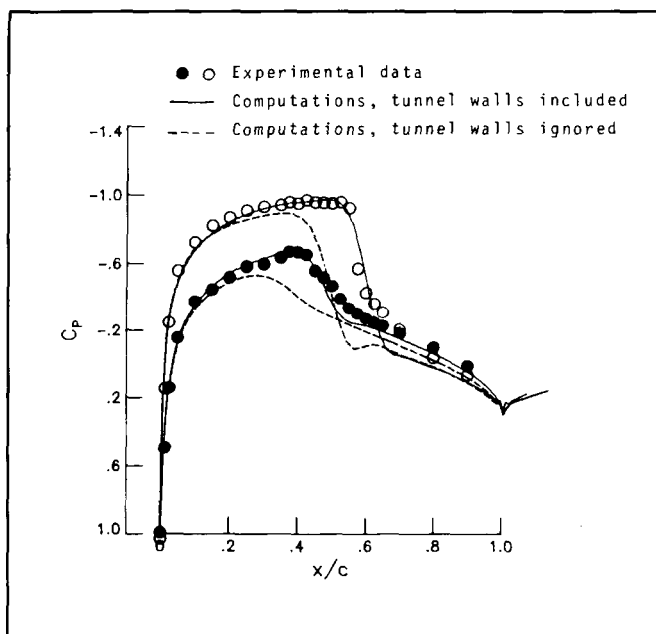
### **Numerical Method for Computing Transonic Flow Over Wings in Wind Tunnel**

A numerical scheme developed for computing high Reynolds number viscous flow over isolated wings in free air has been extended to simulate flow over wings mounted inside a wind tunnel. A multistage Runge-Kutta-type time-stepping scheme is used for solving Reynolds-averaged, thin-layer Navier-Stokes (TLNS) equations. At the present time, boundary-layer growth on tunnel walls is ignored, and flow tangency conditions are imposed at the tunnel walls. Characteristic-type boundary conditions are employed at the inflow boundary. At the outflow boundary, pressure is specified, and the remaining flow variables are extrapolated from the interior.

The accuracy and usefulness of this method is checked by comparing the present results with the free-air (i.e., ignoring existence of wind tunnel walls) calculations and the experimental data for an untapered swept NACA 0012 wing at a free-stream Mach number of 0.825, an angle of attack of  $2^\circ$ , and a chord Reynolds number of  $8 \times 10^6$ . The pressure distributions (at a 50-percent spanwise location) for this test case are shown in the figure. It is noted that the predicted shock location based on free-air calculations is approximately 15 percent upstream

of its measured value on the upper surface of the wing. By modeling the flow as an internal flow inside the tunnel, however, the overall agreement with the pressure data, in general, and the shock location, in particular, improves significantly.

(Veer N. Vatsa, 2627)



Surface pressure distributions for NACA 0012 wing.

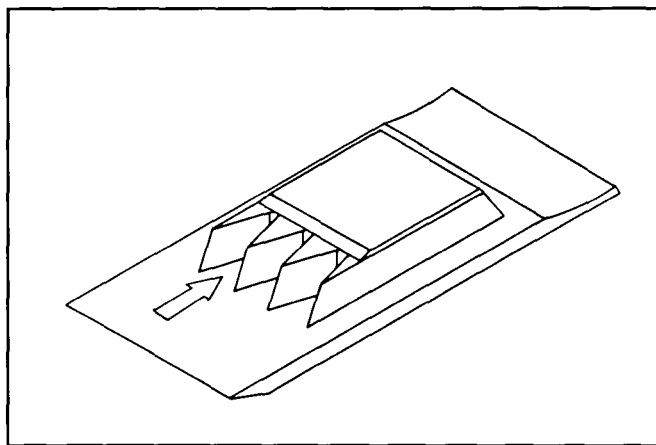
### Multiple-Module Scramjet Inlet Analysis

Work is currently under way to study the propulsion/airframe integration problem at high speed. As a step in this direction, an experimental, as well as analytical, program has been devised. The goal of this program is to predict performance and interactions of multiple scramjet inlet modules mounted on a forebody. As shown in the first figure, the model has three modules mounted on a flat plate that simulates the forebody boundary layer. This model will be tested over a range of Mach numbers,

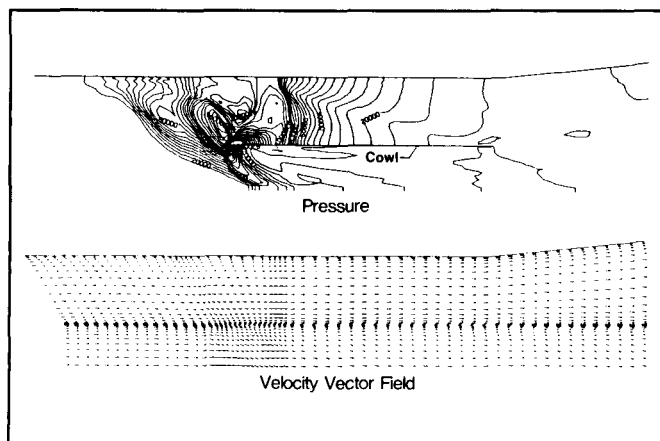
angles of attack, and yaw angles. The experimental conditions will be numerically simulated using a three-dimensional Navier-Stokes code, SCRAMIN. The results from these calculations will be compared against the experiment.

Preliminary calculations have been made at  $0^\circ$  and small angles of attack and yaw for Mach 4 flow conditions. A two-dimensional Navier-Stokes code is used on the front flat plate to determine the flow profiles at the face of the modules. These profiles are then used as the inflow conditions for the SCRAMIN code to analyze the flow in the modules. Sample results at an angle of attack of  $0^\circ$  are presented in the second figure, which shows the pressure contours and velocity vectors in the vertical symmetry plane of one of the modules. The pressure contours show a swept shock structure caused by the swept compression surfaces of the modules. The velocity vector plot shows a significant downturn in flow direction ahead of the cowl resulting in some flow spillage. This downturn in the flow is caused by the sidewall sweep and the interaction between the internal and external flow due to the aft placement of the cowl on the undersurface of the modules. Once the inlet flow passes behind the cowl leading edge, it is turned back parallel to the cowl plane. This turning results in a shock on the upper side of the cowl and an expansion on the underside of the cowl which can be seen clearly in the pressure contour plot.

(Ajay Kumar, 3171)



Schematic of multiple-module scramjet engine.



*Pressure contours and velocity vector field in symmetry plane. Grid is  $61 \times 91 \times 61$ , geometric contraction ratio is 4.0, and angle of attack is  $0^\circ$ .*

### Vortex Breakdown Simulation by Direct Method

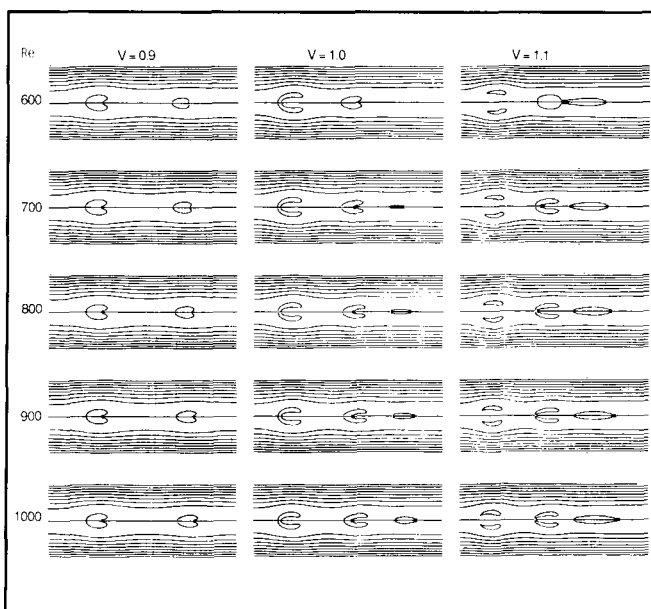
The phenomenon of vortex breakdown (an abrupt change in the structure of the core of a swirling flow) has been under investigation for more than 30 years. An example of this phenomenon is the breakdown of the vortex shed from the highly swept leading edge of a delta wing. The effect of vortex breakdown on the aerodynamics of the wing is very important because it degrades the performance of the wing.

In the past, several investigators have simulated vortex breakdown using different iterative numerical techniques. The performance of these algorithms deteriorates rapidly beyond Reynolds number  $Re$ , based on the vortex core radius, of 200.

In the present study, the incompressible, axisymmetric, steady Navier-Stokes equations are written using the stream-function-vorticity formulation. The resulting equations are linearized and then solved using an exact lower/upper (LU) decomposition, Gaussian elimination, and Newton iteration. Solutions are presented for Reynolds numbers ranging from 600 to 1000 and swirl parameters  $V$  ranging

from 0.9 to 1.1. The convergence rate is quadratic, provided the initial conditions are good. For large Reynolds number simulations, a continuation process is used.

(Manuel D. Salas and Geojoe Kuruvila, 2627)



*Calculated streamlines depicting recirculating bubbles.*

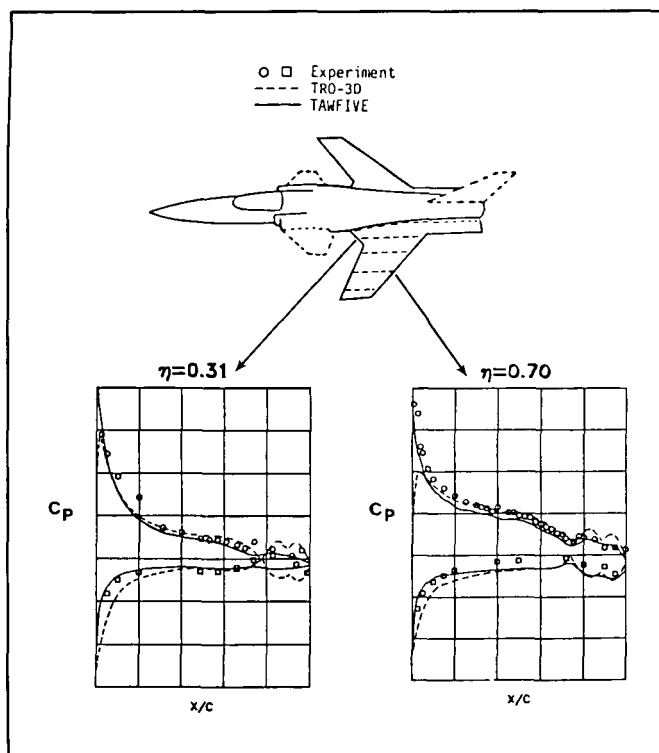
### X-29 Computational Support

A cooperative effort with the Fluid and Flight Mechanics Branch, Ames/Dryden Flight Research Facility has been established to enhance the understanding of the unique aerodynamics of the X-29A Advanced Technology Demonstrator. The approach is to use advanced state-of-the-art transonic computational analysis techniques in conjunction with wind tunnel and flight experimental data to investigate the complex fluid mechanics and component interactions of the forward-swept-wing aircraft.

A detailed computational model of the configuration has been defined for use in various analysis codes. The model definition makes few compro-

mises for the details of the aircraft geometry while generating a model for which computationally valid component mappings can be generated. An incremental approach has been defined for the code calibration phase. The approach involves a systematic buildup of the configuration components and code-to-code and code-to-experiment comparisons. Results shown in the figure are comparisons of experimental wing pressure distributions with computational predictions from a small-disturbance (TRO-3D) and a full-potential (TAWFIVE) analysis code for the wing/body configuration. These analyses allow the complete configuration to be analyzed with significantly increased confidence and understanding than if the complete configuration were analyzed initially.

(E. G. Waggoner, 2601)



Comparison of wind tunnel data and computational results for X-29A wing and fuselage at Mach number of 0.6 and angle of attack of  $7.7^\circ$ .

### Three-Dimensional Design Method for Transonic Wings

The application of advanced aerodynamic technologies, such as supercritical and natural laminar-flow airfoils, to new or existing aircraft offers the potential benefits of improved performance and lower operating costs. Since both of these technologies depend on generating specific types of pressure distributions over the wing, an approach to aerodynamic wing design is needed that can insure that a prescribed pressure distribution will result.

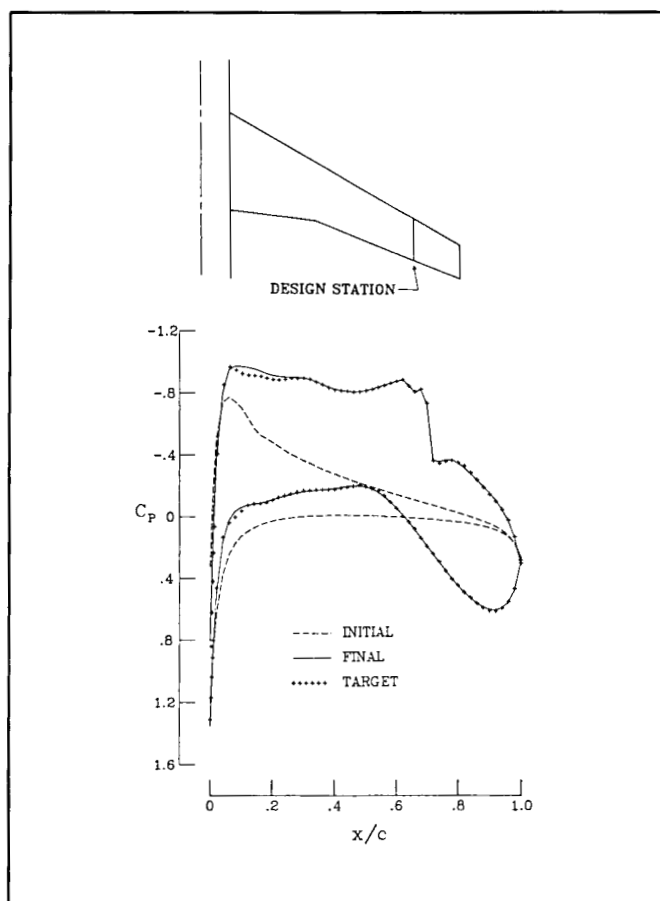
A method for designing wings that generate specified pressure distributions has been developed. The approach involves the iterative interaction of a design module with an existing aerodynamic analysis code. The analysis code calculates the pressure distribution for a given wing shape, then the design module modifies the wing shape until the desired pressure distribution is achieved. The modifications to the wing geometry are determined by an algorithm that relates increments in pressure coefficient to increments in wing surface curvature and slope at a given location.

Two pilot transonic wing design codes have been created which employ this method. The first code uses a full-potential analysis code, and the second uses a small-disturbance code that includes static aeroelastic wing deflections in the computations. Design cases for forward- and aft-swept transport wings and fighter wings having leading-edge sweeps as high as  $70^\circ$  have been successfully run in these codes. Results from the design of an aft-swept supercritical transport wing are shown in the figure. The target pressure coefficients were generated by running a wing-fuselage configuration in the small-disturbance code at a Mach number of 0.85 and an angle of attack of  $1^\circ$ . An initial wing for the design process was then created by replacing the supercritical airfoils with NACA 0012 airfoils. The target, initial, and final design pressure distributions for the wing station shown indicate that, even though the initial and target pressures are significantly different, the design code was able to achieve the desired pressure distribution.

(Richard L. Campbell and Leigh A. Smith, 2601)

It was necessary to experimentally verify the design and to obtain performance data on the modified configuration before modification of the actual aircraft commenced. Experimental wing pressure distributions for the initial glove design are compared with theoretical results from the TAWFIVE three-dimensional transonic code (as shown in the figure). The Mach number of 0.7 and the angle of attack of  $2.95^\circ$  represent the high-altitude, level-flight design condition for the flight experiment. The analysis code was first run matching the experimental angle of attack. While overall correlation was good, the suction peak and the slight adverse pressure gradient that occurs at the leading-edge inboard in the experimental data were not predicted. Often, in comparing potential flow calculations with experimental data, it is found that the codes underpredict the lift levels and must be run at slightly elevated angles of attack relative to the experiment. Additional calculations were made with the angle of attack increased to  $3.25^\circ$ . These results more closely match the experimental pressure levels and gradients near the leading edge. The success of the design effort allowed minor modifications to the inboard region of the glove to be accomplished without the necessity of further experimental verification.

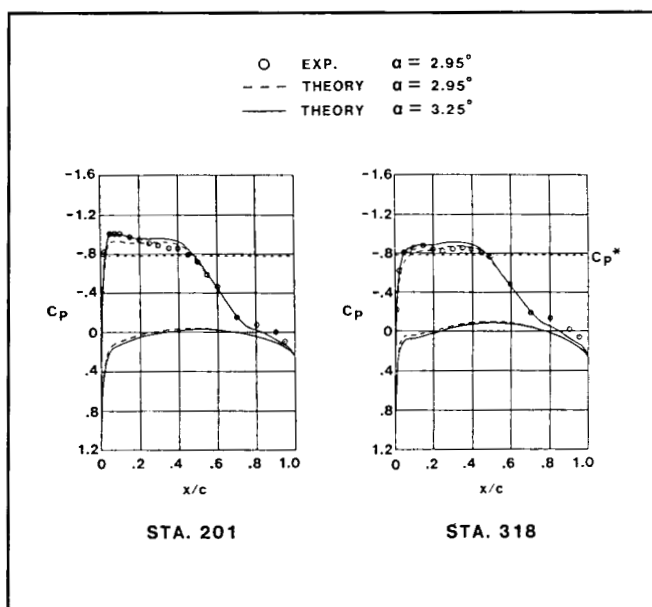
(E. G. Waggoner, 2601)



Transport wing design results.

## F-14A VSTFE Wing Glove Design

An outer-panel glove has been designed and tested in the National Transonic Facility (NTF) in support of the F-14 Variable Sweep Transition Flight Experiment (VSTFE). The objective of the flight research is to obtain in-flight wing pressure and boundary-layer data that will be used to develop a reliable laminar-flow transition prediction method. The approach to this flight experiment is to modify the wing outer panel by gloving on a foam and fiberglass contour such that favorable pressure gradients will be generated over a range of Mach numbers, wing sweep angles, Reynolds numbers, and lift coefficients. The glove contour was designed computationally using a combination of two- and three-dimensional potential flow analysis and design techniques.



Comparison of theoretical and experimental pressure distributions at Mach number of 0.7.

---

## Wind Tunnel Wall Effects on Delta-Wing Flow Fields

The Free Vortex Sheet panel code has been used to compute the effects of wind tunnel walls on the flow field around delta wings. This effort was initiated in support of planned wind tunnel tests that are focused at generating laser velocimetry flow measurements around delta wings for validation of advanced aerodynamic computer codes. One such effort involved the determination of a model size for a  $65^\circ$  delta wing to be built and tested in the Low-Turbulence Pressure Tunnel (LTPT). The goal was to build as large a model as possible to increase the resolution of the measurements yet have minimal flow interference from the tunnel walls. A doublet-panel description of the LTPT walls was constructed around a similar description of the  $65^\circ$  delta wing at the angles of attack. Three ratios of model-to-tunnel span  $R_b$  were examined. The largest ratio,  $R_b = 0.667$ , corresponds to the size of an existing wing to be tested in the National Transonic Facility (NTF), while the other two ratios represent scaled reductions.

An important result of the study was the development of a higher-order wall correction method. As with classic methodology, the higher-order method produces an averaged wall-interference upflow correction angle that is superimposed with the wing angle of attack. Application of the method results in acceptable corrections to the flow field as evidenced by good agreement in upper-surface spanwise pressure distributions between solutions for the wing confined within the tunnel walls and the wing in free air but corrected for wall effects. The good agreement was present at angles of attack  $\alpha$  of  $15^\circ$  and  $30^\circ$  for the two smaller wings ( $R_b = 0.444$  and  $0.5$ ). For the largest wing ( $R_b = 0.667$ ), differences were noticeable at  $\alpha = 30^\circ$ . These differences indicate that this size of wing is approaching an outer boundary where the assumption of superposition breaks down.  
(Neal T. Frink, 2601)

## Airfoil Designed for High-Altitude, Long-Endurance Remotely Piloted Vehicle

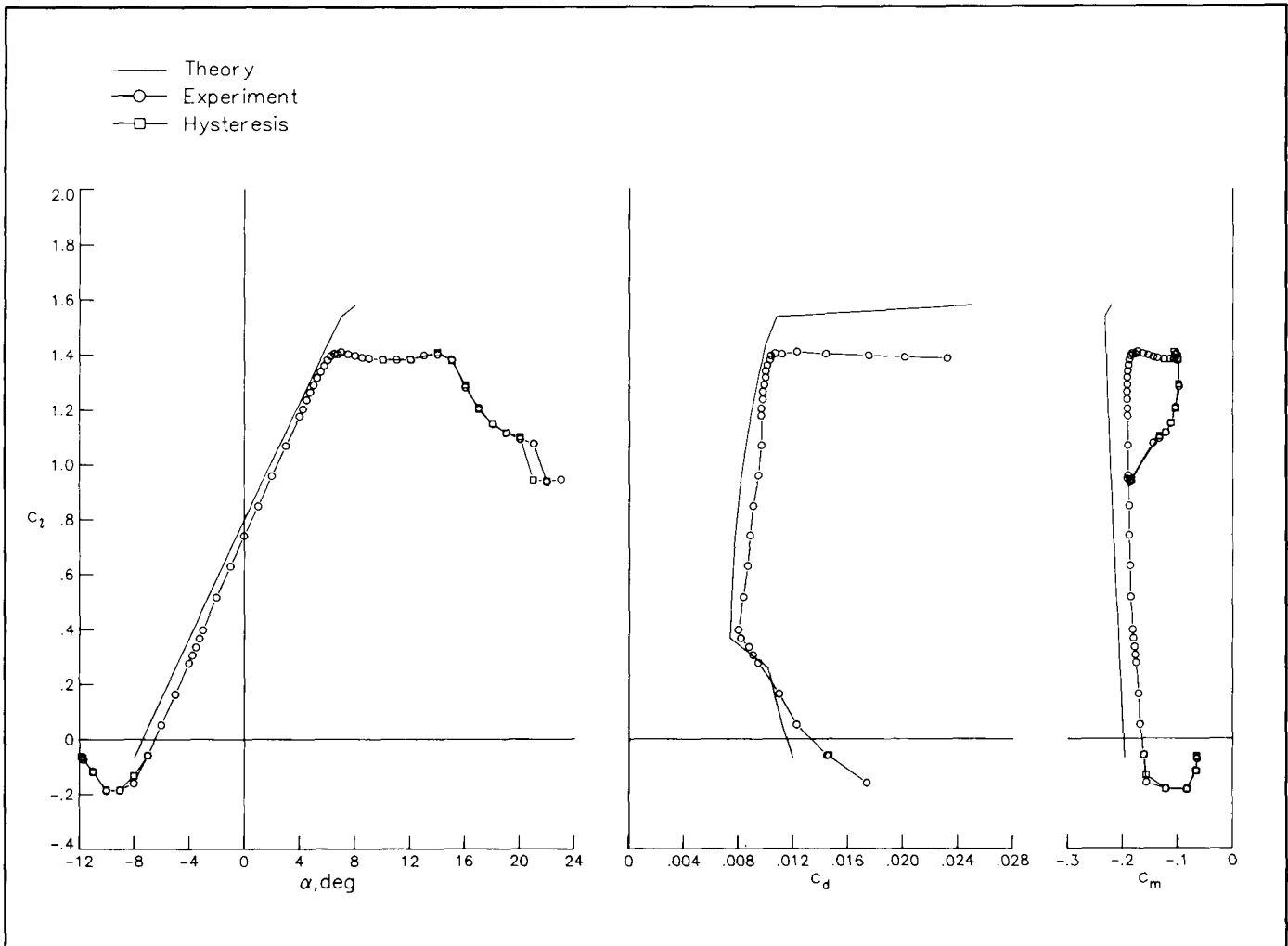
Currently, there is interest in the development of high-altitude, long-endurance remotely piloted vehicles for a number of proposed missions including communications relaying, weather monitoring, and providing targeting information for cruise missiles. The preliminary design and sizing of such aircraft is complicated, however, by the fact that data regarding suitable airfoils are limited. This limitation is due to the fact that such vehicles, unlike those for which the majority of airfoils have been developed in the past, operate at fairly high lift coefficients and at relatively low Reynolds numbers. Thus, to provide realistic airfoil performance information for preliminary design efforts, a generic airfoil has been designed which is suited for use on aircraft with missions similar to those noted.

The airfoil, designated the NLF(1)-1015, is unflapped and has a thickness of 15-percent chord. The design Reynolds number range is  $7 \times 10^5$  to  $2 \times 10^6$ . Low drag is predicted for lift coefficients ranging from 0.4 (the lift coefficient providing high-speed dash capability) to 1.5 (the maximum endurance design condition). Further, the airfoil is designed specifically such that the maximum lift coefficient (approximately 1.8) is unaffected by surface contamination. Consequently, takeoff and landing in rain, or with insect residue on the wings, should present no special difficulties.

An experimental investigation has been conducted in the Langley Low-Turbulence Pressure Tunnel to obtain the basic, low-speed, two-dimensional aerodynamic characteristics of the airfoil. The results have been compared with predictions from the Eppler Airfoil Design and Analysis Program as shown in the figure.

**Dan M. Somers and Mark D. Maughmer,**  
4516





Comparison of theory and experiment for NLF(1)-1015.

### Experimental Calibration of Incompressible and Compressible Stability Theory

The accurate prediction of transition is essential in the design of low-drag airfoils that depend upon tools to model the boundary-layer characteristics or stability modes correctly. Currently, the most widely used and reliable prediction technique is the  $e^N$ , or N-factor, method which is based on linear stability theory. The major objective is to calibrate this semiempirical technique, for subsonic and transonic

speeds, which depends on transition correlation with disturbance environment in tunnels or flight.

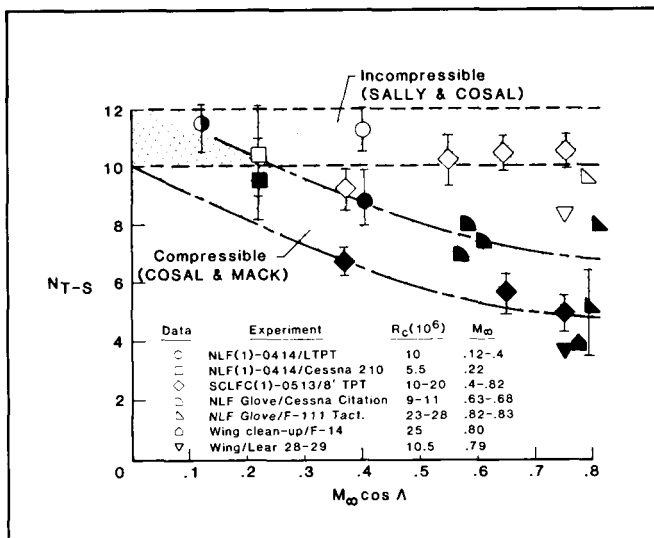
Experimental data have been recently obtained on the upper surface of advanced swept and unswept laminar-flow control (SCLFC(1)-0513) and natural laminar-flow (NLF(1)-0414) airfoils in the Langley Low-Turbulence Pressure Tunnel (LTPT), the 8-Foot Transonic Pressure Tunnel (TPT), and Cessna 210 flight tests. The same measured surface pressure and suction distributions in each case were input into the SALLY incompressible code and COSAL code for compressibility effects to calculate and compare local disturbance growth rates and integrated amplification ratios (N-factors). Corresponding transition locations influenced by characteristic environmental disturbances were compared with the calculated Tollmien-Schlichting (T-S) disturbance waves

to arrive at transition N-factors (as shown in the figure) and are compared with other reference data obtained using either the MACK or COSAL compressible codes.

The incompressible N-factors fall within a band between 10 to 12, while those from the compressible codes vary significantly over the same speed range and are about 50 percent lower at a Mach number of approximately 0.8. The results indicate allowable levels and trends for the same input data cases that were generated using the envelope method of solution in the SALLY and COSAL codes.

The consistency of the wind tunnel and flight data and between different codes calibrates and extends the use of incompressible and compressible linear stability theory for design. However, the fact that lower N-factor values were obtained for compressible compared to incompressible codes implies that compressibility is not conservative.

(William D. Harvey, 2631)

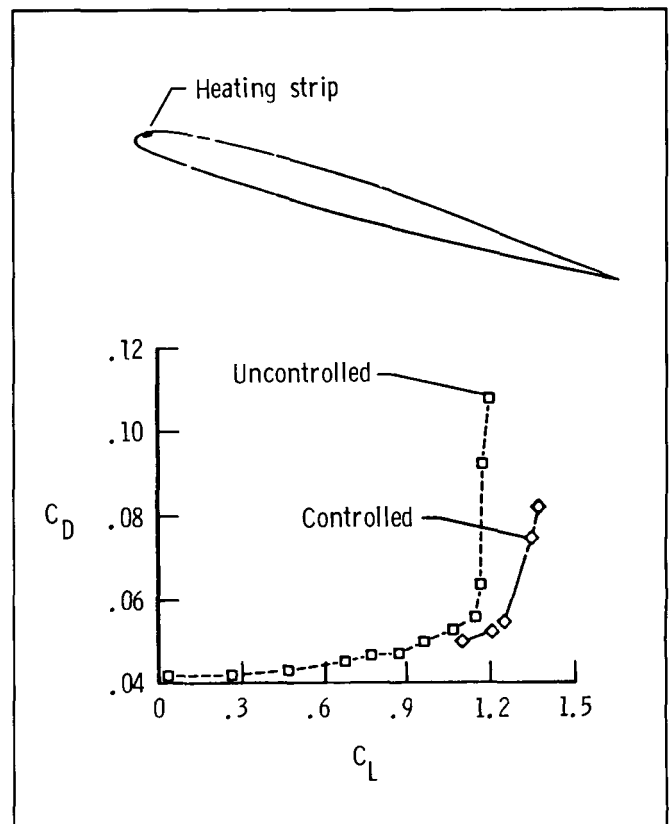


Allowable T-S disturbance amplification ratios at measured transition.

## Unsteady Flow Simulations About an Airfoil: Application to Model Helicopter Blade With Active Control

An important design consideration for the rotor and blades is to operate at high-lift conditions. Ideally, in this situation, the boundary layer must not separate; however, if the angle of attack is increased sufficiently, separation is unavoidable. Using flow control techniques, a number of benefits can be envisioned, one of which is to improve lift and stall characteristics.

Applications of active control both in the laboratory and in numerical experiments have been performed successfully. The present simulations are performed about an  $R_c(6)$ -08 airfoil by numerically integrating the compressible two-dimensional Navier-Stokes equations solver. Active control is simulated



Lift and drag coefficients for uncontrolled and controlled runs.

by local modification of the temperature boundary condition over a narrow strip on the upper surface of the airfoil (as shown in the figure). Results for laminar and for turbulent separation show significant increase in lift and reduction in drag with increasing angle of attack. Both mean and perturbed profiles are favorably altered when excited with the same natural frequency by moderate surface heating for both laminar and turbulent separation. Shear layer is found to be very sensitive to localized surface heating in the vicinity of the separation point. The figure shows the variation of the lift and drag coefficients  $C_L$ ,  $C_D$  for turbulent separation at a Reynolds number of  $5.2 \times 10^6$  and a Mach number of 0.35. The excitation field at the surface sufficiently alters both the local as well as the global circulation and therefore causes an increase in lift and reduction in drag.

(Lucio Maestrello and Forooz F. Badavi, 2631)

### Novel Approach to Detection of Laminar Separation and Reattachment

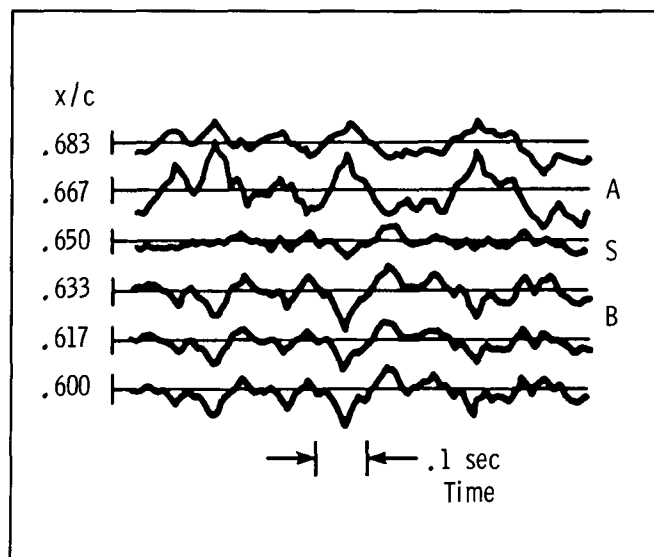
A chronic need has existed in wind tunnel and flight test applications to develop a simple and reliable technique to accurately determine regions of flow separation and reattachment and transition from laminar to turbulent flow. The development of multielement hot-film sensors has made it possible to accurately detect laminar, transitional, and turbulent boundary layers. However, when laminar separation takes place, the shear layer in the neighborhood of the separation "point" is laminar upstream as well as downstream. The signals from different surface films located in this region look indistinguishable. Furthermore, when hot-film signals indicate transition and turbulence, it is not possible to conclude whether these changes have occurred in a boundary layer or within a separation bubble.

A major breakthrough has been achieved recently with the discovery of phase reversal in low-frequency dynamic shear stress signals across regions of flow separation and reattachment. This phase reversal has made it possible not only to map laminar, transitional, and turbulent flow regions, but also to simultaneously locate flow separation and reattachment (when present). The time history of signals from hot films in the neighborhood of separation is shown in the figure. These signals were obtained by

increasing the gain to retrieve information from laminar shear stress signals that were otherwise indistinguishable. Separation is indicated both by the low amplitude of dynamic shear stress ( $x/c \simeq 0.65$ ) and by the phase reversal across the separation (points A and B). Similar results were obtained at reattachment when the high-frequency signals were filtered out.

The multielement sensor can be used for the diagnostics of complex steady and unsteady flow structures such as shock boundary-layer interaction and buffet. The technique has significant potential for wind tunnel and flight test applications with great savings in time and effort.

(John P. Stack and Siva M. Mangalam, 2631)



*Time history of signals from films in neighborhood of laminar separation.*

### Wall Interference Assessment/Correction of Transonic Airfoil Data From Adaptive Wall Tunnel

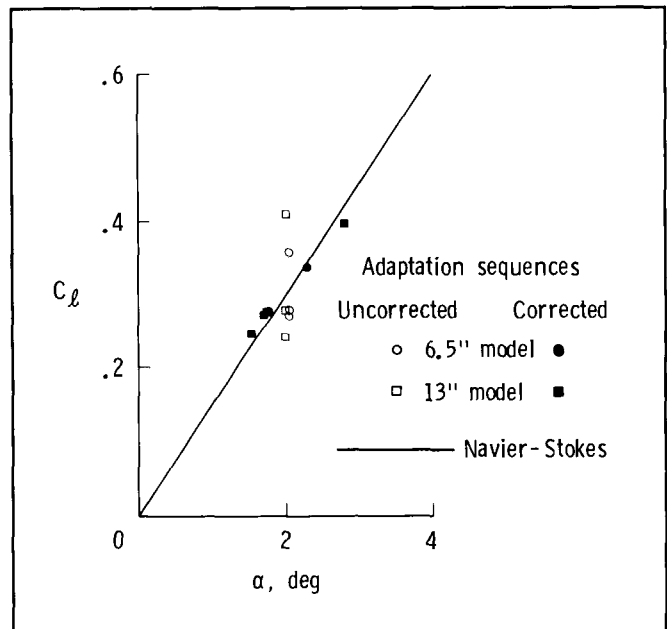
Wind tunnel wall interference effects on transonic airfoil tests arise from top and bottom wall confinement of the model flow field and viscous and inviscid interactions near the model and tunnel sidewall

junction. Reliable and robust means to eliminate and correct for these effects are required. Ventilated and adaptive-wall transonic test sections are used to reduce or minimize aspects of the wall interference; useful corrections for residual interference effects can often be obtained from a wall interference assessment/correction (WIAC) code. For airfoil tests, Kemp's WIAC code TWINTN4 models the in-tunnel flow field at the measured flow conditions with model and wall pressures prescribed to determine an effective shape and then finds a corresponding free-air flow at corrected flow conditions. This code, originally developed for ventilated-wall tunnels, has been modified to account for shaped solid top and bottom walls. The modified WIAC code was then applied to the first airfoil data from the new 13- by 13-in. adaptive wall test section of the 0.3-Meter Transonic Cryogenic Tunnel (0.3-Meter TCT). A comparison of results from two sizes of an NACA 0012 airfoil serves to validate the procedure.

An example of the WIAC application to this NACA 0012 data from the 13- by 13-in. test section is shown in the figure. The data were taken during adaptation sequences with wall shapes ranging from nominally straight to fully adapted contours. The nominal tunnel flow conditions were approximately a Mach number of 0.65, an angle of attack of  $2^\circ$ , and a chord Reynolds number of  $9 \times 10^6$ . The various uncorrected lift coefficients at the same nominal angle of attack signify a range of wall interference effects for the seven different model and tunnel configurations. Open symbols denote the uncorrected data (circles represent a 6.5-in. model and squares a 13-in. model). The WIAC corrected data are denoted by filled symbols (circles represent the 6.5-in. model and squares the 13-in. model). Corrections to lift curve data appear primarily as changes in the angle of attack. To a lesser degree, the corrections appear as a change in the lift coefficient due to renormalization at the corrected Mach number. There is good correlation among the two sets of WIAC-corrected data and the curve calculated using the Swanson-Turkel two-dimensional, free-air Navier-Stokes code. The largest corrections are, as expected, obtained for the least-adapted wall points, although small corrections are obtained even for the best adapted wall points, clustered around a lift coefficient  $C_l$  of approximately 0.28. The corrections improve the correlation among these sets of NACA 0012 data which contained different wall interference effects at the

same nominal flow conditions. Similar improvements in correlation of WIAC-corrected data have also been seen in the drag rise characteristics for these models; drag rise curves more clearly illustrate the effects of the Mach number corrections.

(Lawrence L. Green and Perry A. Newman, 2627)



Lift coefficient versus angle of attack for NACA 0012 airfoil in partially adapted wind tunnel. Data are for 13- by 13-in. adaptive wall, 0.3-Meter TCT with  $M_T \approx 0.65$ ,  $\alpha_T \approx 2^\circ$ , and  $Re_c = 9 \times 10^6$ .

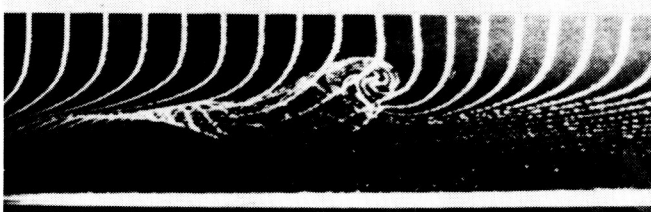
## Laminar Breakdown of Boundary Layers

Detailed understanding of the underlying mechanisms that govern the transition of a fluid as it evolves from a laminar to a turbulent state has been an outstanding problem in the research community for the last several decades. With the advent of large supercomputers, it has become possible to directly simulate the beginning stages of the transition process, called laminar breakdown, of an incompressible

wall-bounded flow (in this case, water). This simulation is done by solving the governing equations for fluids (the Navier-Stokes equations) with no approximations.

The upper part of the figure shows the result of one such simulation and the comparison against an experiment performed more than 20 years ago. Hydrogen bubbles are released periodically from a wire placed normal to the plate and are convected with the fluid. The rollup of the hydrogen bubble lines is directly related to the laminar breakdown of the boundary layer. The bottom part of the figure is obtained from a direct numerical simulation and shows the same characteristics. This simulation was performed on a discrete grid of over  $4 \times 10^6$  nodes. With the confidence gained from this validation of the numerical algorithms developed over the past several years, researchers can now devise diagnostic tools that were inaccessible to the experimentalist and can shed some new light on many remaining unresolved issues.

(G. Erlebacher, T. A. Zang, and M. Y. Hussaini, 3171)



Experimental

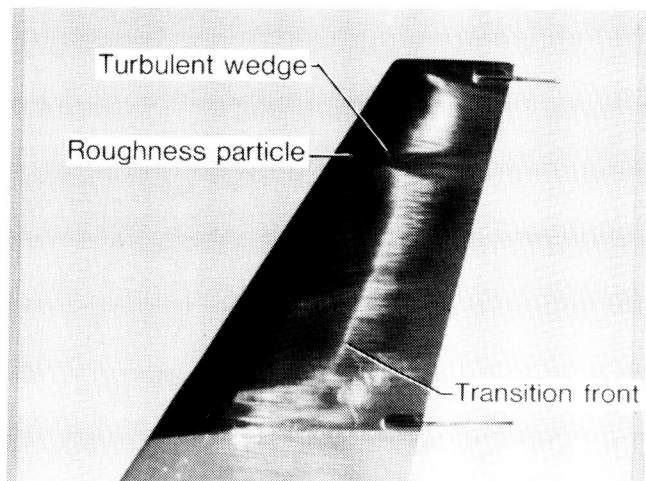


Numerical

*Experimental and numerical visualization of laminar breakdown in incompressible flow.*

## Liquid Crystals for Boundary-Layer Flow Visualization

A new method for boundary-layer flow visualization in aerodynamic and hydrodynamic testing has been developed. This technique is based on the ability of liquid crystals to change color in response to changes in shear stress and temperature. Although the liquid crystals appear as oily liquids, they have certain mechanical properties that are analogous to solid crystals. In particular, liquid crystals scatter light very selectively. Thus, when the liquid crystals are subjected to certain physical influences (primarily shear stress and temperature), the wavelength of reflected light changes accordingly. Since the fundamental chemical structure is unaffected by these changes, a liquid-crystal coating will respond quickly and repeatedly to the physical changes.



L-86-1401

*Boundary-layer transition visualization using liquid crystals on Lear 28/29 airplane winglet.*

A liquid-crystal coating is formulated for a particular application to change colors in response to differences in relative shear stress within the temperature environment of the test article. These formulations can be made to respond at test conditions as low as  $-22^{\circ}\text{F}$  and up to  $480^{\circ}\text{F}$ . Liquid crystals have been used to visualize the boundary layer in flight at speeds up to Mach 0.8 and altitudes up

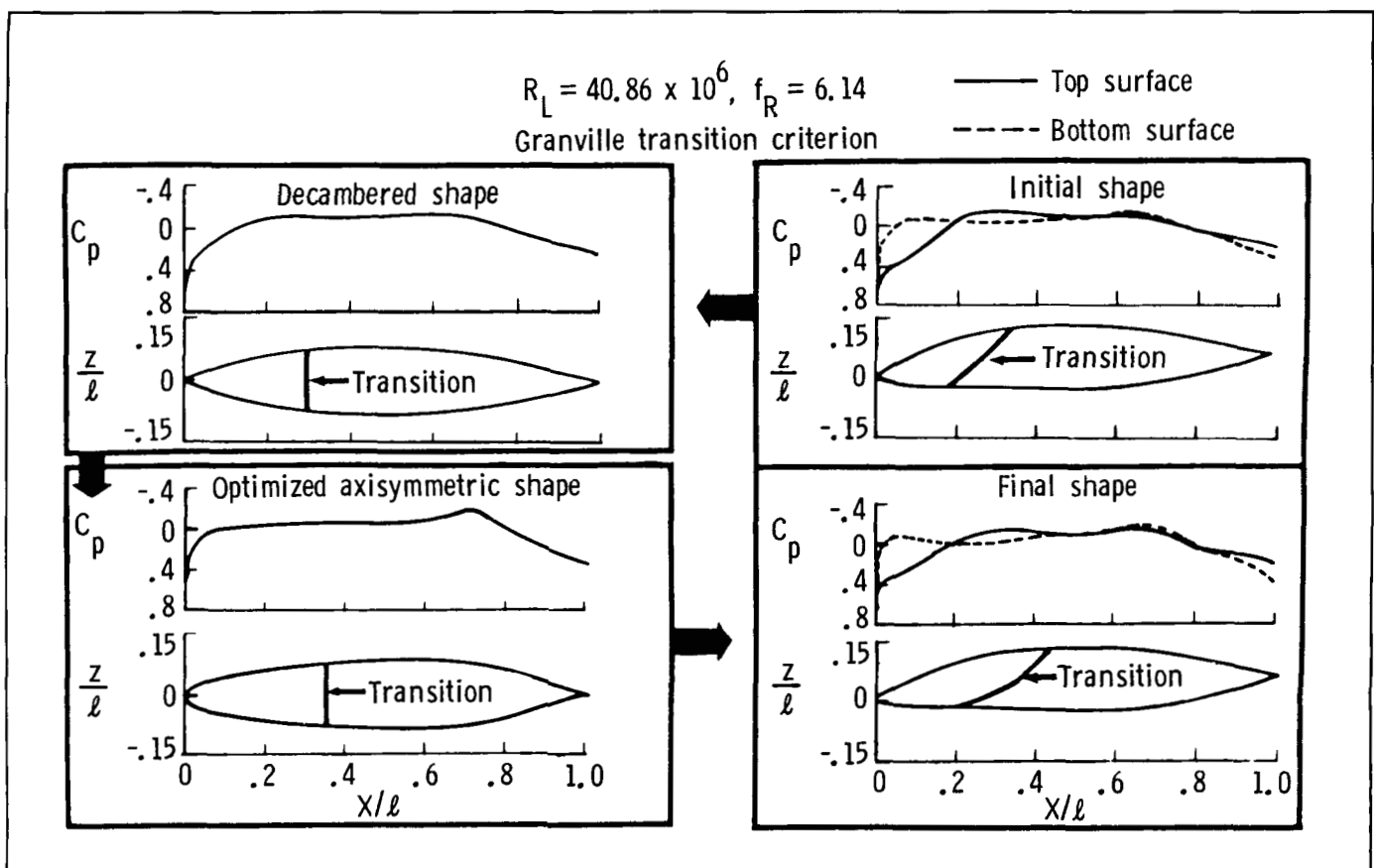
to 48,000 ft using a Lear 28/29. The photograph shows the boundary-layer transition location on the winglet as a change from dark to light. The higher shear stresses associated with the turbulent boundary layer downstream of transition produced brighter colors (color figure is available from the author). Liquid crystals have also been used in wind tunnels at dynamic pressures as low as 5 lb/ft<sup>2</sup>. Another successful application of the liquid-crystal technique has been on surfaces tested under water. In addition to visualization of boundary-layer transition locations and modes, liquid crystals have been used to observe other aerodynamic phenomena such as shock locations, laminar separation bubbles, and separated flows.

(Clifford J. Obara, 3274)

## Design of Natural Laminar-Flow Fuselages

Recent technological advances in airplane construction techniques and materials have paved the way for the production of smooth aerodynamic surfaces permitting long runs of natural laminar flow (NLF). These advances lead to excellent opportunities for reducing the drag of airplanes by increasing the extent of NLF on all airframe surfaces including fuselages. However, until recently no validated computational tools have been developed for the design of nonaxisymmetric laminar bodies.

A simplified computational procedure has been developed to design nonaxisymmetric subsonic NLF fuselage shapes with minimum drag. The process of



L-86-3704

Body shape optimization procedure.  $R_L$  is length of Reynolds number,  $f_R$  is ratio of length to maximum thickness,  $C_p$  is pressure coefficient,  $z/l$  is body ordinate, and  $x/l$  is nondimensional axial distance.



designing efficient nonaxisymmetric shapes is illustrated by an example in the figure. An axisymmetric fuselage shape is obtained by starting the analysis using the same thickness distribution and fineness ratio as for the initial nonaxisymmetric fuselage shape. This simplifying approximation allows the influence of body shape changes on transition to be estimated using very efficient computation of boundary-layer parameters. The design program consists of an optimizer, an aerodynamics analyzer, a boundary-layer transition predictor (a Granville transition criterion), and a drag estimator. The axisymmetric body can be described by a very small number of design parameters. Boundary-layer transition length or drag is chosen as the objective function. In the design program, the objective function is optimized subject to certain geometric and aerodynamic constraints chosen to generate realistic and practical designs. Converged design variables representing an optimized axisymmetric fuselage shape for large extents of NLF are derived. The "optimized" nonaxisymmetric fuselage shape is then constructed by superimposing the camber distribution on the optimized axisymmetric shape. The "optimized" nonaxisymmetric fuselage will have a larger amount of natural laminar flow than the initial nonaxisymmetric shape. The computational design procedure described is efficient and economical in comparison to the methods in which the nonaxisymmetric fuselage shape is described directly by a very large number of design variables. As more advanced three-dimensional codes and data become available, the accuracy of this simplified design method will be evaluated.

(S. S. Dodbele, 3274)

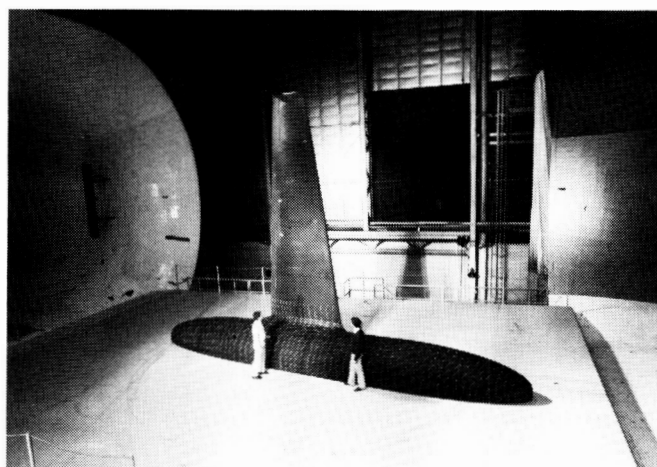
### Full-Scale Semispan Tests of Natural Laminar-Flow Airfoil

Tests of a full-scale semispan model were conducted in the Langley 30- by 60-Foot Tunnel to study the low-speed high-lift characteristics of a three-dimensional wing using the HS-NLF-0213 airfoil section. The test setup is shown in the figure. The tests were conducted at a Reynolds number of  $3.7 \times 10^6$  based on the wing mean aerodynamic chord and over an angle-of-attack range from  $-10^\circ$  to  $30^\circ$ . A slotted

28-percent chord flap that extended from the wing root to a span location of  $2y/b = 0.79$  was the high-lift device used for these tests.

A  $C_{L_{\max}}$  of 1.4 was achieved with the flap undeflected, and a  $C_{L_{\max}}$  of 2.6 was achieved with the flap deflected  $40^\circ$ . The net result of having a significant amount of laminar flow for drag reduction was illustrated by fixing the boundary-layer transition at a chord station near the leading edge of the wing. With transition fixed at  $x/c = 0.05$  on both the upper and lower surfaces, an increase in drag coefficient  $C_D$  of 0.003 was obtained at a lift coefficient  $C_L$  of 0.27. Data from two-dimensional tests indicate an increase in  $C_D$  of 0.004 for similar conditions. Data on the effect of boundary-layer transition on the lift characteristics showed a slight loss in lift near  $C_{L_{\max}}$  for this airfoil. This reduction in  $C_L$ , however, is small, and its effect on performance would be minimal. These results indicate that the high-lift characteristics of the HS-NLF-0213 airfoil are generally representative of those of more conventional airfoils, and this maximum lift capability is adequate to satisfy the landing requirements of advanced transport and commuter designs.

(David E. Hahne and Frank L. Jordan, Jr., 2184)



L-87-00300

*Large-scale semispan natural laminar-flow airfoil model.*

## Light Airplane Spin Resistance

A complementary program of wind tunnel model testing and airplane flight testing is developing means to improve the safety of light airplanes through improved stall departure and spin resistance characteristics. Leading-edge modifications have been developed to improve the high-angle-of-attack aerodynamic characteristics of wings for improved lateral stability and enhanced spin resistance. Aircraft manufacturers have begun applying this technology to both new and existing airplanes. The Schweizer Aircraft Corporation has added leading-edge modifications to their SA2037A surveillance airplane for improved controllability at low speeds. Both the 2-place DeVore Aviation Corporation Sunbird and the 10-passenger OMAC, Inc. Laser 300 are incorporating this technology for improved high-angle-of-attack characteristics.

Researchers at Langley Research Center are assisting the General Aviation Manufacturers Association (GAMA) and the Federal Aviation Administration (FAA) in the development of criteria for certification of spin-resistant airplanes. To aid in the validation of the criteria, two representative light airplanes were tested against the criteria. Both basic wing configurations and modified wing leading-edge configurations for enhanced spin resistance were tested. Failure of the basic configurations to meet the

spin resistance criteria and ability of the modified-wing configurations to meet the criteria showed that the criteria contain a recognizable increase in spin resistance beyond that of current airplanes and that the criteria are achievable. Both DeVore Aviation Corporation and OMAC, Inc. have received permission from the FAA to certify their airplanes using the spin-resistant criteria.

Research is continuing to refine the spin-resistant wing design, and at the request of both the FAA and industry, selected pilots are being familiarized with spin-resistant characteristics using one of the NASA spin resistance research airplanes.

(H. Paul Stough, III, 3274)

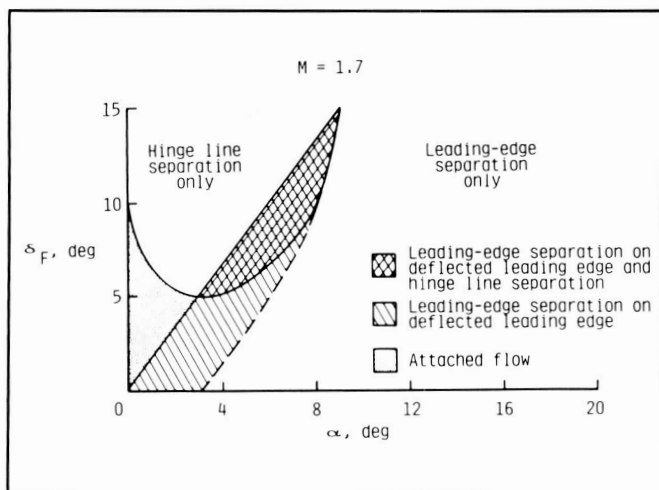
## Study of Leaside Flows Over Conically Cambered Delta Wings at Supersonic Speeds

It is necessary to understand the flow that exists about a wing before significant improvements in aerodynamic performance can be achieved. One area in which a small amount of data exists is wing leading-edge vortex flow at supersonic speeds. To address this need, a flow visualization study has been conducted on a series of conically cambered delta wings to determine the feasibility of extending the vortex flap design concept to supersonic speeds.

The test models are a series of delta wings which vary in leading-edge camber only. Wing camber is achieved by deflecting the outboard 30-percent section of the local wing semispan for a reference  $75^\circ$  sweep flat delta wing. The four wing models have leading-edge deflection angles  $\delta_F$  of  $0^\circ$ ,  $5^\circ$ ,  $10^\circ$ , and  $15^\circ$ , measured streamwise. Vapor screen, oil-flow, and tuft-flow visualization results were obtained for Mach numbers  $M$  of 1.7, 2.0, 2.4, and 2.8 over an angle-of-attack range  $\alpha$  of  $0^\circ$  to  $20^\circ$ . Analysis of the flow visualization data identified five distinctive leaside flow types that may be characterized in terms of  $\delta_F$  and  $\alpha$  as shown in the figure. The five flow types shown comprise various forms of leading-edge and hinge line separation. The single cross-hatched area corresponds to the condition of leading-edge separation residing on the deflected leading edge with



*Modified outboard leading edge.*



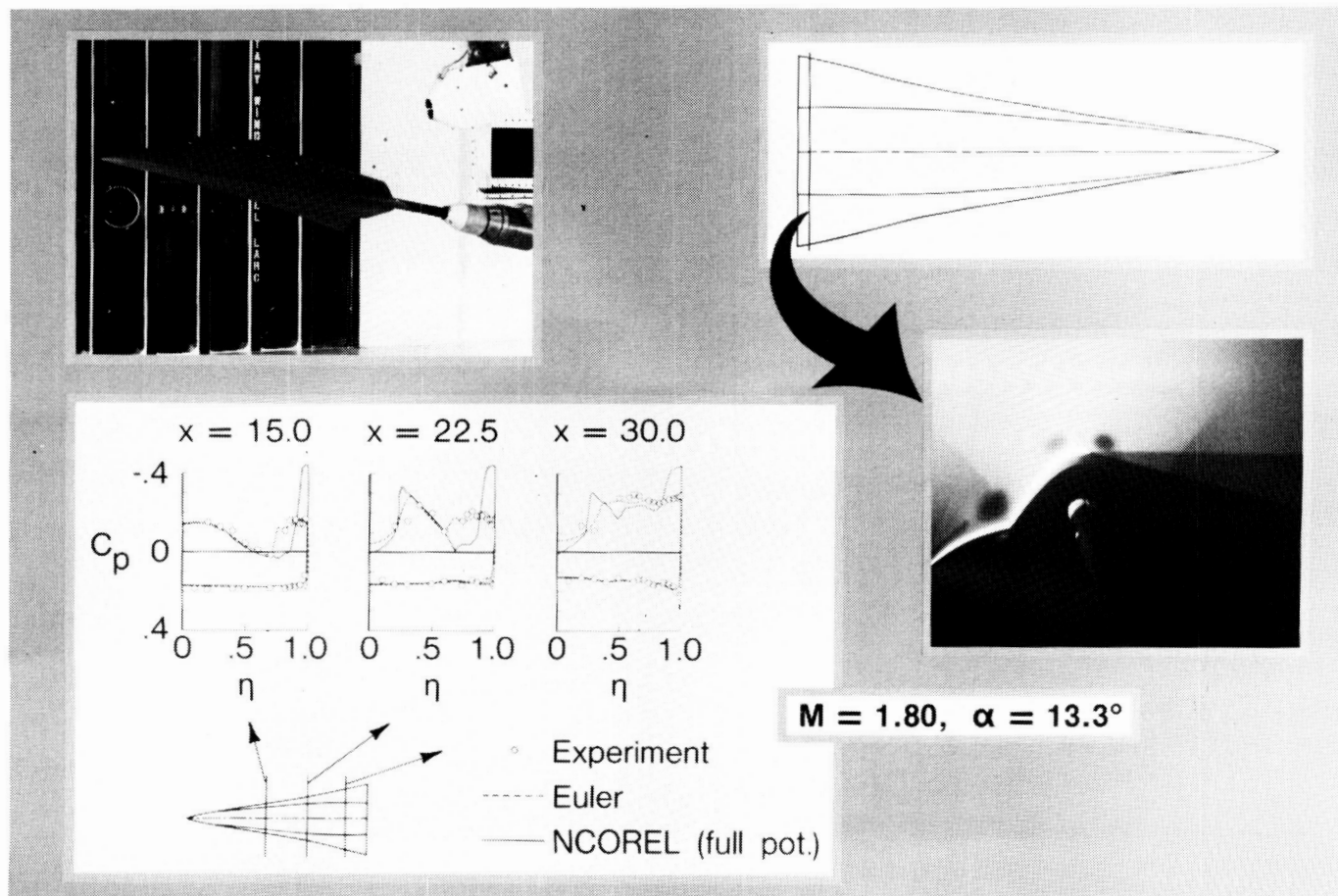
Typical leeside flow characteristics of vortex flap concept.

reattachment prior to the hinge line. The area to the right of the cross-hatched area is the condition in which the leading-edge separation (vortex) has migrated inboard over the hinge line.

(Richard M. Wood, 3181)

### Investigation of Separated Flows Over Forebody-Cambered Strake at Mach 1.80

An experimental and computational investigation of the separated flow over a fighter-type forebody with a cambered strake has been conducted. Extensive surface-pressure, vapor-screen, oil-flow, and



Forebody-strake flow field study at subsonic speeds.

force data were obtained to validate the computational methods at Mach 1.80 across an angle-of-attack range of  $0^\circ$  to  $13^\circ$ . A full-potential and an Euler solver were evaluated across the entire angle-of-attack range.

The high angle-of-attack flow field is clearly shown by the vapor-screen photograph at a Mach number  $M$  of 1.80 and an angle of attack  $\alpha$  of  $13.3^\circ$ . The vapor-screen photograph, which was taken near the trailing edge of the test article, indicates the presence of a large vortex above the strake and a pair of vortices above the forebody. An embedded flow field shock is located above the strake vortex. The experimental oil-flow and vapor-screen data show that this embedded shock formed aft of the canopy and moved outboard over the strake as the trailing edge was approached. This embedded shock apparently induced the vortex above the forebody.

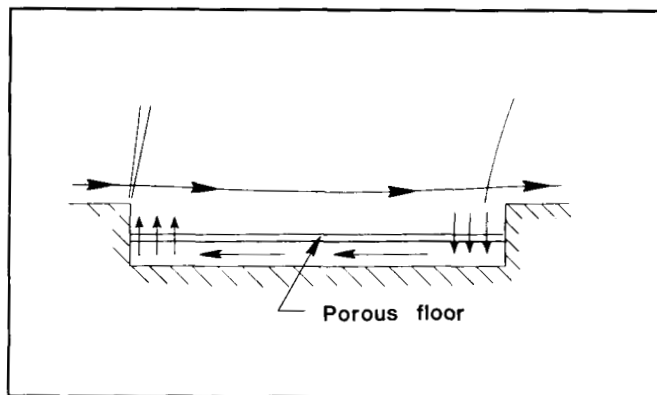
The full-potential (NCOREL code) and Euler methods accurately predict the spanwise pressure data on the lower surface where the flow remains attached. The close agreement between these two solutions indicates that entropy losses through the bow shock are small for this flow condition. As expected, the full-potential method does not predict the vortices since the full-potential equation does not contain rotational terms. However, the leading-edge vortex flow above the strake is predicted by the Euler solver through an interaction of numerical artificial viscosity with the nearly sharp leading edge of the strake. Inboard of the strake on the forebody, both methods correctly predict the surface pressures and the embedded shock, which can be seen at  $n \approx 0.4$  for  $x = 22.5$  in. and  $x = 30.0$  in. (where  $n$  is the nondimensionalized spanwise ordinate and  $x$  is the longitudinal distance from the nose).

(James L. Pittman, 4004)

### Passive Venting System for Reducing Cavity Drag

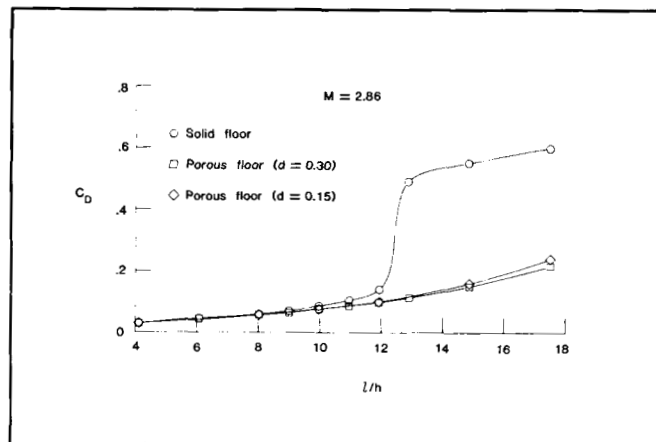
Existing data available in the literature have shown that at supersonic speeds the drag of rectangular cavities increases substantially as the cavity

flow field switches from open to closed at a length-to-height  $l/h$  ratio of approximately 12. An experimental investigation was conducted to determine the effectiveness of a passive venting system for reducing this drag increase.



Porous floor cavity flow field sketch.

As shown in the first figure, the concept employs a porous floor over a vent chamber that will permit the high-pressure air at the rear of the cavity to vent to the low-pressure region at the front of the cavity. A wind tunnel test of this concept was conducted at Mach numbers of 1.60, 1.90, 2.16, and 2.86 and at a Reynolds number of  $2 \times 10^6$ . The wind tunnel model consisted of a flat plate, cavity pallet, and balance. The cavity pallet was mounted on a one-component (axial force) balance such that only the drag of the cavity was measured. The porous floor contained approximately 3,370 holes of 0.025 in. diameter which resulted in a porosity of 11.2 percent based on the total floor area. Both solid and porous floor configurations were tested.



Effect of porosity on cavity drag.

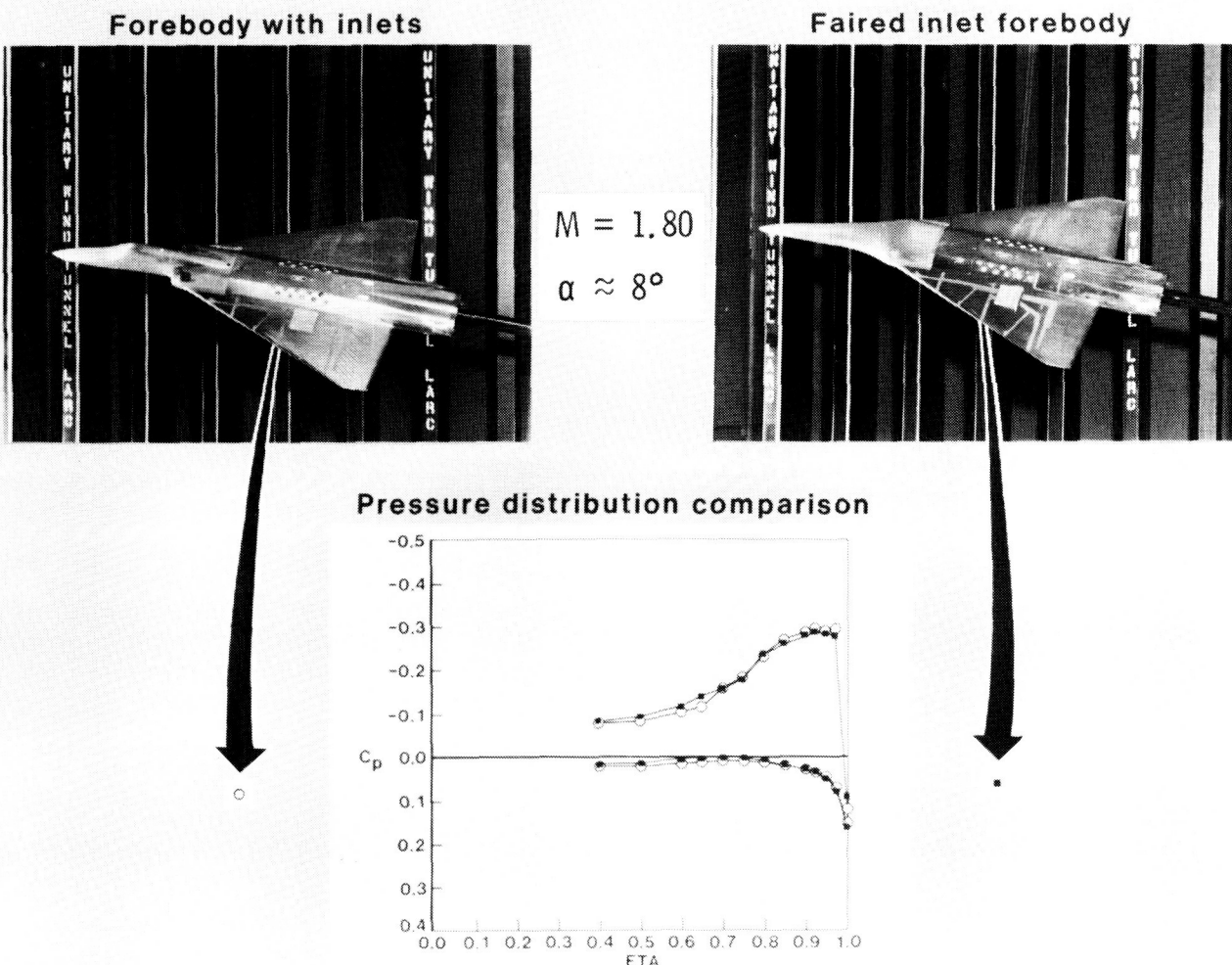
The solid floor cavity drag data show the typical large drag increase at  $l/h$  of approximately 12, whereas the porous floor data show the elimination of this drag increase. Varying the vent chamber height  $d$  had no effect on the porous floor cavity drag for  $l/h$  of less than approximately 12 and had a minimal effect for  $l/h$  of greater than approximately 12. (Floyd J. Wilcox, 4010)

### Equivalent Forebody Concept for Supersonic Speeds

An investigation was conducted to develop a method for generating a simple faired forebody that

would produce an influence on the wing equivalent to that of a forebody with flowing inlets. The approach was to use the PAN-AIR linear-theory panel code to design an equivalent forebody that would produce the same PAN-AIR predicted flow field disturbances as produced by the forebody with the flowing inlets. This concept was validated for a generic fighter configuration in the Langley Unitary Plan Wind Tunnel. The successful validation of this concept could also make it possible to use much simpler and less costly equivalent forebody models in wind tunnel tests that are directed primarily at studying wing aerodynamics.

As shown in the figure, the experimental validation was conducted by measuring wing pressures for a model configured with an equivalent forebody. At



Equivalent forebody for supersonic speeds.



the design conditions of  $M = 1.80$  and  $C_L = 0.3$ , the agreement between the two pressure distributions is excellent; data at the off-design conditions are being analyzed to determine the range in applicability of this particular equivalent forebody.  
(Davy A. Haynes, 4008)

## Wing Tip Vortex Turbine for Transport Aircraft

A wind tunnel investigation has been conducted in the 14- by 22-Foot Subsonic Tunnel to determine the location and strength of the wing tip vortex on a  $1/8$ -scale model of a Boeing 737 transport configuration. The tests are part of a program to investigate the feasibility of using a wing-tip-mounted turbine to extract energy from the strong tip vortex. An existing Boeing 737 wind tunnel model was modified to simulate the turbine on the right wing. The wing tip flow field was measured with a survey rake mounted on a traverse mechanism to determine the position of the vortex relative to the wing at cruise angles of attack. A scaled wing tip turbine, also mounted on the traverse mechanism, measured rotational strength of the vortex.

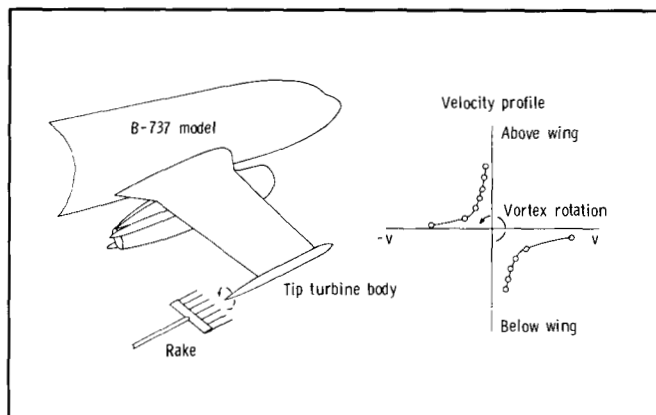
Tests were conducted at a free-stream dynamic pressure of  $30 \text{ lbf/ft}^2$  at angles of attack of  $0^\circ$ ,  $2^\circ$ , and  $4^\circ$ . The rake that had 2-in. spacing between probes and the tip turbine are positioned in 0.5-in. increments from 8 in. below to 8 in. above the wing tip at several downstream locations.

The data indicate an increase in velocity associated with the installation of the vortex turbine nacelle (without turbine blades) when compared to the basic wing tip. These data also indicate that the vortex center is located approximately 2 in. (model scale) above the basic wing tip and only 1 in. above when the turbine nacelle is installed.

The vortex turbine blades were positioned behind the turbine nacelle, and a maximum rpm of 750 was measured at the location corresponding to the vortex center. This rotation decreased and ceased at one blade radius (4.5 in. model scale) above or below the vortex center indicating no rotational flow away from the vortex. These results will play an important

part in the flight turbine blade design and the position of the turbine at the wing tip of the Boeing 737 for maximum vortex energy recovery.

(John W. Paulson, Jr. and Claude C. Patterson, 4812)



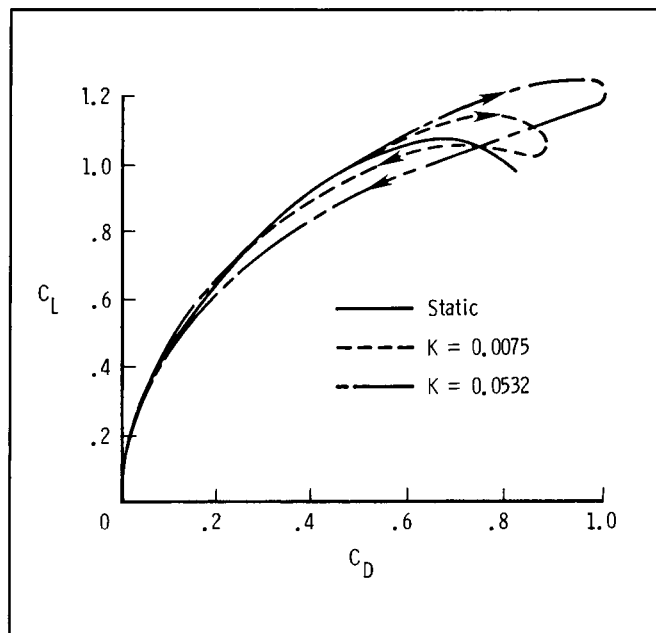
Boeing 737 test setup and tip vortex velocity profile.

## Dynamic Stall Effects on Aircraft Configurations

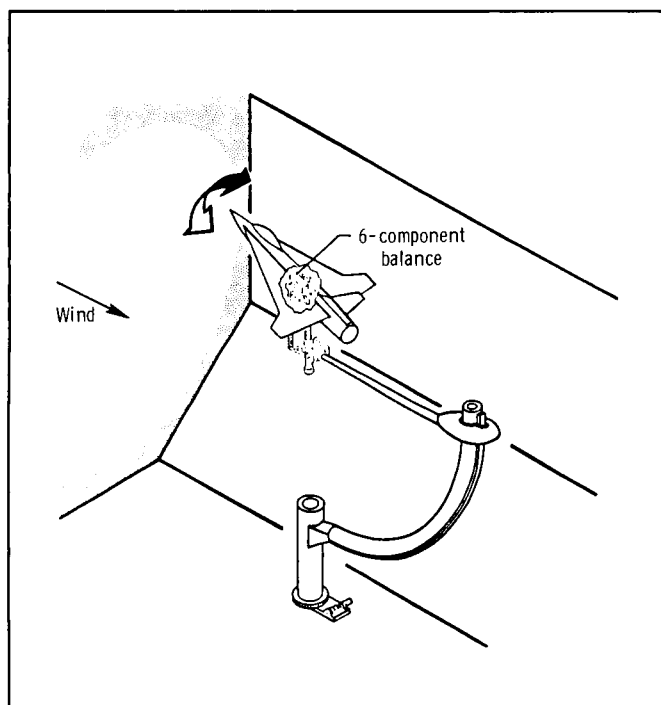
Effective high-angle-of-attack maneuvering is becoming increasingly important in modern air combat. Current fighter aircraft design trends include the capability to perform controlled transient maneuvers at high angles of attack including excursions into post-stall conditions. At present, understanding of the very complex flow phenomena that occur at these flight conditions is limited. A research program is under way to further understand unsteady flow characteristics for aircraft undergoing large-amplitude motions at high angles of attack.

As a first step in the research program, a  $70^\circ$  delta wing has been tested in the Langley 12-Foot Low-Speed Wind Tunnel. The model, shown in the first figure, was oscillated in pitch at various frequencies and tunnel speeds. Conventional six-component force-and-moment measurements were obtained during model oscillation. Smoke flow visualization was utilized to gain insight into the flow mechanisms involved.

Test results have shown large effects of pitch rate on aerodynamic coefficients even at very low frequencies of oscillation. Lift and drag overshoots and hysteresis loops were observed which closely follow trends observed for two-dimensional airfoils undergoing pitch oscillations. The second figure shows a drag polar of the delta wing at frequencies of oscillation compared with static data. The oscillating frequency is reduced to nondimensional form through the relation  $K = \omega \bar{c} / 2V$  where  $\omega$  is the oscillating frequency in radians per second,  $\bar{c}$  is the mean aerodynamic chord in feet, and  $V$  is the free-stream velocity in feet per second. The effect of pitch rate is to extend the drag polar curve beyond the static values. An increase of pitch rate gives a corresponding increase in maximum lift. As the model starts pitching down, the hysteresis loop adds a significant increment of drag at a given lift coefficient. These observed effects were seen to be related to a lag in the vortex development/burst cycle as the model was oscillated. (Jay M. Brandon and Gautam H. Shah, 2184)



Effect of reduced frequency on  $C_L$  versus  $C_D$ .



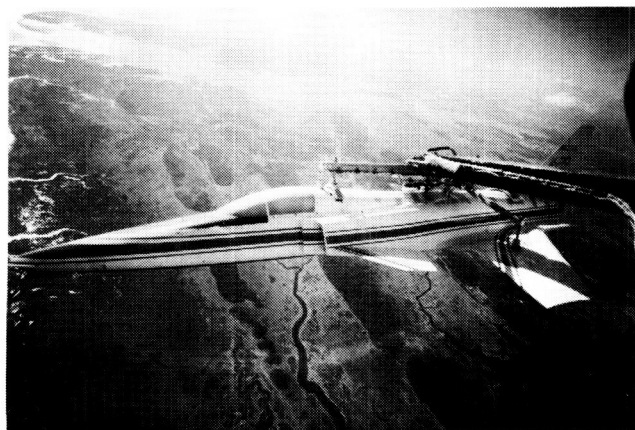
Dynamic pitch rig.

### High-Angle-of-Attack Drop Model Research on X-29

A 22-percent scale model of the forward-swept wing X-29 configuration is being tested at the Langley Research Center Plum Tree Island Drop Facility to explore the high-angle-of-attack flight characteristics and to develop and evaluate high-angle-of-attack control law concepts for application to the full-scale test aircraft.

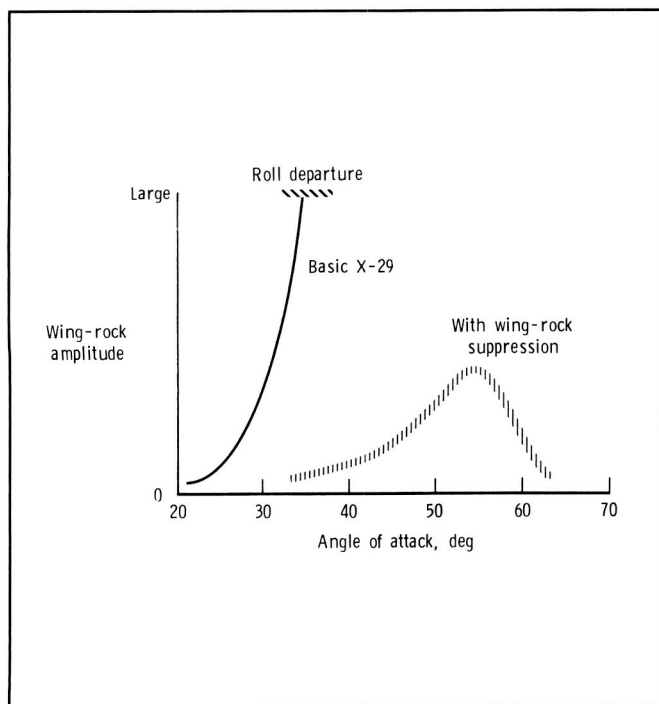
The free-flying tests are conducted by dropping the unpowered model from a helicopter at an altitude of 6000 ft. The X-29 model mounted to the helicopter is shown in the first figure. Specific test flight maneuvers are conducted down to about 2000 ft, and the recovery parachute is deployed at 600 ft. The model is controlled by a pilot at a ground station using information provided by a video image of the model and conventional flight instruments. Stability and control augmentation is implemented on a ground-based computer and combined with pilot commands and control surface inputs that are transmitted to the model.

Test flights designed to assess the flying qualities using the control laws currently implemented on the full-scale aircraft show that the configuration is susceptible to a large-amplitude oscillatory lateral instability called wing-rock. As shown in the second figure, the instability begins just above an angle of



L-87-03588

X-29 drop model mounted on helicopter.



Effect of control law modifications on wing-rock motions.

attack of  $20^\circ$  and grows in severity with increasing angle of attack until the configuration experiences a snap roll departure. A wing-rock suppression control law scheme, using a high authority high gain roll damper, was developed on a computer simulation of the X-29 and was subsequently tested with the drop model. The results of the flight tests indicate that the wing-rock suppression scheme significantly reduced the severity of the dynamic instability. Incorporating a scheme of this nature in the full-scale aircraft will result in considerably improved handling qualities. Other areas of the high-angle-of-attack flight regime are being addressed and include departure and spin susceptibility, spin prevention, and enhanced maneuverability. The overall drop-model test effort is focused on producing a safe yet effective operation in the stall and poststall flight regimes.

(Mark A. Croom, 2184)

### Navier-Stokes Predictions of Multifunction Nozzle Flows

Increased mission requirements for tactical aircraft have given rise to the consideration of multifunction nozzles to provide both thrust vectoring and reversing for enhancement of aircraft maneuver, attitude control, and takeoff and landing performance. Inherent in this general class of nozzles is the large number of design options available to the designer. Very often nonconventional nonaxisymmetric nozzle designs result, and they require extensive testing and analysis. Advances in computational fluid dynamics have produced a number of tools that have the potential to provide the nozzle designer with aid in screening multifunction nozzle designs.

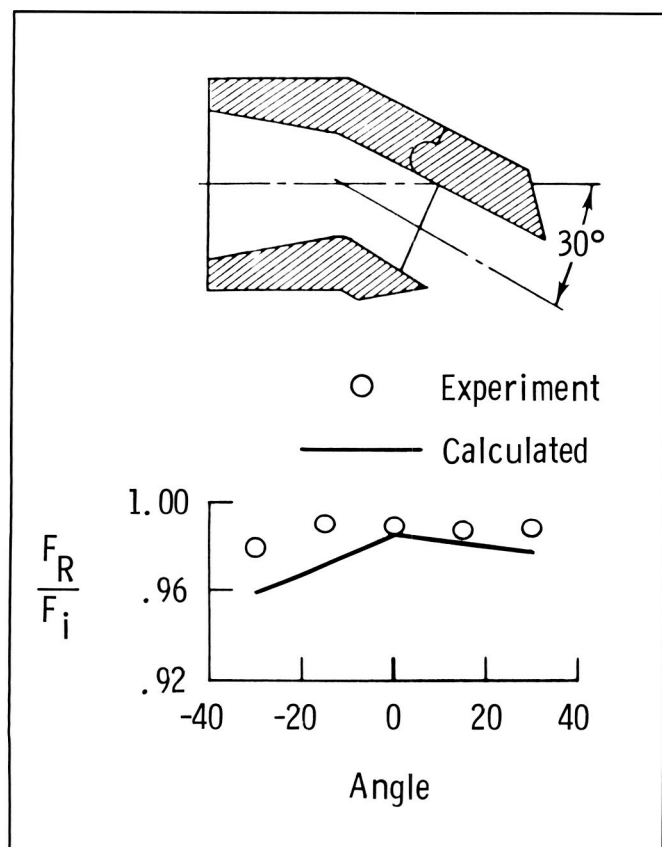
One such tool is a two-dimensional, time-dependent Navier-Stokes code, TRV, which has been developed by Imlay for predicting flows in nozzles with thrust vectoring and reversing. This code is based on the implicit, finite-volume method of MacCormack. Comparisons of predictions with experiments have shown that, for a wide range of nozzle configurations, the code can accurately predict both the flow fields and performance for nonaxisymmetric nozzles where the flow is predominantly two-dimensional in nature. Both pressure distributions



and performance parameters have been shown to agree well in most cases at nozzle pressure ratios at or above the design values. Discrepancies can occur at low nozzle pressure ratios where flow separation is present.

A sample of the results obtained on a vectoring two-dimensional convergent-divergent (2-D/C-D) nozzle with aft flap is shown in the figure. The resultant thrust ratio (nozzle efficiency  $F_R/F_i$ ) is shown as a function of nozzle vector angle. The comparison between theory and experiment indicates that the code did a reasonably good job in predicting both the levels and trends.

(R. G. Wilmoth, 4953 and L. D. Leavitt, 2674)



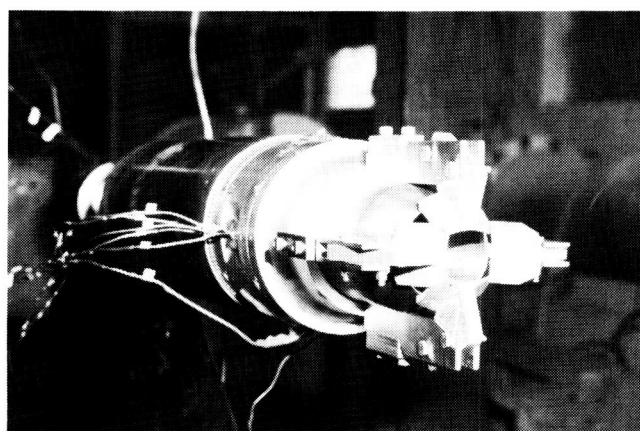
Experimental and analytical comparisons of resultant thrust ratio versus nozzle vector angle for 2-D/C-D nozzle with aft flap.

## Nozzle Post-Exit Vanes for Multiaxis Thrust Vectoring

Modern air combat requires the aircraft to maneuver effectively at high-angle-of-attack conditions. However, the angle-of-attack envelope of current fighters is limited by a combination of degraded stability characteristics and inadequate control effectiveness. One promising means to provide large control moments that are not dependent on angle of attack and dynamic pressure, as are aerodynamic controls, is vectoring the engine exhaust. One concept that can provide control moments in both the pitch and yaw planes involves the use of exhaust deflection vanes mounted externally aft of the nozzle exit (post-exit vanes). A static (no external flow) test has been conducted over a nozzle pressure ratio range from 1.6 to 6.0 to determine the performance of an axisymmetric nozzle with the post-exit vane concept installed. The effects of vane curvature, vane location relative to the nozzle exit, number of vanes (a four-vane configuration is shown in the figure), and vane deflection angle were determined.

The results of this investigation indicate that the thrust-vectoring capability of some of the post-exit vane configurations was competitive with other thrust-vectoring concepts. However, all of the post-exit vane configurations incurred large gross thrust losses between 1 and 2 percent per degree of turning to achieve vectored thrust. In general, any change in geometry which produced larger thrust vector angles also caused larger resultant thrust losses.

(B. L. Berrier and M. L. Mason, 2674)



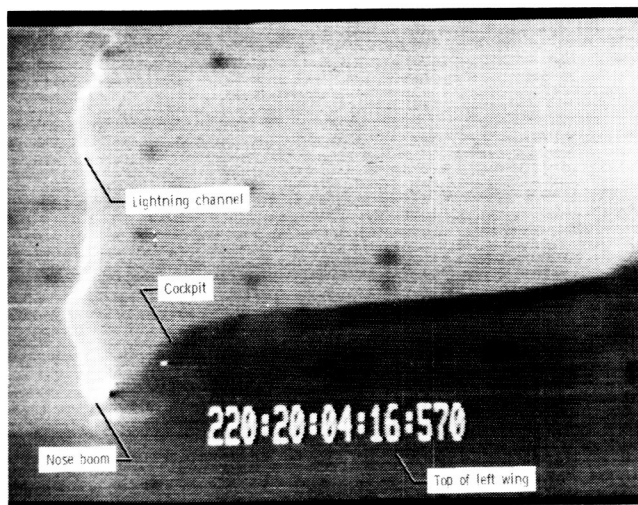
L-85-3424

Four-vane post-exit configuration.

## Storm Hazards Program

The NASA Storm Hazards Program concluded operations in 1986 with the F-106B airplane receiving 24 additional direct lightning strikes. This brought the total to 714 hits in the 7 years of thunderstorm flying. The onboard instrumentation included 12 channels of electromagnetic data with 5- and 10-ns time resolution and several video and film camera systems. In 1986, the onboard camera systems included a pair of video cameras mounted on the left wing tip to allow time series photographs of swept-stroke lightning paths from the nose boom to the tail.

Results obtained in 1986 confirmed the earlier experiences that aircraft strike rates increase with colder temperatures (higher altitudes) in thunderstorms. From 1980 to 1986, only 98 direct strikes were experienced at altitudes below 20,000 ft, where most strikes to commercial and military aircraft in routine operations have been reported. Ground-based data indicated that several strikes may have been cloud-to-ground strikes, and that most lightning strikes obtained at high altitudes were triggered



*Lightning channel attached to nose boom of F-106B airplane. View is from left wing tip.*

by the presence of the aircraft. The lightning electromagnetic measurements have established a statistical basis for peak rate of change of current and peak rate of change of electric flux density during tests be-

tween 15,000 and 40,000 ft altitudes; the peak rate of change of current was found to be several times larger than previous design criteria. The onboard camera systems have shown that the entire exterior surface of the F-106B airplane may be susceptible to direct lightning attachment, necessitating a rethinking of lightning attachment zone concepts used in aircraft design.

Finally, mathematical models that include thunderstorm electrification parameters are being developed to generalize the results from the all-metal F-106B airplane to composite aircraft employing low-voltage digital flight control and avionics systems. (Bruce D. Fisher and Felix L. Pitts, 3274)



L-83-2753

*Storm hazards F-106B research airplane.*

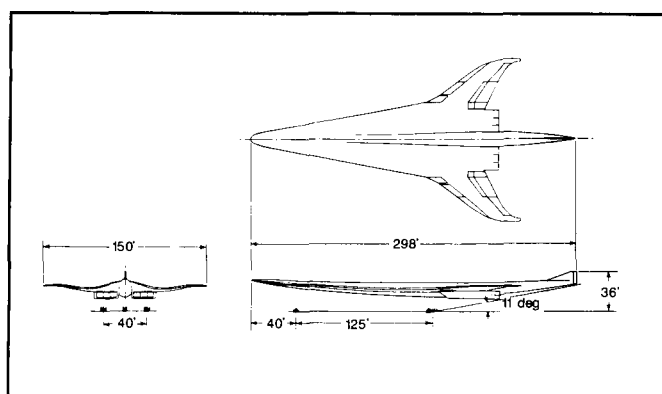
## High-Speed Civil Transport Study

A renewed interest in long-range, high-speed civil transportation has taken place both in the U.S. and internationally. The need and the opportunity for such a system were best stated in the *National Aeronautical R&D Goals: Agenda for Achievement* published this year by the Executive Office of the President, Office of Science and Technology Policy. One of three major vehicle-type goals was

the achievement of "long-distance efficiency and environmental compatibility" for supersonic commercial aircraft. The action plan set forth was to develop the fundamental technology, design, and business foundation for a long-range, supersonic transport in preparation for a potential U.S. industry initiative. NASA has undertaken both in-house and contracted studies in response to this national goal.

An early output of the in-house studies is a Mach 3 baseline concept designed to carry 250 passengers 6,500 nm. The concept utilizes wing and body blending and an advanced wing planform to achieve a high level of aerodynamic efficiency across the Mach range. Careful attention to the low-speed aerodynamics has resulted in substantially improved estimated low-speed aerodynamics performance that results in improved takeoff and landing performance and lower associated noise. Utilizing propulsion system, materials, structures, and control systems technology estimated to be available by the year 2005, the takeoff gross weight for the 6,500-nm mission with reserves is calculated to be less than 700,000 lb. This concept will provide a focus for study and evaluation of emerging technologies, such as low boom concepts, supersonic laminar flow, advanced propulsion systems, and advanced materials.

(A. W. Robins, 1014 and S. M. Dollyhigh, 3294)

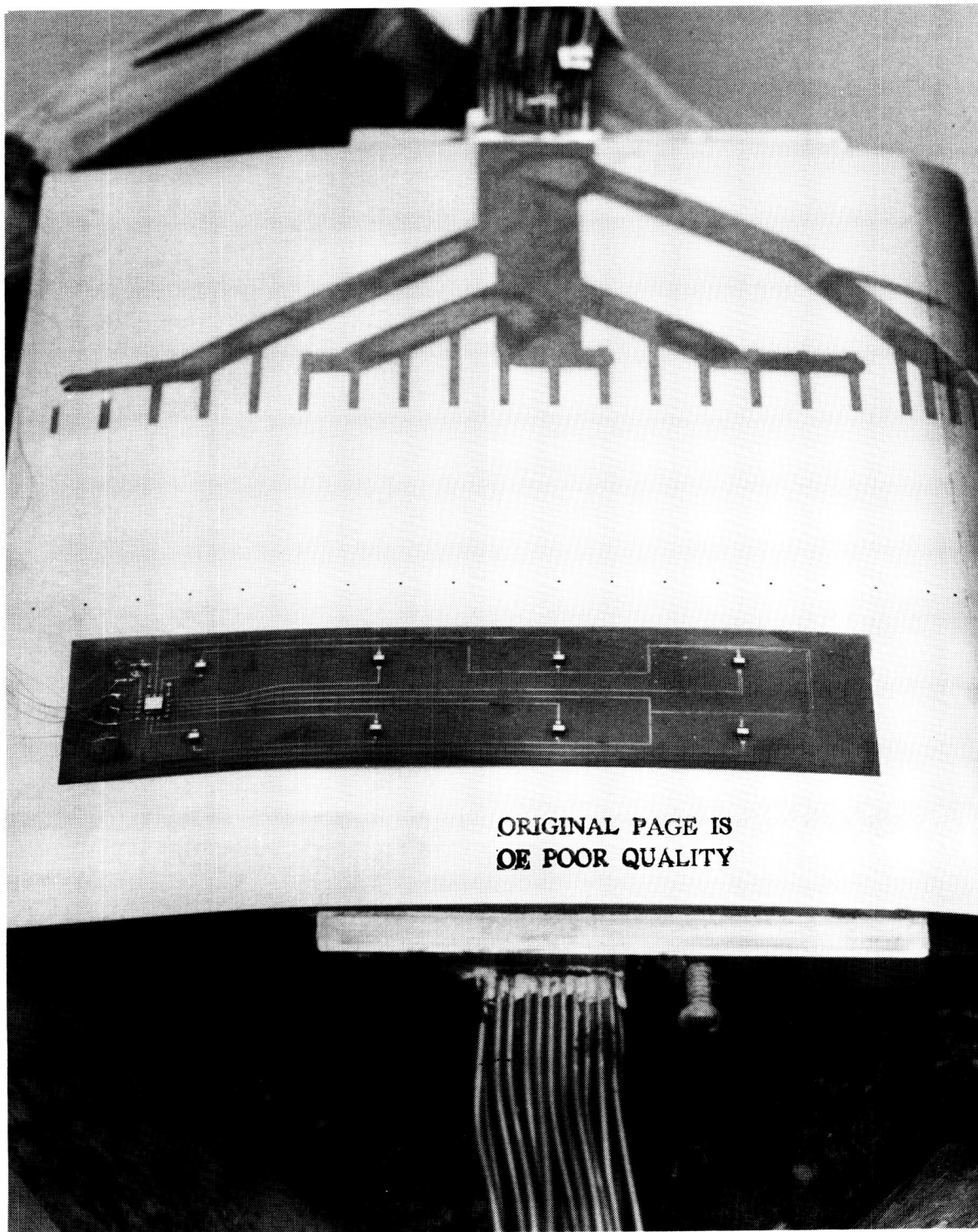


*Mach 3.0 high-speed civil transport baseline.*



# Electronics Directorate

---



The Electronics Directorate is responsible for the planning, direction, and evaluation of research and applications programs in the areas of measurements and computer science which will potentially benefit the Center's aerospace activities. This directorate also manages the Center's instrumentation, data acquisition, and data processing resources through the four divisions, each of which has specific support functions.

The Analysis and Computation Division is responsible for the development and application of mathematical and computer theory to the solution of computational problems arising from theoretical and experimental aerospace research activities performed at Langley Research Center. Additional responsibilities include conception, design, implementation, and management of advanced centralized data processing systems, flight software systems, and flight simulators, as well as providing consultation on Langley Research Center application of computer technology.

The Instrument Research Division provides instrumentation and measurement support for experimental aerospace research activities performed at Langley Research Center, with primary responsibility for the instrumentation of ground-based facilities. This division conducts research and development programs in instrument areas where present measurement capabilities are deficient or nonexistent to satisfy both current and future aerospace test program requirements. Additional responsibilities include providing engineering and application expertise to support computer-based data acquisition and control requirements, developing and maintaining measurement standards, calibrating and repairing instruments, and managing an instrument pool.

The Flight Electronics Division is responsible for the development and application of electronic and electro-optical systems for aerospace flight and flight-related projects. This division conducts research and development programs in electronics, optics, lasers, and related disciplines to provide measurement, communication, and data processing systems. Additional responsibilities include design, fabrication, testing, and operation of ground and flight electronic equipment and instrumentation for approved flight projects and applications.

The Projects Division is responsible for the implementation and management of Langley Research

Center participation in major projects, including the Earth Radiation Budget Experiment/Stratospheric Aerosol and Gas Experiment (ERBE/SAGE II) Project, the Long Duration Exposure Facility (LDEF) Project, the Control of Flexible Structures (COFS) Project, and the Scout project.

### **Process for Making Highly Active Noble Metal-on-Metal Oxide Catalyst**

A unique two-step process for preparing and depositing coatings of a Pt/SnO<sub>2</sub> or Pd/SnO<sub>2</sub> catalyst on an inert substrate has been developed. High surface area silica microspheres were used as a catalyst support. In the first step of the process, the spheres were coated with a monolayer equivalent of SnO<sub>2</sub>, and they were deaerated by boiling in deionized water. Sufficient powdered tin metal was added to coat the spheres with a monolayer equivalent of SnO<sub>2</sub>, and then HNO<sub>3</sub> was added to the hot mixture and slowly stirred. The acid reacted with the tin and deposited metastannic acid on the spheres. Evaporation and drying transformed this acid into SnO<sub>2</sub>.

In the second step, the coated spheres were loaded with a fractional monolayer equivalent of Pt or Pd. After deaerating the spheres as before, a chloride-free compound of Pt or Pd, sufficient to form a desired fractional monolayer equivalent of the metal, was dissolved in hot deionized water. This solution was added to the water with the spheres and slowly stirred. A chloride-free reducing agent, such as formic acid, was added to reduce the Pt or Pd and deposit it on the spheres, and the mixture was evaporated until dry. Chloride-free compounds were used because chloride can poison the catalyst. The catalyst product was a black powder consisting of a monolayer equivalent of SnO<sub>2</sub> on silica microspheres with a fractional monolayer loading equivalent of Pt or Pd. The catalyst made by this process was found to be 10 times as active as a commercially available catalyst when tested under similar conditions.

The new catalyst is being used in research to control decomposition products that are formed in the high-voltage region of a closed-cycle CO<sub>2</sub> laser. The recombination of these decomposition products

is necessary because they act to reduce laser power and lead to unstable laser operation.

(I. M. Miller and B. T. Upchurch, 2466)



Magnified image of Pt/SnO<sub>2</sub> catalyst-coated microspheres.

## Radio Frequency Strain Monitor

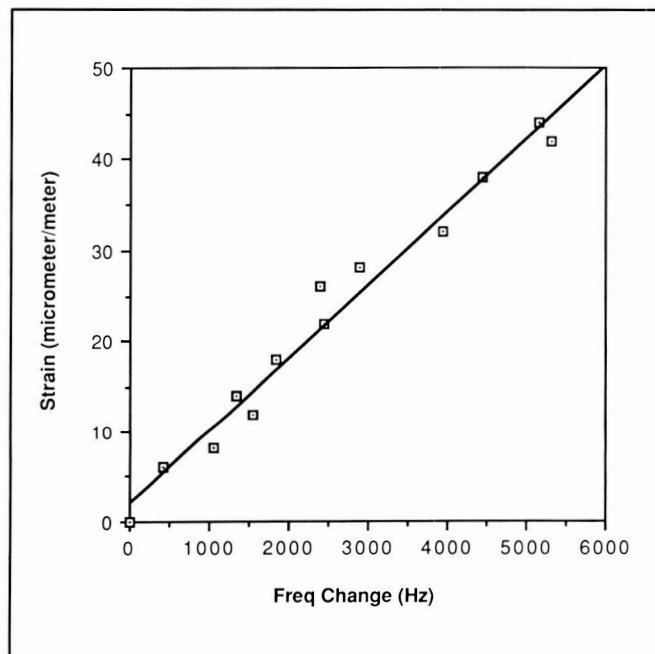
A phase-locked loop has been developed to measure small changes in the length of a waveguide. The system has been tested with optical (optical fibers) and radio frequency waveguides. The device is capable of measuring fractional length changes  $\Delta L/L$  of  $10^{-7}$ . Some recent data, presented below, demonstrate the concept of a radio frequency strain monitor. These data were taken with a radio frequency transmission line bonded to a sample of 1020 stainless steel (approximately 1.25 cm in diameter) subjected to loads up to 2200 newtons in a load frame. The transmission line was constructed from a fiberglass circuit board 15 cm in length. The strain measurement was made with a standard knife edge strain gauge attached to the steel in the load frame.

The frequency change plotted in the figure is for a phase-locked loop operating at a nominal frequency of 300 MHz. The cumulative frequency change is due

to the elongation of the transmission line attached to the steel under tensile stress. The small increase in length causes a small change in the phase of the radio frequency signal which is compensated for by a change in frequency of the oscillator in the loop. The figure indicates an excellent correlation between frequency change and strain as monitored by the strain gauge.

This sensor can monitor micro-strain as well as macro-strain. For example, large deformations ( $\Delta L/L > 0.5$ ) can be measured with a device similar to a line-stretcher-style phase shifter. The distributed strain can be measured in large structures (such as bridges) with radio frequency transmission line attached to the structure.

(Robert S. Rogowski and Joseph S. Heyman, 3036)



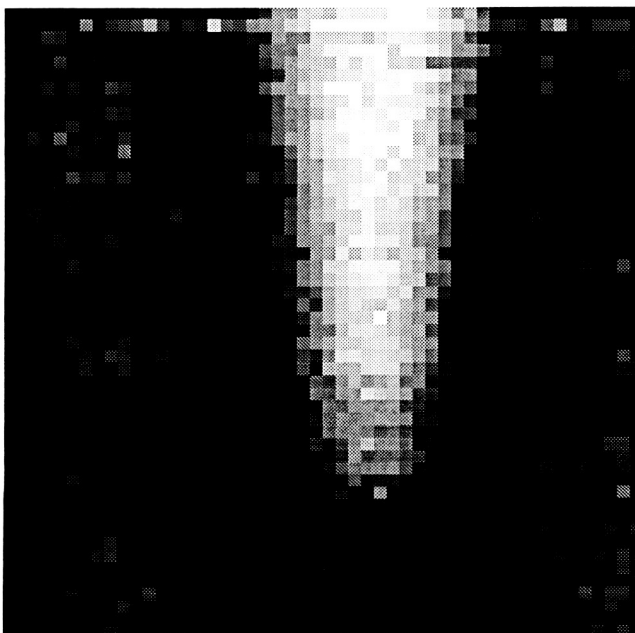
Radio frequency strain measurements.

## Ultrasonic Testing of Space Shuttle SRM Bond Lines

Nondestructive evaluation of the solid rocket motor (SRM) is critical for the safety, reliability, and



maintainability of the Space Shuttle fleet. Previous testing of the SRM system did not provide the depth of inspection required. One effort has been to develop ways to evaluate the different bond lines between the case, insulation, liner, and fuel layers of the membrane regions of the SRM. The possibility of disbond regions in the different layers of the SRM is an important factor in the flight safety of the Space Shuttle. The failure of the Air Force's Titan rocket launch in 1986 was believed to be the result of case-to-insulation disbonds. The similarity of the Titan rocket to the SRM underscores the need for accurate nondestructive evaluation (NDE). The main problems are that the insulation and fuels are highly attenuating to ultrasound and that they give poor-quality ultrasonic echoes for evaluation purposes.



*Ultrasonic image of wedge-shaped disbond region between liner and fuel of solid rocket motor.*

Our approach toward solving this problem has been to theoretically model the transmission of ultrasonic waves into a layered structure and combine those results with measurements on samples that approximate the SRM structure. From these results we can then decide how to best interrogate those regions of the layered structure. Theory and experiment indicate that by looking at very specific ultrasonic

frequencies we can obtain the best interrogation of the many layers. In practice, we transmit long tone bursts of ultrasound into the sample that comes to an equilibrium state of excitation. At the end of the excitation, the ultrasonic energy then dies out, and the decaying amplitude is measured. That amplitude of ultrasonic energy is dependent on the bond quality of the sample.

Shown in the figure is an image made from a sample that was built by Morton Thiokol, Inc. The sample contains layers of steel, insulation, liner and fuel, and has a wedge-shaped disbond built into the deepest layer interface. The figure shows regions of good bond integrity as dark areas and the wedge-shaped disbond as a white area. The size of the image is approximately 5 in.  $\times$  5 in. It is felt that this technique will be the basis of a testing system that will be capable of testing approximately 80 percent of the full-scale rocket motor bond lines. An effort is presently under way to try to transfer these techniques from the Langley Research Center laboratory into the manufacturers' facilities.

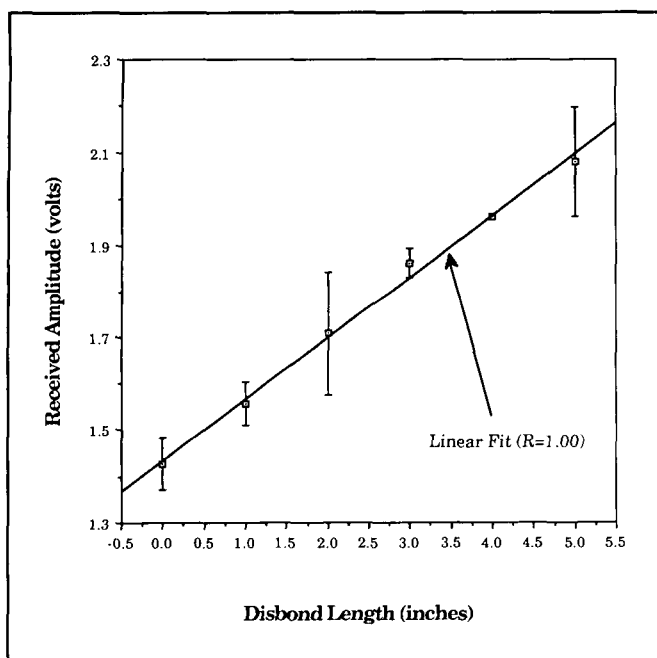
(Eric Madaras and Bill Winfree, 3036)

### **Surface Wave Nondestructive Evaluation of Space Shuttle Solid Rocket Motor Field Joint**

The bond between the steel case and rubber insulation in the field joints of the Space Shuttle solid rocket motors is a critical area for the safe operation of the motors. Testing of this bond with available methods is prohibited by the complex geometry of the field joints. New methods are required to allow reliable inspection of this difficult region.

An approach to the problem is being investigated in which the case/insulation bond line on the clevis end is interrogated using surface-traveling waves introduced into the bond interface. The surface waves are launched on the inside steel surface of the clevis leg, and they propagate into and along the case/insulation bond line. As they propagate along the bonded surface, some acoustic energy is absorbed by the rubber insulation and some leaks into the steel case as bulk waves. The magnitude of the ultrasonic

energy leaking from the surface wave into the steel is monitored on the outer surface of the steel case. The working hypothesis is that the magnitude of energy received at the outer surface of the case is proportional to the magnitude of energy in the surface waves. In an unbonded region those waves will be poorly coupled to the insulation and will result in reduced attenuation and an increase in received signal.



*Signal versus disbond in clevis test specimen.*

A low-frequency contact surface-wave-transmitting transducer is under development at Langley Research Center for this purpose. The prototype design consists of a linear array of longitudinal-wave transducer elements with a resonant frequency of 500 kHz and an interelement spacing equal to one-half the wavelength of 500 kHz surface waves in steel. The face of the array is placed in acoustic contact with the steel, and 500 kHz tone bursts are applied in such a way that each element is driven 180° out of phase with its two neighbors. This procedure drives a traveling surface wave while the bulk acoustic modes tend to cancel out in the region near the array. Measurements on a test specimen indicate a good correlation between received signal amplitude and the

length of disbond in the interface between the array transmitter and the receiver. These measurements suggest the validity of this working hypothesis (as shown in the figure). Work is continuing to establish reliable calibration procedures for this technique and to adapt this measurement approach for use on the new capture feature on the tang side of the field joint.

(Patrick H. Johnston, 3036)

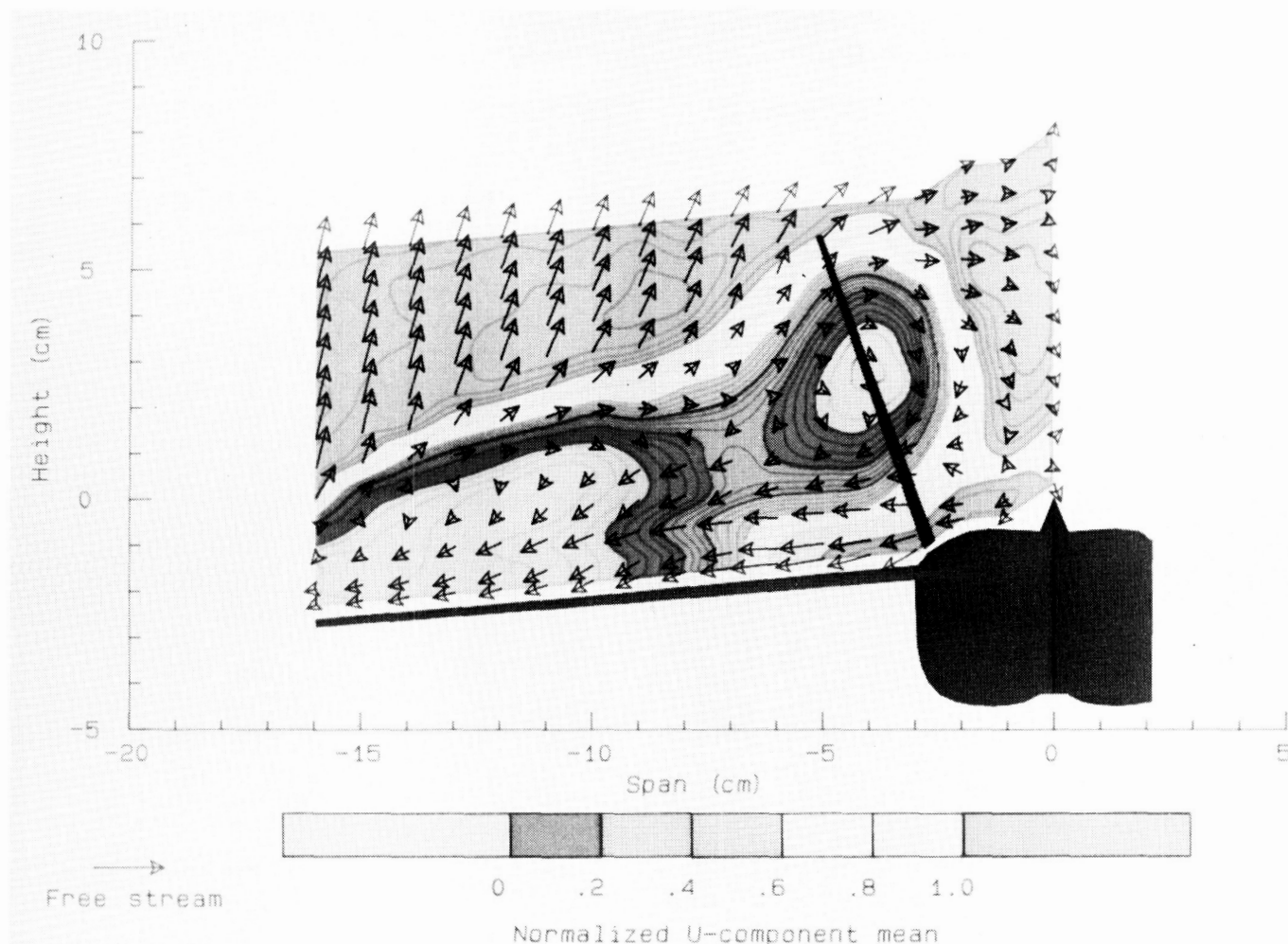
### Three-Component Laser Velocimeter Used to Measure Vortex Flow Field Above YF-17 Model

An orthogonal three-component laser velocimeter system has been used to measure the vortex flow field above a YF-17 model in the Langley Research Center Basic Aerodynamic Research Tunnel. The laser velocimeter had full directionality measurement capability and used a side scatter configuration to reduce the measurement volume to a 150- $\mu$ m-diameter sphere. This configuration minimized effects of velocity gradients on the turbulence measurements and allowed a closer approach to the model than other configurations. This investigation was conducted under full automated computer control with on-line data reduction and graphics to allow the researchers to monitor the progress of the velocity surveys. The flow field was seeded with 0.8  $\mu$ m polystyrene particles to minimize measurement uncertainties due to particle dynamics.

The example three-component velocity flow field map represents the mean velocities obtained within a plane orthogonal to the model axis located at the base of the leading edge of the vertical stabilizer. The model was inclined at an angle of attack of 25.0°, and the wind tunnel was set to a dynamic pressure  $Q$  of 30 lb/ft<sup>2</sup>. The contour map represents the  $U$  or streamwise velocity component in the model coordinate system, and the arrows represent the resulting vector in the cross flow plane. The results indicate full flow separation at the wing tip extending to approximately 40 percent span with flow reversal in the  $U$  component direction. The leading-edge extension (LEX) vortex had burst and was centered on the vertical stabilizer.

(James F. Meyers and Timothy E. Hepner, 2791)





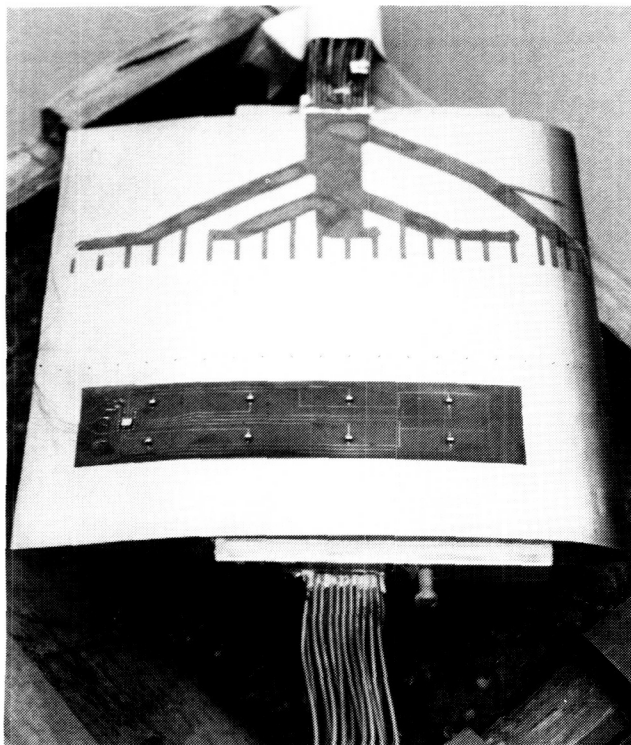
*Laser velocimeter measurements above YF-17 model at angle of attack of 25°.*

### Flexible Thermal Mapping Surface Sensor

The measurement of component and aerodynamic model surface temperatures is of significant importance to designers and researchers. Most approaches to obtain surface temperatures result in the attachment of many single sensors; however, a new surface temperature sensor has been developed at Langley Research Center to obtain the temperature of an area using film circuitry and microchip technology. The sensor array shown in the figure measures

1 in. by 4 in., is constructed of gold-etched circuitry on 0.002 in. flexible Kapton film, and is instrumented with eight AD590 temperature sensor chips mounted in an array. The temperature chips are multiplexed with a CD4051B chip to obtain the array of thermal measurements. The operating range of the sensor is -40°C to 120°C with a  $1 \mu\text{A}/^\circ\text{C}$  linear digital output. The sensor's ability to conform to contoured surfaces and to eliminate the need for numerous monitoring cables makes it most attractive.

(L. A. Dillon-Townes and P. B. Johnson, 2466)



L-87-4690

*Prototype sensor installed on test airfoil.*

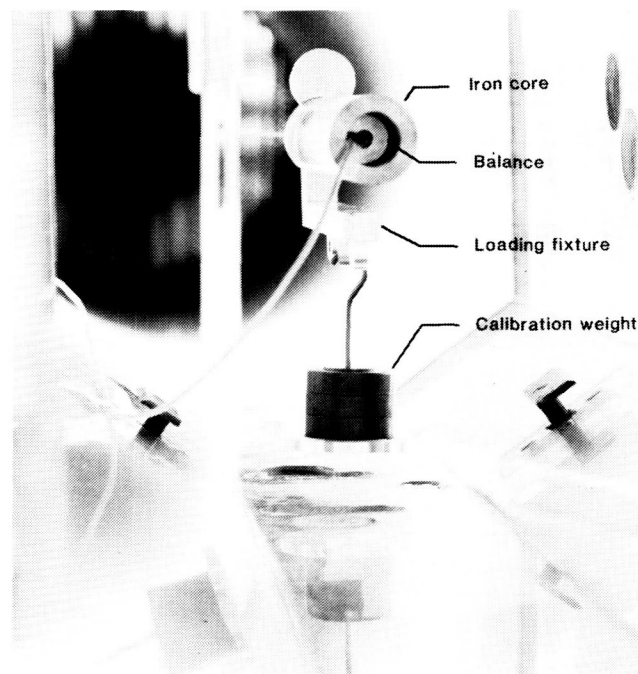
### Advancements in Instrumentation for Magnetic Suspension and Balance System

Three advancements in instrumentation have recently been made in Magnetic Suspension and Balance System (MSBS) technology at Langley Research Center. These advancements include improvements in data acquisition systems using a strain-gauge balance, development of an onboard telemetry system, and development of a five-component electro-optical model position-sensing system.

The concept of using a strain-gauge balance to calibrate a magnetic suspension system was successfully demonstrated on Langley Research Center's 13-in. MSBS. The approach greatly simplifies the calibration procedure and improves accuracy by directly measuring the input loads to the MSBS and eliminating load alignment (input) uncertainties. The idea of

using an active balance and telemetering data for actual force testing is being pursued.

A battery-powered telemetry package has been developed to transmit pressure data from a magnetically suspended wind tunnel model. The system consists of a miniature transducer, signal conditioning circuitry (which includes a voltage-to-frequency (v/f) converter), and an infrared (IR) light-emitting diode (LED). The system has special circuitry that provides very low-duty cycle pulses to the LED to reduce the power requirements. A receiver, which demodulated the signal and provided an interface to a personal computer for data reduction and display, was located outside the tunnel. The system has demonstrated a 2-hr operational life and an overall precision of 0.5 percent of full scale.



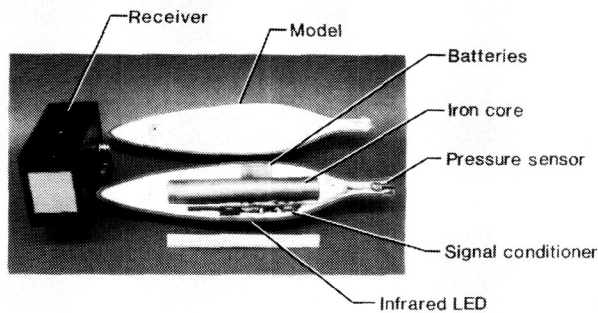
L-87-1704

*Calibration of MSBS with strain-gauge balance.*

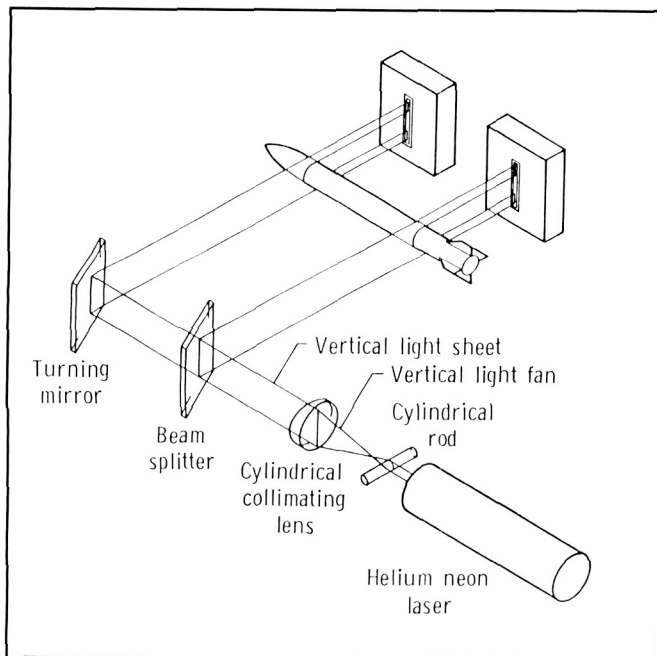
A five-component electro-optical system for detecting the position and providing a control feedback signal for a magnetically suspended wind tunnel model has been developed. This nonintrusive position measurement system, using small lasers as light sources and self-scanning linear photodiode arrays as the sensing elements, is operational in the 13-in.

MSBS. The useful full-scale ranges of the system are  $\pm 0.45$  in. and  $\pm 8^\circ$  for linear and angular movements, respectively. The system has an overall precision of  $\pm 0.002$  in. and  $\pm 0.02^\circ$  in linear and angular measurements, respectively.

(P. Tcheng and P. Roberts, 3483)



Single-channel pressure telemetry system.



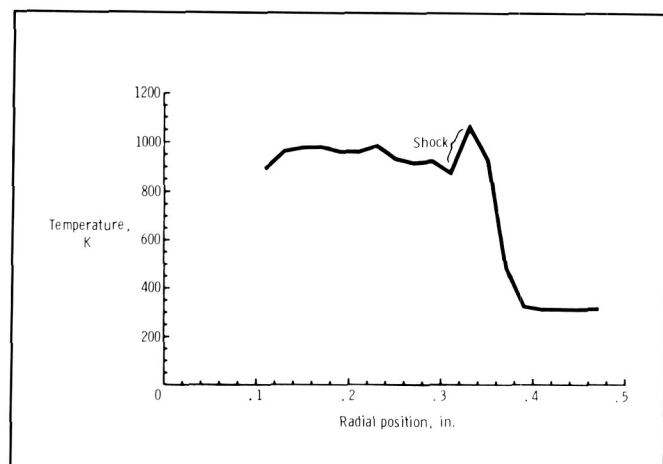
Schematic of typical electro-optical model position sensing system.

## CARS Measurements in Supersonic Combustion Flow

A coherent anti-Stokes Raman scattering (CARS) instrument has been developed which has the capability of simultaneously measuring the temperature and density of two major species. This instrument is currently being used to obtain measurements of temperature, nitrogen density, and oxygen density in hydrogen combustion Mach 2 flow. This flow is simulated by preburning hydrogen, oxygen, and air inside the combustor. Fuel (hydrogen) is injected coaxially within the center of the flow to produce external combustion. Measurements in this flow are being used to validate computational fluid dynamics (CFD) codes that are being applied to supersonic combustion.

The figure indicates the ability to make noninvasive temperature measurements in this hostile environment. The influence of the shock structure on the temperatures is clearly seen. These temperature values are obtained from 10 ns laser shots in a 3-mm sample length. The short time scale and small sample length are important in turbulent environments. Density values from nitrogen and oxygen have also been measured simultaneously with these temperature values. These measurements are currently being compared with CFD calculations.

(Richard R. Antcliff, 2791)



Radial temperature profile.

ORIGINAL PAGE IS  
OF POOR QUALITY

## Dual-Block Grid Generation and Euler Flow Calculations About Fighter Aircraft Configurations

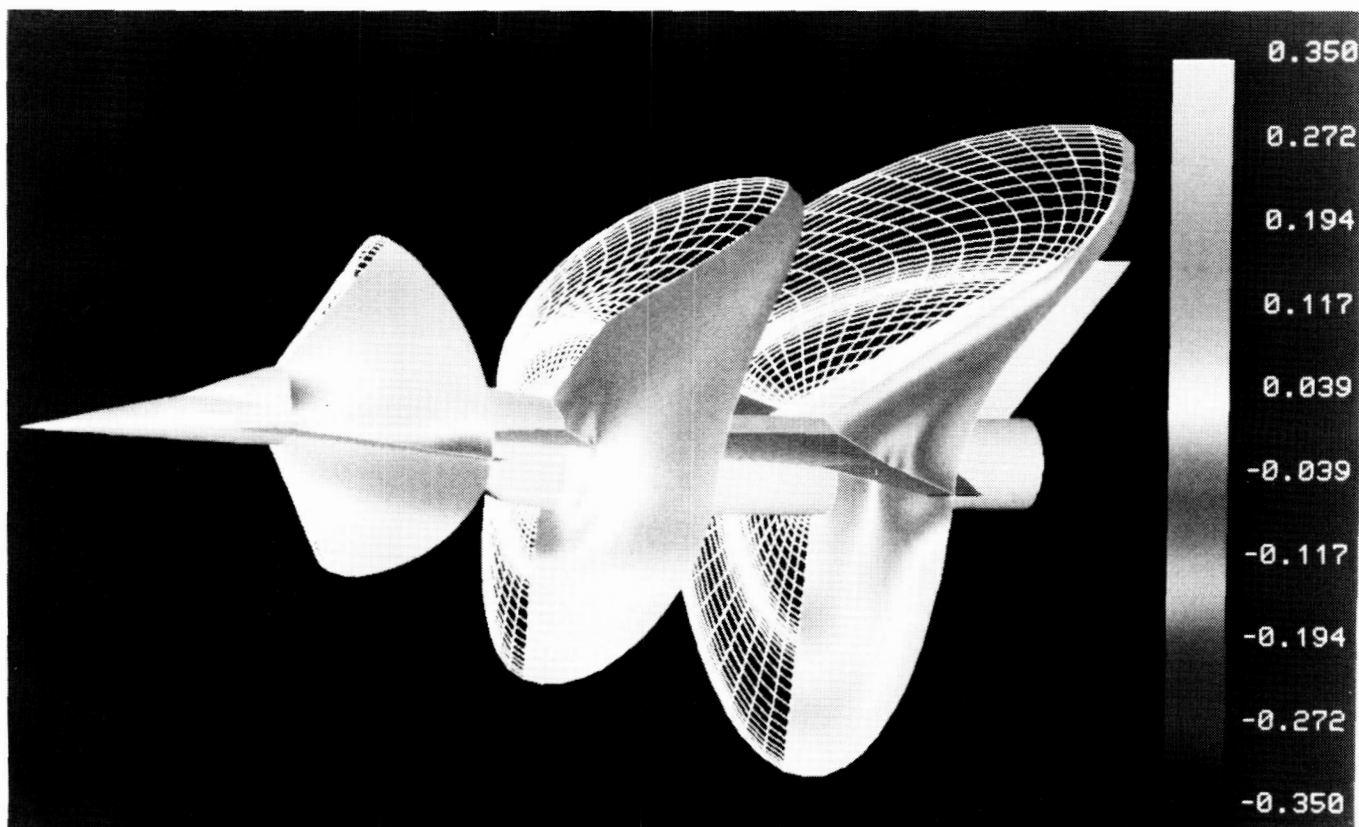
A major task in computational fluid mechanics is the generation of grids and the computation of inviscid compressible flow about aircraft configurations. In the past, single-block grids have been used with great success on a large class of problems with simple boundary geometries, but for more complex boundaries, it is recognized that multiblock grids are more effective.

For a dual-block grid topology, an Euler equation solution procedure and associated computer software to generate grids and compute inviscid compressible flow about fighter-type aircraft configurations have been developed at Langley Research Center. A patched dual-block grid is used because the conservation of mass, momentum, and energy is eas-

ily maintained across patched grid interfaces and because a dual-block grid offers high overall resolution for this type of aircraft geometry. The grid generation is algebraic and based entirely on transfinite interpolation. A finite-volume Euler solver, using an explicit Runge-Kutta time-stepping scheme, has been adapted to this grid system, and supersonic flow has been computed for an experimental aircraft with fuselage, canard, 70-20 cranked wing, and vertical fin.

Solutions for this configuration have been obtained at Mach number 2 and angles of attack of  $0^\circ$ ,  $4^\circ$ ,  $7^\circ$ , and  $10^\circ$ . For these computations, 264,000 grid points have been used. The figure shows the aircraft configuration, several grid surfaces, and the coefficient of pressure depicted as shades of gray (original color figure can be obtained from the author) on the surfaces for a case with an angle of attack of  $4^\circ$ .

(Robert E. Smith, 3978)



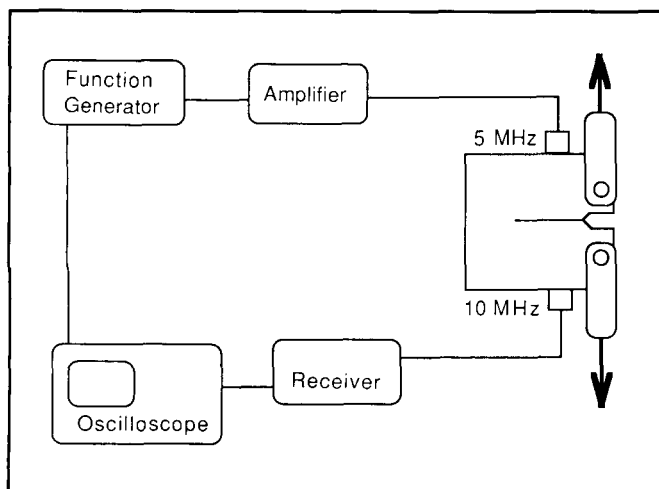
Experimental configuration with coefficient of pressure;  $\alpha$  equals  $3.79^\circ$  and  $M$  equals 2.0.

## Ultrasonic Harmonic Generation to Determine Crack Opening in Compact Tension Specimens

When a crack has been grown in a compact tension specimen (a specific geometry of a metal plate with a carefully machined notch), the material around the crack distorts so that when the plate is released from load, the cracked region is compressed. To open the crack, the sample must be pulled sufficiently to overcome this compression. Until now, there has not been a direct, reliable measurement technique to determine when the crack begins to open. Recently, a new ultrasonic technique has been developed to determine this onset of crack opening in these specimens.

An ultrasonic wave is launched into the metal so that it is perpendicular to the plane of the crack. When the pull on the sample is too small to open the crack, much of the wave traverses the crack plane. When the crack just begins to open, however, the surfaces of the crack respond to the ultrasound in such a way that they clip the portion of the ultrasonic wave which crosses the crack surface. Because of this clipping, the wave contains a much larger proportion of harmonic distortion, which can readily be detected and measured.

The first figure shows the equipment setup. A 5 MHz toneburst, formed by the function generator,

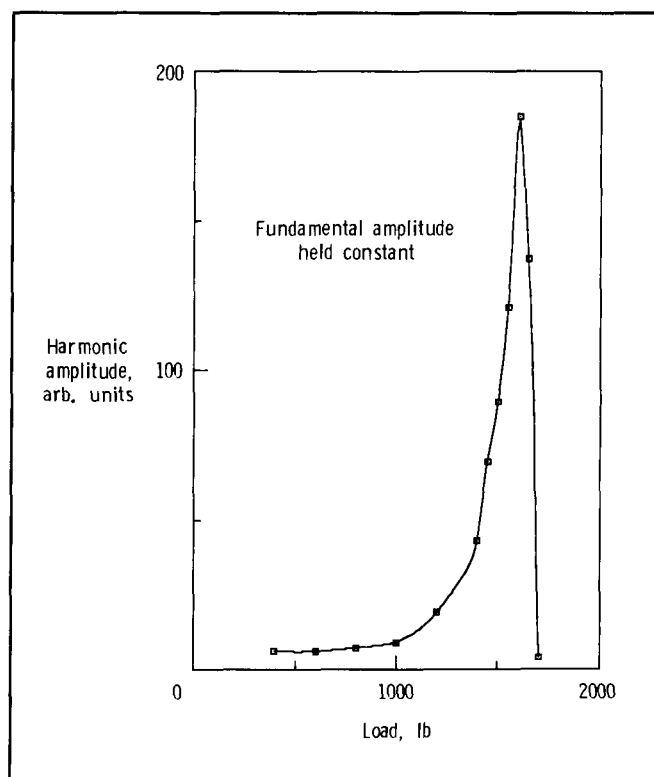


Equipment setup.

is amplified and sent to the 5 MHz transducer, which launches an ultrasonic wave in the specimen. The wave traverses the sample, including the cracked region, and is received by the 10 MHz transducer. The tuned receiver can be set to receive the 5 MHz and the 10 MHz signals that are displayed on the oscilloscope.

The second figure gives data taken from a compact tension specimen that was operated under very specific conditions. The second harmonic amplitude (Y-axis) of the ultrasound was measured as a function of load (X-axis) pulling on the sample (the received fundamental amplitude was held constant). Using finite-element analysis, it was calculated that, with the conditions of operation, the crack should open when the sample was pulled by a load in the range of 1500 lb to 1600 lb. The ultrasonic data show that the crack opened at about 1575 lb.

(W. T. Yost and Min Namkung, 3036)



Harmonic amplitude versus load for compact tension specimen.

## Remote Noncontacting Heat Transfer Measurements for Detection of Boundary-Layer Transition in Wind Tunnel Tests

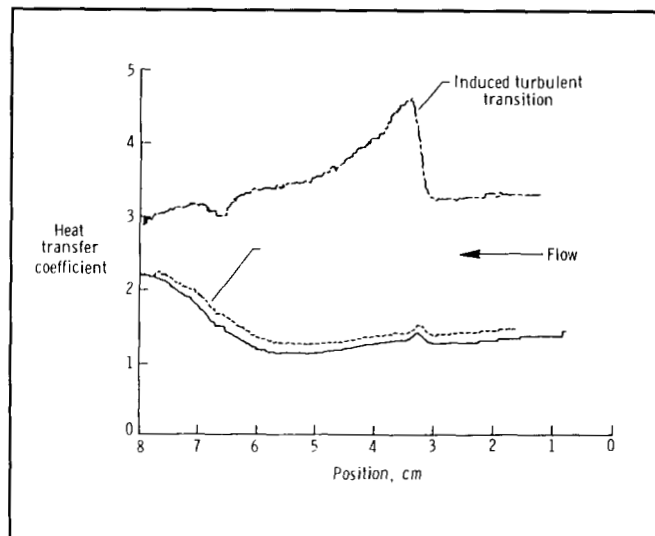
The existence of turbulent-flow conditions over airfoil surfaces is of prime concern in aerospace industries. The resulting increase in drag boosts fuel consumption and costs. In airfoil design it is particularly desirable to detect and locate the position of laminar to turbulent transition on airfoil models. Current techniques require surface modification or complex implementation. A remote, noncontacting infrared measurement technique for measuring heat transfer has been applied to the detection of boundary-layer transition in wind tunnel settings. The measurement system consists of three prime elements that include a laser heating source, an infrared camera for data acquisition, and a video recorder for data storage. A laser beam scans an airfoil and heats its surface to a few degrees above ambient temperature. An infrared camera then measures the temperature of the airfoil (over a two-dimensional field), and these temperatures are stored as a function of time on a video recorder. The resulting temperature pictures are then digitized, and an iterative approximation algorithm is used to extract the heat transfer coefficient. The resulting values are relative to the natural convection condition.

The technique has been used in two fashions to detect the laminar to turbulent transition in low-speed wind tunnel tests. Point measurements were made over a range of wind velocities to detect the occurrence of transition and were compared to well-established hot-film measurements (which were made simultaneously) to confirm the flow conditions. Heat transfer coefficients were determined using a linear pattern at various wind speeds to indicate the position of natural and of artificially induced transition on an airfoil. The technique was shown to be sensitive to transition at low Mach numbers, where previous infrared techniques (using kinetic heating) were found to be insensitive.

Advantages of the technique include ease of use and cost reduction. No complex and costly machining or implementation of contacting sensors during model fabrication is required. No surface preparation is required for the model except for highly reflective surface finishes. In the reflective case, as for

highly polished metal surfaces, a thin film of insulating plastic may be required. This technique also has the potential to view flow characteristics over a large field.

(D. Michele Heath, 3036)



Relative heat loss versus position.

## Ultrasonic Measurement of Nonlinear Elastic Properties of Graphite/Epoxy Composites

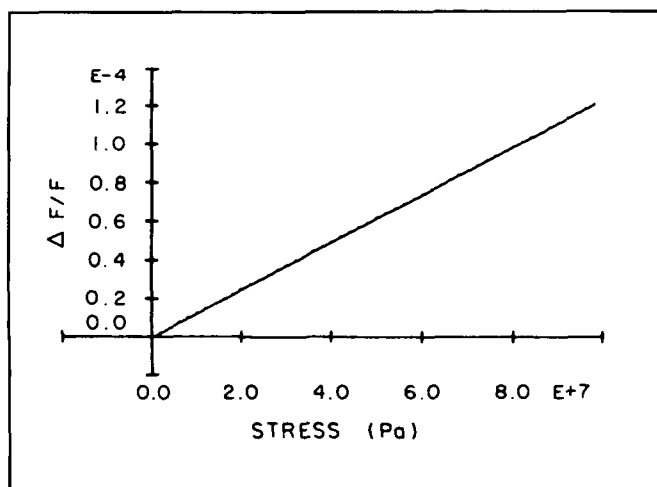
The high strength, stiffness, and light weight of composite materials make them have great potential for structural applications, particularly in the aerospace industry. The usefulness of these materials has been proved by research, but the need to quantitatively characterize important material properties and develop applicable nondestructive evaluation techniques still remains.

Linear and nonlinear elastic properties are important properties in conventional materials. Nonlinear properties are important in the nondestructive determination of applied and residual stress, and a possible relationship between nonlinear elastic properties and ultimate strength in aluminum and carbon steel has been established.



Through research at Langley Research Center, the nonlinear elastic properties of a unidirectional graphite/epoxy composite were determined from measurements of the change in ultrasonic wave speeds with stress and temperature. These changes in ultrasonic velocity were monitored by a pulsed-phase-locked loop ultrasonic interferometer that records them as changes in the frequency of the wave. These measurements were made under a variety of conditions including both hydrostatic and uniaxial stress with ultrasonic waves propagating in varying directions with respect to the fiber direction. The figure shows a typical plot of the normalized change in ultrasonic frequency which is the measured frequency shift at a given stress divided by the frequency with no stress applied. This plot is a dimensionless quantity, versus applied stress. These changes in frequency represent changes in the elastic moduli with applied stress and thus are a manifestation of nonlinear elastic behavior. If the material were truly linear elastic, there would be no change of velocity, and therefore the pulsed-phase-locked loop would display no frequency shifts with changes in temperature or applied stress.

These measurements provide the basis for further investigations into the relationship between nonlinear elastic properties and other important properties such as strength and fiber-matrix interfacial



*Normalized frequency change of ultrasonic wave propagating perpendicular to fiber direction with stress applied along fiber direction.*

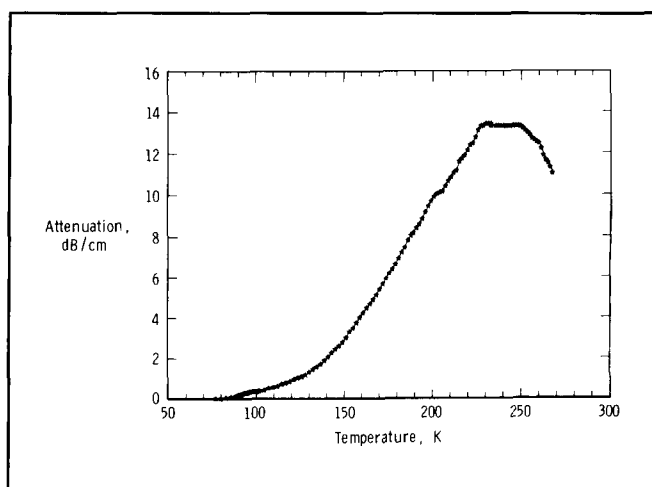
strength in graphite/epoxy composites. This research may aid the development of needed nondestructive evaluation techniques for composite materials.

(W. Prosser, 3036)

### Ultrasonic Measurements for Identification of Superconductivity in High-Temperature Superconductor

It has been speculated that the crystal structure of the copper-oxide superconductors which is different from those of conventional superconductors (transition temperature  $T_c < 20K$ ) plays an important role in exhibiting the high superconducting transition temperature. From the theoretical point of view, whether electron-phonon interaction as described in the Bardeen/Cooper/Schrieffer (BCS) theory is still responsible for the superconducting behavior of these samples is an interesting subject. This subject has stimulated numerous types of measurements to determine the superconducting properties of these samples.

Ultrasonic attenuation and velocity measurements are useful techniques for detecting crystal



*Temperature dependence of ultrasonic attenuation in polycrystalline  $YBa_2Cu_3O_{6+\delta}$ .*

structure changes, dislocation, and internal friction in solids. Ultrasonic attenuation in the superconducting state of a conventional superconductor exhibits characteristic behavior as a result of electron and phonon interaction, and can be employed to find the value of the temperature-dependent energy gap, the superconducting transition temperature, and the critical field.

Temperature-dependent ultrasonic attenuation behavior of polycrystalline  $\text{YBa}_2\text{Cu}_3\text{O}_{6+\delta}$  is shown in the figure. The absence of a sharp decrease in attenuation at the superconducting transition temperature of 91K implies that the electron and phonon interaction in BCS theory is not the predominant mechanism in causing this supposed second-order phase transition of this sample.

(William P. Winfree, 3036)

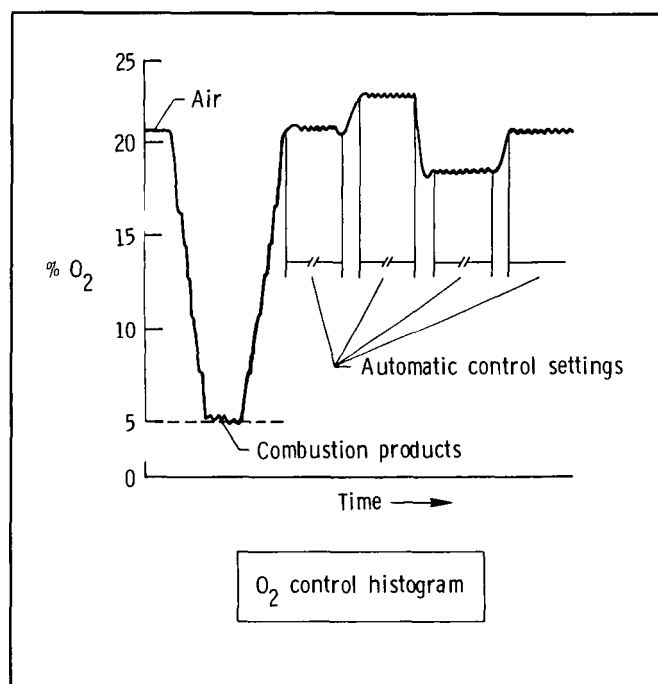
### Oxygen Monitoring and Control System for Langley 8-Foot High-Temperature Tunnel

Future hypersonic studies in the Langley 8-Foot High-Temperature Tunnel (8-Foot HTT), in which combustion products are used as the test medium, will require oxygen enrichment of the air to duplicate the oxygen content of air in the test medium. A study has been undertaken to demonstrate that the oxygen content of the test medium can be measured quickly enough to permit almost real-time automatic control of the oxygen enrichment level.

A  $\text{ZrO}_2(\text{Y}_2\text{O}_3)$ -based fast response oxygen-monitoring and control system was developed and tested in the 7-Foot High-Temperature Tunnel (a 1/12.8 scale model of the 8-Foot HTT) for its speed and stability. The combustion gas was sampled continuously with a probe mounted in the test section. A typical histogram of the  $\text{O}_2$  control process is shown in the figure. Initially, the system showed a decrease in the  $\text{O}_2$  level from 21 percent (air) to about 5 percent as the combustion process was established. The oxygen content was then manually controlled to a level near the desired 21 percent control point for air simulation. Upon switching to automatic mode, the system achieved the 21 percent point in about 0.25 s.

New set points of 24 percent and 18 percent were arbitrarily entered, and the system was switched to the automatic mode. In both instances, the system produced the desired oxygen level in the test section in about 0.25 s.

(Jag J. Singh, 3907 and Richard L. Puster, 3115)



Performance of automatic control system.

### Spaceborne Optical Disk Controller Development

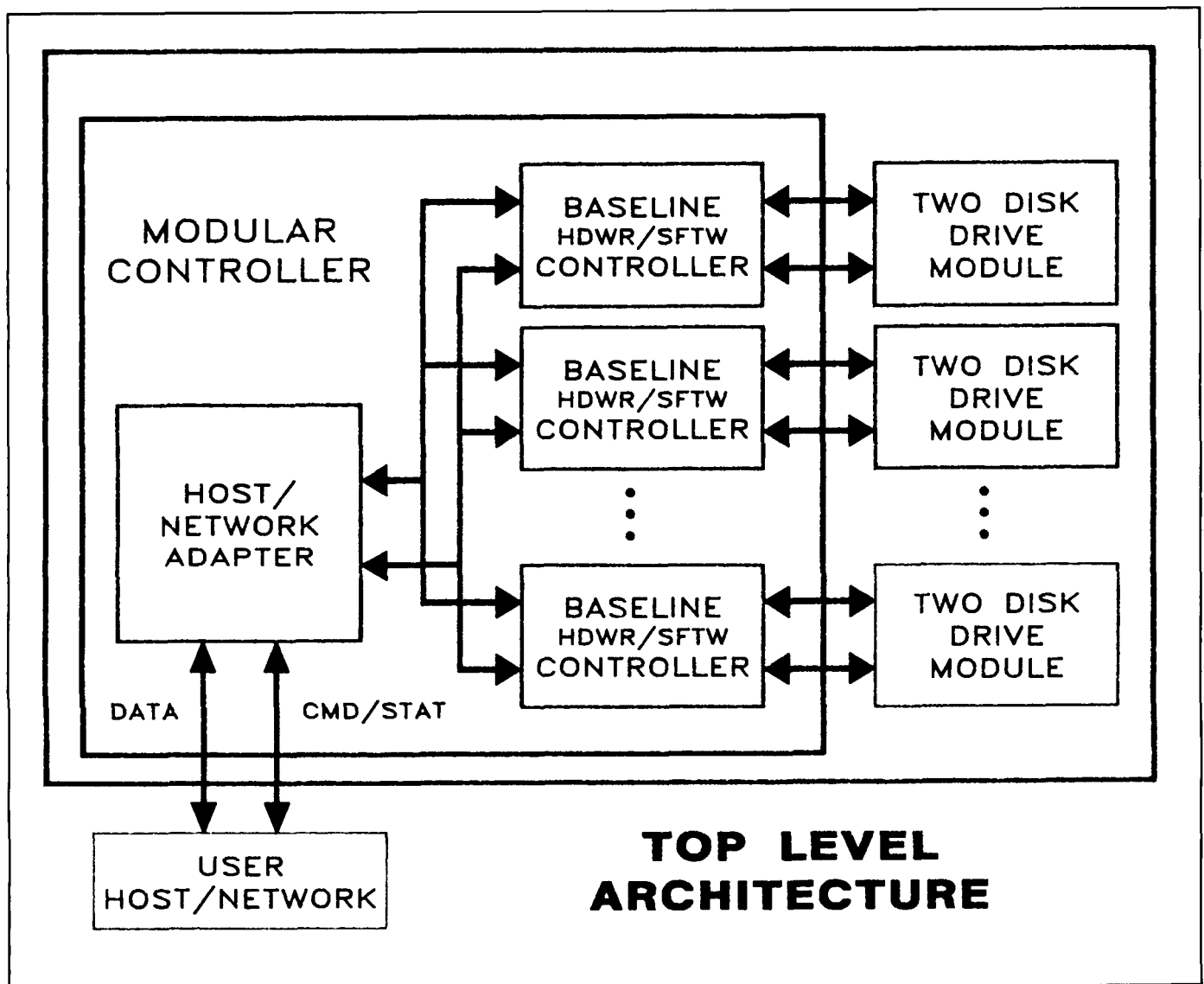
Mass memory systems based on erasable optical disk media are expected to play an important role in the Space Station era of the 1990's and beyond. NASA, along with other U.S. Government agencies, is supporting technology development leading to a high-capacity, high data rate erasable optical disk recorder. The goal of an ongoing contract with industry is to demonstrate write/read/erase capability at 133 megabits per second on a single-sided 14-in.



magneto-optic disk with an 8-track electro-optical head using a 10-element laser diode array.

In addition to supporting the technology demonstration, Langley Research Center is developing system requirements leading to drive and controller specifications for a spaceborne system as part of the Space Data System Research Program. The overall program goals are greater than one terabit (10 to the 12th bits) capacity, at greater than one gigabits per second transfer rate. An application study of

the Optical Disk Mass Memory System (ODMMS), which focuses on the data system and instrument needs of the Earth Observing System Polar Orbiting Platform of the Space Station program, has also been conducted. As a result of the study, Langley Research Center has developed an ODMMS concept based on an expandable system. The system is composed of disk drive modules of two 14-in. disks that rotate in opposite directions, and an associated modular controller. This flexible concept allows for



*Erasable Optical Disk Mass Memory System architecture.*

application-specific system configuration and permits a more structured development program for space-flight applications.

The modular concept, however, places an increased burden on the system controller. Two study tasks have been initiated to address controller architecture and related issues. These tasks focus on error coding and data format strategies, configurability, and implications of spaceborne operation, and they provide a system simulation model. Langley Research Center developed the architecture (as shown in the figure) to serve as a baseline for a variety of applications and integration studies. A preliminary Controller-to-Drive Interface Document is being prepared to isolate the drive from the user and thus enable drive module development to proceed independently.

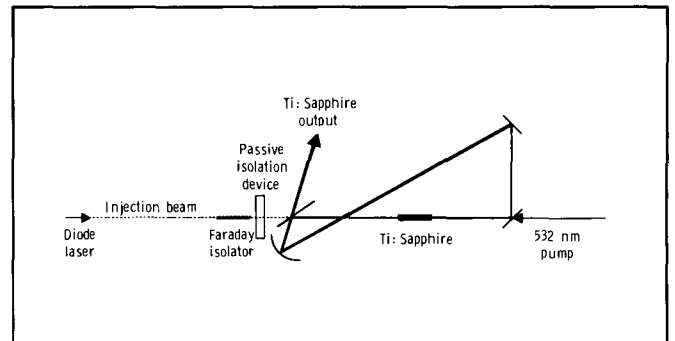
(Thomas A. Shull and Reginald M. Holloway, 3541)

## Diode Laser Injection Control of Titanium-Doped Sapphire Lasers

Remote sensing of atmospheric constituents, pressure, and temperature requires narrow-bandwidth, stable pulsed lasers (that operate in a differential absorption lidar mode) which can be switched between "on" and "off" wavelengths in a few milliseconds. The current practice is to use multiple line-narrowing elements within the laser cavity to achieve narrow bandwidth and to use two lasers to achieve the rapid switching between the "on" and "off" wavelengths. The line-narrowing elements limit the laser efficiency, and the two lasers pose a volume and weight problem for aircraft and spacecraft operation.

A ring cavity titanium-doped sapphire laser with no internal wavelength selection devices has been designed. The ring cavity is an ideal device for narrow-bandwidth solid-state lasers because a ring cavity operates with a traveling wave rather than the standing wave associated with the more common Fabry-Perot cavities. Standing waves result in spatial hole-burning, and they limit the power available for narrow-bandwidth operation. Although ring cav-

ities normally have waves traveling in two directions, active injection control or passive feedback results in unidirectional operation. Injection control of a ring cavity titanium-doped sapphire laser has been achieved using continuous wave (CW) diode lasers as injection sources. This is an important step in demonstrating an all-solid-state narrow-bandwidth tunable laser system for remote sensing from space. (Philip Brockman and Clayton H. Bair, 2818)



Ring laser with diode injection.

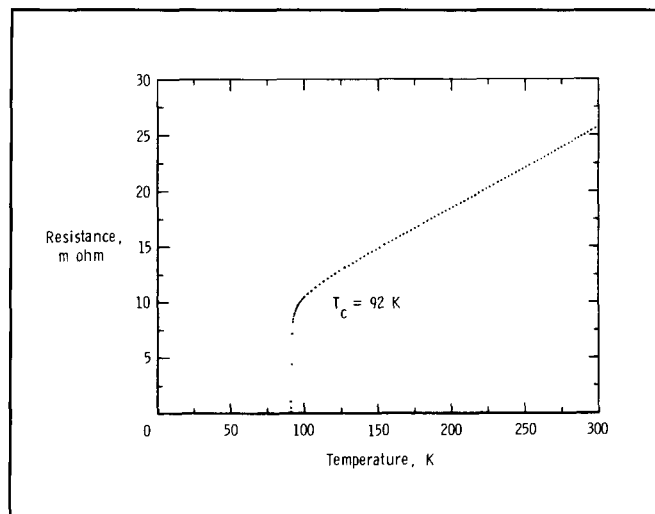
## High-Temperature Superconducting Materials

The recent discovery that the material formed from the mixed oxides of barium, yttrium, and copper (often referred to as BAYCO) has a superconducting phase-transition temperature of 94K has produced an intense international effort in high-temperature superconductor work. Langley Research Center has initiated a materials growth and characterization study of this new class of high-temperature superconducting ceramic-like material. Two areas of immediate application of this research effort have been identified. One application is in the remote sensing of atmospheric species (in the spectral region around  $100\ \mu\text{m}$ ) with superconductor-insulator-superconductor (SIS) detectors fabricated with thin films of these new high-temperature superconducting materials. A second application, which is an important capability for aeronautical research, is the magnetic suspension of wind tunnel models.

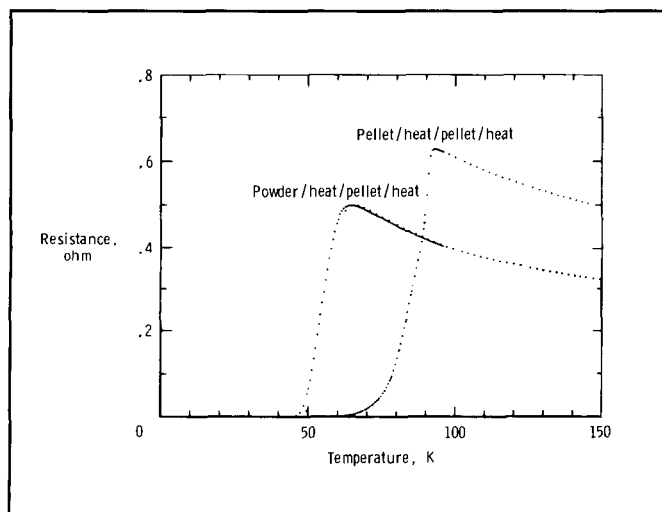
Research at Langley Research Center on this new class of materials has centered on the fabrication and characterization of BAYCO. Characterization of the effects of the initial particle-size distribution of the oxides of copper, yttrium, and barium is one area of interest. Particle size has not been found to affect the superconducting transition temperature. Experiments are now under way to determine the effects of this processing on the alternating current (ac) susceptibility. The first figure shows the effect of processing on the transition temperature for BAYCO. Material formed by heat treating powdered material in air followed by pelletization and oxidation has a significantly lower transition temperature than does the heat treatment of pelletized material followed by the same pelletization and oxidation process. In addition, these materials show a resistance behavior typical of semiconductors for temperatures above the transition temperature. The second figure shows the results of elimination of water vapor from the final oxidation process. The transition to the superconducting state is shown by a sharp curve at 94K. In addition, the resistive behavior above 94K is typical

New mixtures of materials including fluorides are being fabricated to explore even higher transition temperatures.

(C. E. Byvik, 2818)



Resistance versus temperature for BAYCO.



Effect of processing on transition temperature for barium/yttrium/copper oxide superconductors.

of metallic conduction. The characterization techniques now in place to support this research effort are four-point probes for resistance measurements, AC susceptibility, and measurements of specific heat.

## MOPA Performance of $\text{Ti:Al}_2\text{O}_3$

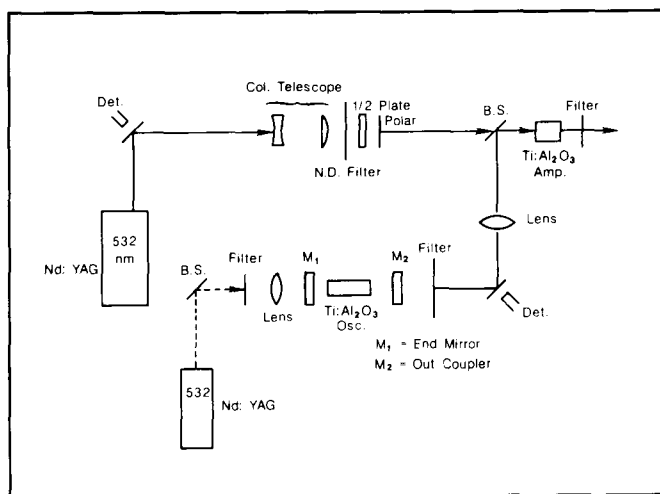
Spaceborne remote-sensing laser energy requirements exceed 1 joule per pulse for some applications. To meet this requirement, Langley Research Center is currently investigating the operation of  $\text{Ti:Al}_2\text{O}_3$  in master oscillator power amplifier (MOPA) configurations. Measurements of two important aspects of the power amplifier (gain and energy extraction) have been performed as a function of probe and pump energy per unit area (fluences) for the combinations of Gaussian pump with both circular and Gaussian probe beam profiles. In addition, the timing between the probe and pump pulses necessary for optimum extraction from the amplifier has been determined.

The broadband output of a gain-switched  $\text{Ti:Al}_2\text{O}_3$  oscillator and the frequency-doubled output of an Nd:YAG laser were used as the probe and pump pulses, respectively. These pulses were directed coaxially in the forward direction into the amplifier rod

in a longitudinal pumping scheme as depicted in the figure. With this result, it is feasible that Langley Research Center will achieve its goal for a large signal gain of 10. Methods for achieving this gain are currently under investigation. These methods include the addition of a second amplifier and increasing the pump volume of the existing amplifier. A large signal gain of 4.8 was observed.

A modeling effort was also undertaken to complement the experimental effort. Effects such as nonuniform pump energy deposition along both the longitudinal and transverse pump directions, nonuniform probe laser energy density, and absorption of the probe laser wavelength could be modeled. Results from the model can be used to predict the absorption efficiency of the pump energy, the extraction efficiency of the probe laser beam, the output energy, and both the spatial and temporal distortions of the probe laser beam.

(James C. Barnes, 3761)



MOPA configuration.

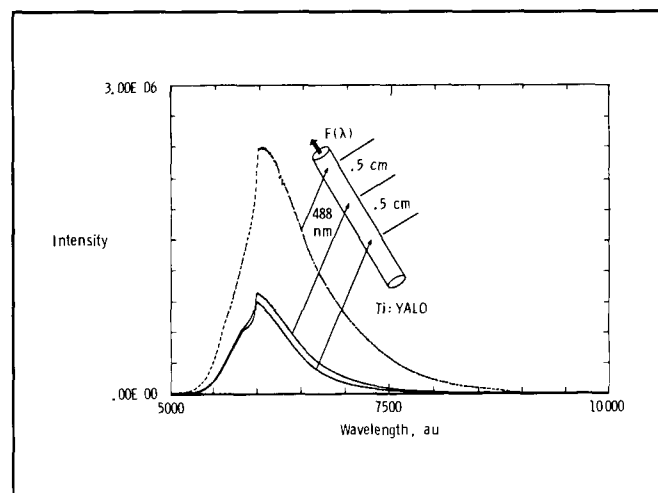
### Crystal Fiber Technology for Evaluation of Solid-State Laser Materials

Remote sensing of atmospheric constituents, temperatures, and pressures from space can be facil-

itated by the development of new efficient laser materials that can be pumped by diode lasers and that can operate in the eye-safe regions of the spectrum. The studies of material laser properties (including absorption, emission, and fluorescence) have been limited due to long turnaround times for standard growth techniques. Recent developments in crystal fiber growth have resulted in rapid turnaround and have allowed evaluations of many different dopants and doping levels.

A new technology has been developed for performing spectroscopy of the fiber-grown crystals. A detector is placed at the end of the crystal, and the crystal is excited by a laser focused into its side. Spectra are taken for several different lengths between the positions of side excitation and the end of the fiber. Laser-induced emission will be affected by the length of material between the point of excitation and the end of the fiber. A dramatic example of the effect is shown for laser excitation along a Ti:YALO crystal fiber. An analytical model describing this absorption process has been derived and is being applied to the spectroscopy of the transition metal ions and the rare-Earth ions in crystal fiber hosts.

(C. E. Byvik, 2818)

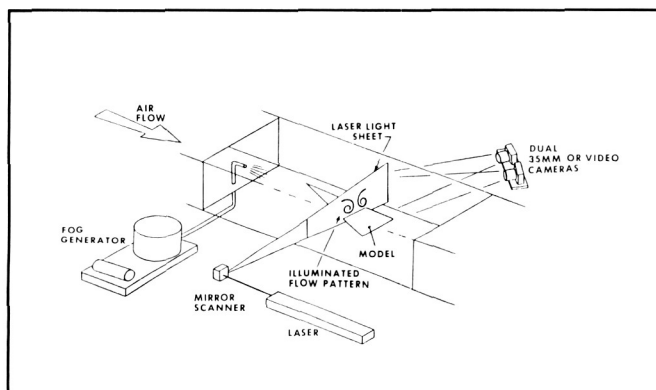


Absorption of fluorescence in Ti:YALO crystal fiber.

## Flow Visualization Using Laser Light Sheets

Visualizing the flow patterns around models in wind tunnel testing is important because an understanding of the flow patterns is fundamental to understanding the aerodynamics of the model. Smoke or water vapor introduced into the flow allows the flow pattern to be visualized by illuminating the flow field with a sheet of light.

Light sheets generated by lasers have found wide application in flow visualization. In general, laser light sheet systems have been designed for a specified test and viewing geometry. The twin mirrored galvanometer laser light sheet system was developed to provide adaptability to a wide range of wind tunnel applications. The design allows the aerodynamicist to control the size and location of the light sheet in real time, generate horizontal or vertical sheets, sweep a sheet repeatedly through a volume, generate multiple light sheets with controllable separation, and rotate single or multiple light sheets.

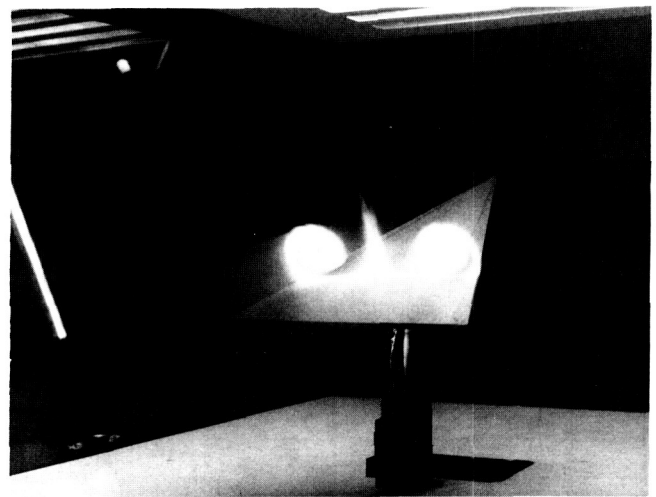


*Twin mirrored galvanometer laser light sheet flow visualization system.*

The system has been used to generate time-averaged light sheets with helium/neon and argon/ion lasers. The light sheet is generated by deflecting the output laser beam with two mirrored galvanometers whose axes are mutually perpendicular. One mirrored galvanometer is used to produce horizontal light sheets, while the other mirrored galvanometer produces vertical light sheets. The num-

ber of light sheets and their orientation are obtained by varying the frequency, amplitude, and shape of the drive signal to each of the two mirrored galvanometers. The illuminated flow field generated by these light sheets is recorded by conventional photographic and video techniques. Twin cameras are used to produce stereoscopic pairs of images which can be examined to yield three-dimensional visualization of the flow field.

(D. B. Rhodes and J. M. Franke, 3234)



L-86-11,889

*Visualization of vortices on delta wing model using laser light sheet flow visualization system.*

ORIGINAL PAGE IS  
OF POOR QUALITY

# Flight Systems Directorate



The Flight Systems Directorate conducts basic research and development in the broad, multidisciplinary area associated with aerospace flight systems. This includes systems hardware and software architecture concepts and design guidelines, validation and verification methods for reliable flight control systems, advanced cockpit interfaces, advanced airborne systems technology, aircraft operating procedures, fundamental electronics research, automation and robotics technology, and aircraft and spacecraft guidance and control system design methods, guidelines, and criteria.

The Advanced Transport Operating Systems Program Office coordinates a wide-scale focused technology research and development effort aimed at developing and improving the technology base for transport aircraft operating systems and the integration of these systems with the current and future air traffic control environments. The office also provides a focus for research and development of improved airborne operations and procedures and operates the NASA Boeing 737 aircraft and associated simulator.

The Information Systems Division conducts research to provide an advanced technology base for future spacecraft and aircraft systems. Specifically, the division performs research in the areas of robotics and automation, fault-tolerant systems validation, reliable software, system architectures, electronic/optical subsystem technology, and software engineering. The scope of activities is broad and ranges from the highest level systems considerations to the investigation of solid-state physics phenomena.

The Guidance and Control Division conducts generic and applied research on aircraft and spacecraft guidance, control, and antenna systems. The research is directed toward the development of a technology base for advanced aircraft and spacecraft systems analysis and design methods, including validation and verification demonstrations of advanced concepts. The division also develops multidisciplinary computer-based tools and techniques which allow appropriate guidance, control, and antenna design issues to be considered through all stages of aircraft and spacecraft design.

The Flight Management Division conducts research to provide a viable technology base for future aircraft and spacecraft flight management systems. Specifically, the division provides technologies

required by designers of crew station systems; defines and evaluates improved guidance and control procedures; and studies advanced airborne systems technology, traffic control strategies, and operating procedures for improving the efficiency of air traffic control operations. In addition, the division provides methodologies and criteria for measuring crew workload and stress.

### **Assessment of Computer Interface Device for Voice Control of Remote TV Cameras**

Human factors research has determined that voice input (recognition) is most effective as a control mechanism in applications that require a "third hand." The control of TV cameras and lights during mobile remote manipulator system (MRMS) operations onboard the Space Station is one such application. Recently, Langley Research Center personnel designed and completed a breadboard implementation of an interface device that allows voice-activated controls in an IBM PC to drive an automated video camera. The completed voice system has been successfully tested with an automated camera in the Langley Research Center Robotics Laboratory.

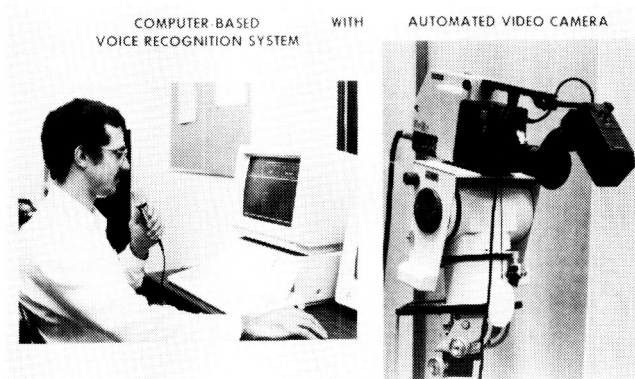
The microprocessor-based interface controls an automated video camera with remote pan/tilt/zoom/focus features. Control outputs from an IBM PC/XT-hosted "continuous speech" voice recognition system were determined as well as the signal requirements for the camera's remote-control features. The interface was then designed with available very-large-scale integration (VLSI) circuitry to decode the serial control information provided by the host computer/voice input system combination into appropriate voltage level on/off signals. The microprocessor was then programmed to handle a variety of commands designed to operate the video camera via voice input.

The voice-operated video camera interface was conceived, developed, and implemented to enable further research in manual versus voice control of automated Space Station cameras. In a previous study of this application, the camera views and operation



were simulated with graphics on an IBM PC. Vocabulary and control/capture timing experiments were conducted with several test subjects. Using the subject interface, a comparison was made of control performance from a real video camera (with mechanical time lags and target image location problems) versus performance obtained from the simulated version. The comparison generally verified the simulation results and contributed to the understanding of voice recognition applications.

(Anthony M. Busquets, 4684)



L-86-9371

*Automated video camera being controlled by computer-based voice recognition system.*

### Attitude Control Stability Analysis for Evolving Space Station

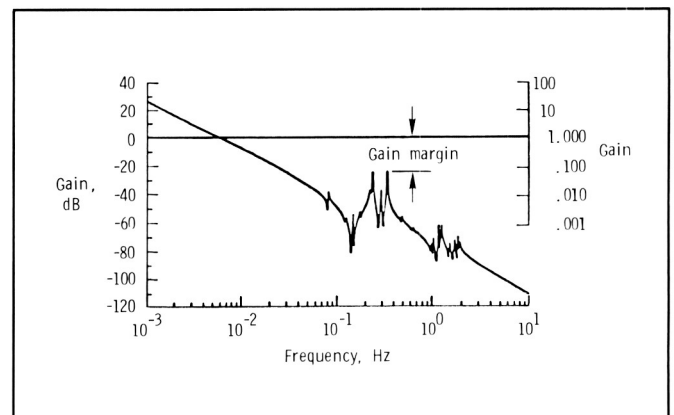
An attitude control system stability analysis was conducted for a number of Space Station configurations in support of the Critical Evaluation Task Force that met at Langley Research Center in the fall of 1986. The study included 5-m and 9-ft bay size versions of the dual-keel station as well as intermediate stages of assembly. The purpose of the study was to compare the attitude control characteristics with respect to relative stability for the station as it progressed from a simple boom structure to a dual-keel configuration.

The attitude control system included the control moment gyro (CMG) assembly used for three-

axis stabilization of the Space Station. The control law consisted of a proportional plus differential (PD) feedback logic with a first-order lag compensation. Analysis of the stability of the control system associated with the CMG's was performed using frequency response (Bode) plots such as that given in the figure. The gain margin shown in the figure was used as a measure of the relative stabilities of the various Space Station configurations.

The results of the study showed that all configurations and truss bay sizes exhibited stable gain margins for the assumed attitude control system. The 5-m structure was found to be superior to the 9-ft model from a control standpoint since it consistently had larger gain margins for corresponding station models.

(John W. Young, 4591)



*Typical frequency response for 5-m Space Station using compensated PD controller.*

### Comparison of In-Flight and Ground-Based Simulator-Derived Flying Qualities and Pilot Performance

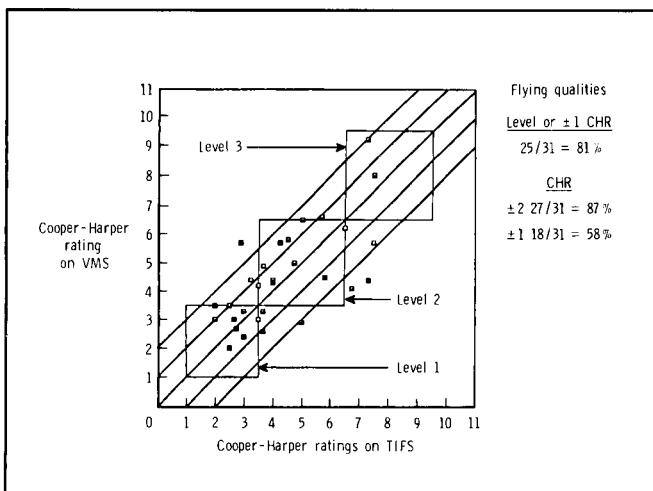
An obvious void of information exists which allows the flight controls/flying qualities engineer to determine and estimate the incremental flying qualities and/or pilot performance differences that may be



expected between results obtained via ground-based simulation tests and flight tests. To help fill this void, pilot opinion and performance parameters, derived from a six degree-of-freedom ground-based simulator (Visual/Motion Simulator or VMS) and a six degree-of-freedom Total In-Flight Simulator (TIFS), have been obtained for a jet transport aircraft with conventional cockpit controllers. The primary piloting tasks were the approach and landing, with emphasis on the flared landing. Thirty-one different dynamic response characteristics were simulated. Four engineering test pilots participated in both simulation programs.

simulators are not adequate for assessing pilot and vehicle performance capabilities for the landing task when the pilot has little depth and height perception from the outside scene presentation; and the ability of the ground-based simulator to predict Cooper-Harper Pilot Ratings (CHR's) was somewhat better for the approach task than for the flared-landing task. For the approach task, the CHR was predicted within  $\pm 1$  for approximately 75 percent of the configurations evaluated, compared to approximately 60 percent of the configurations for the flared-landing task. The example data in the figure indicate the pilot opinion differences for the flared-landing task.

(William D. Grantham, 2132)



*Comparison of pilot opinion of flying qualities obtained on TIFS and VMS for flared-landing task (all configurations).*

The major conclusion drawn from this study was that, in general, the flying qualities evaluation results obtained from ground-based simulators may be considered to be conservative, especially when the piloting task requires tight pilot control. The one exception to this, found in the present study, was that the pilots were more tolerant of control system time delays on the ground-based simulator. Other conclusions drawn from this study were that the effect of pitch sensitivity to control column inputs is more pronounced on a ground-based simulator than on an in-flight simulator; in general, there is a greater tendency for pilot-induced oscillations (PIO) on a ground-based simulator; ground-based

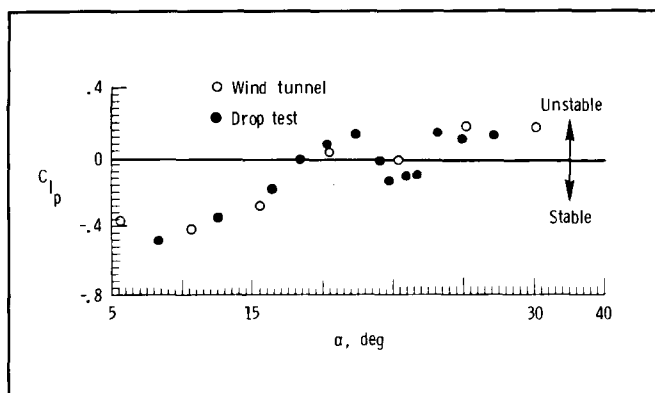
## Parameter Estimation Applied to X-29 Drop Model

The X-29 free-flight drop model is a 22-percent scale replica of the X-29 forward swept-wing demonstrator aircraft. The model is carried aloft by a helicopter, then released for gliding descent. These drop tests provide an important step between wind tunnel and full-scale flight testing because the experiments take place in the actual flight environment and allow extreme maneuvers to be attempted without endangering the pilot or full-scale prototype. Such large-amplitude, high rate maneuvers can provide important information relating to the dynamic behavior of an aircraft. The first drop tests qualitatively confirmed the occurrence of wing-rock (an abrupt amplification of rolling oscillations) which had been predicted from wind tunnel data. In order to obtain quantitative estimates of stability and control derivatives, a system identification process known as the modified stepwise regression (MSR) was applied to the drop test data.

The MSR algorithm yields estimates for stability and control derivatives that can be directly compared with wind tunnel predictions. Since the drop model maneuvers were unconventional and unlike those typically used for parameter estimation, it was necessary to employ an additional technique known as data partitioning, which allows the detection of trends in parameter estimates with angle of attack  $\alpha$ . In the figure, MSR estimates for the roll damping derivative

$C_{l_p}$  are compared with wind tunnel measurements. The flight estimates corroborate regions of unfavorable roll damping which were measured in the wind tunnel (such as that shown occurring between angles of attack of  $22^\circ$  to  $27^\circ$ ). These estimates have also correlated with the wing-rock episodes observed during drop tests. The ability to estimate stability and control parameters from drop test data provides a crucial adjunct to wind tunnel predictions because it may quantify dynamic behavior of the configuration which was not revealed by the tunnel tests. This process also provides an opportunity to corroborate prior data on the configuration and thus reveal discrepancies that may require further investigation.

(D. L. Raney, 3934 and J. G. Batterson, 4887)

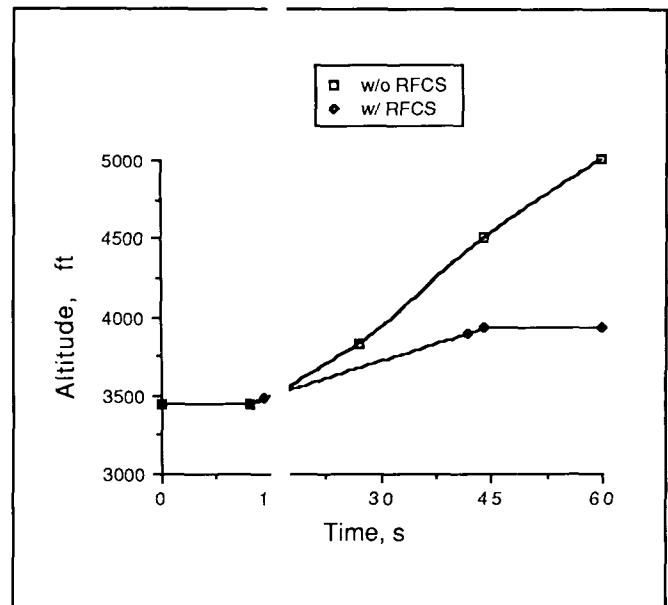


Roll damping derivative estimates.

## Restructurable Flight Control System

Aircraft control element failures can produce unanticipated, life-threatening flight modes that require corrective action in a timely manner, action that is not always intuitively obvious to the pilot. In many such cases a restructurable flight control system could automatically take the proper corrective action by detecting and isolating the failure and reconfiguring the control system to use other control effectors. A methodology for the design of a restructurable flight control system (RFCS) has been developed for a single operating point in the air-

craft's flight envelope. In this methodology, failure detection and isolation (FDI) are based on a decentralized approach that allows the best-known redundancy relationships to be used, thereby increasing the robustness of the FDI in the presence of modeling errors. The control redesign procedure is based on linear quadratic (LQ) methodology to compute new feedback control gains, thus effectively redistributing control among the remaining unfaulted effectors. The automatic retri algorithm solves a quadratic programming problem to obtain feedforward control to reject any constant disturbances (forces and moments) due to the failure.



Aircraft altitude response to hard-up right stabilizer failure.

An RFCS was designed for a hypothetical, modified B-737 airplane and evaluated using a six degree-of-freedom nonlinear simulation. Using the RFCS, the aircraft was able to recover from simulated failures. An example of a failed (hard-up) right stabilizer at  $t = 10$  s coinciding with the start of a climbing turn of 34 s duration is illustrated. The figure shows how the airplane with an RFCS continues to climb after the intended maneuver ends at 44 s. The air-

craft with the RFCS redistributes control among the elevator and other effectors and levels off at the end of the maneuver.

(Aaron J. Ostroff, 3951 and W. Thomas Bundick, 2259)

### Algorithm for Optimally Trimming Airplanes Equipped With Multiple Control Effectors

In order to increase performance and safety, airplanes with multiple longitudinal control effectors are receiving increased attention. Typical of these airplanes are three-surface airplanes and two-surface airplanes with thrust vectoring. Unlike conventional airplanes, the longitudinal load distribution of these aircraft is not uniquely determined for trimmed flight. This characteristic can be exploited by selecting the distribution that yields the minimum trim drag.

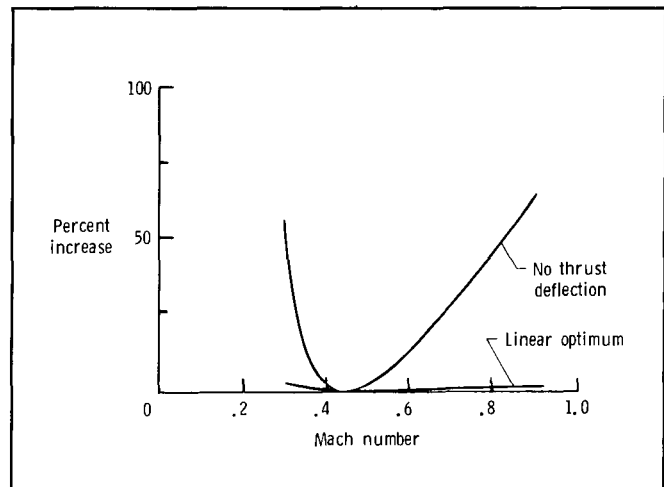
Normally, this minimization problem has been solved using nonlinear optimization. While this approach yields the most desirable distribution, it is often too burdensome. A simple alternative linear-optimum solution has been developed. This solution employs a Lagrangian formulation to minimize a quadratic model of trim drag subject to linear trim constraints.

To validate the performance of the algorithm, the trim drag obtained from the application of the linear-optimum solution was compared to the trim drag obtained through nonlinear optimization and ad hoc trimming procedures for several example aircraft. These comparisons show that the linear-optimum solution accurately predicts the nonlinear optimum. The figure demonstrates the effectiveness of the linear-optimum solution for trimming a two-surface, thrust-vectoring airplane similar to the high alpha research vehicle (HARV). The figure shows the increase in trim drag over the value obtained from the nonlinear solution for the linear solution and a nonoptimum solution. The nonoptimum solution does not utilize the thrust-vectoring capability. From the figure, it can be seen that the linear solution accurately predicts the nonlinear solution and that the

optimum solutions provide trim drag reductions of up to 60 percent compared to the nonoptimum solution.

The linear-optimum solution offers an opportunity to optimally trim aircraft in the conceptual and preliminary design stages with simple analytical procedures. It will also permit experimenters to accurately position model surfaces during wind tunnel tests to reflect in-flight positions. Furthermore, the algorithm is so simple that onboard applications are possible for adaptive controls algorithms.

(Kenneth H. Goodrich, 3744)



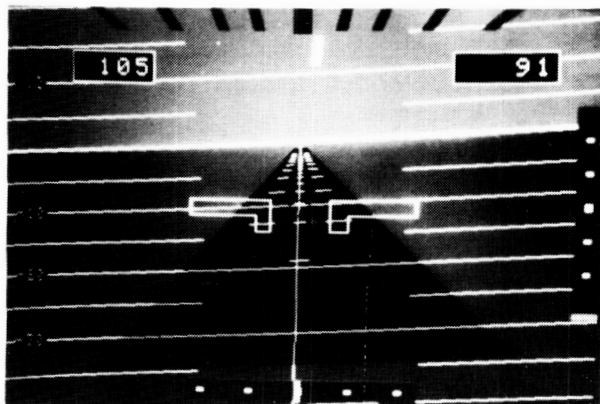
*Percent increase in trim drag over nonlinear-optimum solution for HARV-like airplane.*

### Completion of High-Level Graphics Language for Flight Displays

An established need exists for high-level graphics languages for the programming of programmable display generators (PDG's), particularly for PDG's used to generate real-time flight display graphics. Typically, the more sophisticated, flexible, and efficient the PDG, the lower the level of the available programming tools, and the harder it is to program. To address this problem, Langley Research Center has initiated a contract research effort with the Research Triangle Institute (RTI) in order to develop a

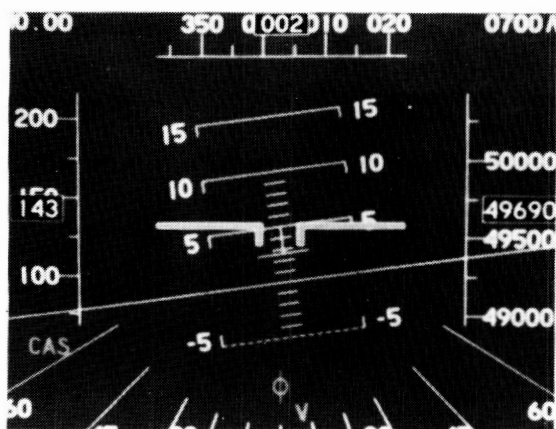
high-level graphics language for programming an experimental high-performance PDG, while still maintaining execution speed and access to and control of its advanced features.

Assembly-based PFD



Assembly language  
8 months

High-level-based PFD



High-level language  
2 months

*Comparison of software development time for two complex PFD's using Assembly language and new RAP high-level language.*

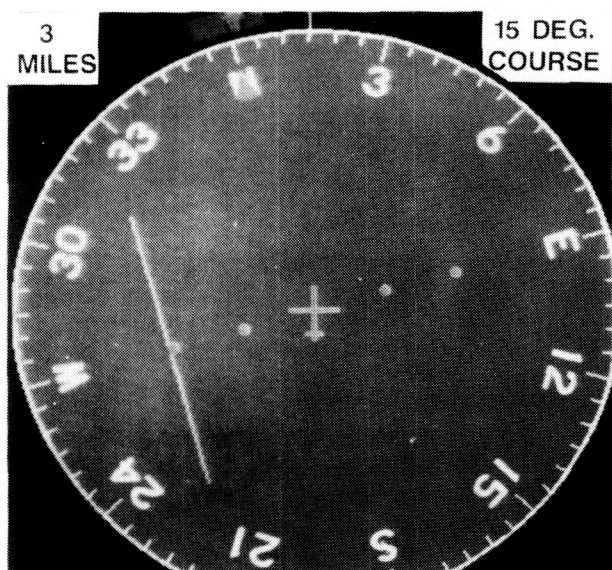
At RTI, a procedural language that consisted of a library of graphics functions and macros was developed with graphics primitives implemented to apply to entire scenes as opposed to individual objects. A unified, flexible set of data structures to support dynamic, shaded two- and three-dimensional graphics was designed. Powerful graphics primitives were conceived, and "C" was chosen as the base language because a flexible compiler existed as a commercial product. This base language was chosen due to the University of North Carolina's research with the experimental PDG. The library was developed into a software package known as RAP (real-time animation package).

RAP supports two- and three-dimensional drawing, dynamic window management, flexible character generation, and hierarchical data representation. Drawing capabilities include wire frames, flat and smooth shading, clipping, and hidden-surface removal. RAP has been used to generate a variety of complex, real-time display formats, such as the primary flight display (PFD) shown in the figure. In a comparison between an Assembly-based PFD and the high-level language-based PFD, the former took 8 months to implement whereas the latter took approximately 2 months to implement. Because RAP is easier to write, debug, and maintain than Assembly programs, it enhances programmers' productivity and reduces the cost and time required for flight display development. This tool has been brought in-house at Langley Research Center and is being used to develop new displays.

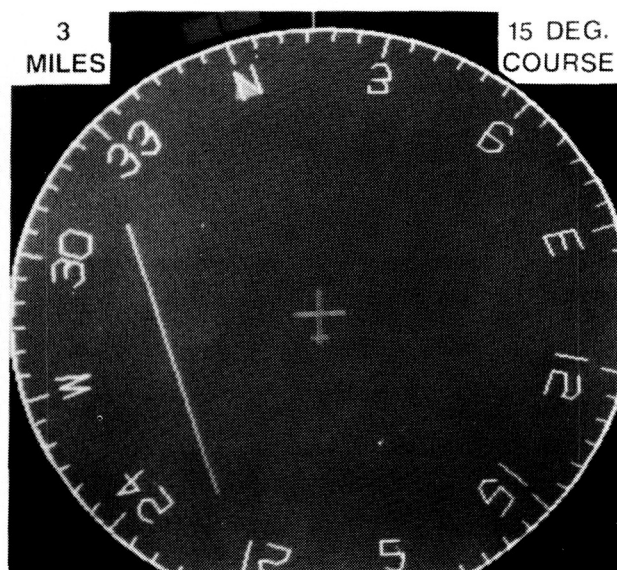
(Jack J. Hatfield, 3917)

### Rotatable Antialiased Character Set for All-Raster Flight Displays

The need for arbitrarily oriented, high-quality alphanumeric characters in all-raster flight display systems has emerged as an essential requirement. This is of importance in situational-awareness displays in which human factor researchers have found that alphanumeric characters which track the orientation of the display provide additional positive cues. This effort determined the feasibility of incorporating a high-quality, rotatable alphanumeric font into the PDG technology base being pioneered by Langley Research Center.



PRESTORED ANTIALIASED FONT



TRANSFORMED RASTER-VECTOR FONT

*Comparison of techniques for character rotation in all-raster horizontal situation indicator (HSI) display format.*

The Langley Research Center experimental PDG has a fourfold image memory storage capacity compared to its image display capacity. The effort took advantage of the extra image memory by storing prerotated fonts at small angular increments which could be copied, in high-speed random access fashion, into the display portion of memory during the run of flight displays to produce seemingly continuously rotatable alphanumerics. An oversized font was entered into the PDG with a digitizing tablet, and the PDG was used to shrink, transform (at  $5.625^\circ$  increments), and antialias the font. The copies of the font were stored in the unused memory. During the run of the flight display, the font copy with the appropriate orientation was copied into the display memory as a function of the resultant display rotation angle. Additional economies were accrued by using a mirroring rule that covered the  $360^\circ$  range of rotation using only the stored first quadrant of the font. This technique and the competing technique of dynamically rotating stick characters were used to generate a horizontal situation display. The quality of the new stored-font technique, in comparison

with the stick-character technique, is readily apparent from the figure.

Several flight displays were generated in real-time with excellent results using the new technique. The study established the feasibility of generating high-quality, real-time, rotatable alphanumerics that are superior in boldness, smoothness, and clarity to those that could be obtained with a vector font. (Jack J. Hatfield, 3917)

### Interactive Editor for Definition of Touch Sensitive Zones

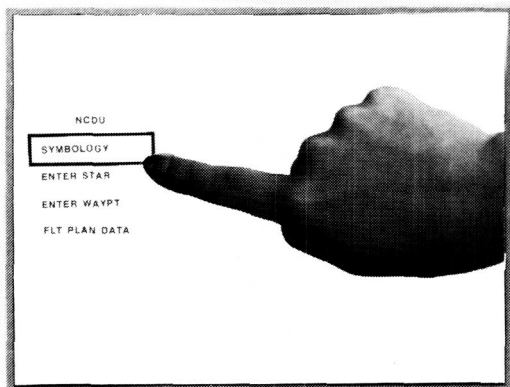
In the effort to develop more efficient man/machine communications methods, touch displays have shown potential as straightforward input systems. Although a wide variety of systems exist, the needed software is often repetitive and requires numerous lines of code. As a result, an interactive editor and applications package have been developed to simplify the process of implementing touch screens as input devices.

The touch editor allows for interactive definition of touch-sensitive areas for graphics displays. Each area is defined by touching the screen in one corner of the desired zone, and then moving to the opposite corner of the zone without leaving the screen. As this is done, a rectangle is drawn on the monitor showing the user the touch zone as it is defined. The rectangular area expands dynamically with the touch



Off-line edit session

L-86-8960



Area definition

L-86-7426

*Interactive editing session that defines touch zones utilizing the touch editor.*

movement, in a manner similar to a rubber band, and stops when the user exits from the screen. As touch areas are defined, the coordinate information is written to a data file that is used by an application program and the application package to determine if an area has been pressed.

The editor is composed of a set of subroutines which links directly to a user's display generating software. It is presently implemented on a VAX-11/780 minicomputer and Adage-3000 programmable display generator, but because of its modular organization the editor can be easily adapted to any hardware. Through the use of the touch editor and associated application package, the process of integrating touch screens as input/output devices in aerospace applications should prove to be simplified considerably and should require much less development time.

(Denise R. Jones, 4684)

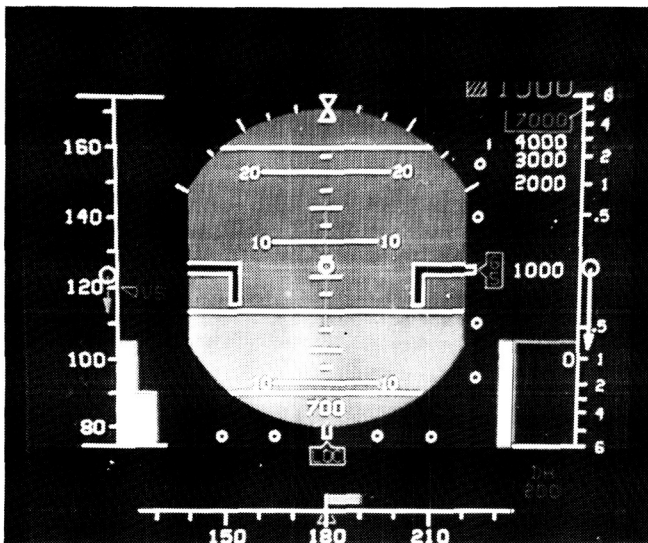
## Defect-Free High-Resolution Electroluminescent Display Achieved

Planar Systems, Incorporated, under a contract funded jointly by NASA and the U.S. Army, has succeeded in producing defect-free high-resolution electroluminescent display panels. These panels are being used in a display system developed by Hycom, Incorporated (also under joint NASA and Army funding) which is capable of displaying video and graphics in 16 shades of gray. Earlier display panels suffered from numerous line and column defects that made the display unacceptable as a flight display.

The display panels are 5.1 x 6.4 in. in size and have 512 rows x 640 columns of picture elements (pixels), corresponding to 327,680 individually addressable pixels in each panel, with a resolution of 100 pixels per in. With this accomplishment, flat-panel electroluminescent display technology can now provide sufficient screen size, resolution, and addressing speed, along with minimal defects, to be considered for primary flight and navigation displays in research simulators. Before the electroluminescent



display technology can be applied in the flight environment, however, its brightness and contrast ratio under high ambient illumination must be improved. (James B. Robertson, 4682)



L-87-3896

TV rendition of an electronic primary flight display (PFD) format on 8-in. diagonal, high-resolution electroluminescent flat-panel display.

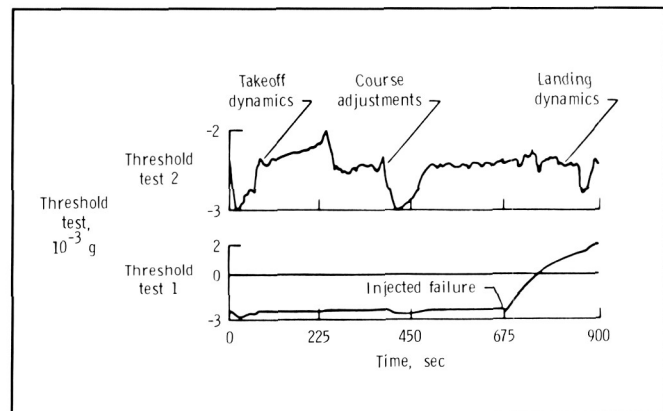
### Flight Demonstration for Failure Detection and Isolation of Redundant Inertial Sensors

To achieve desired performance and economic improvements in the next generation of aircraft, flight control systems will rely heavily on the onboard sensor complement. Safety and flight control system reliability requirements dictate a high level of redundancy for these sensors. To meet these requirements an optimally designed redundant strapdown inertial measurement unit (RSDIMU) operating with efficient redundancy management algorithms has been developed.

Optimality in the RSDIMU design has been realized with a skewed array of sensors. Efficient redundancy management concepts have been devel-

oped with failure detection and isolation (FDI) techniques. Failure detection is accomplished by comparison of the RSDIMU sensor measurements with a failure threshold. Isolation of failed sensors is accomplished through logic techniques. An isolated failure is removed and the system is reset to eliminate corrupted information from the avionics systems.

A series of flights in a commercial transport aircraft was used to test the developed concepts. Simulated failures were added to the RSDIMU gyro and accelerometer sensor measurements during the flights. Timely detection and isolation of the sensor failures provided successful demonstration of the redundancy management concepts. The figure illustrates the failure detection tests for accelerometers during a 15-min flight. Threshold test 1 shows the effects of a sensor failure applied at 675 s. The failure is detected when the threshold test goes positive. Threshold test 2 has unfailed accelerometers and shows the threshold dynamic effects due to aircraft takeoff, course adjustments, and landing. (Frederick R. Morrell, 3404)



Navigation-level threshold tests for failed and unfailed accelerometers.

### Estimating the Distribution of Fault Latency in Digital Processors

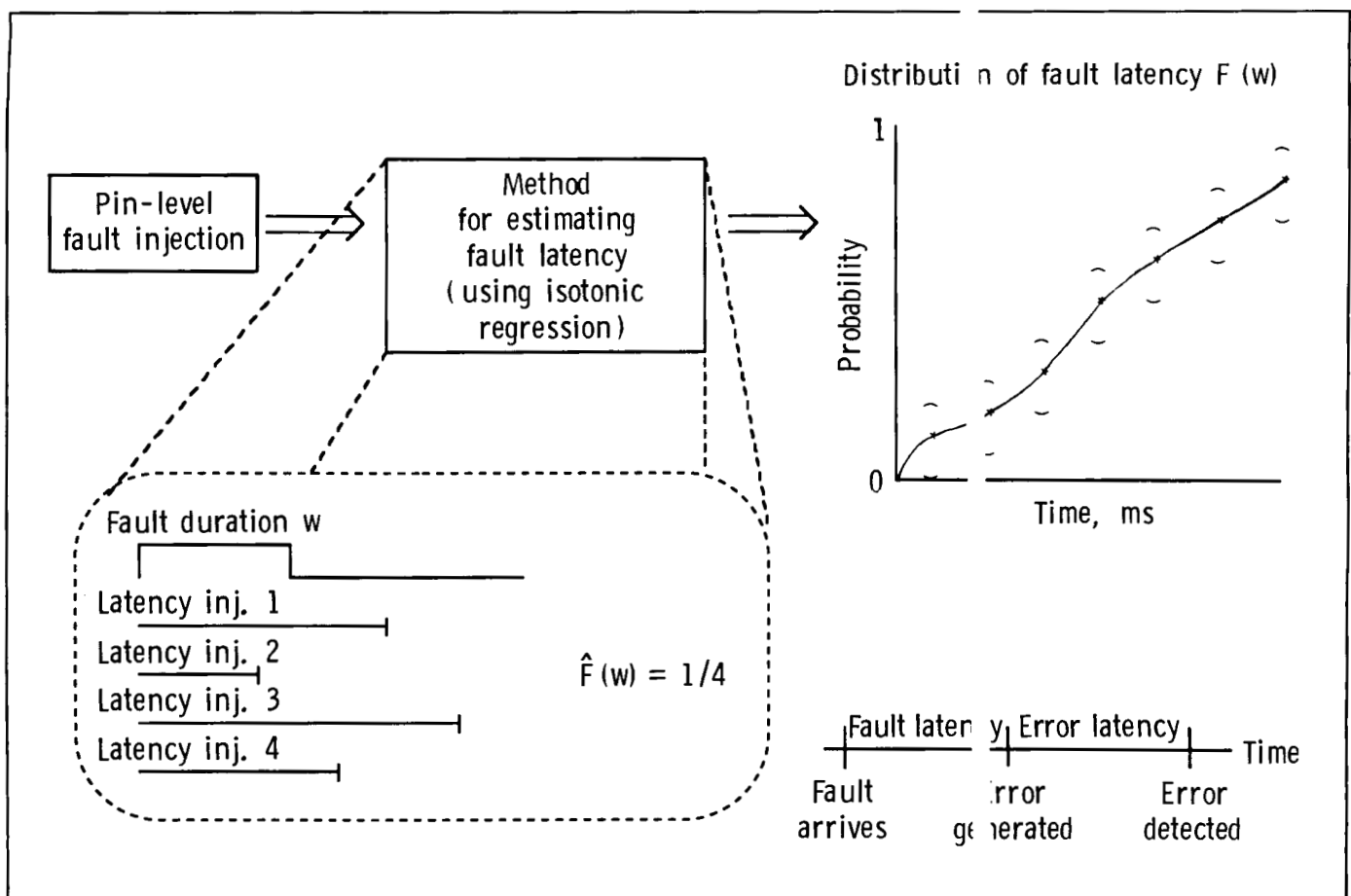
The reliability analysis of a reconfigurable computer system requires detailed information about the



fault occurrence and fault-recovery behavior of the system. A major component of the recovery processes of a fault-tolerant system is fault latency. Fault latency is the time interval from the occurrence of the fault until the fault generates an error. During their latency period, faults cannot be detected and removed by the system's fault-tolerance mechanisms. Consequently, the longer a fault lies latent, the greater is the probability that a fault will arrive in a second processor, and, at some later time, both faults will produce errors simultaneously. These simultaneous errors can defeat the voting system and cause system failure.

Since the time-of-error generation is not directly observable in a physical processor, measurements of fault latency in a digital processor were previously

unobtainable. Recently, researchers at the University of Michigan (working under a Langley Research Center grant) have developed a technique to infer the distribution of fault latency indirectly. Their technique produces an unbiased estimator of the fault-latency distribution from the fault-detection response of a processor injected with fixed duration faults. The technique is based on the observation that the ratio of the number of faults detected by a fault-tolerant processor to the number of faults injected is an estimate of the latency distribution at a point equal to the duration of the injected fault. By repeating this procedure for values of the fault duration over a wide range of values, the distribution of fault latency is obtained. The University of Michigan technique has been improved by in-house Langley Research Center



Schematic of method to estimate fault-latency distribution in digital processor.

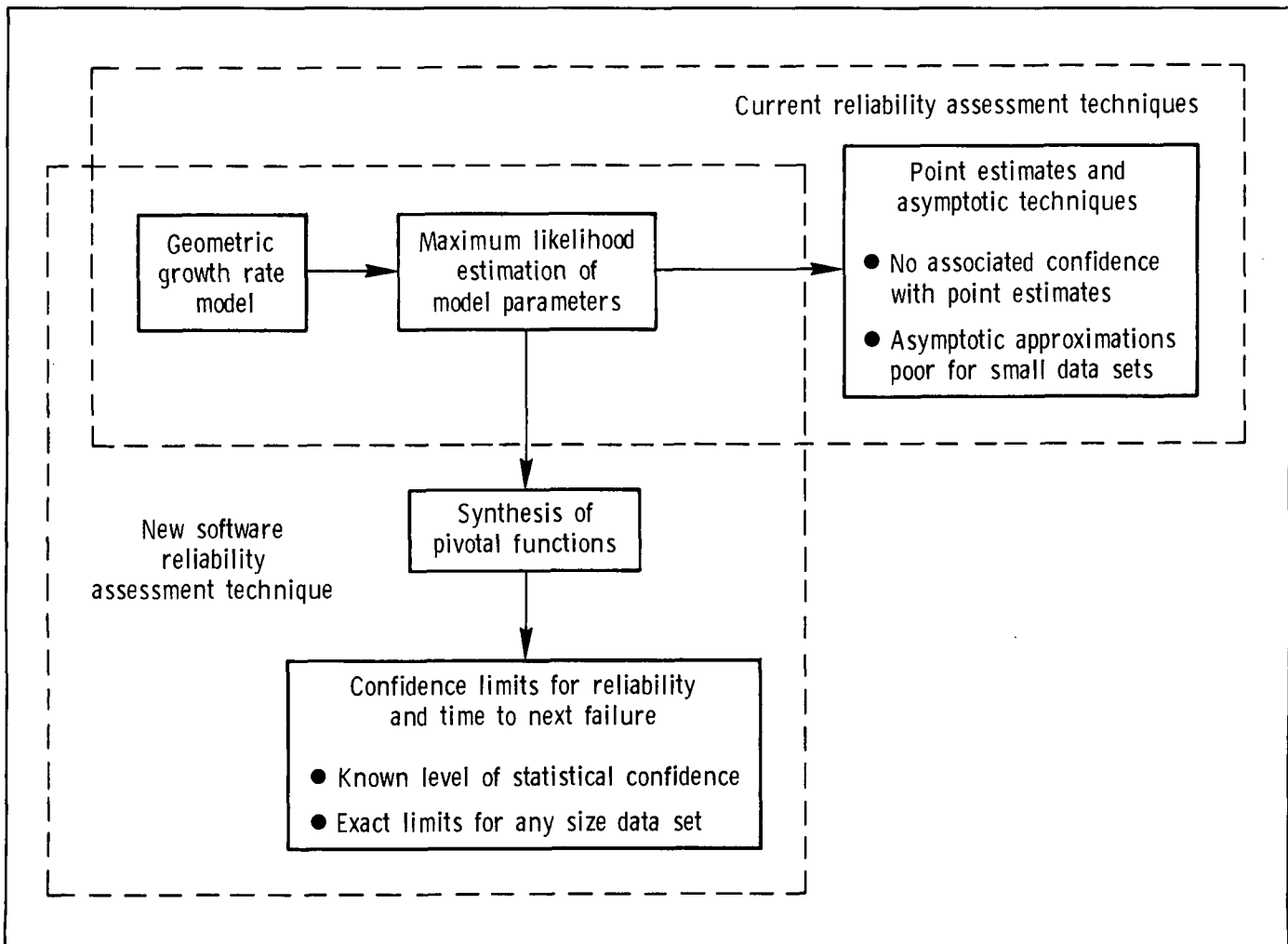
researchers using the statistical theory of isotonic regression to obtain better distribution estimates and to provide quantification of the accuracy of the estimates with statistical confidence bounds.

Fault latency has been measured in two fault-tolerant computers located in the Langley Research Center AIRLAB (Avionics Integration Research Laboratory) Facility. Over 15,000 fault injections have been performed on one of the computers by University of Michigan graduate students providing measurements for fault latency in the central processing unit (CPU) control path, CPU data path, and cache controller. Over 4,500 faults have been injected in the other computer yielding estimates of fault latency in the CPU, memory, and broadcast bus.

Fault latency in physical systems can now be estimated. The method provides estimates of parameters with quantifiable accuracy (i.e., confidence bounds) to which reliability analyses are sensitive. (Ricky W. Butler, 3681)

### Development of Confidence Limits for Estimating Software Reliability

As the demand for highly reliable computer systems increases, accurate estimation of the reliability



*Software reliability assessment.*

of software has evolved into a major concern. Previously, only single estimators with no associated level of statistical confidence were used to estimate reliability and the time to the next software failure, and asymptotic techniques were utilized to construct bounds for software reliability. The goal of this research was to develop a more precise approach to estimating reliability from available software failure data.

To estimate software reliability with corresponding confidence levels, the statistical method of pivotal functions was applied to the widely used Moranda reliability growth model. Two pivotal functions for predicting reliability and the time to the next software failure were constructed from the model. Based on simulations of the pivotal distributions, confidence limits for reliability and the time to the next software failure were generated.

A study of the pivotal distributions with respect to asymptotic techniques has clearly showed that the asymptotic approach to estimating software reliability is inadequate when only a small number of errors are found in the software. This result is particularly important since available software failure data suggest that only a small number of errors will be found during testing. This research also demonstrated the sensitivity of predictions to the assumption that the times between software failures are exponentially distributed. Hence, the Moranda model may not adequately describe the software failure process in all situations. Overall, the pivotal function approach to software reliability has provided a means to determine exact confidence and to predict limits regardless of the number of errors found in the software.

(Kelly J. Dotson, 3681)

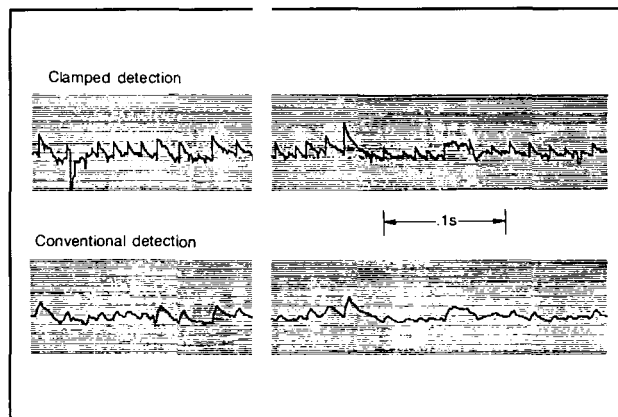
## Wideband Electric Field Measurement System

The ultrahigh frequency radar observations of direct lightning strikes to the NASA F-106 airplane have indicated that most of the 690 high-altitude strikes encountered by the F-106 during direct-strike lightning test flights were triggered by the airplane. Further study of the associated initiation phenom-

ena required electric field data with submillisecond resolution, but the on-board system was capable of nothing less than a millisecond resolution. Techniques were investigated for significantly improving the bandwidth of electric field measurements. Based on these investigations, new signal processing components were designed to achieve the wide bandwidth through implementation of a clamped detection signal processing concept.

The sensor portion of the system is based on a well-established mechanical design consisting of a rotating-vane electric field mill that mechanically induces the electric field by alternately shielding and unshielding fixed sensors to generate a signal that is usable by the highly sensitive, ac-coupled preamplifier. The electronics portion of the system is new and exploits the clamped detection scheme, which continually restores the dc levels of static electric fields lost by the preamplifier. The bandwidth of the new field measuring system was determined in the laboratory to be from dc to over 100 kHz, which is three orders of magnitude greater than the upper bandwidth limits of presently employed designs. Flight tests of the prototype unit were completed, and four systems were installed on the F-106 to gather the first wide bandwidth field measurements data during thunderstorm penetrations.

(Klaus P. Zaepfel 3681)



Comparison of clamped detection (top trace) and conventional detection for F-106B flight data of external electric field

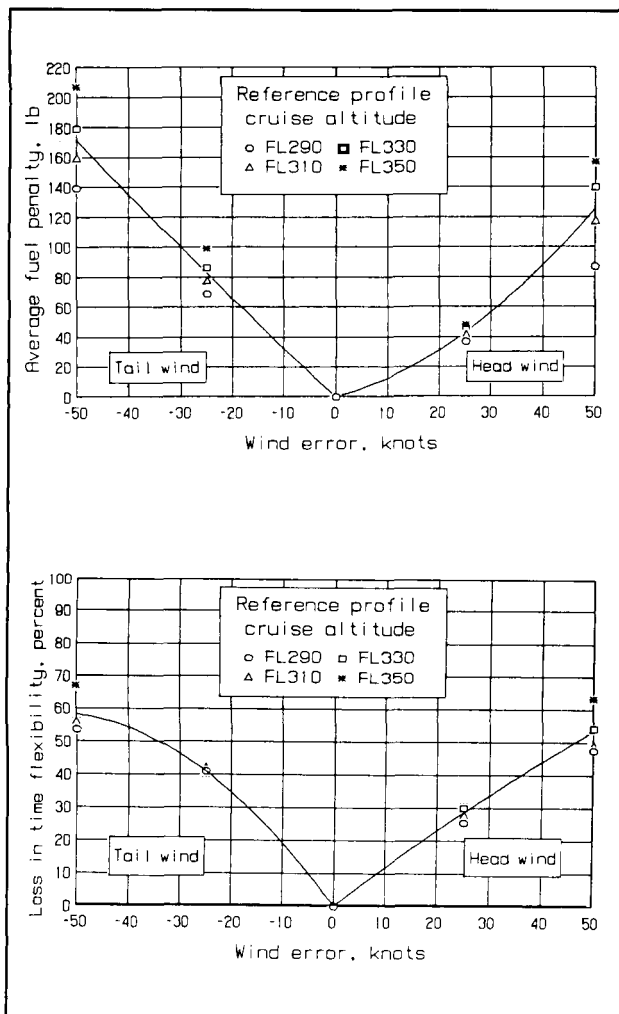
## Assessed Fuel Penalties and Time Flexibility of 4-D Flight Profiles in Mismodeled Wind

Advanced air traffic control systems, which incorporate time-based metering of traffic, are currently being developed. Airplanes in the system must be able to consistently achieve accurate arrival times at predefined metering points. Individual airplane fuel penalties incurred while correcting for mismodeled winds must be outweighed by the benefits of

reduced delays provided by the time-based air traffic system. The objective of this effort has been to quantify the time capabilities and fuel penalties of individual 4-D flight profiles in the presence of wind errors.

These data are useful in cost and benefit studies for determining the level of wind accuracy needed to support cost-effective time-based air traffic control. A parametric sensitivity study has been conducted to evaluate time flexibility and fuel penalties associated with 4-D operations in the presence of mismodeled wind. Sensitivity results have been obtained for a typical 200-nmi cruise and descent flight segment with speeds and altitudes bracketing the capabilities of the airplane. Typical results are shown in the figure. Mismodeled tail winds have been found to penalize the airplane to a greater extent than mismodeled head winds. Higher cruise altitudes have further reduced time flexibility and increased fuel penalties. Airplane drag characteristics and speed capabilities have been found to significantly influence these results.

(David H. Williams, 3621)



Average 4-D fuel penalties and loss in 4-D time flexibility versus wind error for 90,000 lb B-737-100 airplane at 200 nmi cruise and descent.

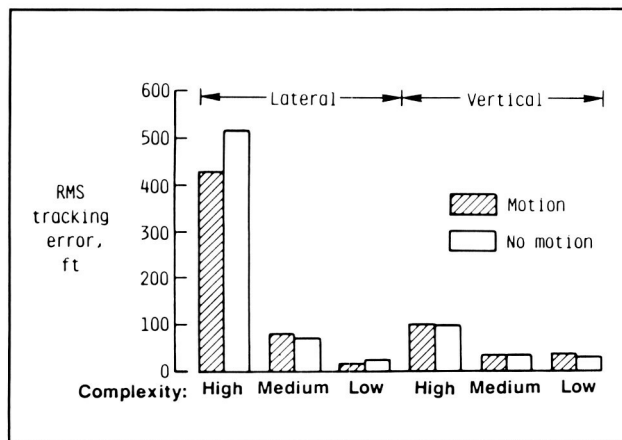
## Effect of Motion Cues During Complex Curved Approach and Landing Tasks

NASA is participating with the Federal Aviation Administration in the Microwave Landing System Advanced Applications Program. This is a multiphase program that uses both fixed-based and motion-based aircraft simulators to define envelopes of usable approach path geometry by considering aircraft instrumentation, path tracking performance, pilot acceptance, and workload. There was concern that both quantitative and subjective measures being used to indicate pilot performance, acceptance, and workload might be affected by motion, or lack of motion, as sensed by the pilot. A study was then conducted to determine the effects of motion cues during manually flown, curved approach-and-landing tasks.

The results from this study suggest that reliable performance measurements are obtainable from fixed-based simulation for low-to-moderate-complexity tasks. For high complexity tasks, how-

ever, the performance measurements obtained in fixed-base simulations are conservative, i.e., the fixed-based simulation predicts somewhat poorer performance than would be achieved during actual flight operations (as shown in the figure).

(Charles E. Knox, 3621)



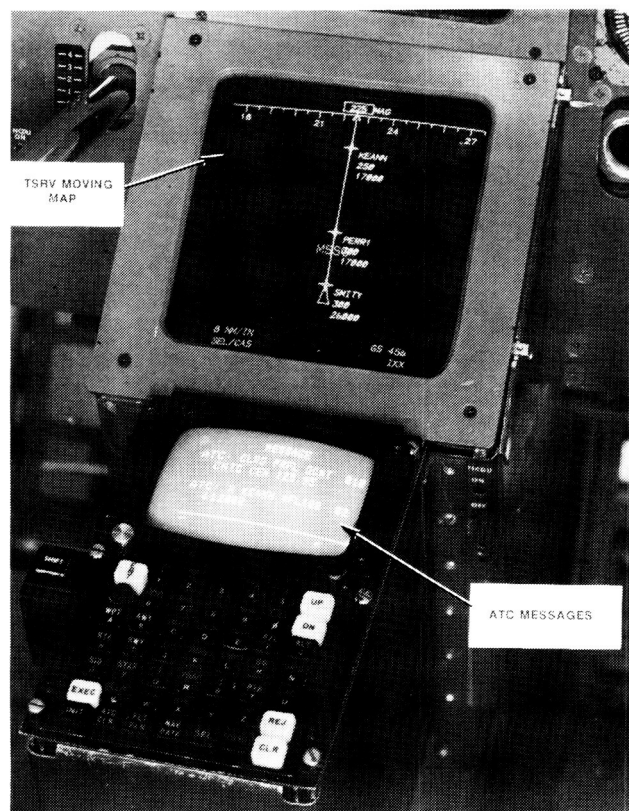
Effect of motion on pilot-in-the-loop simulation results (tracking performance).

## Evaluation of Concept for Data Link Air Traffic Control Message Exchange

Communication clutter on air traffic control (ATC) voice radio frequencies in many busy terminal areas and the resulting flight crew high workload could be eased by using a two-way digital data link to exchange routine ATC messages. The objective of this data link research was to evaluate a baseline concept developed at Langley Research Center for exchange of tactical and certain noncontrol ATC messages between the air traffic services and airborne flight crews. The scope of this real-time simulation concept evaluation was limited to the airborne interface and operational issues in the flight deck.

Under the concept, messages were formatted for presentation on a typical control display unit that required a two-keystroke action by the flight crew to generate and dispatch a "roger" or "unable" re-

sponse. The photograph shows examples of ATC messages received over the data link and displayed in an alphanumeric format. Complete operational protocols and a baseline message set applicable to the concept were developed under an Advanced Transport Operating Systems (ATOPS) contractual effort with the MITRE Corporation. Voice radio contact was maintained for lengthy negotiations and as a backup capability.



L-86-8062

ATC message examples displayed on control and display unit (CDU) in Transport Systems Research Vehicle simulator cockpit.

The test results indicated that the flight crews preferred using the data link for exchanging routine ATC messages and facility status information. The first officer's ATC communication workload was rated lower with the alphanumeric presentation of messages; however, pilot comments indicated that pilots with low flight time, when they are actively flying the aircraft, could benefit by having spoken in-

coming messages in addition to an alphanumeric display. This research has provided a basis for continued development of an ATC message exchange concept based on data link capability. Alphanumeric presentation of messages to the flight crew proved highly beneficial; however, the research identified a need to improve the interface (possibly through application of voice regeneration technology) for the pilot who was actively controlling the aircraft.

(Marvin C. Waller, 3621)

### Takeoff Performance Monitoring System

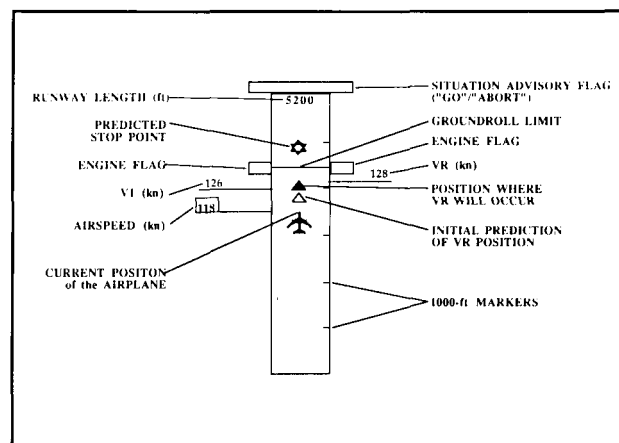
A Takeoff Performance Monitoring System (TOPMS) has been developed to provide pilots with graphics and numeric information pertinent to their decision to continue or reject a takeoff. As shown in the figure, the TOPMS head-down display consists of a runway graphic overlaid with numerics and symbols that indicate: runway length; current position and airspeed; decision speed ( $V_1$ ) and rotation speed (VR) and where each occurs; limit (per FAA regulations) of the ground roll distance available for reaching VR; predicted stop point from current conditions; engine-status flags; and an overall situation advisory flag that recommends continuation or rejection of the takeoff. Initially, balanced field length (i.e., the legal-minimum field length for the aircraft weight and existing ambient conditions) is displayed; after noting this value, the pilot enters the actual length of the assigned runway, and the display adjusts accordingly. When an abort is initiated, all takeoff-related information disappears leaving only the airplane position, speed, and predicted stop point as cues.

Over 30 experienced Air Force, airline, industry, and government pilots working as two-man crews in the Langley Research Center Transport Systems Research Vehicle Simulator have flown, rated, and commented on the TOPMS displays. They rated the system "good" (3 on a 1 to 10 scale). They agreed that the "pilot not flying" should have primary responsibility for monitoring the display. In addition, they agreed that the "pilot flying" should have a simplified head-up TOPMS display implemented on his or her

side. In a following study, 17 pilots evaluated a modified head-down and a simplified head-up TOPMS display. Ratings and comments were quite favorable.

A patent request has been submitted, and the system has received an IR-100 award for 1986.

(David B. Middleton, 3595)



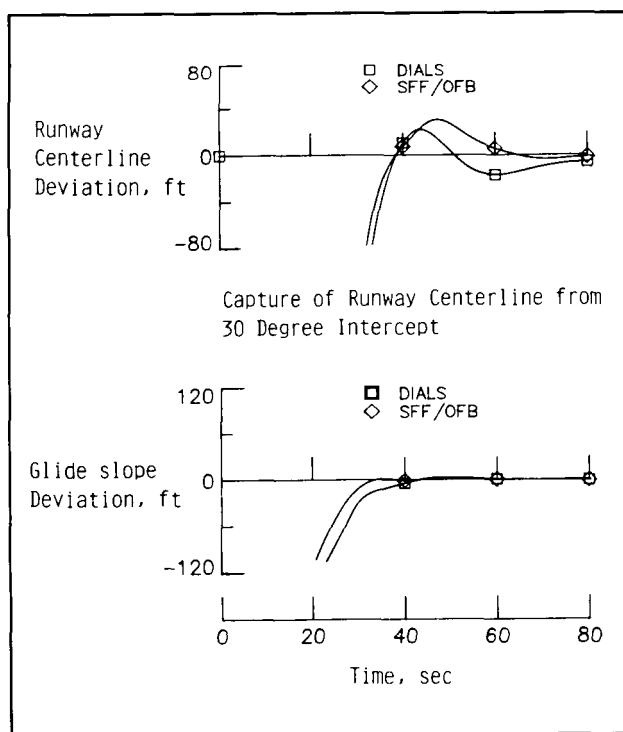
TOPMS display symbology.

### Stochastic Optimal Feedforward/Output Feedback Controls Design Methodology

A practical direct-digital design of multi-input/multi-output (MIMO) flight control system (FCS) has been developed under a Langley Research Center contract with Information and Control Systems, Inc. This design method has been named SFF/OFB for stochastic optimal feedforward/output feedback control.

Current methods for the calculation of feedforward gains are computed using perfect models (models with no noise). In SFF/OFB, the feedforward and feedback gains are computed using stochastic models (based on noise statistics). The methodology allows designers to choose the measurements they wish to use for feedback. These feedbacks may be direct sensor measurements or filtered quantities whose dynamics may be included in the design model without

the added complexity this inclusion would introduce in optimal full-state feedback design. The methodology accommodates integral feedback to eliminate steady-state errors; dynamic compensation to reduce sensitivity to noisy sensors and disturbances such as wind gusts; rate control for smooth control and reduced control activity; incremental implementation to eliminate storage of the trim values as well as the problems associated with integrator buildup; and reduced sensor complement for less hardware complexity and lower costs. In general, an SFF/OFB FCS design will be less complex than the full-state FCS design since SFF/OFB does not require a Kalman filter. Experience has shown that an SFF/OFB design requires 45 percent less memory than a full-state design.



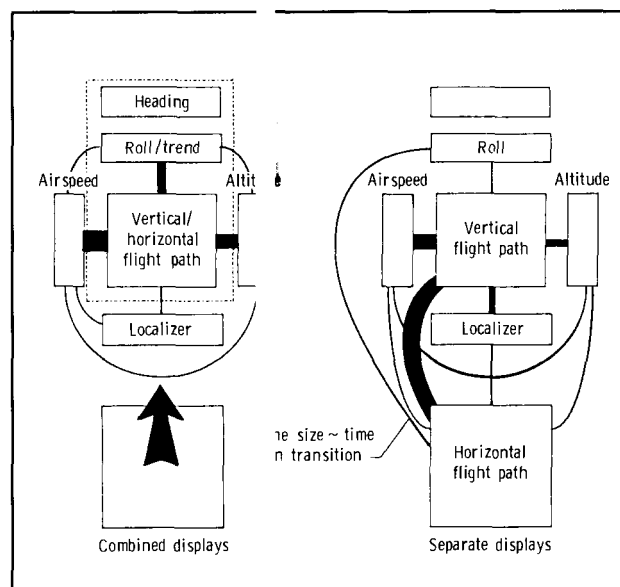
Capture of runway centerline from 30° intercept and 4.5° glide slope.

The SFF/OFB method was applied to the design of an autoland system for the Advanced Transport Operating Systems (ATOPS) Boeing 737 research aircraft, and its performance was tested in a non-linear digital simulation of the aircraft. The plots

compare the simulation results with those of the Digital Integrated Automatic Landing System (DIALS), which is a full-state design successfully flight tested on the ATOPS aircraft. The results show similar performance with this simplified system. (Richard M. Huesgen, 3897)

## Effects of Combining Vertical and Horizontal Information Into Primary Flight Display

Previous studies at Langley Research Center and elsewhere have suggested that the integration of the primary flight information (both vertical and horizontal information) into a single display format could be beneficial, particularly under high workload or critical flight conditions. This assumed benefit may be largely attributed to the reduction in the visual scan area which is brought about by the information integration. This effort has determined what benefits are directly attributable to a reduction in visual scan area produced by combining vertical and horizontal flight information.



Scan behavior evaluation of two display configurations.



Two display configurations were used. The first configuration consisted of two display formats, a primary flight display (PFD) and a horizontal situation display (HSD) format, in which each was placed on separate displays in a conventional PFD above the HSD orientation. For the second configuration, the HSD format was combined with the PFD format. Four subjects participated in this study, with data collected on subjective opinion, performance parameters, pilot-control inputs, and physiological measures to include oculometer measurements (eye scan).

The results showed that, from a performance and subjective standpoint, the combined configuration was slightly better than the separate configuration. Additionally, a potentially significant result was shown in the eye-scan behavior data. If the visual time available for the primary display is considered critical, then a 46-percent increase in available time (that is, dwell time and transition time associated with the second display) would occur when going from a two-displays configuration to a single-display configuration. This result is relevant to pictorial, primary display formats, in which both the vertical and horizontal information are presented on a single display.

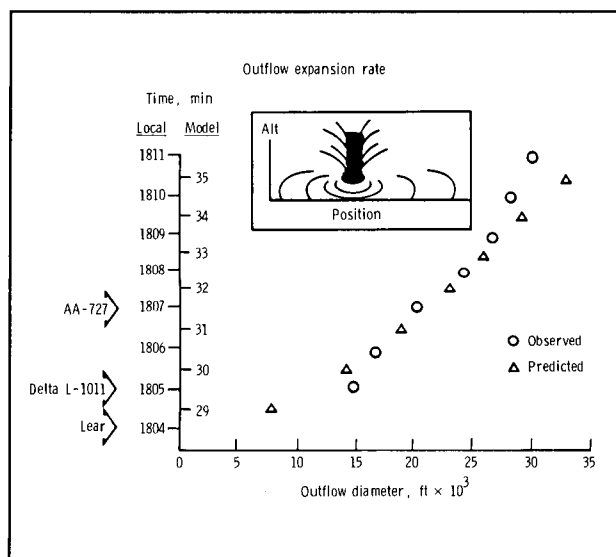
(Terence S. Abbott, 3917)

### Validated Wind Shear Model Through Comparison With Dallas-Fort Worth/Delta Airlines Microburst Event

A wind shear model, based on the atmospheric physics associated with microburst phenomena, has been developed at Langley Research Center in the Wind Shear Research Program. The model (once initialized with a set of ambient atmospheric conditions and followed by an arbitrary triggering disturbance (assuming the initial conditions were conducive)) spontaneously generates the full-state output for the microburst. This output includes, for example, the vector wind field and radar reflectivity as a function of  $X$ ,  $Y$ , and  $Z$ , and time. The objective of this research effort was to provide a validated data set, generated by the model, which corre-

sponded to a specific microburst occurrence. Having thus validated this data set, one can, with a considerable degree of confidence, employ this data set in a host of research, development, and training applications which require the high-resolution, expansive volume, and time-variant characteristics of the microburst state variables.

On August 2, 1985, a Delta Airlines L-1011 encountered a microburst-induced wind shear and crashed during a landing approach at the Dallas-Fort Worth airport. Extensive analysis of that accident by numerous investigators resulted in the development of a great deal of information concerning atmospheric conditions just prior to the occurrence of the microburst, as well as information concerning the microburst event itself (such as the outflow propagation rate at ground level and the existence and location of rain and hail). This atmospheric information was used to initialize the model, which then generated the full-state output of microburst parameters. These parameters were then compared with information deduced from the actual event.



*Dallas-Fort Worth microburst event versus model prediction.*

Excellent agreement was obtained between the model outputs and corresponding data from the microburst. An example of this agreement is shown

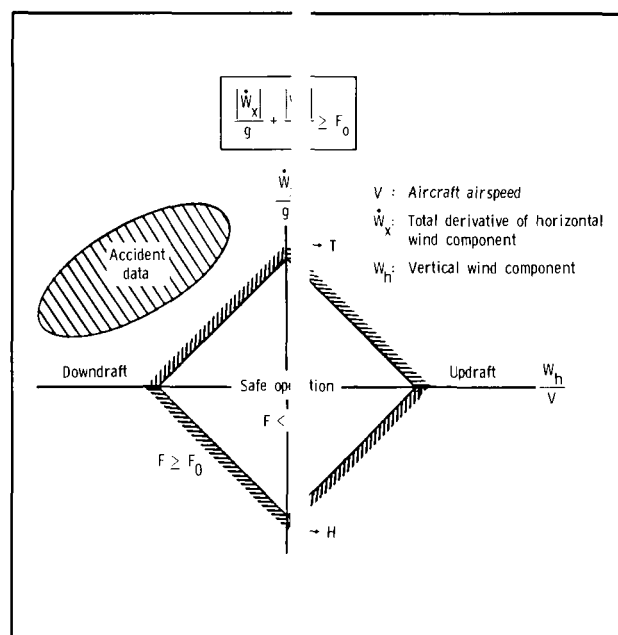
in the figure, which is a comparison of the observed and predicted outflow diameter of the microburst at ground level, as it propagated from a diameter of zero to approximately 6 miles over a period of 7 to 8 minutes. Observed data were provided by a Lear jet prior to the L-1011 wind shear encounter and by an American Airline 727 after the L-1011 had crashed. (Roland L. Bowles, 3621)

### Identification of Wind Shear Hazard Index for Design of Alert and Warning Systems

Key to the development of airborne wind shear detection, warning, and avoidance systems is the identification of a hazard index that exhibits functional dependence on atmospheric states that can be reliably sensed and that scales with available aircraft performance in such a way that the index predicts impending flight path deterioration. This hazard index must also account for factors such as the statistical nature of the wind shear threat, fusion of present position and "forward-looking" sensor capabilities, and development of objective methods for determining system warning thresholds, which consider the potential for nuisance alerts. The objective of this research was to derive an aircraft-specific hazard index based on accepted fundamentals of flight mechanics and current state of knowledge of wind shear phenomena. The accomplished research has yielded new concepts for airborne wind shear warning and alert systems. The significance and impact of the derived techniques have been acknowledged by domestic aircraft and avionics manufacturers and by international companies such as Aerospatiale Company.

An analysis was conducted which revealed the importance of aircraft energy balance for flight in spatially and temporally varying wind fields. The analysis revealed that the rate of change of specific energy (potential climb rate) depends linearly on a nondimensional parameter that only contains information regarding air mass movement. Further analysis indicated that the subject parameter can be physically interpreted as the loss in available excess

thrust-to-weight ratio due to downdrafts and horizontal wind shear, thus providing an aircraft-specific index on which to base warnings. This hazard index, referred to as the F Factor, is defined in the figure. The F-Factor application to a warning system concept is also shown. Positive values of  $\dot{W}_x$  indicate head wind shearing to tail wind ( $H \rightarrow T$ ) and negative values of  $\dot{W}_x$  imply tail wind shearing to head wind ( $T \rightarrow H$ ). A preset hazard threshold  $F_0$  is incorporated which, when exceeded below a specified altitude, provides an alert to the crew. Any combination of horizontal shear and/or vertical wind which falls within the diamond region indicates safe aircraft operation in relation to available excess thrust-to-weight ratio. (Roland L. Bowles, 3621)

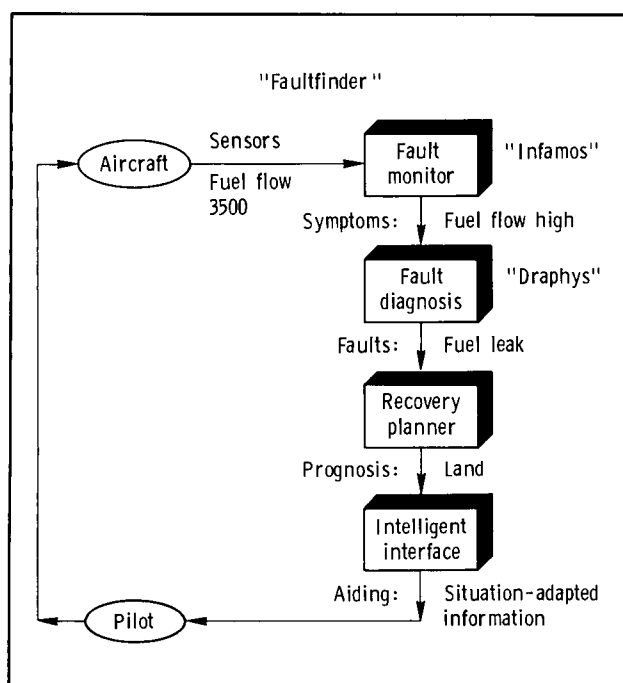


Hazard index.

### Developed Prototype Onboard Fault-Monitoring and Diagnosis Expert System

Current onboard caution and warning systems alert the flight crew to parameters that are outside

the normal operating range. When a failure occurs, many parameters may go out of range simultaneously. Such a situation requires the flight crew to rapidly assimilate a large amount of information and provide a diagnosis. Expert systems technology has demonstrated success in a number of application areas, but mainly in static environments. The objective of this research has been to apply existing technology as appropriate, develop new concepts as necessary, and evaluate the resulting concepts for aiding transport flight crews in performing onboard fault monitoring and diagnosis. The monitoring and diagnosis concepts developed within this research provide potential for improved failure detection time and increased crew situational awareness when failures occur, and therefore may result in reduced losses of life and property.



*Fault-monitoring and diagnosis process.*

A conceptual architecture for an onboard fault-monitoring and diagnosis expert system has been developed and implemented in a computer program called Faultfinder. The approach implemented in Faultfinder separates the monitoring process from the diagnosis, as shown in the figure. Faultfinder

is unique in that it utilizes qualitative, causal, and temporal reasoning to perform diagnosis of known faults as well as unanticipated failures. Faultfinder is currently implemented for diagnosis of an aircraft propulsion and hydraulic subsystem.

(Kathy H. Abbott, 3621)

## Controls/Structures/Electromagnetics Interaction Technology for Large Space Antennas

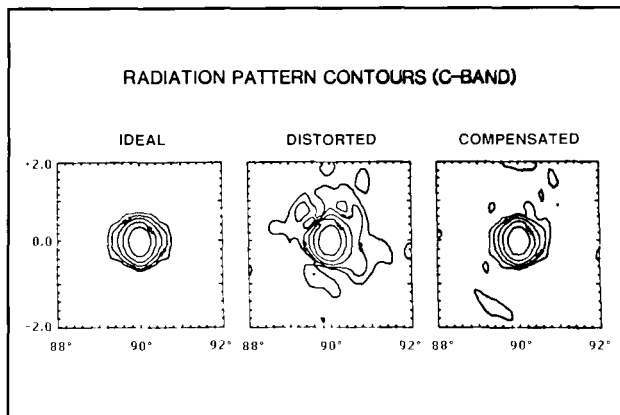
The objective of this research program is to develop multidiscipline methodology for optimizing radio frequency (RF) performance of large space antennas by combining and upgrading discipline technology in the areas of controls, structures, and electromagnetics and to verify this technology through a series of evolutionary experiments using the 15-m antenna as a generic test article.

The 15-m antenna tests will be extended to include motorized surface adjustment, adaptive feed electronic compensation techniques, and an integrated discipline code. Testing will begin with a series of experiments to determine the limit of reflector surface smoothness improvement possible using the motorized control and the deployment repeatability of the antenna. Analytical studies will be made with related experiments to determine the accuracy limit of the engineering analysis language (EAL) structural dynamics model already developed for the 15-m hoop/column antenna.

The surface control system has been designed, parts have been procured, and fabrication of the prototype has been completed. A procedure has been developed for determining the amplitude and phase excitation coefficients for an array feed which will compensate for the degradation in RF performance due to reflector antenna distortion. Some computer simulations have been performed to determine the potential improvement to be realized. The actual measured surface distortion of the 15-m hoop/column antenna was used as a test case. Simulations indicate that with a reasonable number of feed elements (37), levels approaching ideal (undistorted) performance can be achieved. In addition, the gain loss due to surface distortion can be reduced from 0.74 to 0.06 dB

at the C-band. This gain improvement corresponds to an equivalent root mean square (rms) surface distortion reduction from 0.061 to 0.017 in., although the actual rms surface distortion remains at 0.061 in. These initial studies indicate that side lobe interference requirements in a multiple-beam communication antenna system could be achieved by providing amplitude and phase control of the multiple-feed elements during reflector surface distortion changes.

(William L. Grantham and M. C. Bailey, 3631)



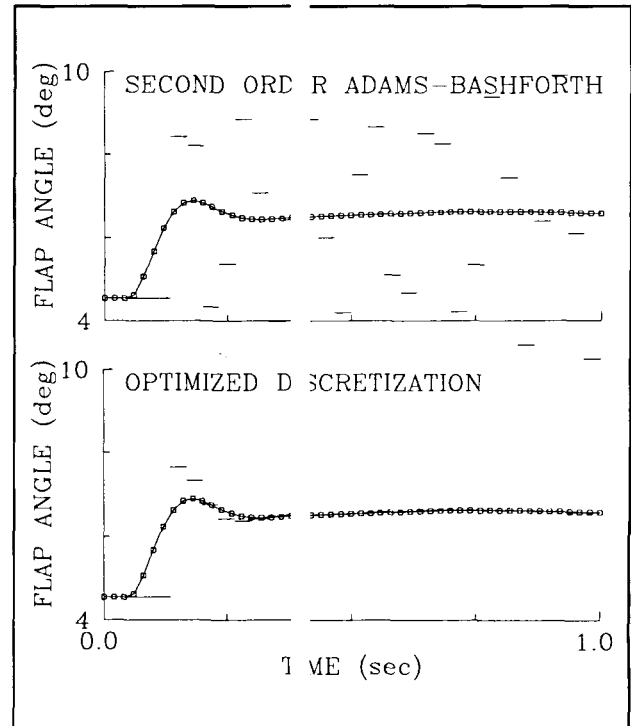
Analytical simulations of adaptive feed compensation using measured 15-m reflector surface.

### Optimal Open Multistep Discretization Formulas for Real-Time Simulation

Real-time simulations of aerospace systems play an important role in training and system development. Unfortunately, either a great deal of computing power or a great deal of time is consumed in calculating the plant state derivative in realistic simulations, and this leads to specification of an expensive computer for implementing the simulation and adoption of a large time step between simulation frames. The latter option is undesirable because of numerical inaccuracy and instability problems that are associated with using large time steps.

This study considered the problem of designing numerically efficient discrete-time representations of plant dynamics for use in real-time simulations. An algorithm was developed for optimizing free parameters in an open multistep discretization structure. The cost function was based on the infinite-horizon time integral of the mean-squared difference between the simulator output and that of the actual plant.

The theory was validated in a numerical study. Optimized two-step discretizations were designed for simulating rigid-body blade dynamics for a helicopter with a fully articulated rotor. These were compared with discretizations based on the structurally similar second-order Adams-Bashforth integration formula. The figure illustrates the transient blade "flapping" motion in the Adams-Bashforth and optimal discretizations, using a 30 Hz update rate. The solid lines give the actual plant response, and the broken lines are the simulator output, reconstructed using a zero-order hold. Although the classical formula has thoroughly destabilized at this update frequency, the optimized formula is well behaved. This is significant:



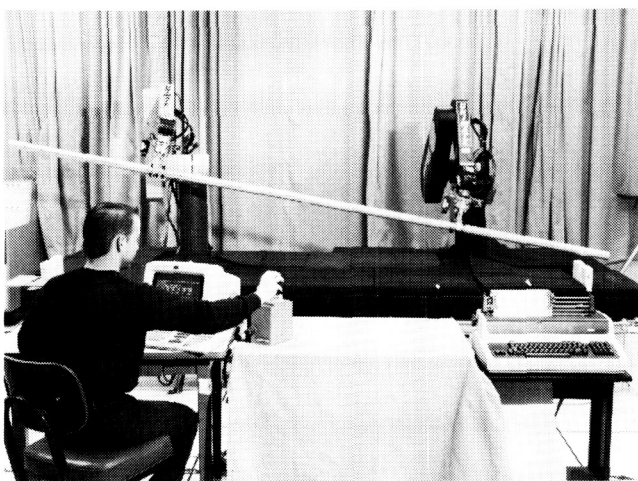
Comparison of simulator transient response using two-step classical and optimized discretizations with 30 Hz update rate.

When good simulator fidelity can be attained with a lower update rate, more detail can be built into the simulation for given computational power. Conversely, a given simulation can be implemented using a less powerful computer.

(D. D. Moerder, 4591)

## Control of Multiple Robot Arms

A general control structure for coordinated movement of multiple robot arms has been implemented. An operator commands an objective to move with a velocity (velocity control) in a desired direction with respect to a selected axis system. Commanded velocity is resolved into robot arm joint rates. Multiarm coordination is achieved by choosing the same object and movement reference frame for each robot arm. Position control ("go to" commands:  $(x, y, z; \text{orientation})$ ) which allows the building of high-level move commands (scripts or task primitives) is also based on this structure by using a velocity proportional to the position error. The control structure incorporates force and torque compensation to null the gravitational effects and for active compliance to control undesired forces.



L-87-468

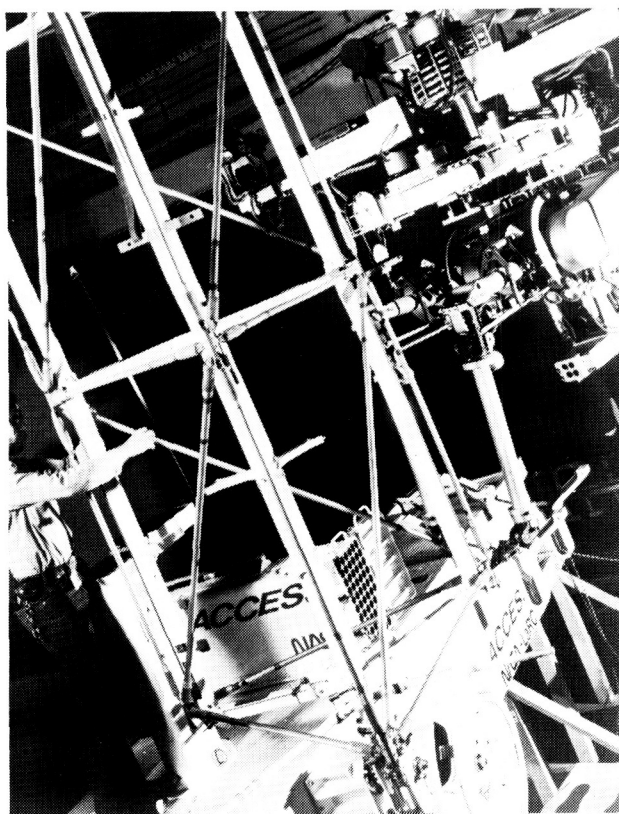
*Dual robot arm control.*

The photograph shows dual robot arm control. The operator, sitting in front of a computer terminal, selects an axis system at the center of a long construction beam. Then, with a six-axis hand controller, the beam is commanded to move (translation and rotation) in a certain direction. In response, both robot arms move the element in a coordinated manner in the commanded direction. Force and torque sensors at the robot wrists are used to detect gravity forces and provide manipulator compliance.

(L. Keith Barker and Donald Soloway, 3871)

## Space Truss Assembly Using Teleoperated Manipulators

The assembly of a truss structure by two extravehicular activity (EVA) astronauts in the bay of the Space Shuttle was successfully accomplished



L-87-2457

*Teleoperator structural assembly task.*

in the Access I experiment in November 1985. To demonstrate the capability of teleoperated manipulators to accomplish realistic space assembly, the Access experiment was repeated in a ground-based laboratory using a teleoperated manipulator. The photograph shows the laboratory tests in progress at the Oak Ridge National Laboratories using the Central Research Laboratory's model M-2 master/slave servo manipulator. The hardware employed was a combination of that actually used on the Space Shuttle and that used to train the astronauts in water immersion facilities for the experiment. In the ground-based demonstration, the manipulator system was substituted in the role of one of the astronauts while a person in shirt sleeves performed the role of the other astronaut.

The unmodified manipulator system was found to have sufficient dexterity to do the task. As was expected, it took longer to complete the task (about three times as long on the average). Also, a relatively small number of components were dropped or otherwise mishandled, an occurrence that could not be permitted in space. It is believed, however, that these mishaps could be eliminated entirely by training and equipment modifications.

(Walter W. Hankins, III and Randolph W. Mixon, 3871)

## Microgravity Crystal Growth on Mission 61A

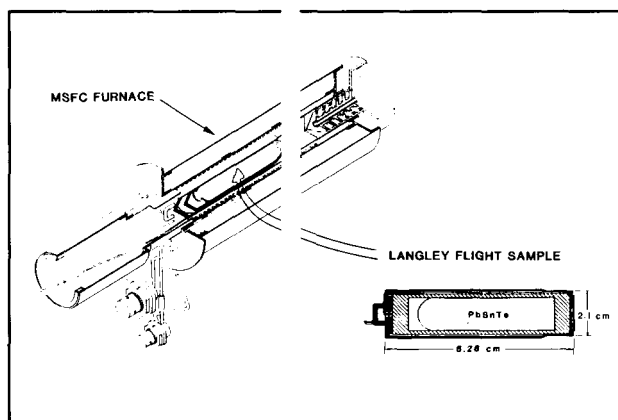
Crystal growth on orbiting spacecraft such as the Space Shuttle and the future Space Station is very important to progress in materials science. Due to the balance of centrifugal force and gravitational force, the net force (or weight) on an object in low Earth orbit is reduced far below the level felt on the Earth's surface. This reduction of net forces produces a concomitant reduction in convection in the crystal growth fluid, and, consequently, a class of crystals that cannot be grown on Earth can be grown in space.

In order to test the limits of fluid flow reduction in low Earth orbit researchers at Langley Research Center designed an experiment to be performed in

the Materials Experiments Apparatus (MEA) furnace that is managed by Marshall Space Flight Center. This experiment involved a material, lead tin telluride, whose liquid is strongly convective in the Earth's gravity field. The experiment was conducted on the Space Shuttle Mission 61A.

The results of the experiment determined that reduced gravity will reduce the fluid motion in even a material such as lead tin telluride, but the motion was not completely arrested. However, the results did show the growth conditions that would be necessary to eliminate the deleterious effects of the residual fluid flow. Experiments such as this are important not only for improved growth of lead tin telluride but also for improvements in the growth of similar materials.

(A. L. Fripp and W. J. Debnam, 3777)



Compound semiconductor directional solidification experiment.

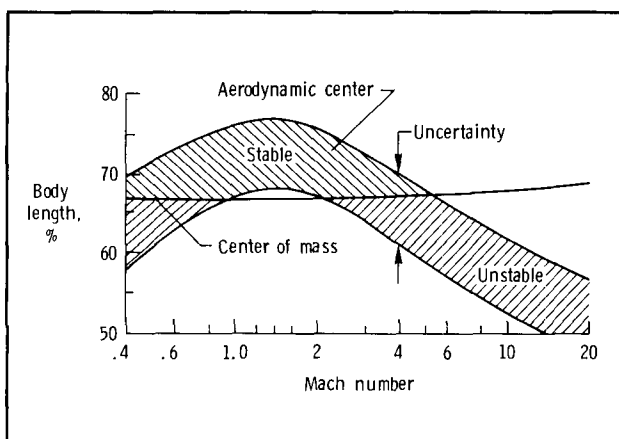
## Identification of Fundamental National Aero-Space Plane Stability and Control Issue

Preliminary stability and control power analyses have been performed for several National Aero-Space Plane (NASP) configurations representative of NASP vehicles. During the course of evaluating tools and

performing analyses, a fundamental issue was identified. For the primary study and similar configurations, the longitudinal aerodynamic center of pressure moved forward from approximately 78 percent body length at Mach 1.5 to 53 percent at Mach 23.5. This very large shift, due to the Newtonian shadowing effect, was calculated by two different stability and control derivative estimation codes (Digital Datcom and Aerodynamic Preliminary Analysis System (APAS)) and is consistent with experimental data from wind tunnel tests. The forward shift in the experimental data is said to be due to boundary-layer growth and flow separation aft of the largest cross sections of the vehicle.

It was also found that control power was reduced significantly at the high hypersonic Mach numbers for similar reasons. The center of mass for the study configuration varied from 67 percent to 69 percent body length, which is representative of evolving NASP configurations. This combination guarantees static stability at high Mach numbers and indicates that active stabilization will be required and simple aerodynamic surfaces may not have sufficient control power to provide the required stability. Hence, a combination of moment-generating devices may be needed to ensure that appropriate stability and control margins can be maintained under uncertainty. Similar issues will exist for the directional axis.

(John D. Shaughnessy, 3608)

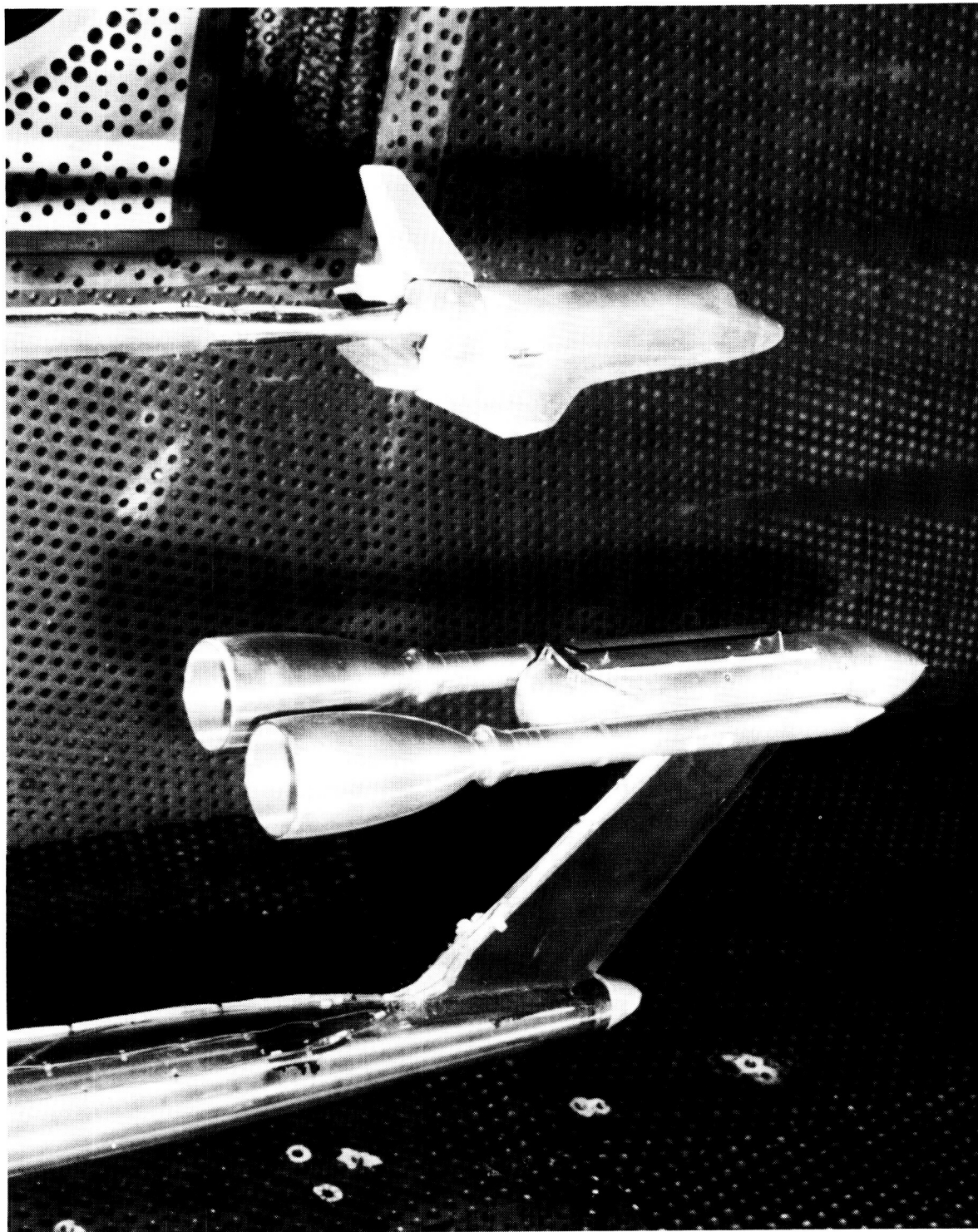


*Typical NASP aerodynamic center and center of mass variation with Mach number.*



# Space Directorate

---



ORIGINAL PAGE IS  
OF POOR QUALITY

The Space Directorate conducts research in atmospheric and Earth sciences, identifies and develops technology for advanced transportation systems, conducts research in energy conversion techniques for space applications, and provides the focal point for conceptual design activities for both large space systems technology and Space Station activities.

The Atmospheric Sciences Division is a leader in the area of atmospheric sciences. Its researchers are involved in seeking a more detailed understanding of the origins, distributions, chemistry, and transport mechanisms that govern the regional and global distributions of tropospheric and stratospheric gases and aerosols, and in the study of the Earth radiation budget and its effect on climate processes. The research seeks to better understand both natural and anthropogenic processes and covers a wide spectrum of activities, including the development of theoretical and empirical models; collection of experimental data from in situ and remote-sensing instruments designed, developed, and fabricated at Langley Research Center; organization of extended field experiments; and development of data management systems for the efficient processing and interpretation of data derived from airborne and satellite instruments.

The Space Systems Division conducts research and systems analysis studies of advanced transportation systems, large space systems, and Space Station concepts; analytical and experimental research in hypersonic aerodynamics and aerothermodynamics; hypersonic computational fluid dynamics code development and studies; and basic research on energy generation and conversion techniques for potential use in space. The division is a leader in the development of highly interactive computer-aided design tools that enable rapid conceptual design and evaluation of space vehicles and spacecraft and identification of technologies needed to develop these space systems. Space systems such as Earth-to-orbit launch vehicles, Shuttle II, utility vehicles, and orbital transfer vehicles are developed and evaluated. Flight experiments are developed that use the Space Shuttle orbiter as an orbital platform and reentry research vehicle and that use entry vehicles launched from the Space Shuttle to study aerothermodynamic and aerodynamic characteristics. The results provide a data base for development of advanced vehicle systems.

The Space Station Office is the focal point for Langley Research Center's involvement in the Agency-wide Space Station Program and is responsible for the implementation and coordination of Langley's direct support of this program. The Space Station Office is NASA's lead office for the identification, definition, and evaluation of the Evolutionary Space Station capabilities and for the identification of technology and advanced development required for long-term evolutionary development. The office represents the engineering community as technology users of the Space Station. It also advocates flight experiments on future Space Shuttle flights which contribute to Space Station technology use as well as flight experiments from technology programs which can contribute to both the initial operational capability and the evolutionary station. The office provides Langley Research Center support to the NASA-wide in-house Space Station systems engineering and integration in areas consistent with demonstrated Langley capabilities and expertise.

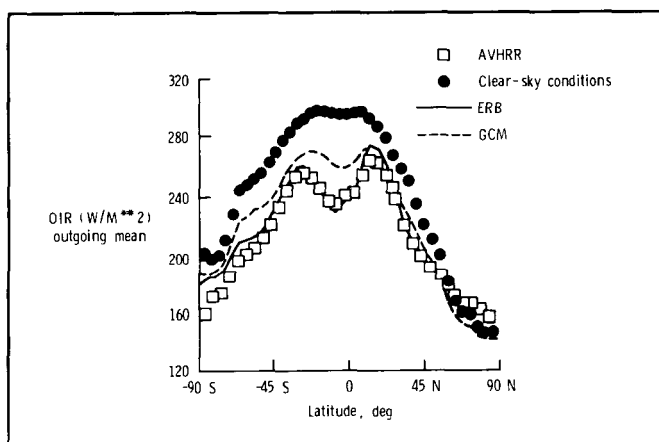
### **Comparison of Climate Model Simulations With Satellite Observations**

Climatic changes, such as those anticipated for increases in the concentrations of carbon dioxide, can be simulated with general circulation models (GCM's). The accuracy of the GCM climate predictions is a crucial issue in modern atmospheric science.

In both a GCM and in nature, the outgoing thermal infrared radiation (IR) balances the incoming solar radiation on a global, annual average. Short-term geographical imbalances in solar heating and IR cooling drive the global weather. The IR is determined by the distribution of temperature, water vapor, trace gases, and cloudiness. The modeled GCM and observed Nimbus 7 Earth Radiation Budget (ERB) and Advanced Very-High-Resolution Radiometer (AVHRR) fields of IR for January have been averaged about each latitude belt and are plotted in the figure.

The GCM (as shown by the dashed line) has a separate field of IR for the model clear-sky condition

(as shown by the circles). The model cloud fields have brought the GCM into close agreement with the Nimbus 7 ERB (as shown by the solid line) and AVHRR (as shown by the squares) satellite observations over much of the globe. Time series analyses of the GCM and satellite IR are being compared to suggest physical processes that should be included in succeeding generations of the model. (Thomas P. Charlock, 1977)



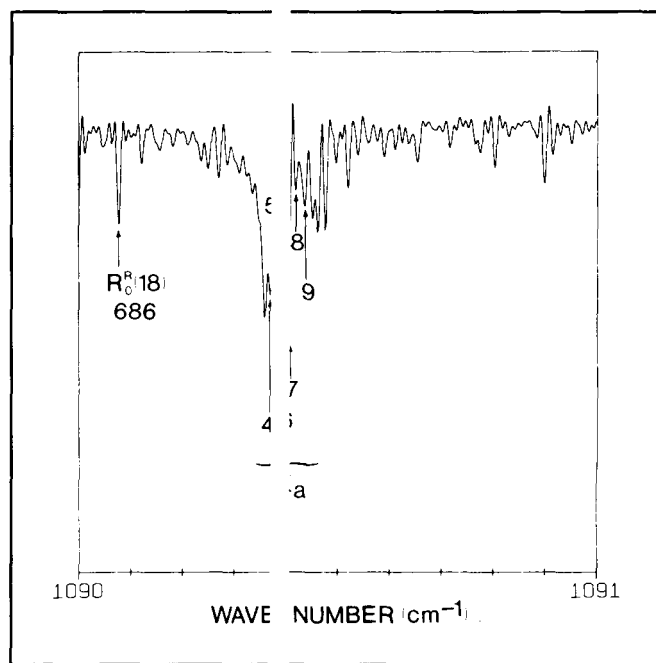
*Zonally averaged outgoing thermal IR in model and satellite observations.*

## Laboratory Measurements of Ozone Infrared Spectrum

Detailed knowledge of the ozone infrared spectrum is needed for accurate calculation of atmospheric heating and cooling rates due to changes in the stratospheric ozone layer. Recent remote-sensing experiments have shown that space-based measurements of infrared absorption or emission can be used to accurately determine the concentration and distribution of stratospheric ozone on a global scale. Laboratory investigations have been performed to improve our knowledge of the ozone spectrum at wavelengths between 5 and 15  $\mu\text{m}$ . These measurements utilized both the McMath high-resolution Fourier transform spectrometer (FTS) at the National Solar Observatory on Kitt Peak, Arizona, and the tunable-diode

laser (TDL) spectrometer laboratory at Langley Research Center. Data analysis was performed at Langley Research Center, and the theoretical interpretation of the results was done in collaboration with investigators at several other institutions, including the Jet Propulsion Laboratory, the University of Denver, l'Université Pierre et Marie Curie, and l'Université de Reims in France.

Results of this work have improved line positions and relative intensities for eight fundamental vibration-rotation bands of the most abundant isotopic form of the ozone molecule ( $^{16}\text{O}_3$ ), and have, for the first time, allowed the scaling of line intensities in these bands to a consistent standard. Analysis of spectra of  $^{18}\text{O}$ -enhanced ozone in the 9- to 11- $\mu\text{m}$  region have resulted in new parameters for the strongest fundamental bands which are substantially improved over those that have previously been available. These laboratory results have already been applied in an investigation of the isotopic composition of stratospheric ozone. Detailed studies of the broadening of ozone absorption lines by air and by nitrogen, using both FTS and TDL measurements,



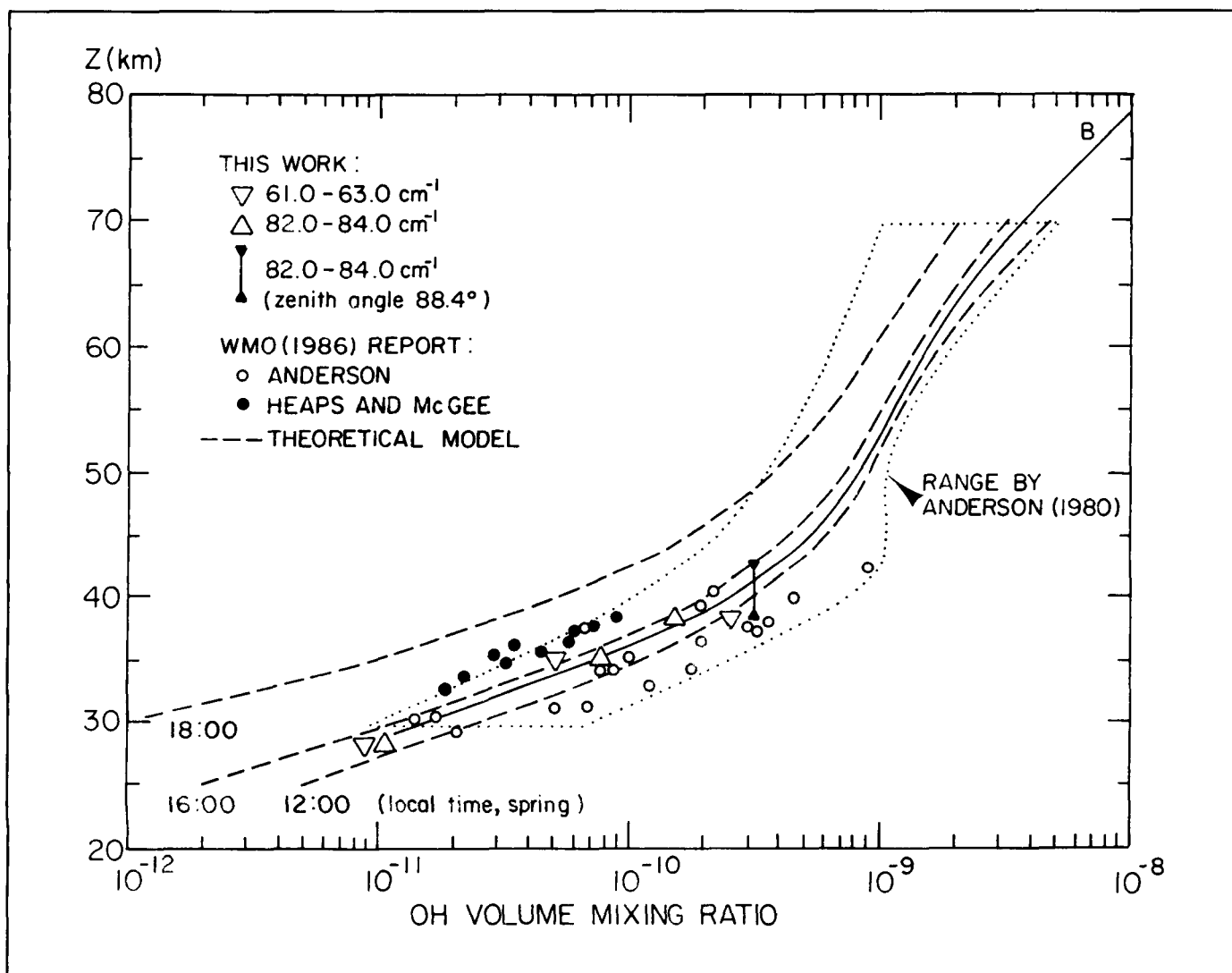
*FTS spectrum of isotopically heavy ozone showing a strong absorption feature (Q-branch) of  $^{16}\text{O}^{16}\text{O}^{18}\text{O}$  at 9.2  $\mu\text{m}$ .*

have resulted in precise broadening coefficients for over 50 spectral lines not previously measured and the first measurements of pressure-induced line shifts for ozone.

(Mary Ann H. Smith, 2576)

## Stratospheric Remote Sensing Using Emission Far-Infrared Spectroscopy

The vertical mixing ratio profiles of  $\text{H}_2\text{O}$ ,  $\text{HDO}$ ,  $\text{O}_3$ , heavy ozone,  $\text{HF}$ ,  $\text{HCl}$ ,  $\text{HCN}$ , and  $\text{OH}$  in the stratosphere are retrieved for high-resolution far-infrared emission spectra. These spectra were obtained with a balloon-borne Fourier transform spectrometer in the spring of 1979 at  $32^\circ\text{N}$ . A non-linear least-squares fit method is used in the analysis. The results are obtained relative to the  $\text{O}_2$



OH mixing ratios retrieved from far-infrared emission spectra. Other reported profiles are from WMO 1986 report (see text).

mixing ratio whose emission features can be found in the same spectra. The retrieval of OH together with other species should be particularly significant for the study of upper stratospheric photochemistry although the errors are relatively large (30 to 35 percent for OH and 20 to 28 percent for other species). The OH mixing ratio distributions retrieved from two spectral intervals (i.e., 61 and 83  $\text{cm}^{-1}$ ) are shown in the figure. Other profiles are taken from the World Meteorological Organization (WMO) 1986 report entitled *Atmospheric Ozone 1985*, Global Ozone Research and Monitoring Project Report Number 16.

In a subsequent balloon flight in the summer of 1983, much stronger emission features of OH have been measured. These data are being analyzed to obtain more accurate vertical profiles as well as the diurnal variation of the OH missing ratio. (Jae H. Park, 2310)

### Infrared Measurements of Atmospheric Gases Above South Pole

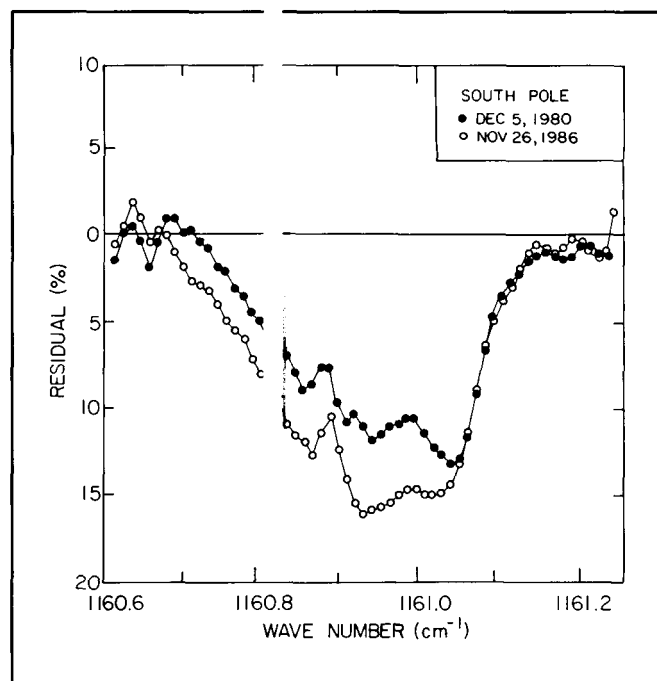
High-resolution infrared solar spectra (recorded shortly after the time of the Antarctic spring ozone hole in 1980 and 1986 by the University of Denver atmospheric spectroscopy group from the Amundsen-Scott Station at the South Pole) have been analyzed at Langley Research Center and the University of Denver. This analysis has resulted in simultaneous measurements of a large number of atmospheric gases, several of which are thought to be key to understanding the chemistry that occurs during the Antarctic ozone hole. The measurements define, for the first time, the levels of these species immediately following the breakup of the polar vortex.

The retrieved amounts for several important gases are different from extrapolations of measurements made at lower latitudes. For example, the total HCl column above the South Pole is considerably larger than would be expected on the basis of earlier Northern and Southern Hemisphere latitudinal surveys. Because the same instrument was used for the 1980 and 1986 measurements and the same spectral line parameters and analysis method were used in analyzing both data sets, the precision in compar-

ing the measurements from these two dates is high. For these reasons, it has been possible to quantify or determine meaningful upper limits for differences between the 1980 and 1986 total atmospheric amounts of a number of species.

As illustrated in the figure, an increase in the absorption by  $\text{CF}_2\text{Cl}_2$ , the most abundant chlorofluorocarbon in the atmosphere here, has been detected. Analysis of these measurements has yielded an estimate of  $3.6 \pm 2.1$  percent per year for the average rate of increase in the total amount of  $\text{CF}_2\text{Cl}_2$  above the South Pole between 1980 and 1986.

(Curtis P. Rinslar 1, 2576)



Comparison of absorption by  $\text{CF}_2\text{Cl}_2$  in South Pole solar spectra recorded in 1980 and 1986.

### Amazon Boundary-Layer Experiment

The Amazon Boundary-Layer Experiment (ABLE) focused on assessing the role of biosphere/atmosphere interactions on the chemistry of the at-

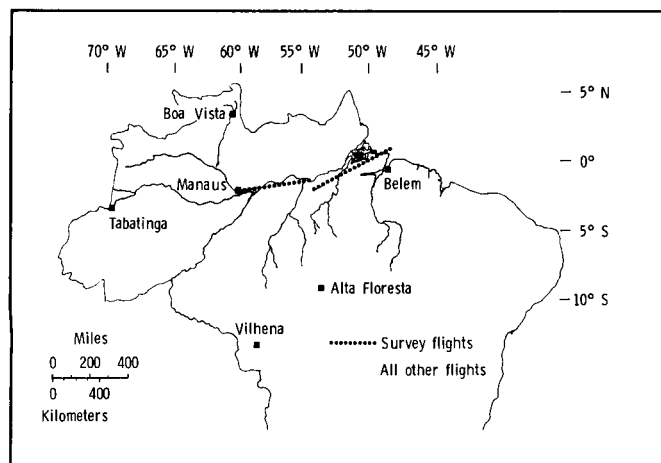
mosphere over pristine tropical forests and wetlands. The ABLE-2A was conducted in July and August 1985 during the dry season in order to characterize the chemistry of the undisturbed (nonprecipitating) atmospheric boundary layer. The ABLE-2B, which was conducted in April and May of 1987 during the wet season, investigated the chemistry and transport of gases and particles influenced by large-scale storm systems. The design and execution of ABLE-2 was a collaborative effort of U.S. and Brazilian scientists sponsored by NASA and the Instituto Nacional de Pesquisas Espaciais (INPE), the Brazilian space agency. Important facilities and logistical support were also provided by the Instituto Nacional de Pesquisas da Amazonia (INPA), Manaus, Brazil. These experiments are part of a longer term study of the chemistry of the atmospheric boundary layer and are supported by the Global Tropospheric Experiment (GTE) component of the NASA Tropospheric Chemistry Program.

Several key results have confirmed the theoretical studies of the importance of these tropical ecosystems to global trace gas chemistry and budgets. Amazonian soils and vegetation are significant sources of methane ( $\text{CH}_4$ ), nitric oxide ( $\text{NO}$ ), and isoprene ( $\text{C}_5\text{H}_8$ ). During the dry season,  $\text{NO}$  levels exceed those required for photochemical processes to produce ozone ( $\text{O}_3$ ) over the undisturbed rain forests of the Amazon. During the wet season,  $\text{NO}$  levels are lower, and photochemical pro-

cesses destroy  $\text{O}_3$ . Other biogenic emissions are also present in the boundary layer where they and their chemical products are subject to vertical transport upward by thunderstorms to the free troposphere. These mechanisms couple the tropical biosphere to the global atmosphere and produce subsequent effects on the Earth's air quality and heat budget. Gas-phase formic and acetic acids were also measured with indications that these organic acids were derived from direct vegetation emissions and from photochemical reactions involving isoprene. In rain water, these organic acids are the primary source of the acid rain of natural origin in the Amazon Basin. Particulates found over the region were primarily composed of organic carbon, and their existence suggests a biogenic origin. The Amazon aerosol was also acid-base neutral, in contrast to the acidic aerosol found over the Northern Hemisphere industrialized regions. The ABLE-2 documented land-clearing fires as an important source of carbon monoxide, nitrous oxide, and ozone in the atmosphere over the central Amazon Basin.

The ABLE-2 expedition has been an initial step toward understanding how the tropical rain forests of the world influence global atmospheric chemistry and climate. The development of new technologically sophisticated airborne and satellite measurement systems made the experiment possible. The expedition demonstrated how ground, aircraft, and space technologies must be integrated with theoretical studies to resolve issues of global habitability.

(J. M. Hoell, Jr., 4779 and R. C. Harriss, 4447)



*Map of Amazon Basin region of Brazil, with locations of ABLE-2B studies shown.*

### **Airborne Lidar Measurements of Ozone and Aerosols Over Amazon Basin During Wet Season**

Extensive ozone and aerosol data were obtained by the NASA Airborne Differential Absorption Lidar (DIAL) system over the tropical rain forest of Brazil during April and May 1987 as part of NASA's Global Tropospheric Experiment ABLE-2B (Amazon Boundary-Layer Experiment). The objective of the airborne DIAL investigation was to study the sources and sinks for ozone and aerosols in the boundary



layer and free troposphere across the Amazon Basin during the wet season. These data were contrasted to results found during the ABLE-2A field experiment, which was conducted over the tropical rain forest during the dry season (July and August 1985). The new capability of the airborne DIAL system to simultaneously make measurements above and below the aircraft permitted the mapping of ozone and aerosol variability from the top of the forest canopy to the upper troposphere. Investigations of ozone and aerosol distributions and atmospheric structure and dynamics were conducted in a broad range of atmospheric conditions over the rain forest near Manaus, Brazil.

In contrast to the data obtained during the dry season over the Amazon Basin, the ozone levels in the mixed layer were low (generally less than 10 ppbv (parts per billion by volume)) with no evidence of remnants of biomass burning or photochemical ozone production. Ozone removal processes in this experiment appeared to be much more efficient at the surface than during the dry season, and substantial mixing throughout the lower troposphere resulted in generally homogeneous vertical profiles at ozone mixing ratios of 16 to 22 ppbv, which is about 10 ppbv lower than in the dry season. The rate of growth of the mixed layer was found to be about the same in both seasons (5 to 10 cm/s); however, the strong trade wind inversion that was seen during the dry season was not present during the wet season. Because of the frequent wet season precipitation, the aerosol loading in the lower troposphere was generally reduced compared to the dry season. Results from this experiment are being interpreted in relation to the chemistry and dynamics of the atmosphere over the tropical rain forest of Brazil during the wet season.

(Edward V. Browell, 2576)

## Modeling Space Radiation Effects

Knowledge of galactic cosmic ray interaction and transport in bulk matter is needed to accurately analyze requirements for shielding astronauts and spacecraft components. Of particular interest is the high-energy heavy ion (HZE) component of the incident space radiation spectrum. As these high-velocity nu-

clei strike the spacecraft, they undergo nuclear fragmentation (breakup), and these fragmented particles may then undergo further interactions with the vehicle structure and components and also with the bodies of the astronauts. Accurate methods to describe the transport of these HZE particles through bulk matter are under development at Langley Research Center. Solution of the HZE transport problem requires solution of approximately 100 coupled, partial differential-integral equations in six-dimensional space. Ultimately, the task of assuring the accuracy and validity of both the equation coefficients and the solution techniques is faced. Ideally, validation should be accomplished using detailed transport data obtained from carefully planned and controlled experiments. Unfortunately, only a paucity of such data exists, and the actual conditions are almost impossible to model experimentally. Thus, other methods of validation must be considered.

Energy, MeV/amu	Mn Flux at 10 g/cm <sup>2</sup>		Mn Flux at 20 g/cm <sup>2</sup>	
	Numerical	Analytic	Numerical	Analytic
.0198	1.772E-6	1.780E-6	5.704E-7	5.768E-7
.1147	1.772E-6	1.7780E-6	5.704E-7	5.768E-7
1.090	1.772E-6	1.779E-6	5.704E-7	5.767E-7
10.07	1.767E-6	1.771E-6	5.696E-7	5.753E-7
100.1	1.504E-6	1.503E-6	5.242E-7	5.291E-7
1059.	7.797E-8	7.806E-8	6.880E-8	6.918E-8
10490.	7.004E-10	7.004E-10	8.728E-10	8.728E-10

*Comparison of benchmark numerical simulation to analytic solution for secondary manganese ions as function of ion energy and depth into aluminum absorber.*

Several different versions of HZE transport codes are available. When used with the same input spectra, interaction parameters, and boundary conditions, all versions should yield comparable results. The history of transport code development, however, suggests otherwise. For this reason, Langley Research Center has developed a realistic, nontrivial, exact analytic solution to the simplified Boltzmann



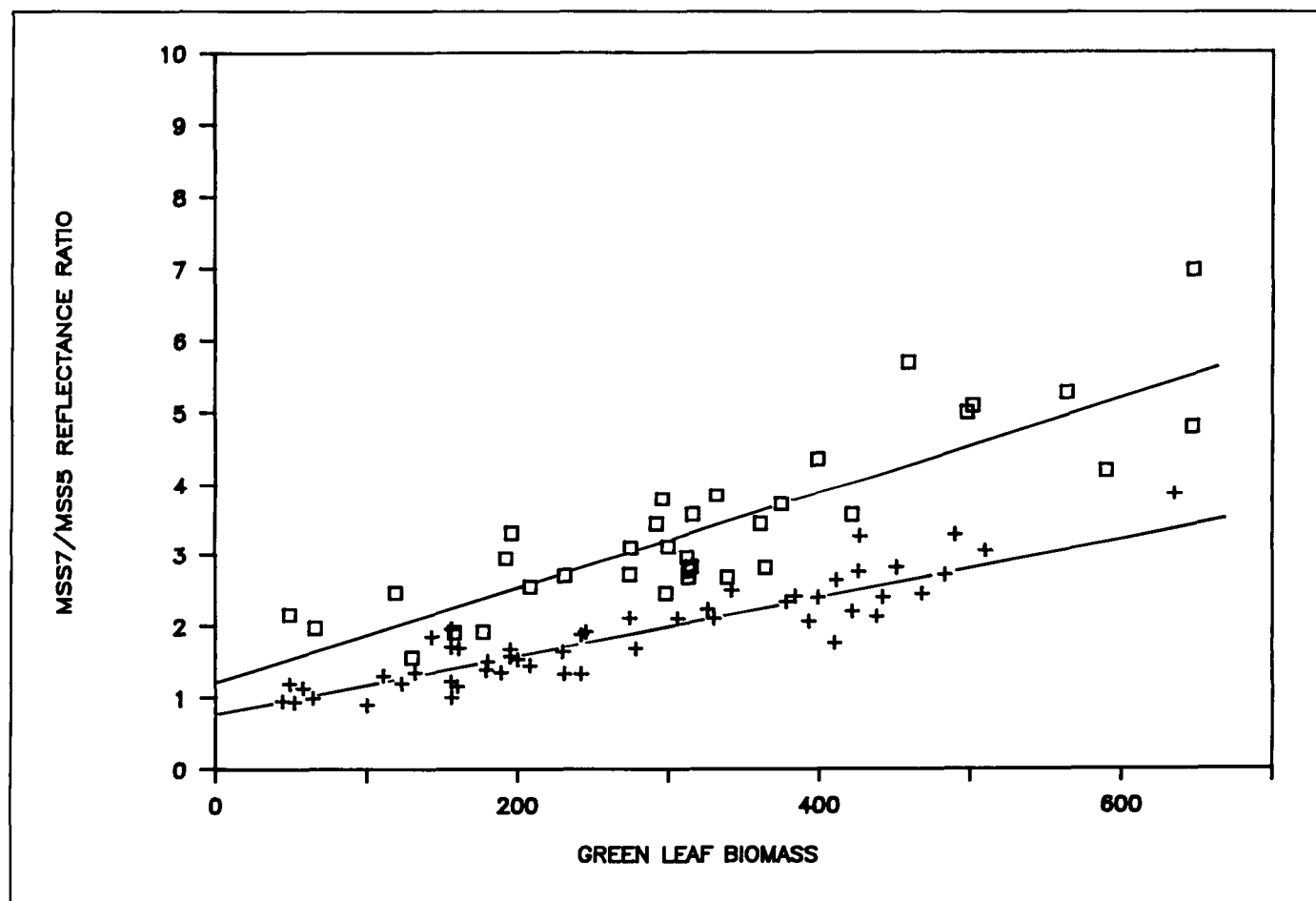
equation used to describe HZE transport. This solution will serve as an absolute standard for code comparison purposes. A comparison between the analytic solution and the Langley Research Center transport code is given in the table. The agreement is within 1 percent in all cases.

(J. Wilson, 4211)

### Analysis of Vegetation Growth/Carbon Cycling at Continental-Sized Geographic Scales

Global models of the cycling of carbon and its impact on atmospheric chemistry and climate re-

quire accurate assessment of terrestrial plant growth (transforming atmospheric  $\text{CO}_2$  into organic material) and decay (releasing  $\text{CO}_2$  and  $\text{CH}_4$  into the atmosphere) over large areas. Experimental studies have found correlations of remotely sensed spectral indices with the mass of living vegetation per unit ground area (biomass), the area of leaves per unit ground area (leaf area index or LAI), and the amount of light absorbed by the canopy for use in photosynthesis (absorbed photosynthetically active radiation or APAR). All of these parameters can be related to the dynamics of plant growth and decay. However, it is not known how effectively these experimental results can be extrapolated to continental, and larger, sized areas of the Earth. An experiment has been conducted in which field measurements of canopy



Relationship of commonly used remote spectral index (MSS7/MSS5 reflectance ratio) to green leaf biomass ( $\text{g/m}^2$ ) in widely dispersed plots of a North American coastal plant. Plots north of  $37^\circ 30' \text{N}$  ( $\square$ ) show a different relationship than those south (+) of this latitude.

spectral characteristics, biomass, and LAI were made in plots scattered throughout the range of a single, widely distributed wetland plant.

Important, systematic changes in the spectral reflectance characteristics of this plant occurred within its 17° latitudinal range. Mean near-infrared reflectances of canopies in the northern half of the range are nearly double those of the southern half. The transition from one regional canopy type to the other occurs quite abruptly near the center of the plant's latitudinal range (at approximately 37°30'N). Reflectance at visual wavelengths is unaffected. The result is that continental assessment of biomass using the common near-infrared/visible spectral indices would be severely affected (as shown in the figure).

The use of spectral indices to assess more fundamental radiative transfer properties of the canopy is not subject to the observed latitudinal changes, suggesting that large area studies can more reliably address canopy parameters such as APAR. The observed changes in canopy geometry also have potential functional consequences for the plant which would be of considerable interest if similar trends are found for other plants and regions. It is concluded that orbital assessment of vegetation over large geographic areas will be most consistent and useful if directed at the radiative transfer (e.g., APAR) rather than structural (e.g., biomass) characteristics of plant canopies.

(David S. Bartlett, 4345)

### Microbial Activity, Atmospheric Gases, and Life on Mars

Nitrous oxide ( $N_2O$ ) is a trace gas in the Earth's atmosphere which has a mixing ratio of only 0.33 parts per million by volume. Nitrous oxide in the middle atmosphere controls the global chemical destruction of ozone, which protects us from solar ultraviolet radiation. In addition, nitrous oxide is a greenhouse gas that impacts the thermal balance of our planet. Even though the concentration of  $N_2O$  is only a fraction of a part per million by volume, it is more than 10 orders of magnitude greater than would be expected from theoretical thermodynamic equilibrium

calculations. This paradox can be explained by the overwhelming production of atmospheric nitrous oxide by microbial activity in soils. Microbial metabolic activity is an important disequilibrium chemical process that significantly impacts the trace gas composition of the atmosphere. The processes and parameters that control the production of nitrous oxide and other biogenic gases in soil have been studied in controlled laboratory experiments and in experiments conducted in the field. Methane, ammonia, and hydrogen sulfide are other important trace atmospheric gases produced by microbial activity.



*Mars as photographed during the Viking 2 approach in August 1976. The Viking Project, managed at Langley Research Center, included a search for life at both lander sites.*

The existence of these gases in the atmosphere of Mars may indicate the existence of an active microbial biosphere on the Martian surface. Thermodynamic equilibrium calculations indicate that these

gases should not be present in the atmosphere of Mars; our photochemical calculations indicate that the lifetime of these gases should be extremely short, if they exist at all. An experiment, which involves high-resolution spectroscopic measurements of the atmosphere of Mars from a Mars orbiter and/or *in situ* measurements from a Mars lander or rover, has been designed to search for these biogenic gases. It is believed that the detection of trace gases of biogenic origin in the atmosphere of Mars would be an unambiguous indication of the presence of an active microbial biosphere.

(Joel S. Levine, 2187)

## Atomic Oxygen Beam Generator

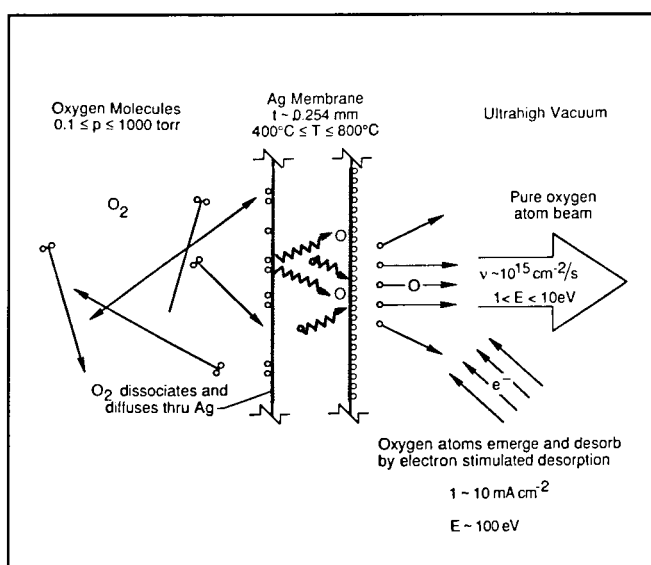
The combination of a spacecraft's orbital velocity with the composition of the atmosphere at orbital altitude (200 to 1000 km) results in hyperthermal atomic oxygen O impinging on the spacecraft surfaces with a flux of  $10^{15} \text{ cm}^{-2}/\text{s}$  and a kinetic energy  $E$  of approximately 5 eV. The high chemical reactivity of this O-atom flux has caused substantial degradation of organic materials onboard the Space Shuttle and suggests that materials on the proposed Space Station, composites used in large space structures, exterior coatings on the optics of the Hubble Space Telescope, proposed ultraviolet telescopes, and future laser communications systems may have substantially reduced lifetimes. It is therefore essential to study the reactivity of these materials toward atomic oxygen in ground-based laboratories.

A promising approach for developing a laboratory atomic oxygen gun to simulate the orbital condition involves the use of two unique phenomena: the unusually high permeability of oxygen through silver and electron stimulated desorption. Normally, when the O atoms arrive at the vacuum interface, surface diffusion occurs and results in coverage of the surface with a chemisorbed layer of atoms ( $< 500^\circ\text{C}$ ). By using an incident flux of low-energy electrons (100 to 500 eV) upon this surface, the O atoms are excited to antibonding states and desorb predominantly as hyperthermal O neutrals with energies  $2 < E < 6 \text{ eV}$ .

Results of laboratory experiments have demonstrated proof of this concept and have shown that

oxygen transport through the silver membrane proceeds via the grain boundaries. Present research efforts are centered around minimizing the silver grain size to increase the atomic oxygen flux levels to  $1 \times 10^{15} \text{ cm}^{-2}/\text{s}$ , thus providing a close approximation to orbital conditions. Applications of this technique include mass spectrometer calibration, surface physics, chemical kinetics, and materials degradation.

(R. A. Outlaw, 4264)



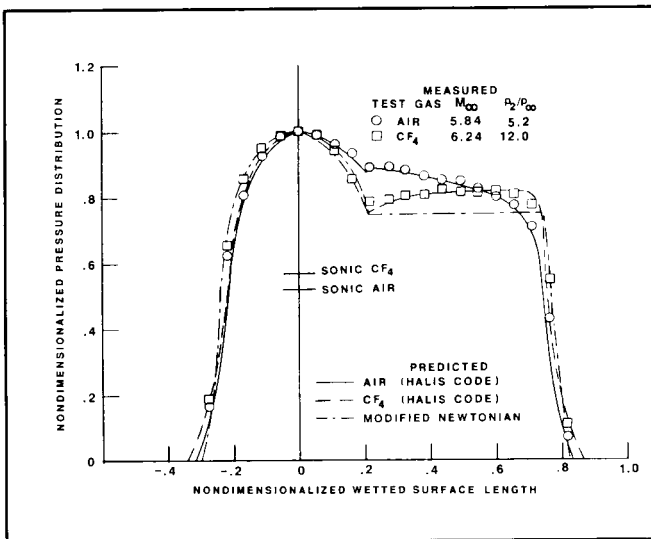
*Oxygen dissolves in silver, permeates membrane, and is desorbed by electron-stimulated desorption to produce atomic oxygen beam.*

## Simulation of Real-Gas Effects on Aeroassist Flight Experiment Vehicle

An important phase of future space transportation operations is the transfer of cargo and personnel from low- to high-Earth orbit. A class of vehicles known as aeroassisted orbital transfer vehicles (AOTV's) have been proposed for this task. By using the vehicle's aerodynamic lift and drag forces to capture an orbit, payloads would be increased

over an all-propulsion braking orbital transfer vehicle (OTV). Because of the lack of flight data at the high altitudes and velocities of the AOTV's, a precursor flight experiment referred to as the Aeroassist Flight Experiment (AFE) will be performed.

Development of an extensive aerodynamic and aerothermodynamic data base for the AFE configuration has been initiated at Langley Research Center. This data base will provide a better understanding of AFE vehicle performance and will be used to calibrate computational fluid dynamics (CFD) codes for use in future AOTV designs. Tests in hypersonic wind tunnels to determine the effects of angle of attack, Reynolds number, and normal shock density ratio on AFE pressure distributions have been performed. A significant effect of density ratio (a real-gas simulation parameter) in the nose/cone expansion region of the configuration was observed, and the magnitude of this effect decreased with increasing angle of attack. A negligible effect of Reynolds number was observed for the present test conditions.



*Effect of density ratio on pressure distributions for AFE.*

Predictions from an inviscid flow field code developed at Langley Research Center and known as HALIS (High ALpha Inviscid Solution) were in good agreement with the experimental data. Pressure distributions predicted with modified Newtonian the-

ory were in good agreement with experiment over the nose and skirt of the configuration but in poor agreement over the cone section.

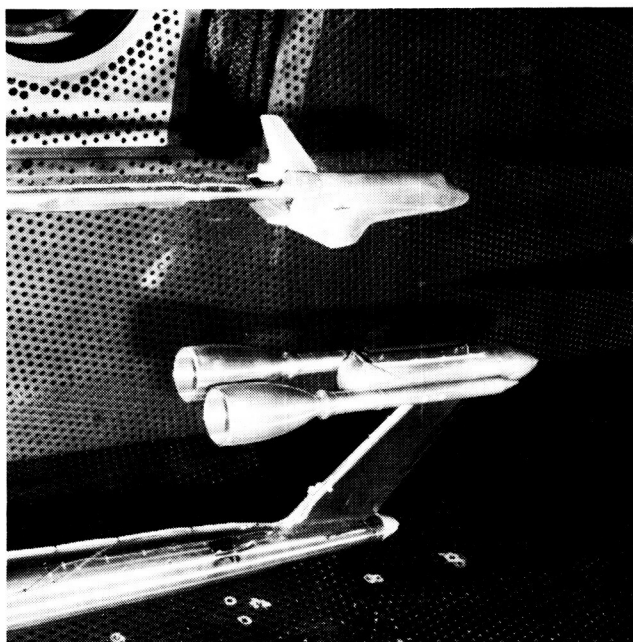
(John R. Micol, 3984)

## Experimental Investigation of Space Shuttle Orbiter Ascent Separation

In response to The Presidential Commission on the Space Shuttle *Challenger* Accident, Langley Research Center is investigating means of safe crew escape during launch abort. One phase of this investigation concentrated on examining the possibility of aerodynamic separation of the orbiter from the external tank and solid rocket boosters (lower stack) during ascent while the boosters were firing. This investigation required detailed wind tunnel studies at vehicle abort attitudes in and out of the presence of the lower stack (studies that were not investigated during the Space Shuttle development). The tests were made at subsonic and transonic speeds in the Calspan 8-Foot Transonic Wind Tunnel and at supersonic speeds in the LTV High-Speed Wind Tunnel. These facilities were selected because each had the special equipment to test two independent bodies in the presence of the other while moving them remotely through a predetermined trajectory.

Two 0.01-scale Space Shuttle ascent models were designed specifically for tests in these tunnels. The rocket exhaust plumes from the solid rocket boosters were simulated by solid bodies sized for each Mach number. Aerodynamic characteristics (and interference effects) were measured over a test area extending from the normal Space Shuttle orbiter-attachment position to the lower stack in the mated configuration to about one orbiter length (1290-in. full-scale size) in the z-direction (vertical or perpendicular to the relative wind) and one orbiter length extending in the x-direction (aligned with the relative wind). Tests were also made with the orbiter alone to obtain interference-free data. Analysis of the data from these tests indicates that the aerodynamic forces on the orbiter in the presence of the lower stack are in a direction to aid natural separation. The pitching moments on the orbiter taken

about the aft attachment strut are in the nose-up direction. It may be possible, therefore, to release the forward attachment, allow the orbiter to rotate to a higher angle of attack (which increases the orbiter's lift), and then at the desired lift, release the aft attachment to provide a clean separation. When the aft attachment is released, the point of rotation for the orbiter reverts back to its own center of gravity, which should stabilize the vehicle. Thus, these data



*Shuttle ascent model mounted for wind tunnel tests in Calspan 8-Foot Transonic Wind Tunnel.*

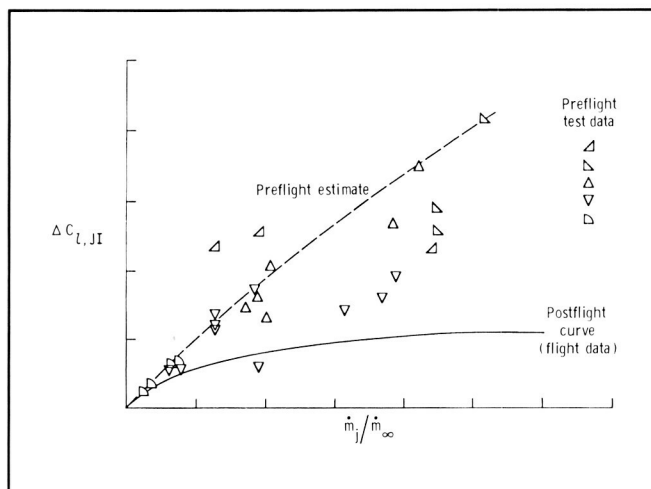
suggest that an aerodynamic separation of the orbiter intact from the lower stack during ascent may be possible.

(George M. Ware, 3984)

## Reaction Control System Plume and Flow Field Interaction

The first entry flight of the Space Shuttle orbiter *Columbia* revealed that the effect of the interaction

between the reaction control system (RCS) rocket plumes and the leeside flow field on the rolling moment of the orbiter was greatly overpredicted. Large disagreement between the preflight wind tunnel data and the postflight curve, shown in the figure, resulted in noticeable excursions in the vehicle attitude during the first navigation bank maneuver at high altitude. Because of this discrepancy, an RCS plume and flow field interaction technology study was initiated to establish improved ground-to-flight test correlations and flight prediction techniques applicable to future space vehicles. The Space Shuttle orbiter was chosen to be modeled because of the opportunity to obtain ground and flight data on the same configuration.



*Predicted and postflight rolling-moment interaction coefficient  $\Delta C_{l,JI}$  as a function of mass-flow ratio,  $\dot{m}_j/\dot{m}_\infty$ .*

An 0.0125-scale model was tested in the Langley Research Center Unitary Plan Wind Tunnel at Mach 2.5, 3.5, and 4.5, and in the Arnold Engineering Development Center (AEDC) Tunnel C at Mach 10. Surface pressure measurements were obtained on the upper surface of the wing, fuselage side, and vertical tail with the model RCS on and off for various test conditions. These are the first wind tunnel measurements that demonstrate the response of the wing upper surface pressures to the plumes from the RCS yaw thrusters. Differences in surface pressures between RCS "on" and "off" were integrated over the

affected areas to determine the increments in moment resulting from the RCS plume and flow field interaction. Tests at Mach 10 indicate that the new wind tunnel data (which are classified) are in better agreement than the original data with flight results taken from the onboard inertial measurements, and for a given momentum ratio, the interactions are insensitive to plume shape or number of thrusters fired.

A flight program with additional pressure sensors installed on the wing, fuselage, and vertical tail surfaces of *Columbia* would permit highly valuable correlation and potential extrapolation of wind tunnel measurements to flight conditions.

(William I. Scallion, 3984)

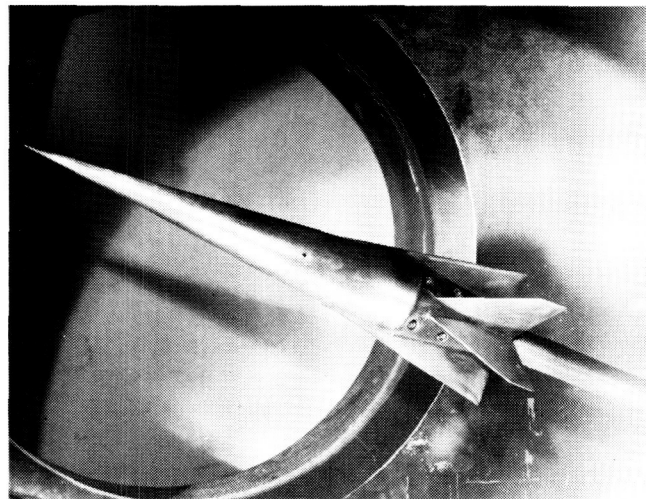
### Aerodynamic Characteristics of Transatmospheric Vehicle Concept Over Wide Speed Range

Transatmospheric vehicles (TAV's) proposed for the 1990's would routinely take off from a conventional runway, accelerate using air-breathing propulsion to achieve low-Earth orbit, reenter, and land horizontally. One generic TAV concept of interest (as shown in the first figure) is a winged-cone configuration that offers design advantages in efficient vehicle packaging and the orientation of multiple engines. An experimental investigation of aerodynamic characteristics for a winged-cone configuration without engines has been performed over the approximate flight Mach number range of the vehicle ( $0.6 \leq \text{Mach} \leq 20$ ). The primary purposes of this study were to establish a timely aerodynamic data base for this class of TAV's and to compare predictions made with engineering codes (e.g., the Hypersonic Arbitrary Body Program) with measurement.

The variation of the measured drag coefficient at zero lift  $C_{D_0}$  with Mach number is shown by the circular symbols in the second figure. These data reveal a steep transonic drag rise followed by a more gradual decline in drag levels supersonically. Engineering code predictions of  $C_{D_0}$  at the present supersonic and hypersonic flow conditions and model scale (shown by the solid and dashed lines) are generally in good agreement with measurement. A large move-

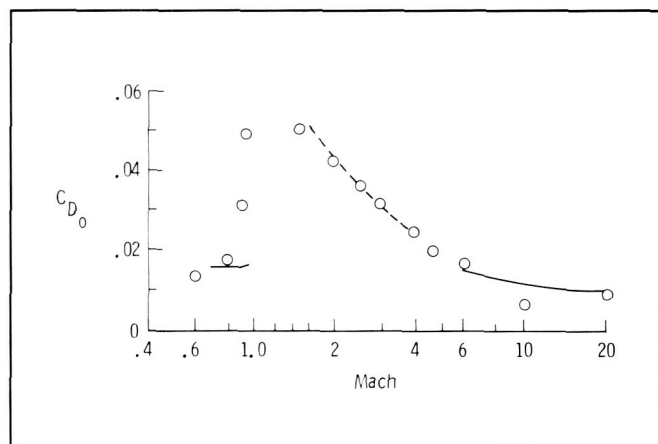
ment in the longitudinal center of pressure (approximately 23 percent of the vehicle length) was observed to accompany an increase in Mach number from 1.5 to 20. Such a large center of pressure variation with Mach number will dictate the need for large, effective control surfaces to facilitate flight at low angles of attack.

(W. Pelham Phillips, 3984)



L-86-4901

*Transatmospheric vehicle mode mounted in 20-Inch Mach 6 Tunnel.*



*Variation in zero-lift drag with Mach number.*

## Space Shuttle Orbiter Stability and Control Characteristics at High Angles of Attack

Langley Research Center is continuing to support the refinement and updating of the aerodynamic data base of the Space Shuttle orbiter. One area recently under study addresses an alternate means of crew escape during an ascent abort. The Space Shuttle orbiter, however, has only one entrance, which is the side hatch. Previous tests have shown that unassisted bailout from this hatch during steady gliding subsonic flight at normal flight attitudes is very risky. The current series of tests were conducted with the thought that if the orbiter could be safely

trimmed at very high angles of attack  $\alpha$ , a slower descent rate might be achieved and more benign bailout conditions might exist. It might also be possible to exit the vehicle from the upper cabin windows located on top of the fuselage.

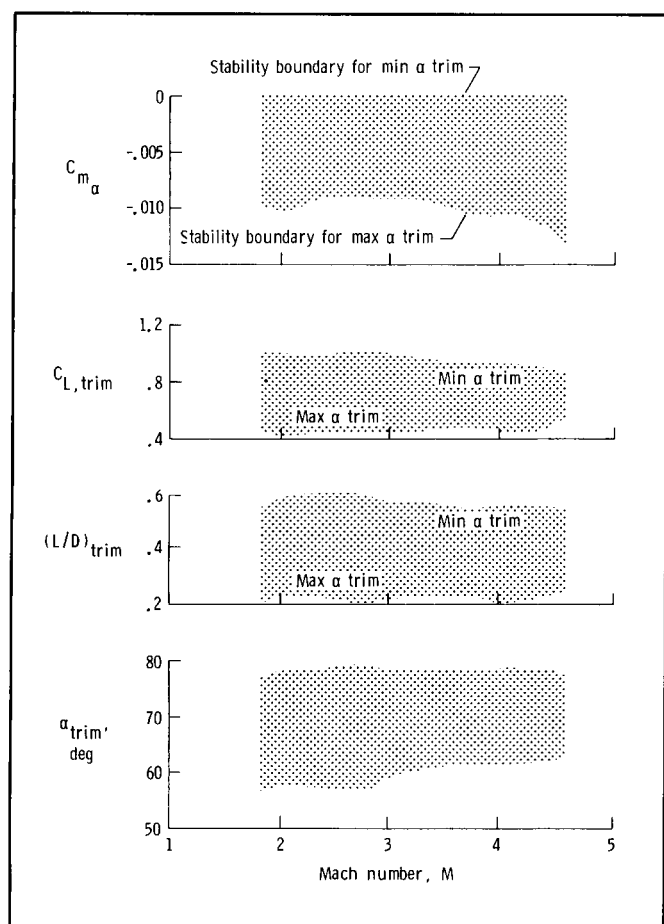
Tests were conducted in the Langley Low-Turbulence Pressure Tunnel, the Langley Unitary Plan Wind Tunnel, and the Calspan 8-Foot Transonic Wind Tunnel over a Mach range from 4.6 to 0.30 to determine the high-angle-of-attack characteristics of the orbiter. Even though bailout was considered only at the slowest speeds, the study was carried to the high Mach numbers because it may be advantageous to trim the orbiter to high angles of attack early in the gliding return at high Mach numbers and allow the vehicle to slow down while in that attitude. The results of the tests are summarized in the figure, which shows that the orbiter is longitudinally stable and has the ability to be trimmed over a wide range of lift  $C_L$  and lift-to-drag  $L/D$  values, thus producing a more favorable environment for bailout. (B. Spencer, Jr., 3984)

## Crew Emergency Rescue Vehicle

For a permanently manned Space Station, some type of crew emergency rescue vehicle (CERV) is needed. Dependability, speed of recovery, ride quality, risk, and cost are all considerations. Many alternatives are being considered, from ballistic shapes to vehicles that can fly and land like airplanes. The objective of this study was to evaluate a lifting body as a potential CERV.

The guidelines for the study included the accommodation of up to eight persons, delivery to orbit in the Space Shuttle, ability to stay docked at the Space Station in a ready state for at least 180 days without resupply, and ability to loiter on orbit for up to 24 hours after separation from the Space Station. Because of an additional guideline that there may not be a trained or healthy pilot aboard, it is necessary to include the architecture for the avionics that would provide for an automated entry and landing.

Trajectory calculations starting over Cape Kennedy show that the vehicle has enough cross



Summary of Space Shuttle orbiter model high  $\alpha$  stable trimmed characteristics.  $C_{m_\alpha}$  is change in pitching moment with respect to  $\alpha$ .



range to land at either John F. Kennedy Space Center or Edwards Air Force Base on the first four orbits, or at Edwards on the fifth orbit. When John F. Kennedy Space Center, Edwards Air Force Base, Hawaii, Guam, and Dakar (West Africa) are considered as landing sites, a return from the Space Station is possible on every orbit.

An analysis of the entry heating indicates that the peak surface temperature (in the nose stagnation region) is about 30-percent higher than that for the Space Shuttle, but it is considered to be within the present capabilities of existing thermal protection materials. (The higher temperature is due principally to the smaller nose radius of the CERV when compared with the Space Shuttle.)

Other characteristics of the vehicle include a titanium structure, a durable thermal protection sys-

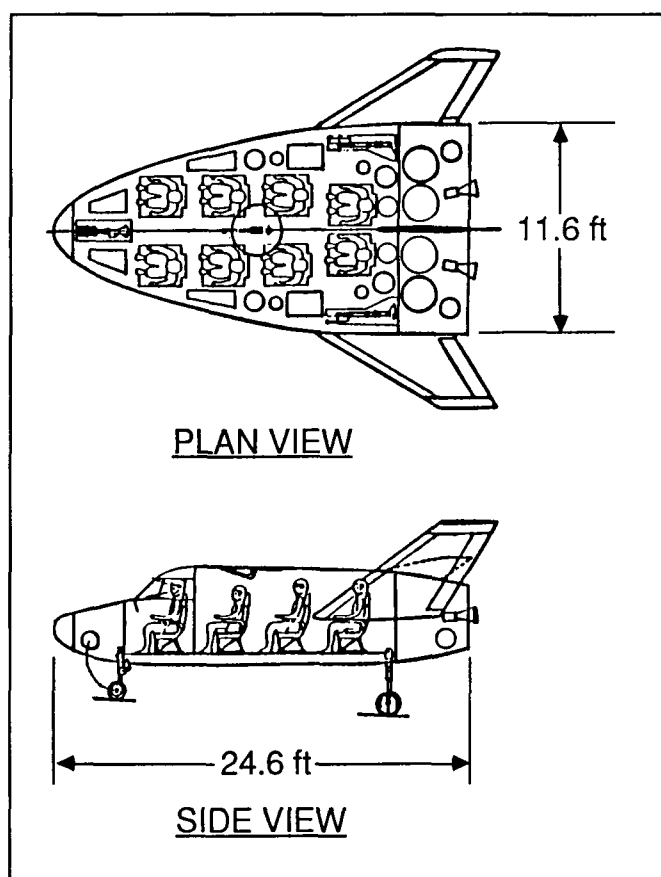
tem, a battery power system, all-electric actuators for control surfaces, and hinged wings so that the vehicle can be accommodated in the Space Shuttle cargo bay. The study resulted in the inclusion of a lifting body as a viable candidate in the Space Station contractual activities for a rescue vehicle.

(I. O. MacConochie, 4963)

### Calculation of Three-Dimensional Nonequilibrium Viscous Flow Over Space Shuttle Windward Surface

A three-dimensional viscous-shock-layer code has been used to compute the nonequilibrium flow field over the windward surface of the Space Shuttle orbiter for reentry conditions between 75 and 60 km. The computer code used for this work (SHTNEQ) was originally developed through a grant from Langley Research Center and solves the full set of viscous-shock-layer equations and coupled reaction equations to model the nonequilibrium chemically reacting flow of air over the Space Shuttle surface. Modifications made to the program have significantly improved its accuracy and applicability. Comparisons of present predictions of surface heat transfer with previous results show differences of 30 percent, and the new results demonstrate that three-dimensional effects on the Space Shuttle windward centerline heat-transfer distribution are not as significant as previously reported.

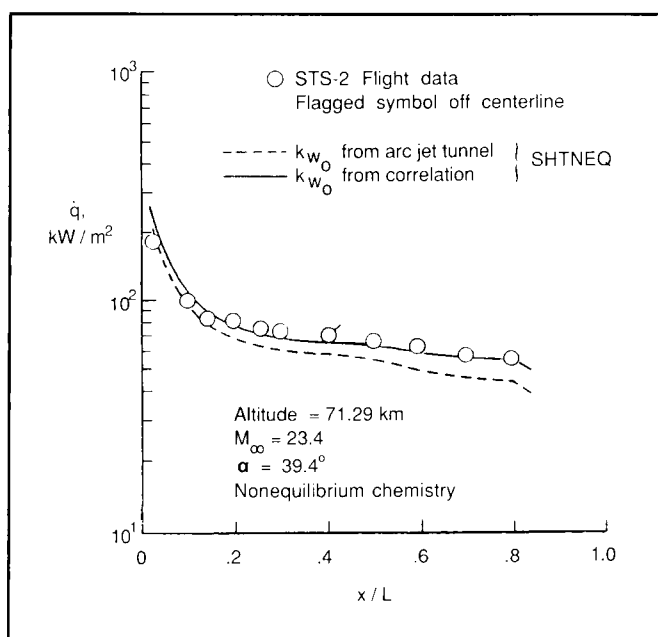
Windward symmetry plane and off-centerline heating predictions obtained with the code have been compared with experimental data from flights STS-2 and STS-3. Different surface recombination rates for oxygen, to account for the catalysis of the Space Shuttle tile surface, have been considered in the predictions. Those results show that a recent correlation for oxygen recombination provides good agreement between predicted heat transfer and that measured in flight. Typical results for heat-transfer distribution  $\dot{q}$  as a function of normalized distance  $x/L$  along the Space Shuttle windward centerline are shown for an altitude of 71.29 km and free-stream Mach number  $M_\infty$  of 23.4. The angle of attack  $\alpha$  for this case



Eight-man CERV inboard layout.

was  $39.4^\circ$ . The two predicted heat-transfer distributions were obtained using the different oxygen recombination rates  $k_{w_o}$  as noted. Comparisons of heating predictions with flight data in the cross flow direction have also been made and show good agreement for the regions computed. Trends in the measured cross flow heating distributions are generally predicted with the three-dimensional viscous-shock-layer code.

(R. A. Thompson, 4328)



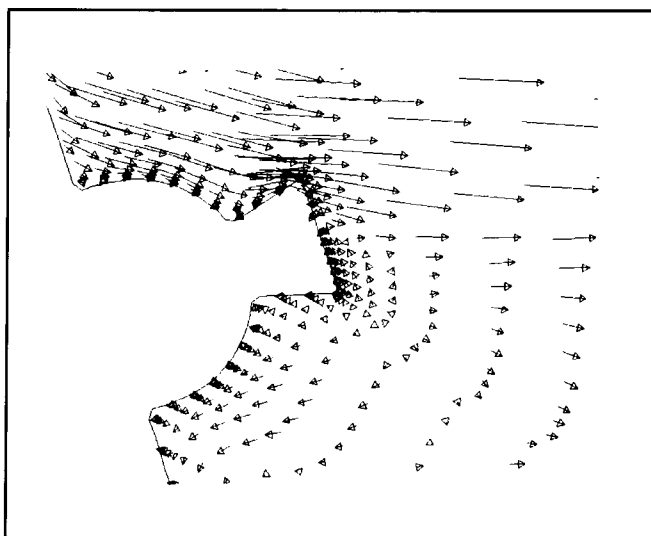
Measured and computed heat-transfer rates in windward symmetry plane of Space Shuttle orbiter.

### Near-Wake Flow Field Over Aeroassist Flight Experiment Vehicle

Program LAURA (Langley Aerothermodynamic Upwind Relaxation Algorithm) has been used to calculate the complete flow field about the Aeroassist Flight Experiment (AFE) vehicle at a single trajectory point. This study is the first attempt to define the near-wake flow field over a close approximation to the actual AFE geometry. Both perfect-

gas and chemical nonequilibrium (single temperature, no species dissipation) assumptions have been used. The results demonstrate the present capabilities and limitations of the LAURA algorithm.

The Symmetric Total Variation Diminishing (STVD) algorithm used in LAURA has been demonstrated to be robust for the simulation of the near-wake flow field behind the AFE at a flight trajectory point using perfect-gas assumptions. Calculations on two different grids at the same trajectory point have given consistent prediction of flow field phenomena. Calculations at two different Reynolds numbers exhibit the correct phenomenological trends. Of particular interest are the predictions of a strong flow impingement on the lip of the AFE rocket nozzle and of the correspondingly high heating rates at that location. This impingement is evident in the symmetry-plane mapping of velocity vectors computed for a flight condition of Mach number  $M_\infty$  equal to 32 and Reynolds number  $Re_{\infty,D}$  equal to 79000, at the design angle of attack (as shown in the figure). A survey of the local Knudsen number throughout the flow field indicates that a continuum analysis is generally well founded, but there are isolated regions in the near wake close to the body where, at a minimum, slip conditions should be imposed; it is possible that



Velocity vectors in near-wake plane of symmetry of AFE vehicle.

continuum results are in error at the maximum dynamic pressure trajectory point. The higher densities associated with real-gas flows relax this restriction on the continuum analysis.

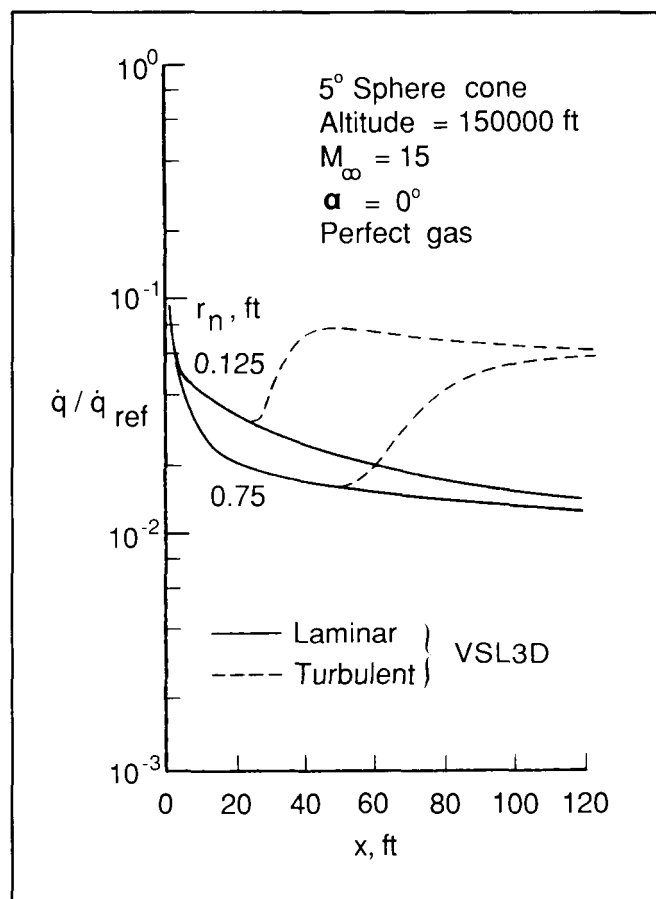
(P. A. Gnoffo, 2921)

### Aerothermodynamic Study of Slender Conical Vehicles

Recent interest in transatmospheric vehicles and the National Aero-Space Plane (NASP) has renewed the need for development and verification of prediction techniques that may be used to analyze the viscous hypersonic flow over slender vehicles. Consequently, a study was initiated to investigate the applicability of several existing techniques for the slender-body aerothermal problem. These techniques ranged in complexity from a finite-difference solution of the three-dimensional viscous-shock-layer equations (VSL3D) to approximate engineering-type analyses. Using these techniques, comparisons were made between predicted results and flight and wind tunnel data, for both laminar and turbulent flow and perfect gas and equilibrium air chemistry. Comparisons of the predicted heat-transfer rates with flight data from the Reentry F vehicle showed the method to be generally accurate; however, some deficiencies in the engineering techniques were noted, particularly at angle-of-attack conditions.

As a second part of this study, these codes were used to illustrate the effects of nose bluntness and angle of attack on the heat transfer, transition onset, and zero-lift drag coefficients for a slender cone at a free-stream Mach number  $M_\infty$  of 15. Those results showed the quantitative benefits of increased nose bluntness, which resulted in decreased local heat-transfer rates and overall heat loads, and delayed boundary-layer transition. Total vehicle drag was not adversely affected by increasing nose radius  $r_n$  for the laminar case and was decreased for the turbulent condition, using the given transition model. The figure shows the nondimensional heat-transfer rates  $\dot{q}/\dot{q}_{ref}$  versus axial distance from the nosetip  $x$  at an angle of attack  $\alpha$  of  $0^\circ$  for bodies with different  $r_n$  for both laminar and turbulent flow.

(R. A. Thompson, 4328)



*Nose radius effects on heat transfer to slender cones in hypersonic flow.*

### In Situ Upper-Altitude Density Measurement From Space Shuttle Orbiter Accelerometry

A Space Shuttle orbiter experiment, the High-Resolution Accelerometer Package (HiRAP), provides a new and unique source of measurements of atmospheric density. The HiRAP experiment is a triaxial set of high-resolution accelerometers which measures the aerodynamic deceleration rates of the orbiter during the high-altitude portion of its atmospheric entry. By comparing these measured vehicle responses to aerodynamic forces with the aerodynamic characteristics of the orbiter, the atmospheric

density may be inferred. Aerodynamic models for both the normal and axial aerodynamic components are used in the density extraction process. Data taken on 10 flights of 2 instrumented Space Shuttle orbiters (OV-102 and OV-099) have provided density measurements of unusual character. The uniqueness of the measurements resides in the fact that the orbiter enters the atmosphere nearly horizontally because of its shallow reentry flight path angle. The ratio of the orbiter's ground-track distance to descent distance is about 80:1 for each mission. This horizontal component of the atmosphere is rarely, if ever, obtained by sounding rockets, since they traverse relatively short down-track distances and are essentially limited to taking vertical atmospheric soundings. Orbiting satellites, on the other hand, can provide the same type of measurements but cannot enter the region of the atmosphere from 80 to 130 km.

figure, undulations in density on the order of 30 percent appear in both channels of data and are typical for all 10 flights examined to date. It is believed that this wave-like feature is atmospheric in origin. Unlike the orbiter, future vehicles (e.g., aeroassisted orbital transfer vehicles and the National Aero-Space Plane), which will spend more time in the upper atmosphere, may have to account for these density variations in various subsystems design, such as guidance and control.

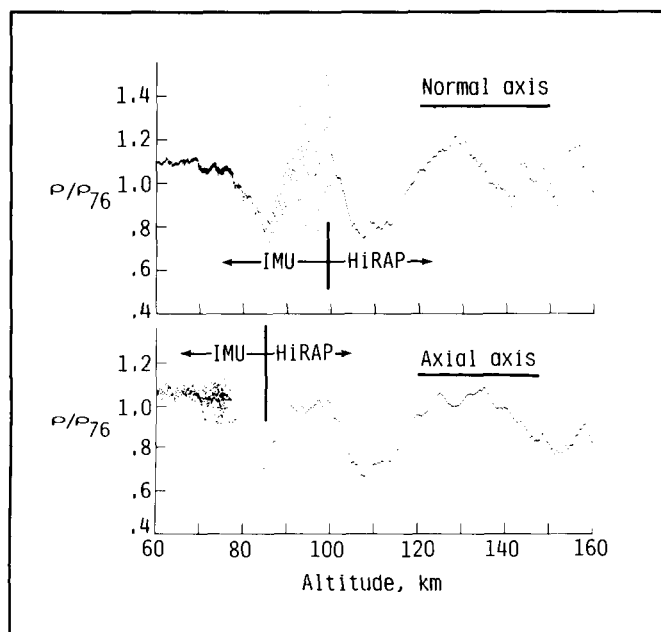
(R. C. Blanchard, 3031)

### Q-Switched Solar-Pumped Iodine Lasers

Research on solar-pumped lasers was initiated in 1980 for the purpose of evaluating their feasibility as space-to-space power transmitters. For example, space laser power transmitters placed on a high-altitude orbiting power station can transmit power to a low-altitude satellite with space manufacturing factories. Such transmitters require at least 1 MW output to be practical. Most laser power receivers are designed for continuous wave (CW) power reception; however, other important applications (including laser propulsion) are better suited for pulsed power sources.

One pivotal technology receiving detailed study involves the use of sunlight to directly pump a gas laser. Significant progress was achieved over several years with photodissociation iodine lasers using an organic-iodide lasant and a solar-simulator. Since the first solar-pumped lasing was achieved in 1980, the output power levels of iodine lasers increased from less than 1 mW pulsed to 10 W CW, which is the highest CW power ever achieved with photodissociation iodine lasers (as reported in NASA Langley Technical Memorandum 89037, 1986).

Recently the peak laser power was boosted by more than an order of magnitude by adapting a Q-switching technique to the CW system. The Q-switching technique is a method for generating high-power laser pulses at high repetition rates by depositing large quantities of energy in very short time increments before loss mechanisms can begin to operate. For this experiment, Q-switching was accomplished by placing a fast mechanical chopper in the



*Atmospheric density derived from STS-6 Space Shuttle orbiter accelerometry.*

The inferred density data shown are normalized to the 1976 U.S. Standard Atmosphere so that deviations can be readily observed. The HiRAP data have been merged with data derived from the orbiter's inertial measurement unit (IMU) to extend measurements to lower altitudes. As seen from the

laser cavity. The popular Q-switching method, Pockels cell, cannot be used because of the intolerable insertion loss at the  $1.3\text{ }\mu\text{m}$  laser wavelength. A train of high power (up to 150 W) laser pulses was continuously produced at various repetition rates while the solar simulator, a Vortek Industries, Ltd. argon arc, pumped the laser medium at steady optical power. This is the first reported Q-switching of CW iodine lasers. By this method, the highest-ever laser power for solar-pumped gas lasers was achieved. The flow of the laser medium,  $n\text{-C}_3\text{F}_7\text{I}$  vapor, was longitudinal and maintained by the pressure differential between an evaporator and a liquid-nitrogen-cooled condenser. The dependence of CW and Q-switched

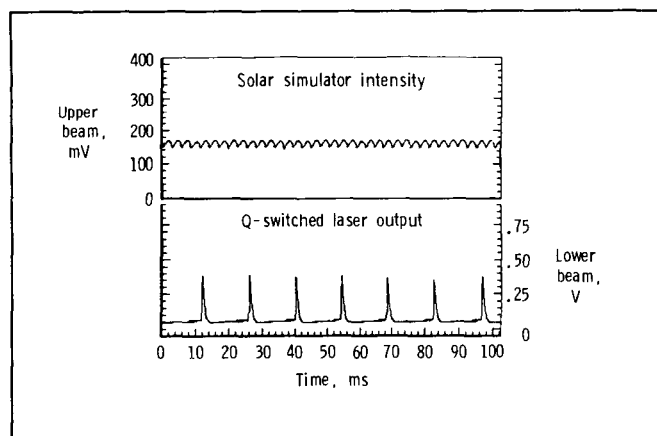
laser power on parameters such as iodide vapor pressure, gas flow rate, and chopping speed was determined and analyzed.

(J. Lee, 4332)

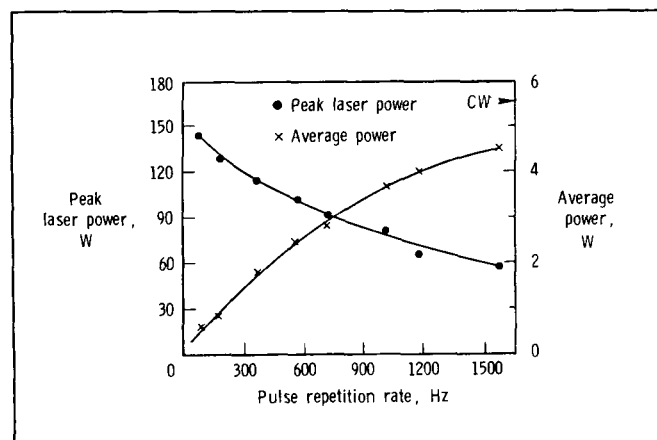
## Engine Selection for Advanced Earth-to-Orbit Vehicles

Studies, which are currently under way at major rocket engine companies, could lead to the development of new engines for the next generation of Earth-to-orbit vehicles. These vehicles include unmanned heavy-lift vehicles that might be partly reusable as well as fully reusable Shuttle II concepts. The baseline efforts are directed toward a hydrocarbon engine for the boosters called the Space Transportation Booster Engine (STBE) and a hydrogen engine for the upper stages called the Space Transportation Main Engine (STME). These baseline engines (STBE and STME) have been selected because they can be developed relatively quickly with existing technology. In addition to the baseline engines, other designs are being considered which might improve the vehicle even though they may require technology development. The conceptual design analyses performed at Langley Research Center have incorporated results from these studies (directed by Marshall Space Flight Center) to show the effect of these advanced engines on single-stage vehicles with vertical takeoff and horizontal landing.

The figure shows that the baseline engines can be used in a parallel-burn dual-fuel vehicle, and the resulting vehicle dry mass would be 111 Mg for a payload of 13.6 Mg. The best advanced engine, called the dual-fuel, single-bell engine, could reduce the vehicle dry mass about 20 percent to 90 Mg. In addition, only one engine would need to be developed. Another concept, the variable-mixture ratio engine, could reduce the vehicle dry mass and also simplify the operations because only one fuel, hydrogen, would be needed. A third concept, the dual-bell engine, could be used by itself, but the results showed that the vehicle dry mass would be increased with this approach. Using the dual-bell engine with the STME provided some improvement. This dual-bell concept could also be applied to the STME for additional improvement,



Solar-simulator pumping intensity and Q-switching iodine laser output signals.

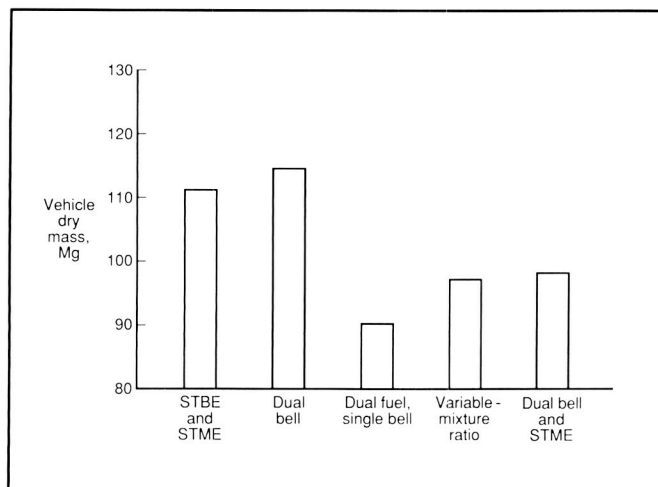


Peak laser power versus pulse repetition rate.

C-2

or it could be applied to the dual-fuel, single-bell engine. Overall, these results have shown that there are improved engine concepts that should be considered before beginning full-scale development of the next generation of rocket engines.

(J. A. Martin, 4964)



*Effect of engine selection on dry mass of single-stage-to-orbit rocket vehicle.*

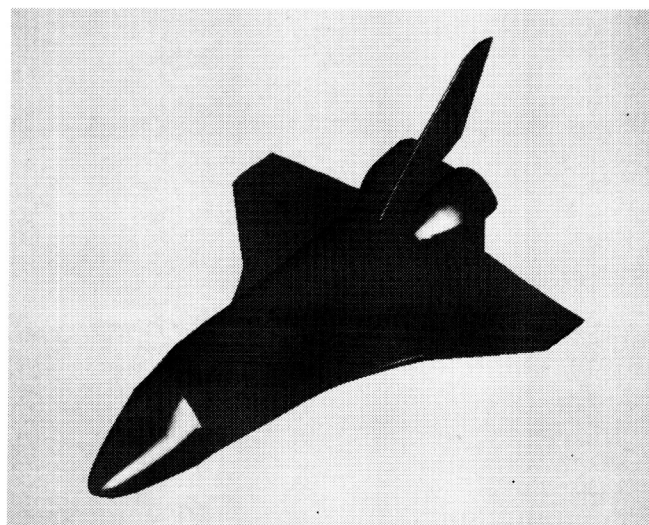
### Solid Modeling Aerospace Research Tool

A new geometry modeler has been developed for the second-generation AVID (Aerospace Vehicle Interactive Design) system. The new modeling program, called SMART (Solid Modeling Aerospace Research Tool), takes advantage of state-of-the-art computer graphics hardware to substantially increase the productivity of the design engineer. Complex configurations can now be quickly and accurately generated and, through interfaces, can be sent to applications programs, such as aerodynamics and structures for detailed analyses. Realistic color pictures of configurations can be generated. For example, the figure shows the black-and-white version of a color photo of a Space Shuttle orbiter produced by the SMART program.

To provide this capability, SMART was developed with analytical surface descriptions and bicubic Bezier patches that provide accuracy and completeness; an effective user interface that makes the system easy to learn and convenient to use; geometry generation techniques that are tailored to aerospace applications; an interface to other analysis programs which is available through the LaWGS (Langley Wire-frame Graphics Standard) system; and an advanced graphics hardware of the Silicon Graphic IRIS workstation that allows geometry generation, modification, and manipulation in real time.

After one and one-half years of development, SMART has entered production use. It has been applied with great success to the National Aero-Space Plane (NASP) Program. A number of complex configurations have been generated, and the geometries for these configurations have been successfully transferred from SMART to structural analysis and computational fluid dynamics programs.

(J. J. Rehder, 4967)



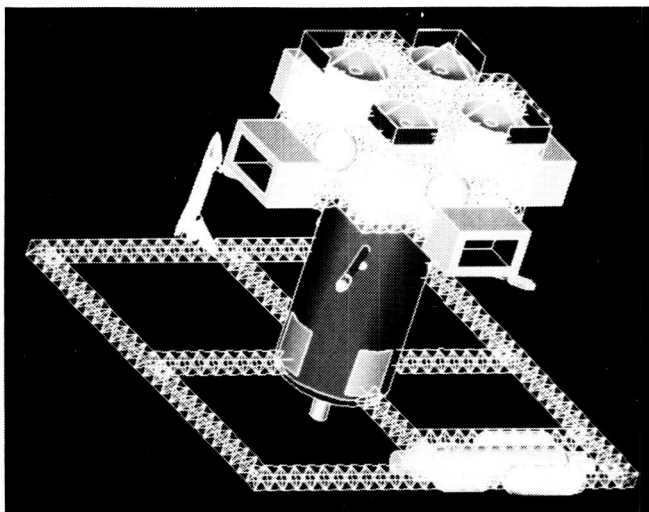
*Space Shuttle orbiter configuration produced by SMART program.*

### Transportation Base Space Station for Year 2025

The current Space Station reference configuration, scheduled for service in 1994, will be required to

function in many capacities, including orbiting laboratory, satellite-servicing facility, experiment platform, orbiting construction site, and as a base for the orbital maneuvering vehicle (OMV) and orbital transfer vehicles (OTV). Future transportation demands, however, would quickly overwhelm the Space Station as the Space Shuttle, Space Shuttle-derived vehicle, and OTV traffic increases. A fully dedicated transportation base Space Station would be the most efficient method to meet the transportation needs of the twenty-first century.

The figure shows one concept of a fully dedicated transportation base Space Station that operates in low-Earth orbit. The concept has been developed with the IDEAS<sup>2</sup> conceptual design software, and it features four docking ports for Space Shuttle-type vehicles as well as four large enclosed hangars. These hangars would support OTV servicing, repairs, and storage as well as satellite servicing and repair, including refueling operations. The large truss structure would serve as a bay for the construction of large space structures and for the assembly of Mars, lunar, and interplanetary vehicles, thereby adding the function of a staging base to the station.



*Transportation base Space Station concept.*

With the development of this concept, additional studies will be initiated, such as interfaces with current and future transportation concepts and associated propellant requirements. The various subsys-

tems will be sized, and a mission scenario will be developed. On-orbit performance will be evaluated, and technology advancement requirements will be defined. Alternate concepts may also be developed in order to assess the relative merits of each.

(A. Don Scott, 4981)

### Concept for Low-Gravity Research Facility

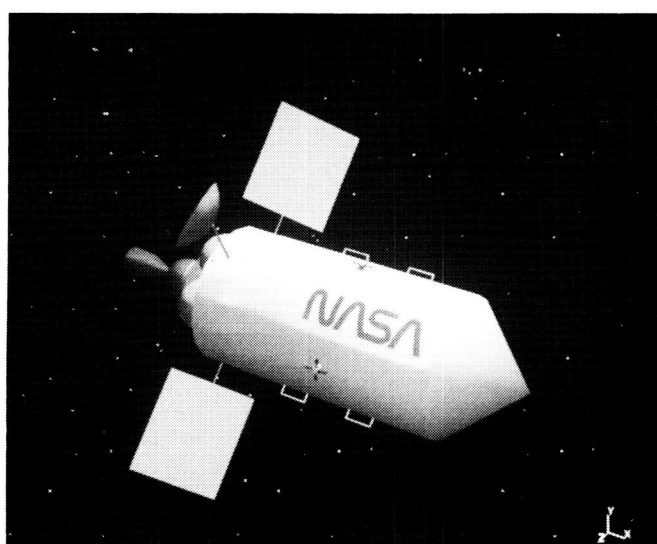
One of the biggest payoffs of space technology in the future is expected to be in the area of low-gravity research. Advances in a variety of disciplines such as materials science, electronics, fluids, astrophysics, and medicine are expected as laboratories in space become available. Spacecraft that are specialized to meet this demand are being studied, and unmanned free-flyers have emerged as a promising concept. The figure shows an early configuration developed with the IDEAS<sup>2</sup> computer program.

Unmanned free-flyers can be utilized to maintain low-acceleration environments for long periods of time. Concepts involving free-flyers composed of an outer shell separated from the inner low-gravity module (LGM) are currently under study. The standardized outer shell flies around the LGM during periods when a low-acceleration environment is needed and acts as a platform for the subsystems needed to support the experiment. These subsystems include power, propulsion, thermal control, guidance, navigation, and control.

The low-gravity module is completely surrounded by the outer shell and is separated from it by an evacuated gap. The acceleration environment of the LGM is dominated only by altitude-dependent gravity gradient accelerations and those accelerations caused by moving portions of the experiment itself. The LGM will be experiment dependent but also must be of a fixed configuration in order to mate correctly with the shell. The LGM will remain in free-fall at all times during the experiments. Accelerations due to atmospheric drag, charge buildup, solar and albedo pressures, as well as those caused by normal subsystem function (such as antenna and radiator movement), are all isolated from the LGM by the gap.



A fleet of these free-flyers could be serviced either by the Space Station or by a specialized tender spacecraft. Since the gravity gradient accelerations decrease with altitude, engines mounted on the shell will be used to boost the spacecraft to the desired orbit and then bring it back after the experiment is over. At the Space Station the LGM will be pulled out and replaced by a new one while the shell is refurbished for another mission. Since many free-flyers could be orbiting simultaneously at different altitudes and for different durations, many



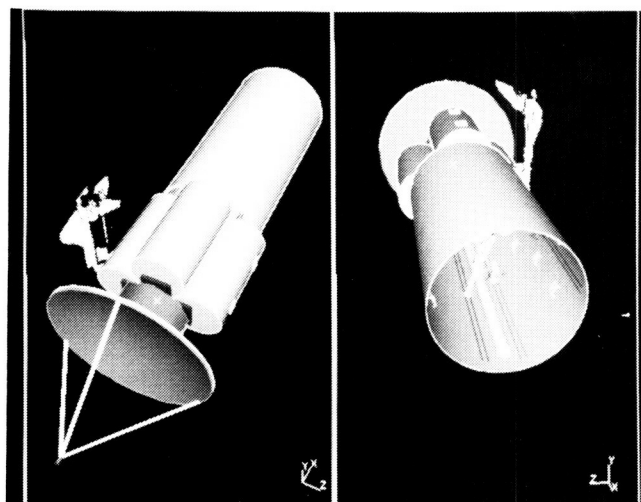
*Low-gravity research facility concept.*

varied experiments could take place in a brief time. This concept would also be well suited for a continuous manufacturing process in which the shells and modules may be serviced by a specialized spacecraft. (Gary Martin, 4976)

## Advanced Satellite-Servicing Facility

As the population of active polar-orbiting and near-polar Sun-synchronous satellites increases, the need to effectively manage the satellites in this group of orbits may eventually require an on-orbit manned

facility dedicated to serving their needs. The presence of such a facility could significantly reduce the cost of high-inclination space operations by providing a number of common services from a permanently manned platform. Technology requirements of such a facility in the year 2025 are being examined. The prime technology needs are crew and facility safety, a large satellite-servicing capacity with a quick turnaround, the reduction or elimination of extravehicular activity in all operations, and minimization of the frequency of launches needed to support facility operations. One candidate for a satellite-servicing facility is the concept shown in the figure. This configuration has been developed using IDEAS<sup>2</sup>, an interactive computer program for conceptual design.



*Concept for advanced satellite-servicing facility.*

The mission areas being examined are facility-based satellite assembly, checkout, and deployment, retrieval and redeployment for satellite refueling, repair, or systems upgrade; remote satellite refueling, repair, or systems upgrade; ferrying materials and consumables to and from manufacturing platforms; the deorbit, removal, repositioning, or salvage of satellites and debris; and crew rescue of other manned vehicles in high-inclination orbits. The technology issues identified to date include easily used and maintained expert systems capable of controlling many facility operations, telerobotic and autonomous systems capable of performing a large number of varied tasks from rendezvous/docking to component

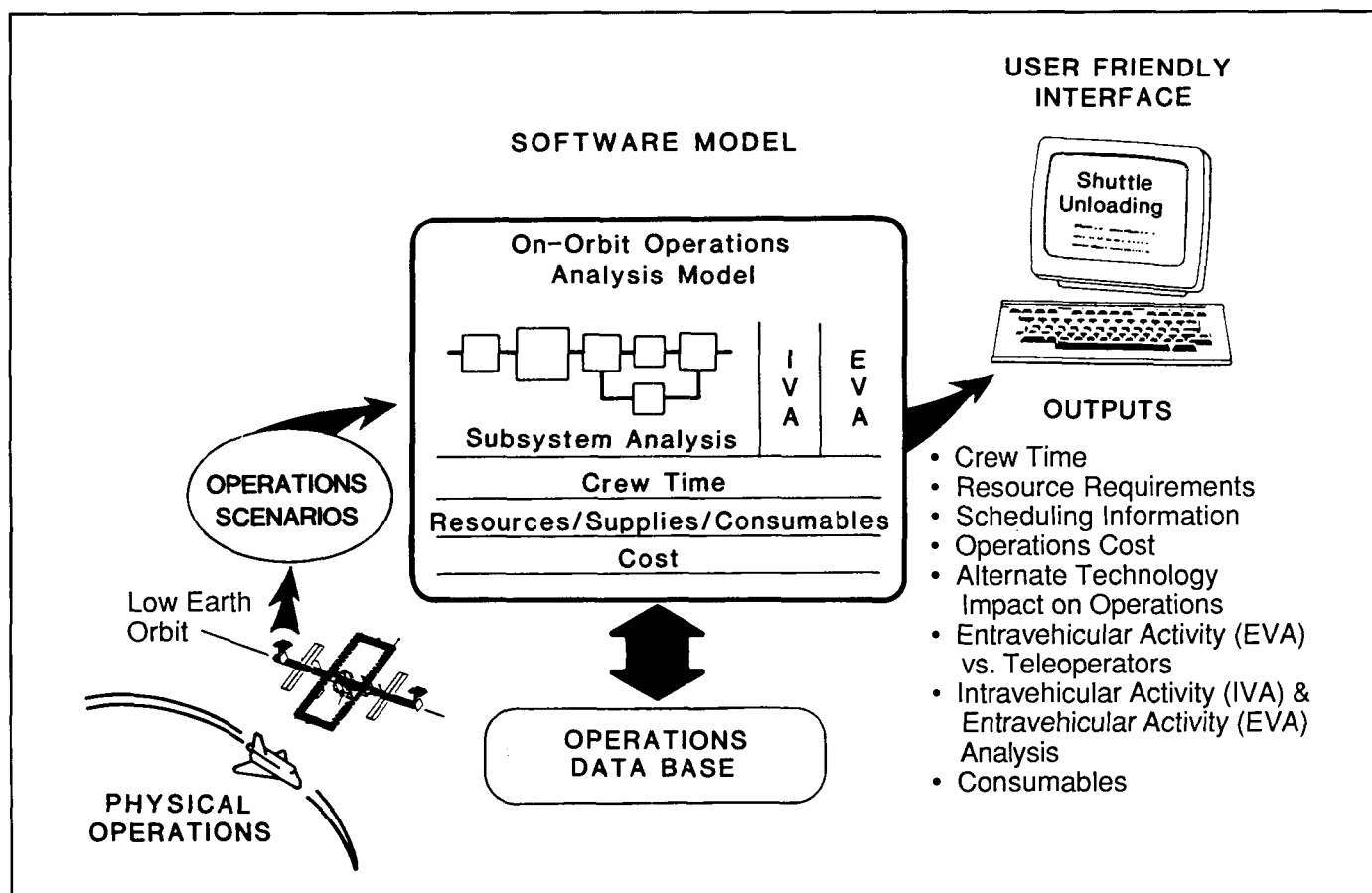
changeout and refueling, closed-loop life support systems, and methods of lessening or arresting the physiological effects of long stays in orbit. (Garry Qualls, 4976)

## Space Station On-Orbit Operation Model

The operations area of NASA space programs is an essential element that requires substantial resources during a program lifetime. The current Space Station effort addresses one of the most complex concepts proposed to date. In addition to the usual

requirements of spacecraft design and the added complexity of a manned presence, the very long mission duration (15 to 20 years) increases the emphasis on operational cost. Within the on-orbit operations area, crew time has been identified as a most valuable and limited resource for the Space Station. The objective of this effort is to provide NASA with a state-of-the-art computer modeling technique for on-orbit operations modeling and assessment.

Langley Research Center and the Computer Sciences Corporation have developed an operations model (OPSMODEL) which permits a user to assess the impact on crew time of system/subsystem designs, technologies, and operational philosophies for a given station design. The basic concept for this model is presented in the figure. The OPSMODEL



OPSMODEL concept.

employs discrete event simulation to model crew activities and keeps track of all consumables and resources. The simulation model is composed of a data base manager and an operations simulator. The data base manager is programmed in R:BASE 5000, and the operations simulator uses a general-purpose simulation programming language, SIMSCRIPT II.5.

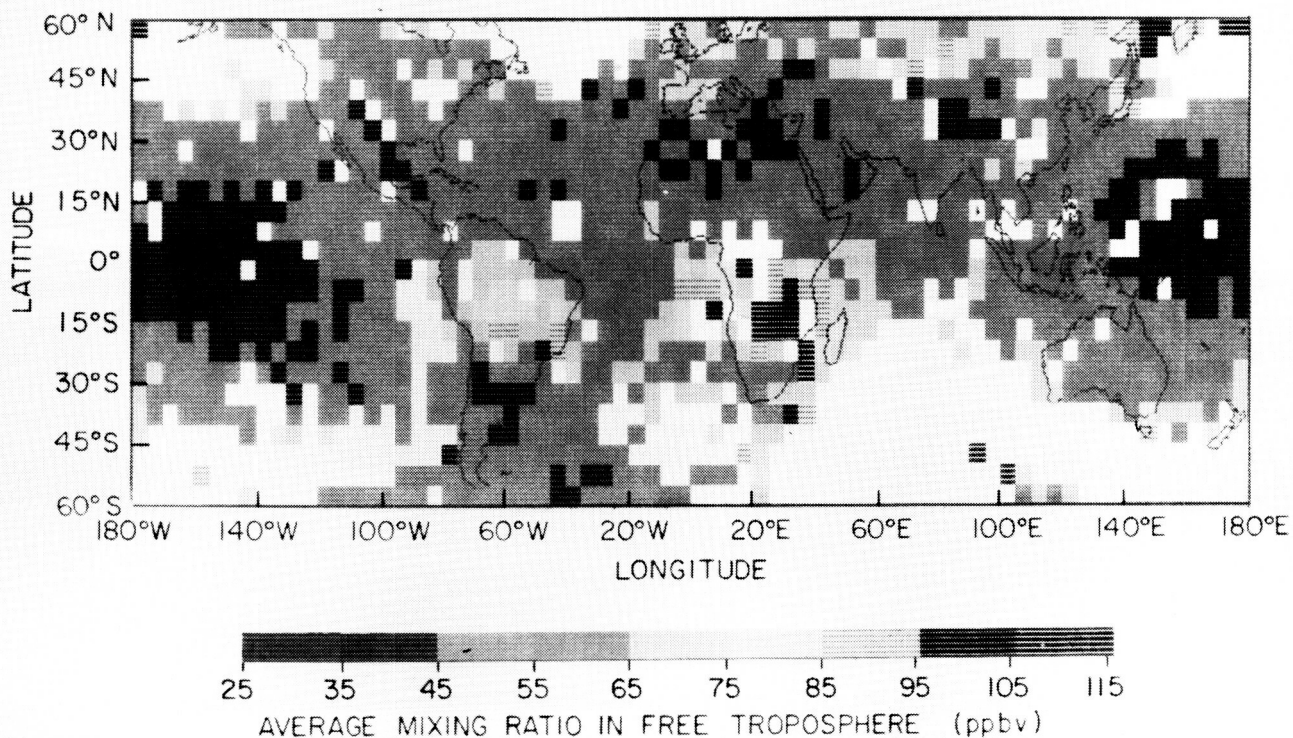
Crew activity is modeled using tasks that can be represented at any level of detail. Tasks are linked together to form operations or complete segments of work. By using these principles, total crew activities can be modeled over the desired mission time. Model output includes crew "busy," "waiting," and "idle" times; resource profiles; and cost reports. Event and crew member traces assist the user in problem resolution. The menu-driven model runs on an IBM-PC-AT or XT computer requiring no programming, recompiling, or special computer skills of the user. The OPSMODEL is intended to improve NASA's capability to expose operations areas in which there may be increases in Space Station productivity or reductions in cost.

(William R. Jones, 4978)

## Global-Scale Distribution of Carbon Monoxide as Measured From Space Shuttle Platform

The Measurement of Air Pollution from Satellites (MAPS) experiment was flown onboard the Space Shuttle during November 1981 and again during October 1984. The purpose of the experiment was to measure the distribution of carbon monoxide in the atmosphere between the altitudes of 3 and 15 km. Carbon monoxide is an air pollutant that is emitted both as a result of man's industrial and agricultural activities and as a result of natural processes. At the present time, it is felt that man's emissions are about equal to the natural emissions. Because carbon monoxide can perturb the global-scale chemistry and, thereby, possibly affect the climate of the Earth, it is extremely important to understand both the sources and the distribution of the gas.

The MAPS data have shown that the amount of carbon monoxide in the atmosphere is highly variable over the Earth. As can be seen in the figure, which



*Distribution of carbon monoxide as measured by MAPS experiment during October 1984.*

shows the data from the 1984 flight, the amount of carbon monoxide in the atmosphere is relatively low and uniform over the tropical Pacific Ocean. In contrast, the atmosphere over Europe, northern Asia, South America, and southern Africa all show enhanced mixing ratios. Examination of Space Shuttle-borne photographs and of eyewitness reports from the astronauts indicates that there were many agricultural ground fires burning during the mission in both South America and southern Africa. These fires are thought to be the source of the carbon monoxide measured over those areas, and they represent a significant source on the global scale. Further, they are a large source of carbon monoxide in the Southern Hemisphere, an area previously thought to be free of significant carbon monoxide sources.

(Henry G. Reichle, Jr., 2576)

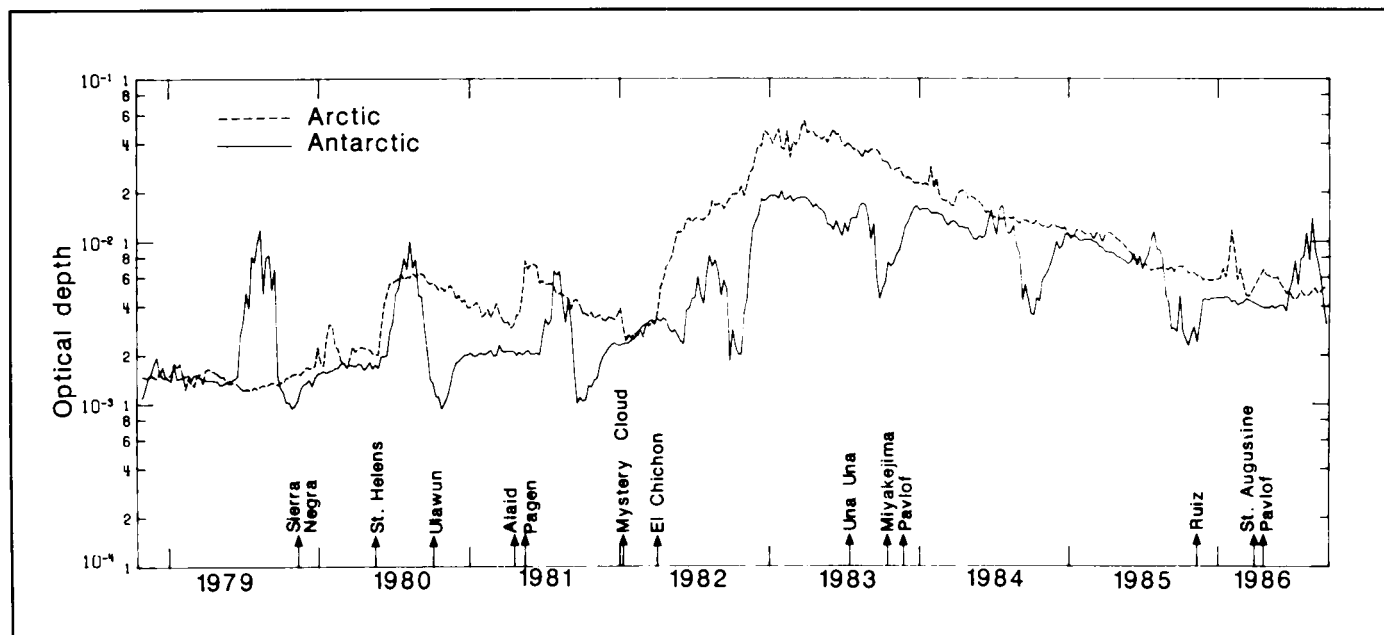
### Satellite Measurements of Stratospheric Polar Aerosols

In October 1978, the Stratospheric Aerosol Measurement (SAM) II experiment was launched on-board the Nimbus 7 spacecraft to obtain detailed

information about the high-latitude stratospheric aerosol layer. The SAM II instrument remains fully operational, and a large and unique data set has been assembled for examining the characteristics of polar stratospheric aerosols as well as providing information on the long-term variation of the aerosol layer.

The weekly averaged stratospheric aerosol optical depth is presented in the figure for the period of October 1978 to October 1986. This record shows that the overall yearly values in the two polar regions are influenced by seasonal variations and controlled by volcanic perturbations. The impact of volcanic eruptions is much more apparent in the northern high latitudes, partly because of the greater number of eruptions in the Northern Hemisphere and partly because of the more favorable seasonal circulation patterns following these eruptions. The eruption of El Chichon in April 1982 created the largest enhancement in optical depth recorded in both hemispheres.

Pronounced enhancements are also visible yearly, especially in the southern high-latitude observations each mid-winter. These episodes are due to the formation of polar stratospheric clouds (PSC's) when temperatures descend below about  $-80^{\circ}\text{C}$ . Antarctic PSC's are present for periods of approximately 3 to 4



*SAM II stratospheric aerosol optical depth record. Dashed and solid lines represent measurements made in the Arctic and Antarctic region, respectively. Dates of significant volcanic eruptions are indicated.*

months (from early June until late September). Arctic PSC's are also observed in each Northern Hemisphere winter season, but are much less frequent because of generally warmer stratospheric conditions.

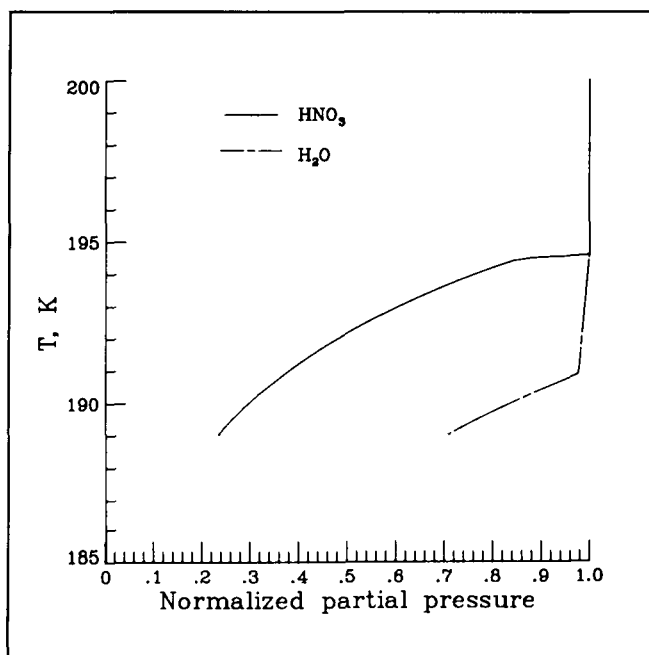
Another recurring feature in the data is the depression in optical depth observed in late September and early October in the Southern Hemisphere. This phenomenon has been observed immediately following the disappearance of PSC's at the latitudes measured by SAM II. It is believed that this relative minimum is produced by the loss of aerosols within the vortex by both gravitational settling of the PSC particles during the coldest segment of winter and the general subsidence of air induced by the mean diabatic circulation. These low values of optical depth are maintained until the vortex breaks up, usually about November, when increases are observed as the aerosol from lower latitudes moves into these higher latitudes. This period of low optical depth agrees well with the observed low total ozone at similar latitudes. (M. P. McCormick, 2065)

### Polar Stratospheric Clouds and Antarctic Ozone Hole

One of the most controversial and important topics in atmospheric sciences today is the dramatic decrease in stratospheric ozone observed in Antarctica during recent Southern Hemisphere spring seasons (September and October). Although other theories have been proposed for the development of this "ozone hole," many scientists feel that man-made chlorofluorocarbons (CFC's) are involved. These CFC's release halogen atoms and molecules when dissociated by sunlight in the springtime Antarctic stratosphere; the halogens, in turn, can catalytically destroy ozone if the supply of gaseous odd nitrogen ( $\text{NO}_x$ ) compounds is insufficient to retard the catalytic cycles. It has recently been suggested in the literature that a large fraction of the gaseous  $\text{NO}_x$  supply may be removed (in the form of nitric acid,  $\text{HNO}_3$ ) from the Antarctic stratosphere by the formation of polar stratospheric clouds, which have been identified as recurring Antarctic phenomena through measurements by the orbiting Stratospheric Aerosol Measurement II sensor.

A new theoretical model of polar stratospheric cloud formation and growth which incorporates a stage of  $\text{HNO}_3$  vapor deposition has been developed. Recent calculations tailored to the altitude regime in which the Antarctic ozone depletion is observed to be the most severe (near 17 km) suggest that up to 80 percent of the ambient  $\text{HNO}_3$  vapor (and 30 percent of the ambient  $\text{H}_2\text{O}$  vapor) may be consumed by polar stratospheric cloud formation if the temperature should fall to 189 K. More importantly, the cloud particles may grow to a radius of 4 to 5  $\mu\text{m}$  and then fall quickly from the region in which they were formed, thereby depleting the formation region of gaseous  $\text{NO}_x$ .

(L. R. Poole, 2065)



*Depletion of  $\text{HNO}_3$  and  $\text{H}_2\text{O}$  vapor supplies by formation of Antarctic polar stratospheric clouds.*

### Evaluation of Optical Disk System for Archiving Data From Earth Radiation Budget Experiment

The Earth Radiation Budget Experiment (ERBE) is a three-satellite experiment designed to

monitor the Earth's radiation budget. The first satellite was launched on October 5, 1984, by the Space Shuttle *Challenger*. The second and third satellites were launched by the National Oceanic and Atmospheric Administration on December 12, 1984 and September 17, 1986. The data from these satellites are being reduced into science data products at Langley Research Center. Approximately 40 magnetic tapes are needed to store the data from each satellite. After validation by the ERBE science team, the data products will be archived for use by the scientific community.

An optical disk system is being evaluated for storing ERBE archival data. One month of ERBE data can be stored on a single optical disk, which is considerably more compact than the 120 magnetic tapes. Each 12-in-diameter "write-once, read-many" platter stores 1 gigabyte of digital data on each side. Optical disks have an expected lifetime of 10 years with no maintenance requirement, while magnetic tapes have to be retensioned and copied to new tapes every 2 years. This archival technique promises to substantially reduce the cost and logistical problems associated with distributing large volumes of satellite data.

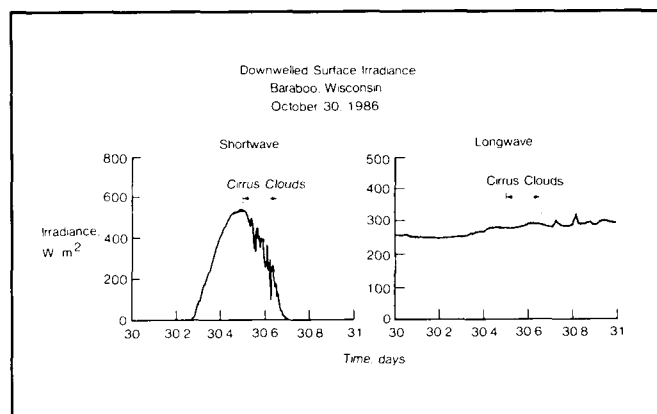
(Michelle T. Ferebee, 3431)

## Surface Radiation Measurements for Satellite Algorithm Studies

NASA has recently established an SRB (Surface Radiation Budget) Satellite Data Analysis Project at Langley Research Center. Objectives are to plan and implement algorithm intercomparison and validation studies prior to computing a global, long-term data set. The strategy is to conduct ground-based experiments to establish data sets for satellite algorithm validation studies. Satellite data are available from operational systems and special experiments such as the Earth Radiation Budget Experiment. Surface measurements are needed for a variety of climatologically important land and ocean areas; however, with the exception of shortwave measurements for some mid-latitude land areas, these measurements are virtually nonexistent.

A major experiment of the SRB Satellite Data Analysis Project was completed this year. This month-long campaign was conducted in cooperation with the FIRE (First International Satellite Cloud Climatology Project Regional Experiment) cirrus cloud experiment in Wisconsin. The SRB measurements were conducted at 18 ground sites, and aircraft observations were made for calibration of satellite measurements. The figure gives an example of results showing the effect of cirrus clouds on the radiation fluxes that hit the Earth's surface. The large shortwave and small longwave changes agree with effects predicted by models. The experimental results are providing the basis for improvements to satellite algorithms for deriving surface radiation fluxes.

(Charles H. Whitlock, 2977)



*Effect of cirrus clouds on shortwave and longwave radiation fluxes at Earth's surface.*

## Infrared Radiation Studies From Nimbus Satellite Data Sets

Two atlases that contain global contour maps of monthly mean outgoing longwave radiation in addition to associated spherical harmonic coefficients have recently been published. The first atlas contains continuous data for 3 years from July 1975 to June 1978 from the wide field-of-view sensor on the Earth Radiation Budget (ERB) experiment onboard the Nimbus 6 satellite. The second atlas contains

continuous data for 7 years from November 1978 to October 1985 from the ERB experiment onboard the Nimbus 7 satellite. Together these two atlases give a data set covering a 10-year time period and will be very valuable in studying different aspects of our changing climate over monthly, annual, and inter-annual scales in the time domain and over regional, zonal, and global scales in the spatial domain.

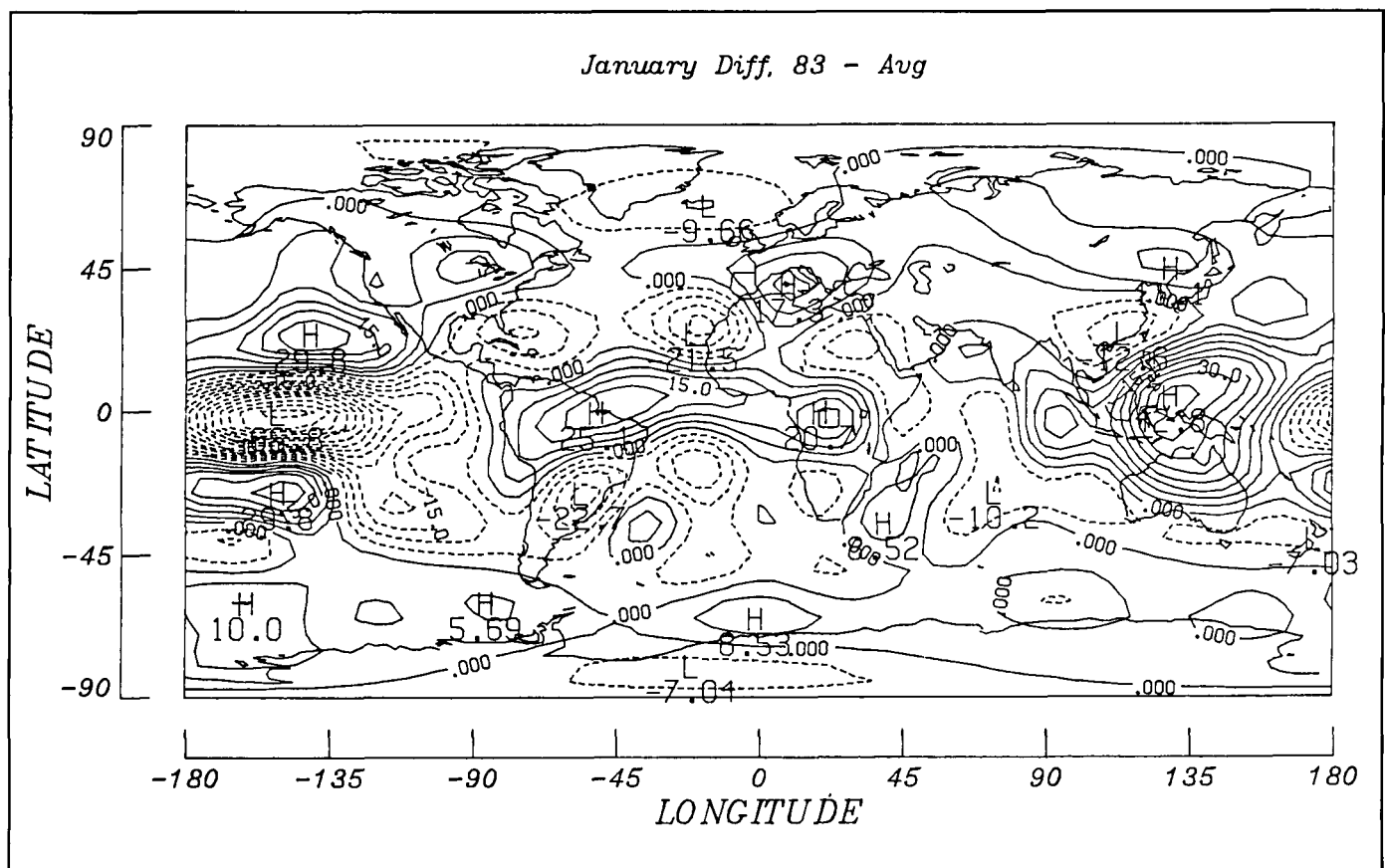
The figure shows a contour map of the change in regional longwave radiation of January 1983 from the 7-year averaged January data as derived from Nimbus 7 measurements. Low areas of outgoing radiation caused by large amounts of cloudiness are denoted by dashed contours. High areas of outgoing radiation are denoted by solid contours. A prominent low of  $-66 \text{ W/m}^2$  in the equatorial region of the western Pacific was caused by the 1983 El Niño event, which peaked in January of 1983. At the same time,

a prominent high region of radiation was evident over Indonesia. For normal conditions (years with no El Niño event), these two regions of high and low radiation would be reversed.

(T. D. Bess, 2977)

### Clouds, Radiation, and Atmospheric Energy

Clouds change the Sun's radiation that is absorbed by the Earth's atmosphere and surface and that the Earth's surface and atmosphere emit into space. A method has been developed and implemented to evaluate the effects of these radiation



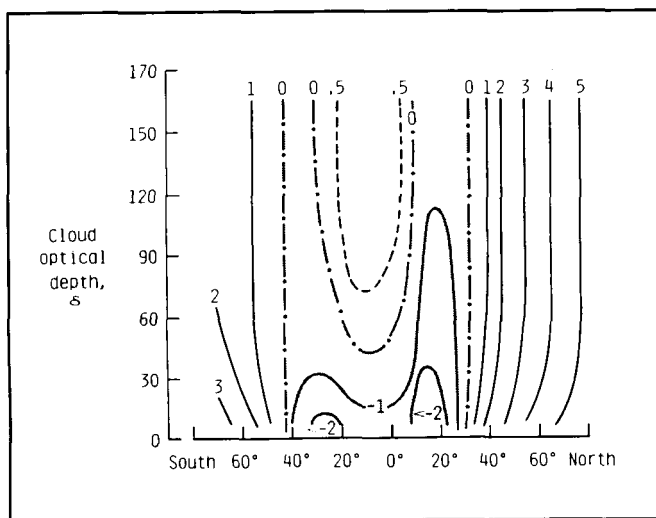
*Change in regional longwave radiation.*



changes on the available potential energy (APE) of the atmosphere. Computations have been performed using a detailed radiative transfer computer code and statistics for clouds. The APE is important in understanding the interaction of energy-releasing and dissipating processes, such as radiation, with the dynamics of the atmosphere. Computations were done for January zonal mean atmospheric conditions.

The effects of clouds in cooling and heating the atmosphere have been found as a function of cloud top height, optical thickness, and latitude. The effects of low clouds on APE are shown in the figure. In terms of the effects of clouds on the general circulation, the globe can be divided into two regimes. One regime is the belt between 40°S and 30°N (i.e., the Tropics and subtropics). The other regime is the remainder of the Earth. In the Tropics and subtropics, a change in optical thickness will significantly contribute to APE, thus intensifying the Hadley circulation and thereby linking tropical sea surface temperature to changes in extratropical circulation.

A mechanism is described whereby the interaction of clouds with radiation produces a strong feedback effect on the development of sea surface temperature anomalies in the tropical oceans (as during an El Niño event). Changes in the cloud pattern over the east Pacific Ocean during the onset of an El Niño



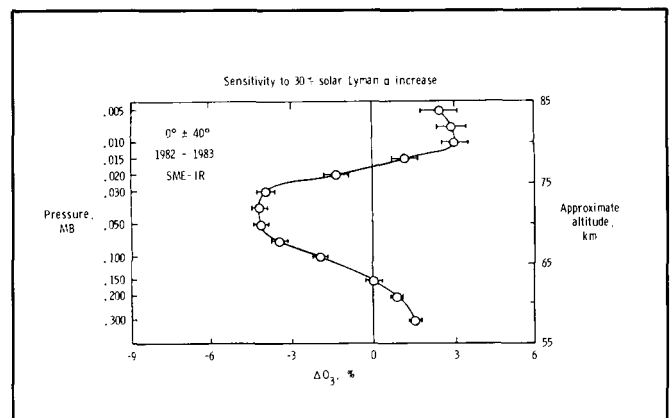
*Effect of clouds on zonal available potential energy due to radiation.*

event result in a strong increase in radiative heating at least as large as the latent heat release.

(G. Louis Smith, 1977)

## Detection of Ozone Depletion Via Solar Lyman Alpha Radiation

A study of 3 years of ozone measurements from the Solar Mesosphere Explorer (SME) satellite's 1.27  $\mu\text{m}$  experiment has resulted in the detection of the response of mesospheric ozone to solar variations. The study was conducted relating short-term variations in solar Lyman alpha  $L\alpha$  radiation (121.6 nm) to short-term ozone variations. Over the 27-day solar rotation period, the solar  $L\alpha$  variations were found to be as large as 30 percent. In order to achieve the precision necessary to detect the corresponding ozone response, a large amount of ozone data from low and mid latitudes was combined. Shown in the figure is the ozone response to 30 percent solar  $L\alpha$  variations as a function of pressure and altitude. A strong ozone depletion is observed which maximizes near a 70-km altitude.



*Mean mesospheric ozone response to short-term solar ultraviolet variability.*

This depletion is thought to result from solar  $L\alpha$  radiation photodissociating water vapor near 70 km, with the resulting  $\text{HO}_x$  acting as a catalyst for the

destruction of ozone. This systematic destruction of mesospheric ozone by  $\text{HO}_x$  has been hypothesized, but the ozone depletion via solar  $L\alpha$  had not been previously detected. This finding should provide a stringent test of  $\text{HO}_x/\text{O}_x$  chemistry in the middle atmosphere which is crucial to understanding the Earth's ozone budget. Once the  $\text{HO}_x/\text{O}_x$  chemistry is validated, a study of the ozone depletion as a function of latitude and season may allow a mesospheric water vapor climatology to be formulated.

(Gerald M. Keating, 2084)

### Electronic Data Base for Stratospheric Trace Gases

Rapid, effective access to the increasing volume of information on stratospheric trace gas concentrations is an important factor in advancing our knowledge of the Earth's atmosphere and its potential for change. These data originate from diverse sources, including both measurements and model calculations, and are found in a variety of locations and in a wide range of formats. The ability to easily obtain and use a wide range of such data sets is recognized as a key element in addressing many of the issues in stratospheric research.

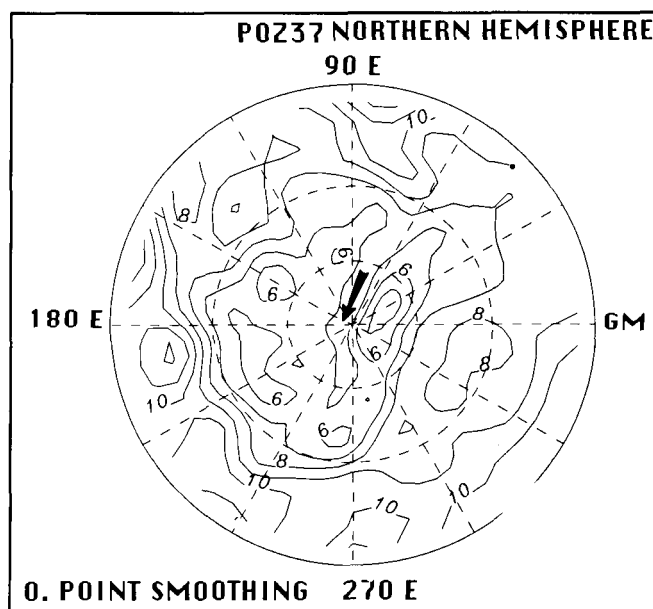
A pilot electronic data base, the Upper Atmosphere Data Pilot (UADP), has been implemented at Langley Research Center to provide the research community with easy access to data on stratospheric trace gases. The prototype system, now operational on a dedicated VAX 8200 computer, incorporates measurements from several major satellite experiments and from individual balloon experiments along with calculations from two-dimensional atmospheric models. Capabilities for browsing, retrieving, and displaying data are provided. A user can access the UADP from a remote site over normal telephone lines, via Telenet, or over the Space Physics Analysis Network (SPAN). During 1987, the UADP was used to support a two-dimensional intercomparison workshop. Utilizing a specialized set of model calculations from five two-dimensional modeling groups, the abilities to easily intercompare specific outputs from the various models and to access data from the workshop site were successfully demonstrated. As

the data sets in the UADP grow with the addition of further available satellite and balloon measurements and model results, it will provide an increasingly effective tool for research and for periodic assessment and intercomparison efforts.

(Robert K. Seals, Jr., 2576)

### Middle Atmosphere Modeling Dynamics and Transport Processes

During the last decade and a half, the potential for ozone depletion in the stratosphere as a result of aircraft emissions, halocarbons, fertilizers, and various other chemicals has stimulated the requirement to understand the complex processes that determine the spatial and temporal distribution of ozone and



*Simulated ozone mixing ratio (parts per million by volume) on the 10 millibar pressure surface ( $\approx 30\text{ km}$  altitude) of the Northern Hemisphere for model day February 7. The outermost circle is the Equator, and the dashed inner circles correspond to  $30^\circ\text{ N}$  and  $60^\circ\text{ N}$ , respectively.*

other important trace constituents in the Earth's atmosphere. A three-dimensional atmospheric circulation and transport model that incorporates comprehensive chemistry has been developed at Langley Research Center to simulate the distribution of constituents from the surface to a 60-km altitude. Comparisons of simulated distributions with data from satellite experiments demonstrate good agreement. The model has been particularly successful in simulating the transport of ozone during highly disturbed conditions such as during mid-winter stratospheric warmings. Of particular interest are the incursions or "tongues" (denoted by the bold arrow in the figure) of ozone-rich air parcels from lower latitudes into the polar cap region associated with a strong cross-polar jet and a displaced polar vortex during the warming event.

The simulation exhibits erosion of the vortex and irreversible mixing consistent with the concept of wave-breaking inferred from satellite data. The model has also successfully simulated the observed evolution of the high-latitude spring maximum in total column ozone. Applications of the model will be focused on Upper Atmosphere Research Satellite model/data interaction studies.

(William L. Grose, 4788)

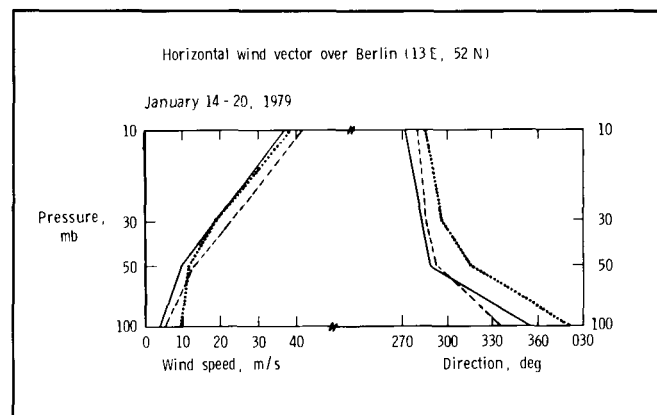
### Validation of Stratospheric Satellite Wind Analyses

The traditional approach to determine horizontal winds in observational studies of stratospheric dynamics is to utilize the geostrophic equation, which represents a balance between horizontal pressure gradient and Coriolis forces. Geostrophic winds can be calculated using layer thicknesses derived from satellite temperature soundings; these thicknesses in turn are added to the height of a radiosonde reference-level pressure surface ( $\approx 100$  mb). Model simulations have recently suggested that nongeostrophic wind components may exert a substantial influence on the winter polar night jet.

This hypothesis has been examined using geopotential height data from the Nimbus 7 LIMS (Limb Infrared Monitor of the Stratosphere) experiment.

Iterative solutions of the nonlinear balance equation were obtained with a successive under-relaxation procedure applied to a  $4^\circ \times 10^\circ$  latitude-longitude grid at 18 pressure levels (100 to 0.05 mbar). Spatial smoothing and enforcement of the appropriate ellipticity criterion for the LIMS height analyses were required to achieve satisfactory convergence of the numerical solutions. The figure compares LIMS geostrophic and nonlinear balanced winds versus Berlin radiosonde measurements for January 14 to 20, 1979. The satellite and radiosonde wind profiles exhibit generally close qualitative agreement, both in terms of vertical wind shear in wind strength and in the variation of wind direction with decreasing pressure. The balanced wind formulation appears to provide more accurate wind direction. These inter-comparisons underline the usefulness of the satellite-derived wind analyses for application in stratospheric transport and dynamics investigations.

(Thomas Miles, 2218)



Comparison of horizontal windflow over Berlin ( $13^\circ$  E,  $52^\circ$  N) between radiosonde (solid lines), LIMS geostrophic (dotted lines), and balanced analysis (dashed lines).

### Launch Vehicle Architecture Study

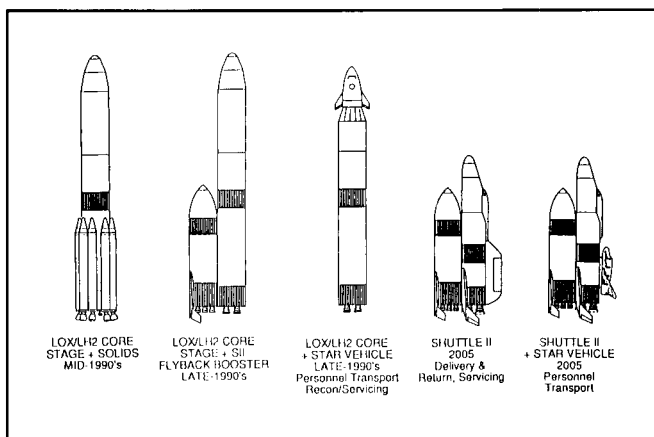
Expansion of man's activities into space over the next several decades will require routine, low-cost,

reliable space transportation. In the future, a multivehicle approach will be used in which unmanned cargo vehicles deliver heavy payloads to orbit, and small manned vehicles perform the man-critical missions. The challenge is to develop a set of vehicles, or architecture, which is not only effective from a life-cycle cost viewpoint but can also enhance this nation's launch capabilities in a timely manner.

The Langley Research Center Shuttle II study has examined characteristics and technologies associated with a future-generation manned launch system. Assuming that a development cycle will be initiated in the early 1990's and there will be evolutionary technology advancements, a two-stage vertical takeoff rocket system has been selected for further in-depth studies. This concept, with its unmanned booster element, lends itself well to the multivehicle phased-approach architecture shown in the figure.

year 2005 and carry payloads in easily processed canisters. For passenger transport, the interim manned vehicle would replace the canisters and provide the added advantage of an independent launch escape capability.

(T. A. Talay, 2768)

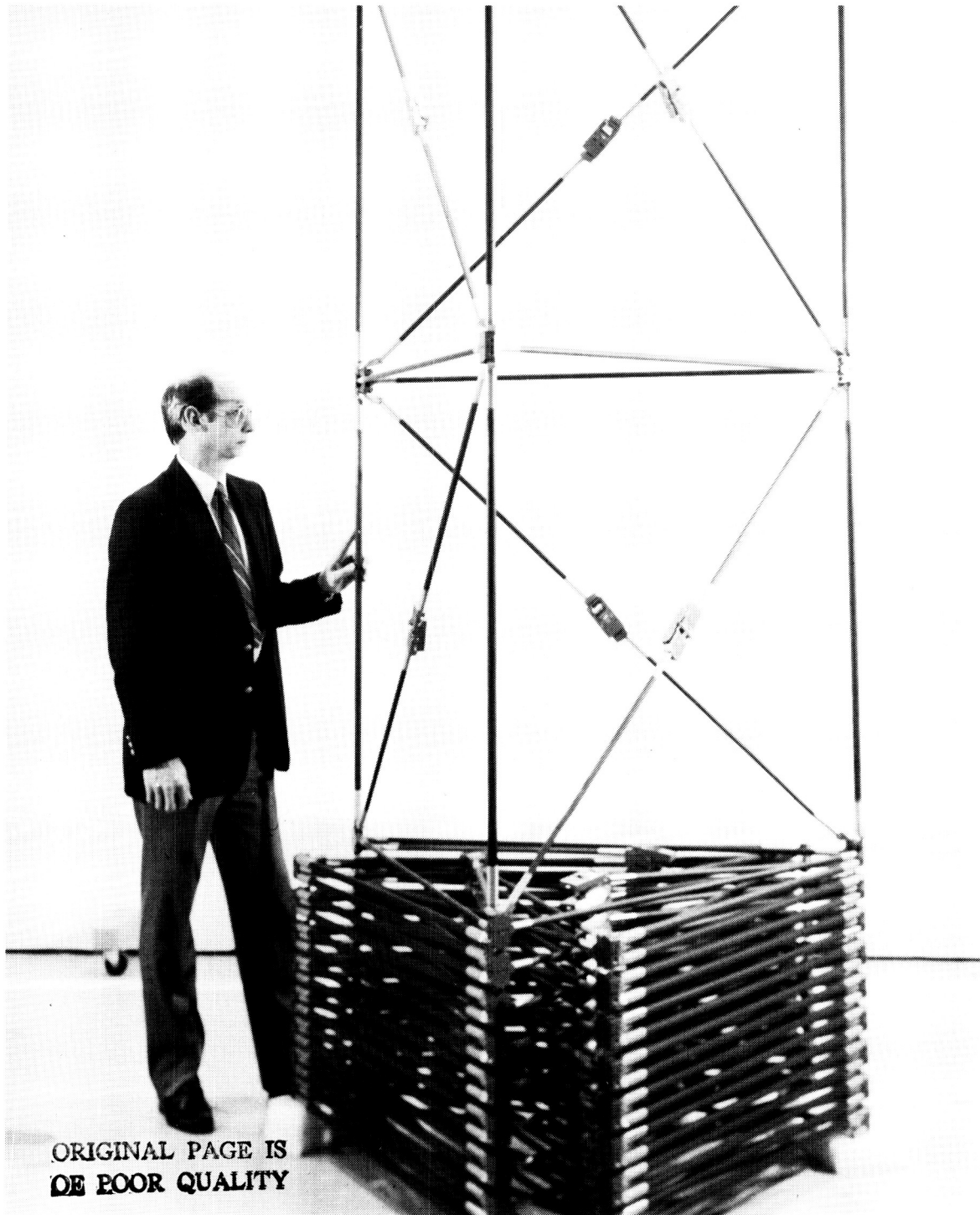


*Space transportation architecture phased approach.*

Under study is a liquid hydrogen (LH<sub>2</sub>)/liquid oxygen (LOX) propelled core stage which when combined with solid rocket augmentation can lift payloads of up to 100,000 lb into orbit. Later incorporation of the Shuttle II glideback booster element, using methane propulsion, increases the core-stage lift capacity to 150,000 lb and reduces launch costs. Manned access to space in the early years of the Space Station is assured with a small, interim manned vehicle that complements the Space Shuttle and is also flown on the core stage. The fully reusable Shuttle II orbiter would become available around the

# Structures Directorate

---



ORIGINAL PAGE IS  
OF POOR QUALITY

The Structures Directorate conducts basic research and develops technology in the areas of advanced aerospace materials and structures, structural loading and aeroelasticity, noise generation by aircraft propulsion systems and structures, and methodologies for interdisciplinary design and optimization. This technology development is directed toward reduction in both weight and cost of aircraft and space structures along with an increase in their reliability and service life. The technology developed also provides improved design capability through more accurate prediction of aerostructural loads, vibration, and noise.

The Materials Division conducts research on advanced materials and their application to aircraft and space structures. The division also develops novel polymeric, metallic, and carbon-carbon materials for these applications. The materials processing and fabrication sciences are developed, and the application of materials to specific flight and space structures is demonstrated. The division conducts research on thermal protection materials and hot structure systems for application to hypersonic and transatmospheric vehicles. The fatigue and fracture behavior of materials is studied in specialized laboratories to provide practical methods for insuring structural integrity. Specialized facilities are also used to study the behavior of materials under extreme conditions of high and low temperature, pressure or vacuum, and electron radiation.

The Structures and Dynamics Division conducts research on structures for advanced aircraft, space vehicles, and the Space Station. Analytical methods are developed for the prediction of static and dynamic stresses and strains in complex structures. Research is conducted on space structures to characterize and control dynamic response. Specialized facilities are used to study the dynamics of aircraft under simulated landing and crash conditions. The division develops new structural systems for aircraft and space structures and is also active in research and development of advanced computational methods for structural analysis and design.

The Loads and Aeroelasticity Division conducts research in aeroelasticity, aerothermal loads, high-temperature structures, unsteady aerodynamic loads, and aeroservoelasticity. Analytical methods are developed for calculating aeroelastic deformations and instabilities, for dynamic, vibratory, and

thermal response of structures, and for the active control of aeroelastic and dynamic behavior of aircraft. Unique facilities are employed in experimental studies of unsteady aerodynamics, aeroelastic behavior, and aerothermodynamic flows.

The Acoustics Division conducts research on the generation and propagation of aircraft noise and seeks to understand the relationships between unsteady aerodynamics, structural dynamics, and noise generation by the interaction of fluids with solid surfaces. This research is directed toward predicting and reducing the noise from helicopter rotors, conventional and advanced aircraft propellers, and turbofan engines. Research is conducted on the propagation of noise from its source through the atmosphere and through aircraft structures.

The Interdisciplinary Research Office develops methodologies for aircraft and spacecraft design which will provide a means of understanding and quantifying interactions among multiple engineering disciplines. The goal is to control and exploit these interactions for improved vehicle performance and increased efficiency of the design process. This research has focused on the development of algorithms and techniques for integrating strength and stiffness designs of large-aspect-ratio wing transport aircraft and of rotorcraft. The methodology has been developed for the optimization of space antenna dish shapes subjected to thermal loadings. Controls, structures, and structural dynamics have been integrated for use in the design of Space Station type structures.

### **Thermally Induced Twist in Composite Tubes**

Composite tubes will be the primary building elements for the Space Station because of their high-specific stiffness and low coefficient of thermal expansion. The dilatation and stress state of the tubular elements during the thermal cycles that are typical of Earth-orbiting spacecraft will be critical to the performance of the Space Station.

A study of the thermal distortion of a candidate composite tube that was subjected to thermal

cycles typical of those of the Space Station has been conducted. Composite tubes, which were made of P75/ERLX1962A graphite/epoxy, had symmetric-balanced, symmetric, and asymmetric wall construction that was approximately 70-mil thick and 2 in. in diameter. These tubes were subjected to thermal cycling from  $-200^{\circ}\text{F}$  to  $200^{\circ}\text{F}$ , and all of the tubes exhibited unexpected measurable twist due to temperature change. This twisting is caused by the difference in the radial positions of off-axis layers which resulted in a moment about the tube axis. Thermal shear strain typical of the tubes with asymmetric wall construction is shown in the figure. The experimental results are in good agreement with a generalized plane strain elasticity analysis, with temperature-dependent material properties.

Both the symmetric and asymmetric tubes had approximately the same amount of twist; however, the magnitude of the twist for the symmetric-balanced tube was very small compared to that of the other tube configurations. Twisting such as this can have serious consequences if the tube is part of a high-precision structure. In long (23-ft) unbalanced tubes, when the temperature change is large ( $600^{\circ}\text{F}$  from stress-free state), the rotation of one end relative to the other can be significant (approximately  $10^{\circ}$  to  $12^{\circ}$ ). Over a long service life, thermal fatigue could be detrimental to a structure. This twisting

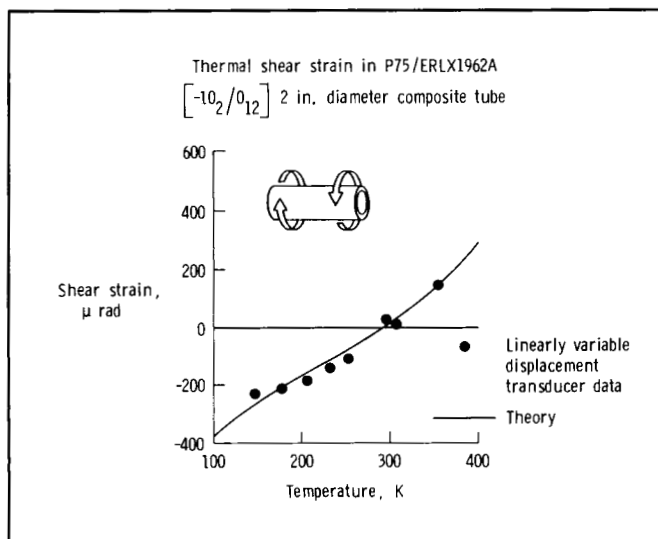
could introduce torsional loads into a structure that was not designed for such loads; however, symmetric-balanced fiber layups will avoid such consequences.

(S. S. Tompkins, 4558)

## Impact Response of Composite Fuselage Frames

Composite materials are presently being investigated as the primary structural material for the next generation of aircraft. The impact properties of composite materials are more complex than metallic materials, and a program has been initiated at NASA Langley Research Center to address the behavior of composite aircraft structures under crash conditions. Structural subcomponent tests are presently being conducted. These tests allow detailed experimental and analytical studies of the substructural behavior under more controlled conditions than are possible in complete aircraft tests. As part of this investigation, circular 6-ft-diameter graphite/epoxy fuselage frames were statically and dynamically tested to failure. These frames have the same cross-sectional dimensions as typical transport aircraft frames but only half the radius. In a crash, the skin and longerons restrict twisting and out-of-plane bending of the frames. This effect was simulated in both static and dynamic tests by sandwiching the frame between a front Plexiglas plate and a rear backstop. The basic failures along the circular frame are in the same typical locations as observed in aluminum structures. Additionally, brittle failures as shown in the first figure occur in the composite frames. These failures are undesirable since structural integrity is lost and less energy is absorbed. It is the task of the designer to develop composite structures with maximum energy absorption.

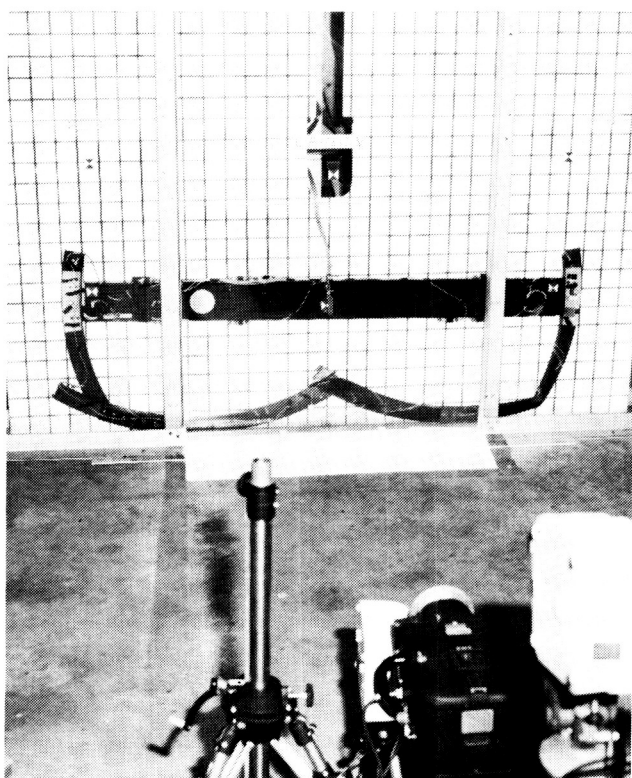
To aid the designer, load and moment distributions in the frame were examined by modeling of the frame with the nonlinear finite-element computer code DYCAST (DYNAMIC Crash Analysis of Structures) developed by Grumman Aerospace Corporation under a NASA Langley Research Center contract. The second figure shows the first 15 ms of the experimental floor-level acceleration of the circular



*Effect of composite tube wall construction on thermally induced twist.*



frame for a 20 ft/s impact and two predictions with the DYCAST computer program. The difference in the two analyses results from the level of constraint applied to the frame in the model. In one case (the in-plane model), frame deformations were constrained to the plane of the frame. In the second case (the free model), the specimen was free to twist and bend out-of-plane. The peak acceleration levels of the experiment and the DYCAST free model agree very well initially. The acceleration in the DYCAST model

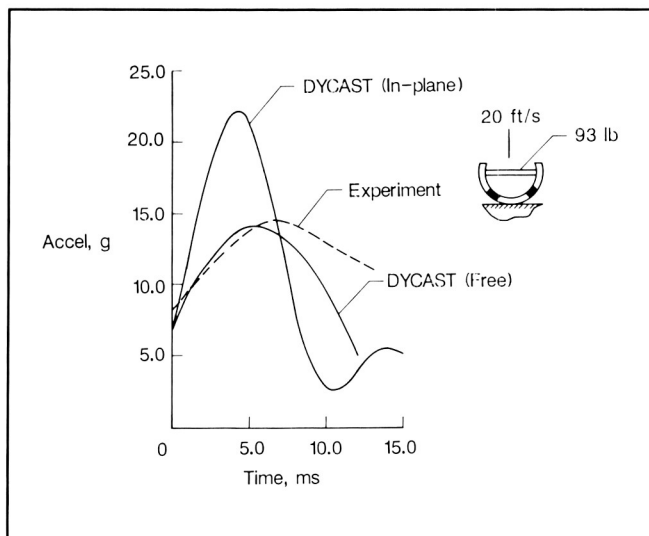


L-86-8236

*Fractured graphite/epoxy frame.*

drops off after the peak value because no lateral support is provided for the specimen. In the actual test an 0.25-in. gap provided clearance between the specimen and test frame. This gap allowed the frame to initially twist and bend out-of-plane before being constrained when contact was finally made with the Plexiglas or backstop. This result emphasizes the importance of boundary conditions in understanding the dynamic behavior of the frame.

(Richard L. Boitnott and Edwin L. Fasanella, 3795)

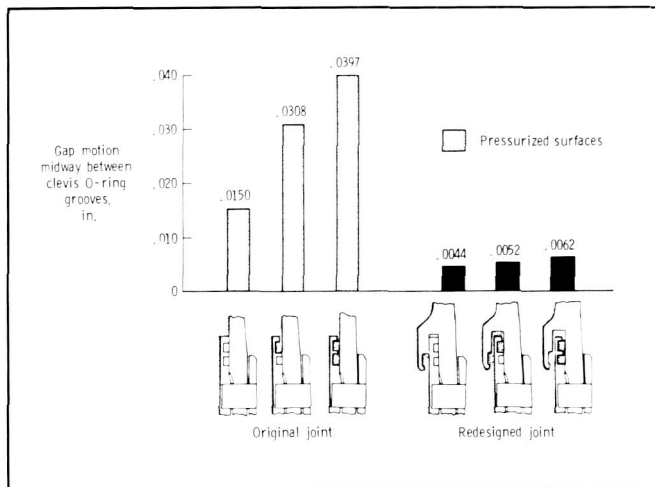
*Composite frame floor acceleration.*

### Structural Response of Redesigned SRM Joint Nearly Insensitive to Pressure Distribution

An understanding of the solid rocket motor (SRM) tang and clevis joint sensitivity to O-ring sealing assumptions was developed by considering characteristic pressure distributions. Detailed three-dimensional-solid finite-element models of a 1° slice of the original and redesigned joints were developed and analyzed using the Ames Cray X-MP/48 computer. A networked computer environment was developed which enabled the use of Langley and Ames computers to perform the parametric studies of the tang-and-clevis joint. This environment allowed large supercomputers to be used for computation as well as small minicomputers to be used for model verification, graphics processing, and output processing to archival media.

Various pressure distributions were considered including that of a factory joint which is completely insulated. Moving from left to right on the figure, the first case is representative of both the original and the redesigned SRM factory joint (joining performed at the factory) for which the internal insulation acts as

the primary seal. For the field joints (joining performed at the launch center facility) using the original tang-and-clevis joint, the case where the primary O-ring does seal and the case where the primary O-ring fails to seal but the secondary O-ring does seal are considered, respectively. The next three cases are for the redesigned SRM joint with an interference fit capture feature. The first case assumes that the O-ring in the capture feature does seal. The next case assumes that the primary O-ring seals, and the final case assumes that the secondary O-ring seals. The results for the original joint indicate that not only is the average gap motion large, but it is also very sensitive to pressure distributions (i.e., performance of the O-rings). However, the redesigned SRM joint is shown to substantially reduce the average gap motion and to be nearly insensitive to pressure distributions.



L-86-11,259

Summary of average gap motions for various sealing assumptions.

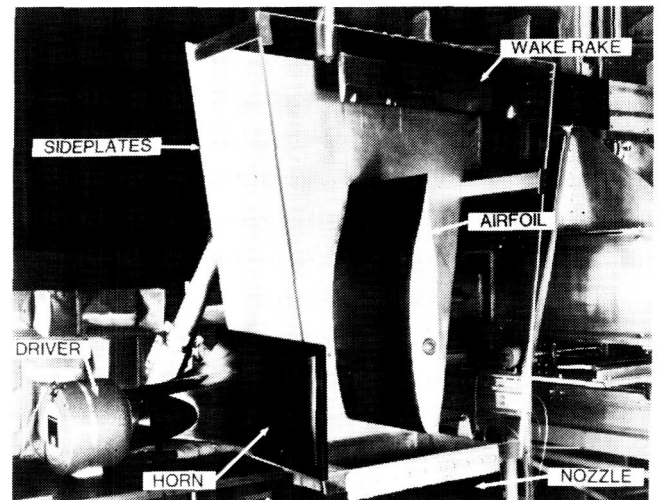
Inclusion of an interference fit capture feature on the SRM field joints will limit the relative motion that can occur between the inner clevis arm and the tang. The redesigned joint will also be nearly insensitive to pressure distributions.

(W. H. Greene, N. F. Knight, Jr., and R. E. Gillian, 4892)

## Acoustic Effects on Airfoil Drag

One of the goals in the airfoil design is to minimize drag, which is affected by the pressure distribution and skin friction on the airfoil. Various physical phenomena will affect skin friction, and one such phenomenon is high-intensity sound.

An extensive in-house program is being conducted to understand the effects of sound on airfoil drag. A two-dimensional natural laminar-flow airfoil (NLF-0414) was subjected to high-intensity sound over a frequency range of 2 to 5 kHz, while it was emersed in a flow of 240 ft/s. Using a wake rake, wake dynamic pressures were determined, and a simple exchange in momentum was used to produce the two-dimensional drag coefficient. The first figure shows the model and sound source, and the second figure shows plots of percent change in drag coefficient as a function of sound pressure level (SPL) at various frequencies. The increase in drag is due to the sound exciting the flow near the airfoil surface causing the existing turbulence to become more intense and increase the skin friction. Fully turbulent airfoils have also been observed to experience a



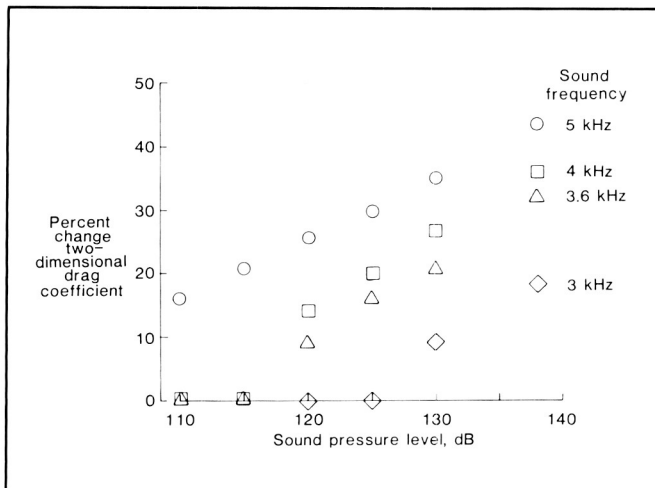
L-02533

Airfoil and sound source.

drag increase under a high-intensity noise environment. Additional drag data will be obtained using a force balance and/or skin friction gauge to validate

this drag change. Measurements of fluctuating surface stresses and local velocity profiles will be made to better understand the physical phenomena.

(John G. Shearin, 4911)



*Percent change in drag coefficient.*

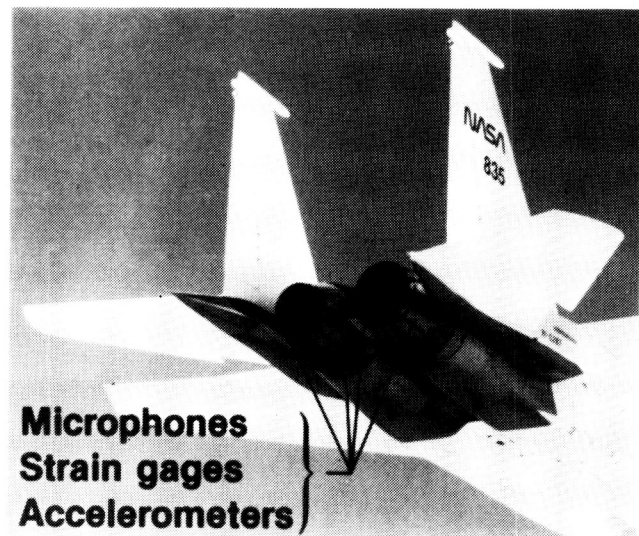
## F-15 Aft End Acoustics

Model-scale acoustic data have shown that high dynamic pressure levels in the inner nozzle region can be associated with supersonic jet plume resonance. These levels are particularly severe when coupling occurs between each plume's large-scale structure. These model results suggested that sonic fatigue of engine nozzle flaps may be due to this phenomenon.

To investigate this possibility, the engine nozzle flaps of the NASA Ames/Dryden F-15 were instrumented to measure dynamic pressure (by using eleven sensors), strain (by using two gauges), and acceleration (by using three transducers). Flap static pressure and temperature were also recorded along with needed engine parameters for the shock noise calculation. Four flights were completed which covered an extensive range of flight Mach numbers and altitudes.

From an initial analysis of the data, pressure fluctuations on the engine nozzle flaps have peak spectral amplitudes near those frequencies predicted for plume resonance. The sample narrowband pressure spectrum shows the agreement between the predicted and measured spectral peaks for an aircraft flight Mach number of 0.86 at 15,000 ft. The corresponding flap response to this load shows that the F-100 engine nozzle flaps have a natural response near 100 Hz. The flap response was found to be highly coherent with the dynamic pressure fluctuations.

(John M. Seiner and James C. Manning, 3094)



*F-15 instrumented for acoustics, accelerations, and structural loads.*

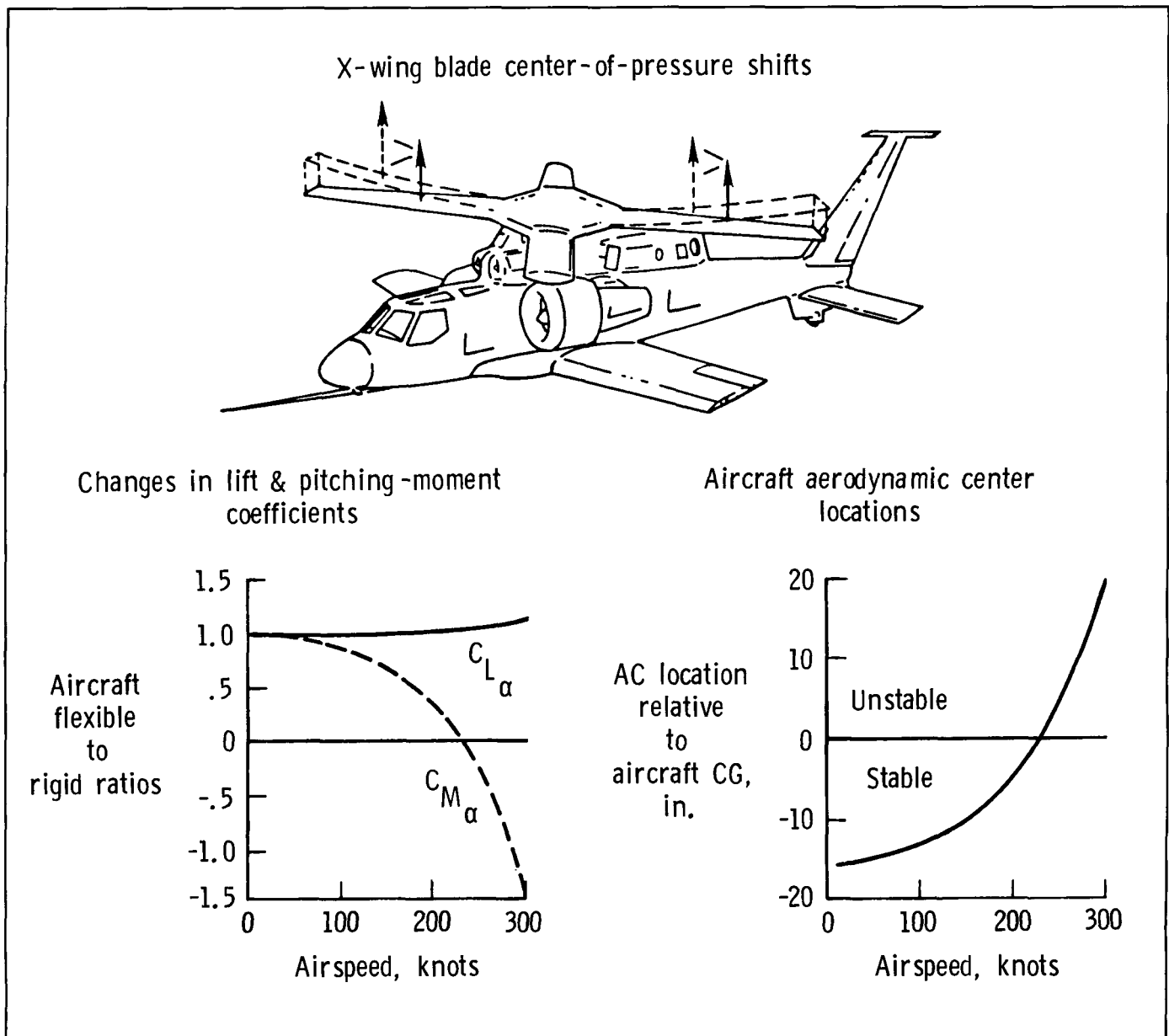
## Changes in RSRA/X-Wing Stopped-Rotor Stability Characteristics Due to Static Aeroelastic Deformation

The Rotor Systems Research Aircraft (RSRA) is being used to test an advanced X-wing rotor system that could lead to high-speed vertical takeoff and landing aircraft designs. An X-wing rotor is a

bearingless four-bladed rotor that is capable of being stopped in flight and configured as two forward-swept and two aft-swept wings.

A mathematical model that describes the longitudinal dynamics of the RSRA/X-wing vehicle in the stopped-rotor no-circulation control blowing configuration was developed and analyzed for changes

in vehicle dynamics due to aeroelastic effects. The Interactions of Structures, Aerodynamics and Controls (ISAC) computer program is the main tool used for these model development and stability studies. Significant changes in aircraft short-period dynamics due to aeroelasticity were found, and the aircraft was predicted to become statically unstable at 230 kn at sea level. The loss of static stability is due to changes



*Aeroelastic effects on RSRA X-wing stability.*

in aircraft lift and pitching-moment coefficients ( $C_{L\alpha}$  and  $C_{M\alpha}$ , respectively) caused by structural deformation. The normalized moment coefficient changed from initially stabilizing to destabilizing at 230 kn, and little change was found in the normalized aircraft lift coefficient as shown on the bottom left of the figure. The moment changes are due to a shift in aerodynamic center (AC) location with respect to the vehicle center of gravity (CG) shown on the bottom right of the figure. This aerodynamic center shift is due to aeroelastic "wash-in" of the forward-swept blades ("wash-in" is the tendency of the local angle of attack to increase with bending deformation) which moves the blade center-of-lift outboard and forward, and the "washout" of the aft-swept blades, which moves the center-of-lift inboard and forward (as shown in the top part of the figure).

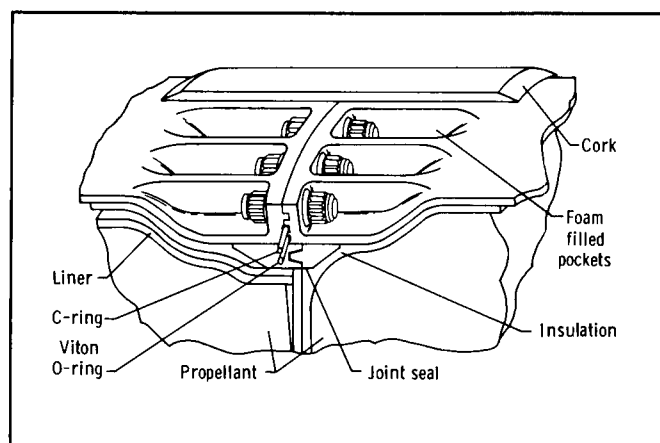
(Michael G. Gilbert, 2388)

a significant weight penalty. A structural optimization procedure has consequently been developed to select the shape for this alternate design. The design requirements included minimization of the joint weight while maintaining the stresses within allowable values and preventing a gap from forming on the inside of the joint at the O-ring seal.

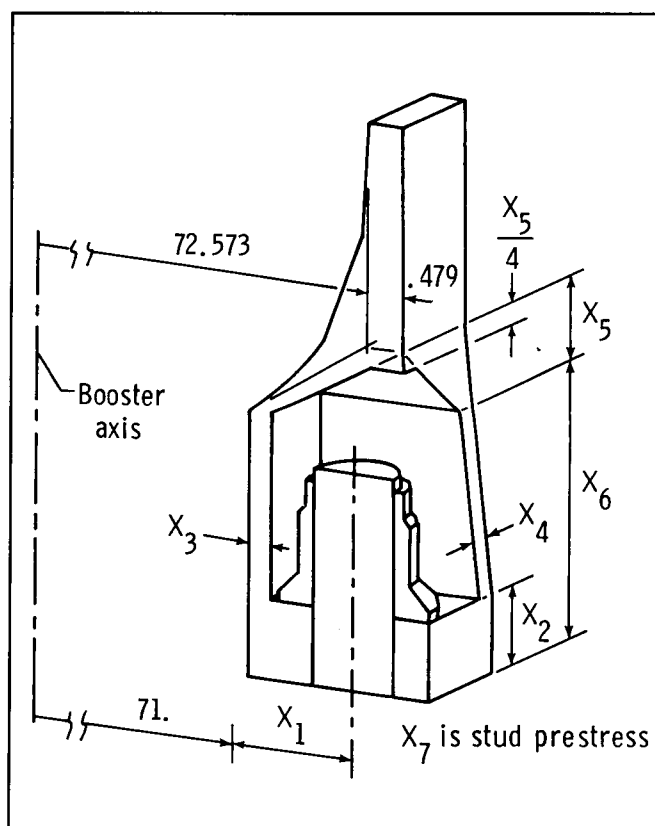
The design model used in this study is described in the second figure. The model was analyzed by conventional finite-element methods. The optimization was conducted using a "usable-feasible" direction nonlinear programming code, and gradient information was generated by a finite-difference procedure. A special-purpose automatic mesh generator was developed to update the finite-element mesh to reflect the changes in the geometry. Also, to speed up the optimization process and thereby multiply the number of design alternatives considered, the proce-

## Shape Optimization of Bolted SRB Field Joint Alternative

In the wake of the January 1986 *Challenger* accident, various alternatives have been proposed for the redesign of the solid rocket booster (SRB) field joints (see also p.135). Researchers at Langley Research Center have proposed a bolted configuration (as shown in the first figure) which is very safe but which has



Bolted joint configuration.



Design model and design variables  $X_i$ .

ture was implemented in parallel on four engineering workstations.

This effort indicates that conventional nonlinear programming techniques can be brought to bear on the challenging problem of shape optimization of complex solid bodies. The study shows that a geometry can be found that insures that the joint remains closed under ignition loads and that the stresses remain within allowable limits, except in localized areas of stress concentration. It is felt that these stresses will be reduced by plastic flow and can be further improved by careful local design. The optimal bolted design is heavier than the original tang-and-clevis concept by 1144 to 2003 lb, depending on the stress constraint formulation. Due to the presence of some areas of three-dimensional stresses, the resulting weight penalty is very sensitive to the stress constraint formulation. Performance analyses indicate that the weight penalty results in a payload penalty on the order of only 114 to 250 lb per joint, depending on the type of trajectory flown.

(J.-F. M. Barthelemy and J. L. Rogers, Jr., 2887)

### Reduction of Blade-Vortex Interaction Noise

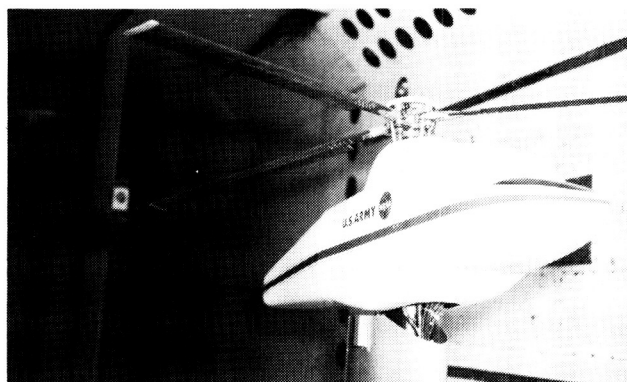
Blade-vortex interaction (BVI) is an intense source of noise which is critical to the acceptability and detectability of a helicopter. A recent in-house analytical study has formulated several concepts for the reduction of this noise source, and these concepts utilize the higher harmonic control (HHC) capability presently under development for reduction of vibratory loads.

A feasibility study of one of these concepts has been carried out in the Transonic Dynamics Tunnel (TDT) utilizing the Aeroelastic Rotor Experimental System (ARES) shown in the first figure. The model employed four untwisted 4.5-ft-radius and 4.24-in-chord blades that rotated at a tip Mach number of 0.628. The second figure displays measured acoustic pressure spectra of the total model noise at a tunnel speed of 52 ft/s and a tip-path-plane (TPP) angle of  $4^\circ$ . In the spectrum labeled "no control," blade-

vortex interaction accounts for the high noise levels at multiples of the blade passage frequency (BPF) in the range 0.3 to 1.2 kHz. To obtain the "control" spectrum, an HHC capability was employed to reduce each blade's pitch angle by only  $1^\circ$  as that blade passed through the region in which BVI was expected. As can be seen, this small control input resulted in a reduction of the BVI noise levels by 3 to 4 dB. Theoretically, greater levels of control would produce even more noise reduction.

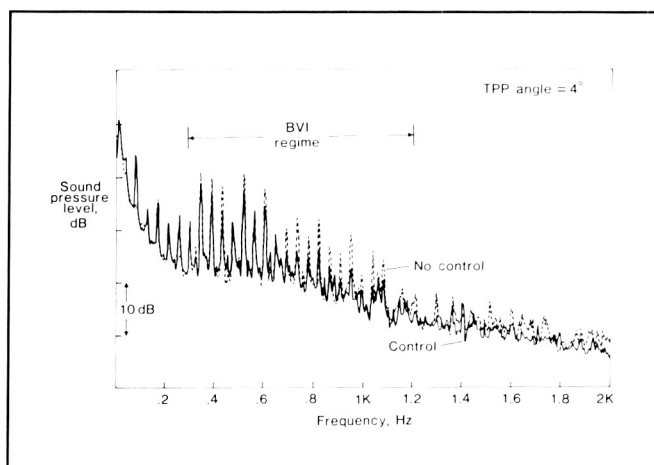
The favorable results of this preliminary proof-of-concept test have justified a comprehensive acoustic evaluation of this and other concepts that utilize HHC for BVI noise reduction. Such a program will be carried out in the TDT in the near future.

(E. R. Booth, Jr. and W. T. Yeager, Jr., 2645)



L-77-7529

*ARES model in TDT.*



L-87-6661

*Effect of HHC on blade-vortex interaction.*

ORIGINAL PAGE IS  
OF POOR QUALITY

## Alleviation of Cavitation in Superplastically Formed 7475 Aluminum Alloy Using Post-Forming Pressure

Superplasticity is the ability of selected metal alloys to undergo large strains (500 to 1000 percent) at elevated temperature prior to localized thinning or fracture. Processes have been developed for superplastically forming complex structural shapes in a single operation and result in significant cost savings compared to forming the same components using conventional means. When some aluminum alloys (such as 7475 aluminum alloy sheet material) are superplastically formed, internal porosity or cavitation is generated due to the metallurgical nature of the alloy.

Methods to suppress or alleviate cavitation in aluminum alloys must be developed to realize the full potential offered by superplastic forming for reducing the cost of aerospace structural components. The figure shows the effects of postforming pressure on cavitation in the 7475 aluminum alloy. Specimens were superplastically formed at a temperature of 960°F using argon gas at a pressure of 100 lb/in<sup>2</sup>. Follow-

ing forming of the sheet material into the tool cavity, the postforming gas pressure was increased and maintained for 1.5 hr. Several levels of postforming pressure were investigated. Following exposure to the prescribed pressure-time profiles, metallurgical specimens were prepared and examined using a light microscope. A comparative image analyzer was used to determine the amount of porosity.

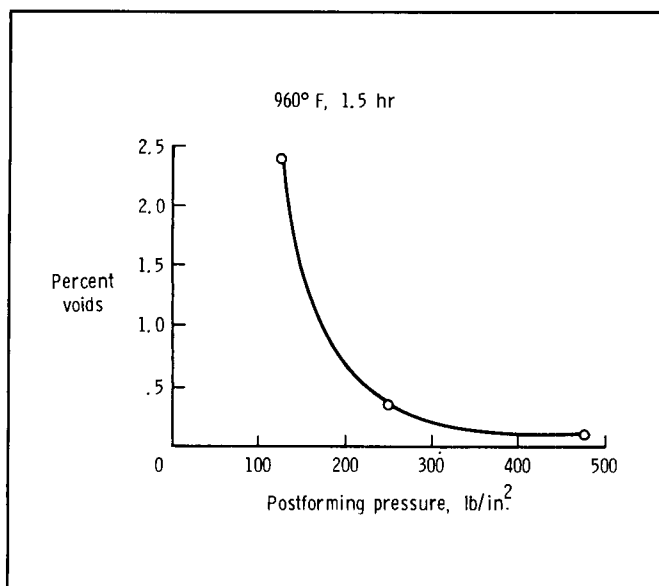
As shown in the figure, the cavitation was reduced from 2.5 percent for specimens subjected to a postforming pressure of 125 lb/in<sup>2</sup> to less than 0.25 percent for specimens exposed to 425 lb/in<sup>2</sup>. Results of this study indicate that postforming pressure can be used to heal cavitation resulting from superplastic forming (SPF). The technique is relatively simple and should extend the maximum forming strains for use in fabricating structural components.

(T. T. Bales, 3405)

## Method of Predicting Energy-Absorption Capability of Composite Subfloor Beams

The next generation of U.S. Army helicopters will be designed using advanced composite materials throughout the aircraft. These helicopters will be designed to stringent crashworthiness requirements. In addition to the landing gear, the subfloor structure will be required to absorb energy. To facilitate the design of energy-absorbing subfloor structures in a manner consistent with conventional structural design practice, a method of predicting the energy-absorption capability of the subfloor structure has been devised.

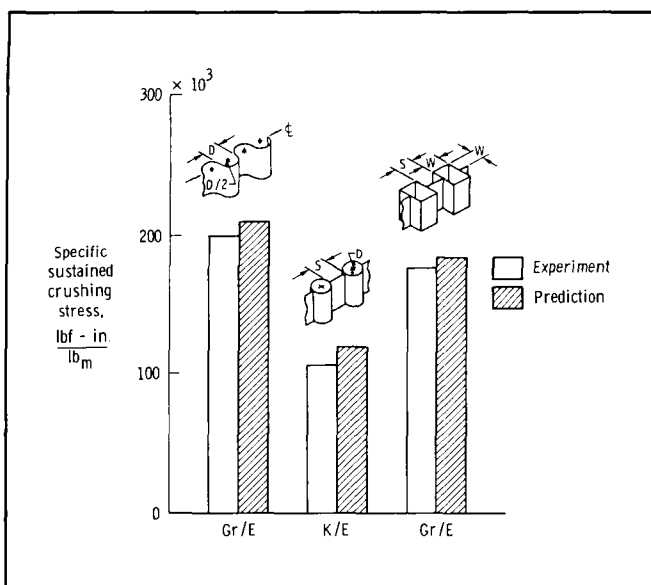
Different types of graphite/epoxy (Gr/E) and Kevlar/epoxy (K/E) stiffened and sine-wave beam subfloor concepts have been experimentally evaluated. Beam geometric parameters investigated were tube diameter  $D$ , distance between stiffeners  $S$ , and width of square cross-section stiffener  $W$ . Through a comprehensive study of the crushing characteristics of composite material, energy-absorbing subfloor beam concepts have been developed which are superior energy absorbers to the comparable metallic beams.



Effect of postforming pressure on cavitation of 7475 aluminum alloy.



Recent test results have shown that the crushing modes of structural composite beams were similar to those of circular and square cross-section tubes of similar composite material and fiber-reinforcement architecture. A hypothesis was formulated for predicting the energy-absorption capability of a structural element. This hypothesis is that the crash energy-absorption capability of a structural element is the sum of the weighted average of the energy-absorption capability of its characteristic elements.



Energy-absorption of composite  $[\pm 45]$  subfloor beam structure.

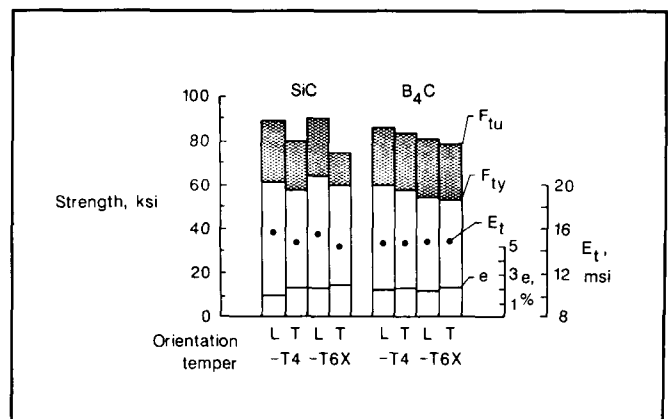
Therefore, if the energy-absorption capabilities are known for composite tubes of different geometries then the energy-absorption capability of a structural element can be predicted. Using this technique the energy-absorption capability of composite sine-wave and stiffened beams was predicted as shown in the figure. Excellent agreement between prediction and experiment was obtained.

(G. L. Farley, 2850)

## Use of $B_4C$ Particulates to Improve Properties in Aluminum Matrix Composites

Aluminum matrix materials reinforced with SiC whiskers have been shown to have properties that make them attractive for a variety of aircraft structural applications. At present, however, the whiskers are relatively expensive, have approximately 15 percent more density than aluminum, and have an aspect ratio sufficiently high (2:1 to 5:1 in final composite form) to result in composites with some anisotropy in properties.

Programs have been initiated to develop other aluminum matrix composites. One of these developments is the boron carbide particulate reinforcement, which has the potential to overcome the shortcomings of Al/SiC. The figure shows the tensile strength  $F_{tu}$ , yield strength  $F_{ty}$ , tensile modulus  $E_t$ , and strain to failure  $e$  of 2124 Al/SiC and 2124 Al/ $B_4C$  composite extrusions for different heat treatments and orientation (with respect to the extrusion direction). Heat treatment has little effect on either composite, whereas the orientation effects are obviously greater for the SiC whiskers than for the  $B_4C$  particulates. In general, the properties of the two composites are about the same. The  $B_4C$ , however, is about 25 percent less dense than the SiC; thus, for the same reinforcement volume fraction, the specific properties (density adjusted) of the  $B_4C$  composite are somewhat better. Because the  $B_4C$  is less costly,



Mechanical properties of 2124 Al/SiC and 2124 Al/ $B_4C$  composite extrusions.

less dense, and results in composites with properties at least as good as SiC whiskers, significant payoffs in terms of structural efficiency and cost may be realized by using the B<sub>4</sub>C reinforcements.

(W. D. Brewer, 4193)

### Three-Dimensional Analysis of Fatigue Crack Closure

All current fatigue crack growth models incorporate a parameter that characterizes the magnitude of the stress field around the crack tip. In the past, the stress intensity factor range was used almost exclusively as the stress field parameter, but in recent years experimental evidence has indicated the need to modify this parameter to account for the effects of crack closure. However, it has only been possible to experimentally evaluate the closure behavior either at the surface of a material or as an "averaged" value for the entire crack front. For thick materials, the closure behavior in the interior may be significantly different from that at the surface.

To provide insight into the closure behavior in the interior of thick plates, a three-dimensional elastic-plastic finite-element code has been written to subject finite-element models to cyclic loads and to simulate fatigue crack growth. As the model is loaded

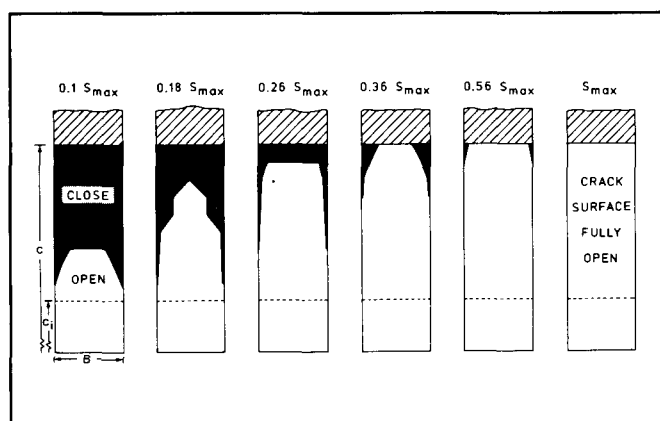
and unloaded, the program computes the stresses and displacements near the crack and identifies the loads at which the crack opens and closes. The figure shows the calculated progression of the opening and closing profiles on the crack surface during the loading portion of a cycle. In the figure, the shaded region indicates areas where the crack is closed,  $C_i$  is the initial crack length,  $C$  is the current crack length, and  $B$  is the material thickness. At a stress of  $0.1 S_{max}$  ( $S_{max}$  equals maximum stress in the cycle), the crack is closed at the crack tip along the entire crack front. At  $0.36 S_{max}$ , the interior is fully open but the exterior layers are still closed. For stresses greater than  $0.56 S_{max}$ , the entire crack is open. This sequence was reversed upon unloading. Based on the computed opening and closing behavior, stress intensity factor ranges can be modified to more accurately represent the conditions at the crack tip.

(J. C. Newman, Jr., 3192)

### Inexpensive Method for Calculating Strain-Energy Release Rate

Structures made of laminated composite materials sometimes contain small delaminated areas. If the delaminated area grows when the structure is subjected to compressive loading, the associated loss of structural stiffness may cause the structure to fail. A promising analysis to determine whether a delamination will grow when subjected to service loads is based on the calculation of a quantity called the strain-energy release rate. The usual method of calculating this quantity for real-world, three-dimensional (3-D) delamination configurations is based on structural parameters that must be determined from a 3-D (solids) elasticity analysis. These 3-D analyses are expensive and limit the use of the strain-energy release rate approach because practical applications require the analysis of numerous potential delamination configurations.

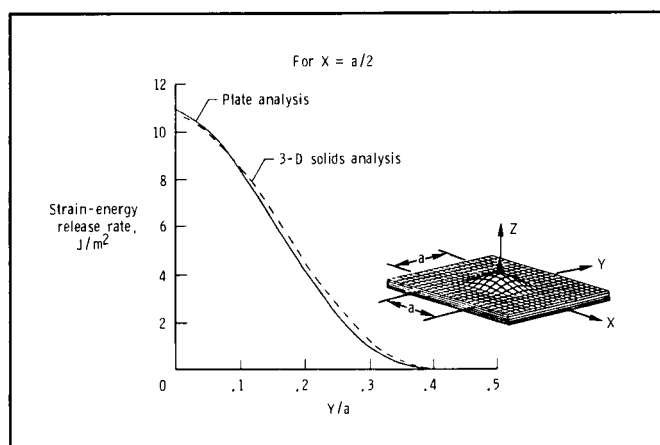
In the current method, information developed from an inexpensive two-dimensional (plate) elasticity solution is used to approximate the parameters needed for the analysis of 3-D delamination configurations. As a check on the accuracy of the current method, the delamination configuration shown in the



Analytically predicted fatigue crack opening sequence during loading cycle.

figure was analyzed by both methods. The delamination is square with a side dimension of  $a$ . The local  $x$ - $y$ - $z$  coordinate system is shown in the figure. The figure shows the distribution of strain-energy release rate for the boundary  $x = a/2$ . The distribution of strain-energy release rate calculated by the inexpensive plate analysis agrees very well with the results from the solids analysis method. The lower cost of the current analysis technique makes the application of the strain-energy release rate approach to delamination growth prediction more practical.

(J. D. Whitcomb, 3046)



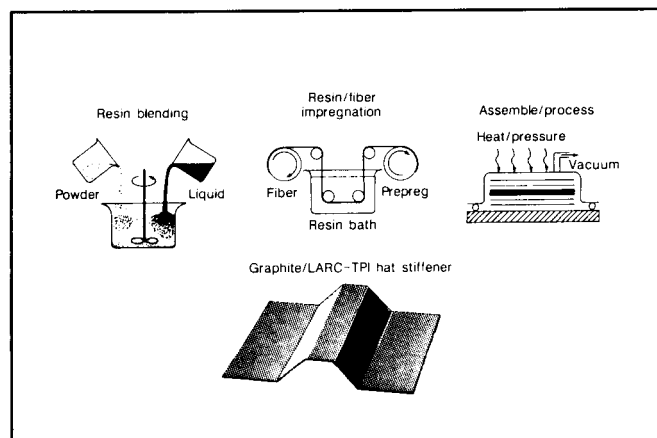
*Distribution of strain-energy release rate at delamination determined by two analyses.*

## Improved Processability of LARC-TPI Composites by Matrix Resin Blending

Advanced polyimide materials currently exhibit excellent toughness, solvent resistance, and thermooxidative stability, but improvement in the flow properties of these materials is required in order to expand their utility as high-performance matrix resins. The addition of low molecular weight semicrystalline LARC-TPI powder to various LARC-TPI precursor solutions has demonstrated a marked improvement in the melt flow properties of this class of thermoplastic polyimides.

Varying percentages of LARC-TPI semicrystalline powder were added to LARC-TPI precursor solutions and created a stable slurry that was utilized as a matrix resin in the fabrication of graphite/LARC-TPI prepreg. The resultant prepreg was thoroughly wet, and the matrix resin was evenly distributed in the fiber bundles. Void-free, well-consolidated laminates and hat stiffener elements were molded from the prepreg by conventional polyimide cure procedures. The mechanical properties of the as-fabricated laminates were superior to the properties of composites fabricated from prepreg made without the semicrystalline powder. Blends of other polyimide compositions, including Langley Research Center's PISO<sub>2</sub>, with LARC-TPI semicrystalline powder have exhibited the same trends of improved prepreg manufacture and composite fabrication.

(Robert M. Baucom, 4197 and Norman J. Johnston, 4198)

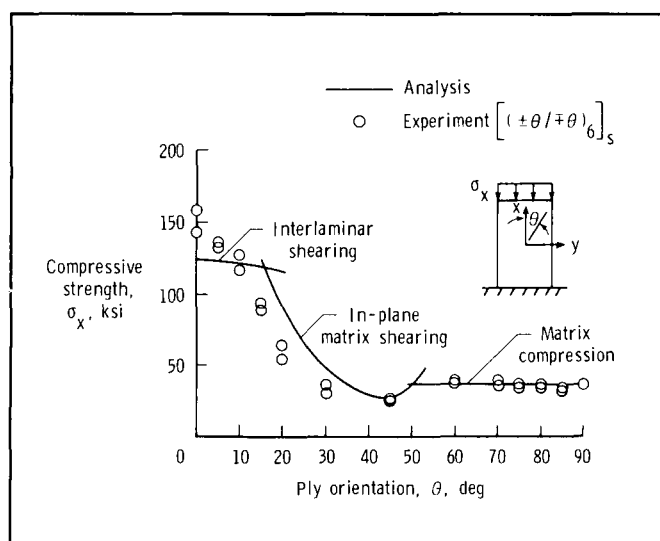


*LARC-TPI fabrication process.*

## General Compressive Strength Theory for Composite Laminates

Efficient designs using composite materials require a thorough understanding of the mechanisms that affect laminate response. Laminate compres-

sive strength is an important design parameter, and researchers have studied the mechanics of this phenomenon for many years. Previous research has focused on specific failure mechanisms and on specific laminates. The present study has developed a general, validated theory that quantifies the dominant mechanisms affecting the compressive strength of a wide range of undamaged composite laminates and has used the theory to predict laminate compressive strength.



Compressive strength of  $[\pm\theta]_s$ -class laminates as a function of ply orientation.

Laminate compressive strength as a function of ply orientation is shown in the figure for  $[\pm\theta]_s$ -class AS4/3502 laminates. The analytical and experimental results from the present study show good agreement. The laminate compressive strength is dominated by three failure mechanisms: interlaminar shearing, in-plane matrix shearing, and matrix compression. The failure stress associated with each failure mechanism is calculated, and the lowest or critical failure stress is referred to as the laminate compressive strength and is plotted on the figure. The theory does not couple the failure mechanisms. The initial waviness of all plies is included in the theory, and an imperfection-amplitude-to-ply-thickness ratio of 0.5 is used as a representative imperfection amplitude that is typical for composite laminates.

Interlaminar shearing caused by initial waviness of the plies initiates laminate failure for  $0^\circ \leq \theta \leq 15^\circ$ . This interlaminar shearing is characterized by laminate brooming and interlaminar cracking. In-plane shearing initiates laminate failure for  $15^\circ \leq \theta \leq 50^\circ$ . This in-plane matrix shearing mode occurs at the fiber-matrix interface and in the epoxy matrix between fibers. Matrix compression initiates laminate failure for  $50^\circ \leq \theta \leq 90^\circ$ . Matrix compression failure is similar to the classic compression failure for isotropic materials. This failure mode is characterized by a failure surface that extends through the material thickness in a plane that is oriented at  $45^\circ$  to the middle surface of the laminate.

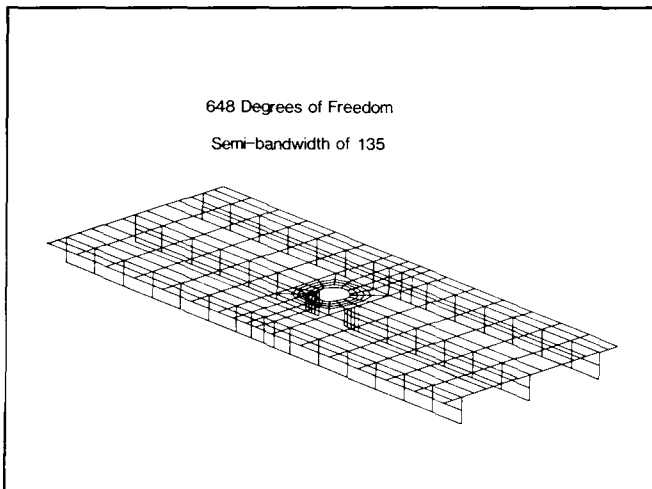
(Mark J. Shuart, 2813)

## Parallel Method for Solving Eigenvalue Problems

Large eigenvalue problems, which include vibration and buckling problems, are a substantial computational burden in structural analysis. A new method has been developed to solve this type of problem on multiprocessor parallel computers, thereby reducing the computational time. The new method is a parallel implementation of the Lanczo's method. The effectiveness of the method has been demonstrated by carrying out a free-vibration analysis of a blade-stiffened graphite/epoxy plate with a circular cutout (shown in the first figure). The analysis time with 16 processors was about one-seventh of the time for one processor.

The basic Lanczo's method involves transforming the original large, general eigenvalue problem into a small problem consisting of a tridiagonal matrix that is easily solved, instead of using the full stiffness matrix. The resulting tridiagonal eigenvalue problem gives eigenvalues that accurately approximate those of interest of the original problem.

The most computationally intensive steps in the process (the decomposition of the stiffness matrix and the forward and backward solution steps) were calculated in parallel on a varying number of processors. The decrease in execution time for the decomposition of the matrix, the solution steps, and the



*Finite-element model of blade-stiffened plate with circular hole.*

Semibandwidth = 135		648 Degrees of Freedom (DOF)				
Calculation Steps	Number of Processors					
	1	2	4	8	16	
Matrix Decomposition	545	275	136	69	47	
Equation Solution	288	153	89	69	61	
Eigenvalue Calculation (Sequential)	34	34	34	34	34	
Total time (seconds)	867	462	259	192	142	

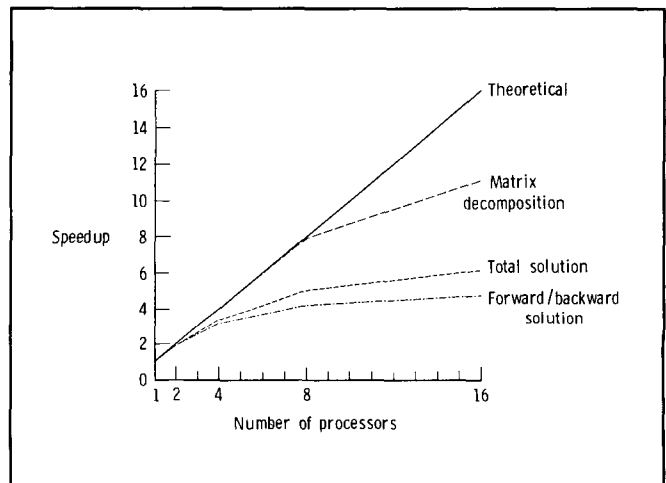
*Time (in seconds) to solve for 10 eigenvalues on up to 16 processors.*

total eigenvalue calculation are shown in the table. The speedups obtained with up to 16 processors are shown in the second figure. The speedups are compared to the theoretical speedup, represented by the solid line, which could only be achieved if all computations were done in parallel and if the workload was exactly balanced.

The time to perform vibration analysis can be significantly reduced by concurrent calculations; however, in order to take advantage of parallel pro-

cessing several factors in addition to available hardware must be considered. Factors to consider include data dependencies inherent in the algorithm, balanced workload among the processors, problem size, and number of calculations that must be done sequentially.

(S. W. Bostic, 3401)



*Speedups obtained on up to 16 processors.*

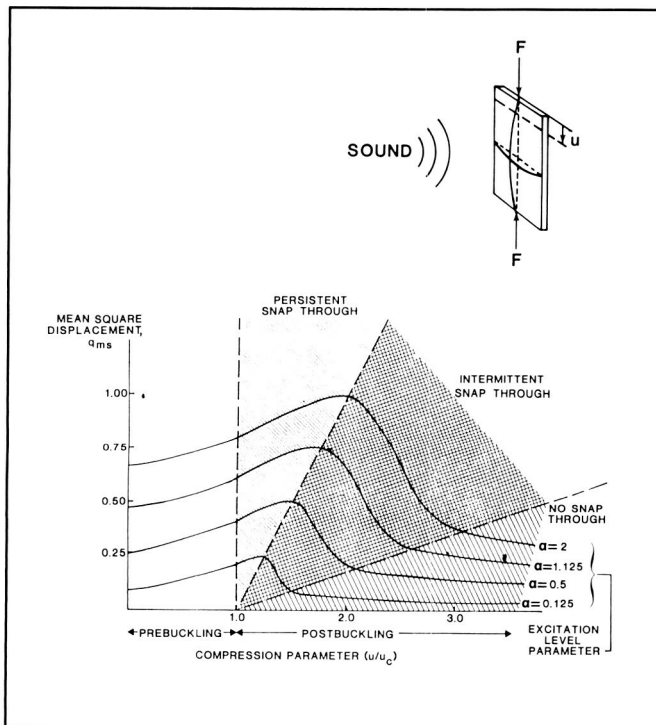
## Response of Buckled Plates to Acoustic Force

Intense acoustic forces can induce fatigue failures in aircraft components such as skin panels. If the panel is curved due to a static buckling load, fatigue can occur in a shorter time if the panel displacement "snaps through" from one static equilibrium position to another. The method of equivalent linearization was used to analyze the "snap-through" behavior of an initially flat panel. This work was done by the second author with support of an NRC resident associateship.

The panel is subjected to a static in-plane compressive force  $F$ , which results in an end shortening  $u$ . When  $u$  reaches the critical value  $u_c$ , the panel buckles into a curved shape. The application

of sound (given by the nondimensional parameter  $\alpha$ ), causes the response  $q_{ms}$ . The response is shown to increase with increasing compression in both the prebuckling and the persistent "snap-through" domains. In the persistent "snap-through" domain, the panel displacement "snaps through" from one static equilibrium position to the other on almost every vibratory cycle. The stresses associated with this motion are calculated to be much higher than those in a flat panel or in the domains where "snap through" does not occur, and they are expected to lead to greatly reduced fatigue lifetimes. As the compression is increased, the curvature becomes so large that the acoustic force is insufficient to cause "snap through" on every cycle (intermittent "snap through"), and finally for very large  $u$  no "snap through" occurs.

(J. S. Mixson and C. F. Ng, 3561)

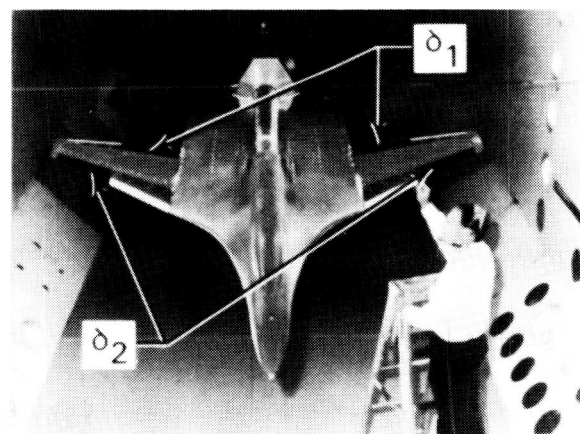


Domains of "snap through."

## Aeroservoelastic Analysis Validated by Wind Tunnel Tests

An aeroelastically tailored wing with active controls was used to test an Active Roll Control (ARC) system. The model, which is shown in the first figure, is aeroelastically scaled with a span of approximately 9 ft and is mounted on a sting in such a manner that the model is free to roll. The model has two leading-edge and two trailing-edge control surfaces on each wing panel. At each test condition the two most effective pairs of control surfaces were chosen for roll control; for the present example these are the trailing-edge inboard pair ( $\delta_1$ ) and the leading-edge outboard pair ( $\delta_2$ ).

Active Roll Control laws were synthesized such that the roll performance of the model and the stability robustness (i.e., gain and phase margins) are constant for all combinations of the feedback parameter  $\kappa$  and input-scaling parameter,  $\kappa_c$ . The quantities that change with  $\kappa$  and  $\kappa_c$  are the deflections of the control surfaces,  $\delta_1$  and  $\delta_2$ . The plot in the second figure presents a comparison of analytical predictions and corresponding experimental results of control surface deflections. Plotted are the values of  $\delta_1$  and  $\delta_2$  which result from applying a given roll-rate command to the model for a constant value of  $\kappa_c$  and several values of  $\kappa$ . The agreement between analysis and experiment is very good.

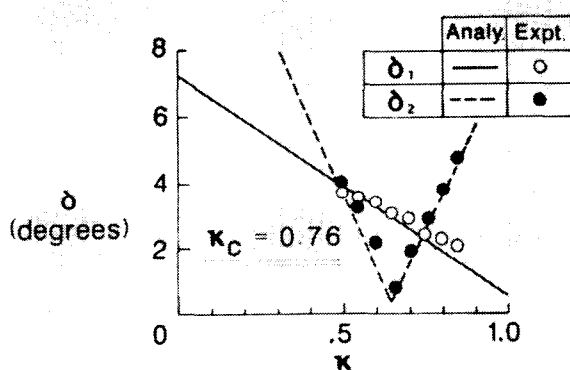


L-87-4671

Active flexible wing model.

Control surface deflection is a measure of the effort required by the control system to perform its function, and this plot (and others like it) allows the engineer to minimize that effort by proper choice of  $\kappa_c$  and  $\kappa$ . In a similar manner, wing loads (shears, bending and torsion moments) during the roll maneuver may be minimized by an alternate choice of  $\kappa_c$  and  $\kappa$ .

(Boyd Perry III, 3323)



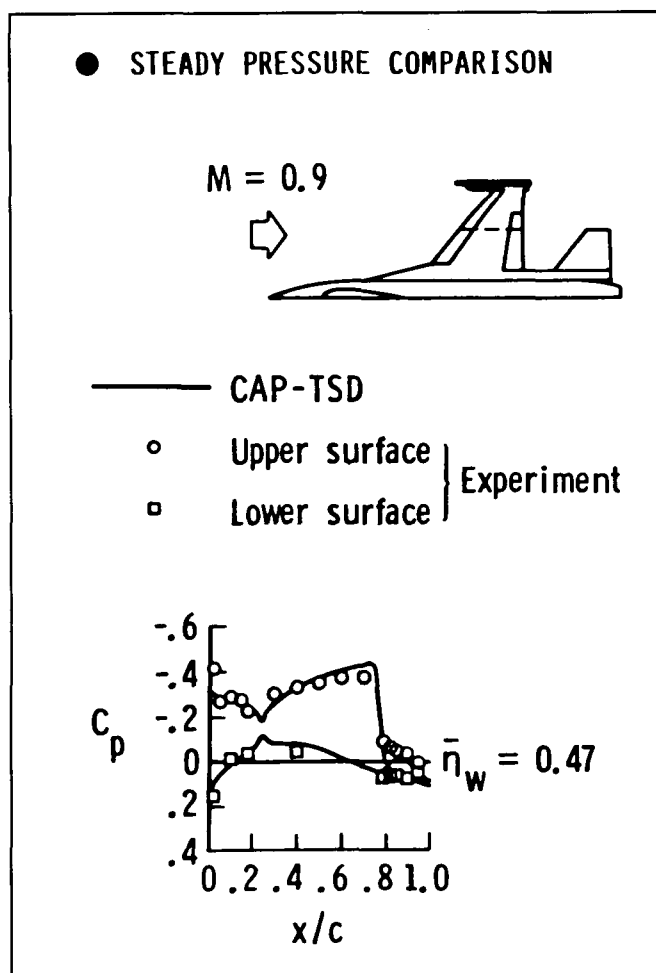
L-87-4671

Control law parameterization for Mach number of 0.90 and dynamic pressure of 250 lb/ft<sup>2</sup>.

### Development of Transonic Aeroelasticity Code for Realistic Aircraft Configurations

A time-accurate approximate factorization (AF) algorithm has been implemented for solution of the unsteady small-disturbance potential equation for transonic flow. The algorithm is very efficient for transonic unsteady aerodynamic and aeroelastic analyses of complete aircraft geometries with multiple lifting surfaces and bodies. A new computer code, Computational Aeroelasticity Program - Transonic Small Disturbance (CAP-TSD), has subsequently been developed to fully exploit the computational efficiency and superior stability characteristics of the AF algorithm.

Calculations were performed for the General Dynamics 1/9-scale F-16C aircraft model using four lifting surfaces and two bodies. The lifting surfaces include the wing with leading- and trailing-edge control surfaces; the launcher; a highly swept strake, aft strake, and shelf surface; and the horizontal tail. The bodies include the tip missile and the fuselage. Steady pressure distributions at the wing nondimensional span location of  $\bar{\eta}_w = 0.47$  are shown in the figure for the F-16C aircraft at a free-stream Mach number of 0.9 and an angle of attack of 2.38. For this case, there is a moderately strong shock wave on the upper surface of the wing, and the CAP-



CAP-TSD calculations for F-16C aircraft model.



TSD pressures agree well with the experimental data. Unsteady pressure distributions have also been obtained, but no unsteady data are available for comparison.

(John T. Batina and David A. Seidel, 4236)

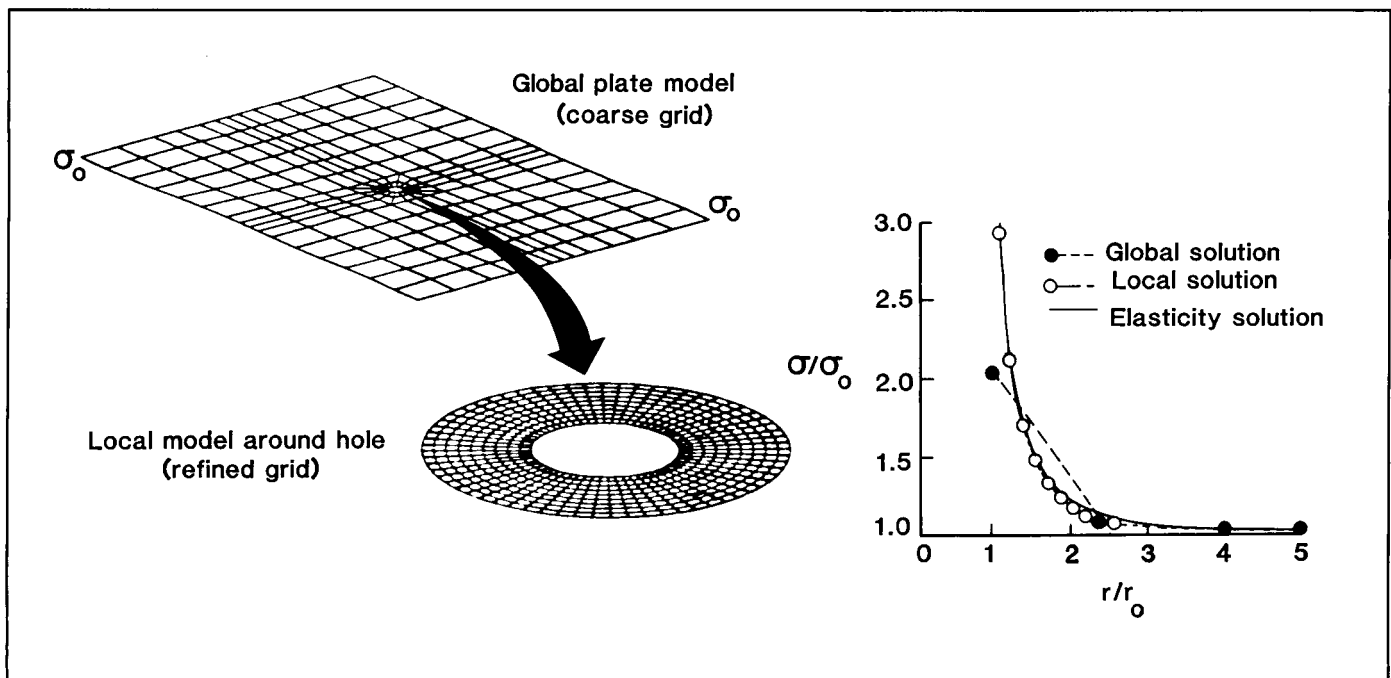
## 2-D Global/Local Analysis Using Computational Structural Mechanics Test Bed

Local discontinuities such as change in thickness, holes, or cracks can cause large stresses and large stress gradients in the vicinity of the discontinuities. This local phenomenon can only be predicted adequately with a detailed stress analysis. A 2-D global/local analysis technique has been developed to carry out such a local, detailed stress analysis within a larger, less-refined analysis model.

Elasticity theory shows that the stress concentration factor for a large, thin isotropic plate with a

small central hole of radius  $r_o$  (a plate that is subject to uniform uniaxial tensile stress  $\sigma_o$ ) will have a value of three at the edge of the hole and will vary with distance from the hole as shown by the solid curve in the graph (at the right side of the figure). The global solution (represented by the solid circles in the graph) provides good agreement with the elasticity solution in the far field but very poor agreement in the region near the hole; errors in the hole region are in excess of 32 percent. This global solution is used to define imposed displacement boundary conditions for the local model using the spline interpolation processors. The resulting global/local solution predicts stress concentration factors (represented by the open circles in the graph at the right of the figure) within 2.5 percent of the elasticity solution in the neighborhood of the hole.

This approach for a 2-D global/local analysis capability provides an accurate prediction of the stress distribution near a discontinuity using a local finite-element model. To achieve this same degree of accuracy, a global model would have to be comparably refined, not just in the region of the hole but also



2-D global/local analysis technique for plates with discontinuities.

away from the hole. The solution of such a large global finite-element model would be extremely expensive in terms of computer resources.

(N. F. Knight, Jr. and S. L. McCleary, 4892)

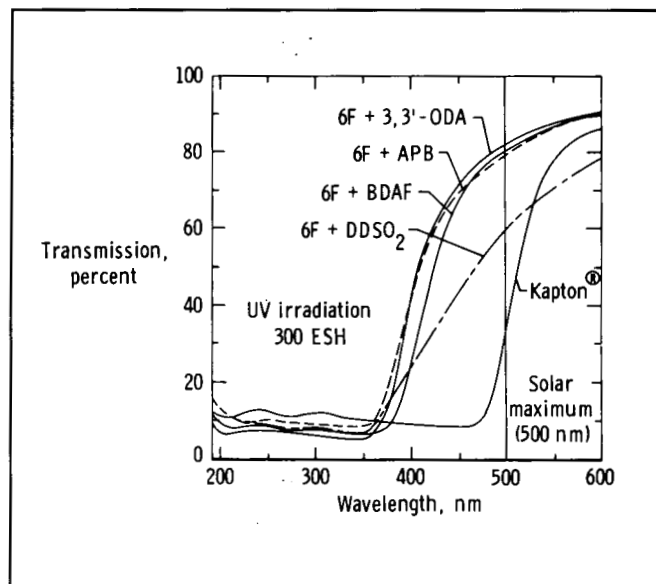
## Fluorinated Polyimide Films for Thermal Control Coatings

Optical transparency is a requirement for high-performance polymeric films used in second-surface mirror coatings on thermal control systems. Colorless aromatic polyimide films synthesized in the Materials Division at Langley Research Center show excellent potential for use in a space environment due to their high optical transparency at 500 nm, which is the wavelength of peak intensity for solar radiation.

Polyimide films based upon the aromatic dianhydride monomer containing hexafluoropropane (6F) were found to be superior to commercial Kapton polyimide film after both ultraviolet (UV) and electron irradiation. Prior to UV or electron exposure, films were mounted on a highly reflecting silver or aluminum surface to simulate a second-surface mirror thermal control coating. The figure displays the UV-visible spectra of films exposed to 300 equivalent solar hours (ESH) of UV radiation in a high vacuum. The 6F-containing polyimide films retained between 62 and 82 percent transparency at 500 nm compared to 35 percent for commercial film. Films containing ether linkages such as oxydianiline (ODA) or bis(aminophenoxy)benzene (APB) and fluorine atoms such as bis[(aminophenoxy)phenyl]hexafluoropropane (BDAF) were superior to those containing sulfone linkages such as the diaminodiphenylsulfone (DDSO<sub>2</sub>). Upon exposure to  $5 \times 10^9$  rad of 1 MeV electrons, all 6F-containing films retained 80- to 90-percent transparency compared to 35 percent for the commercial film.

Many of these fluorinated polyimide films are highly soluble in low boiling solvents and are applicable for use as spray coatings. Both the increased optical transparency and enhanced solubility of these high-performance polymers make them viable candidates for use in thermal control coating systems.

(A. St. Clair and W. Slemp, 2151)



UV-visible spectra of fluorinated polyimide films.

## Augmented Heating Rate Measurements by Shock Impingement on Cylindrical Leading Edge

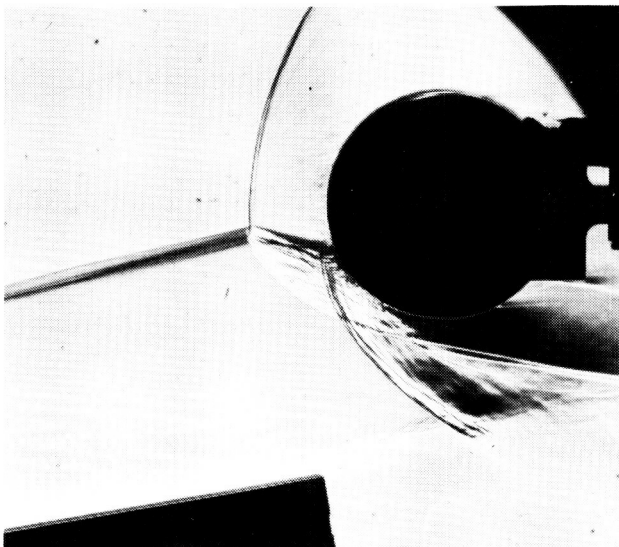
Impinging shock waves that interact with the bow shock of a blunt leading edge produce strongly augmented leading-edge heating rates. The magnitude of the heating augmentation is a function of the flow conditions and the location of the shock interaction with respect to the leading-edge centerline. Flow configurations of this type occur on hypersonic engine inlets, in which, for engine efficiency, it is desirable to have the forebody compression shock incident on the engine cowl (a condition referred to as "shock-on-lip").

The 8-Foot High Temperature Tunnel (8-Foot HTT) and the Calspan 48-Inch Shock Tunnel were used to define the heating and pressure loads on a 3-in-diameter cylindrical leading edge (with a dense population of instrumentation) with an incident shock formed by a wedge shock generator. Detailed measurements were obtained over a range of Mach numbers, Reynolds numbers, shock strengths,

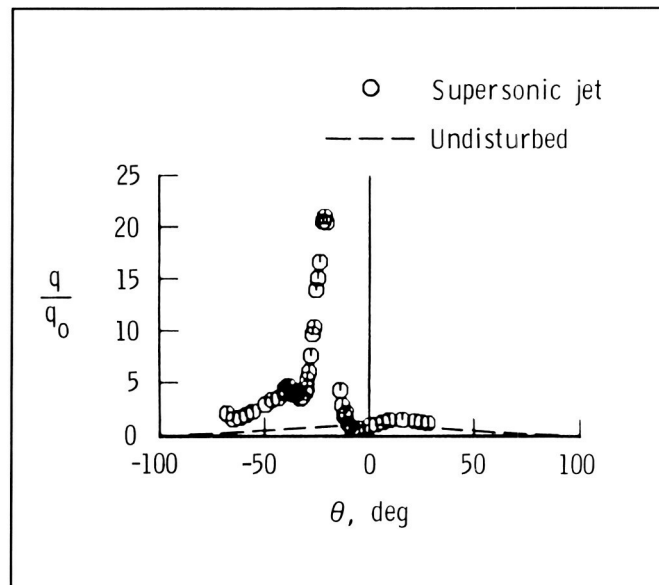
and shock interaction locations. The first figure shows a Schlieren photograph of a Type IV (as defined by Edney) interference pattern.

Data for the heating rate distribution (normalized by the no-shock stagnation heating rate) over the surface of the cylinder for Mach 16 flow are shown at the right of the figure. In this figure,  $q$  represents the local heat transfer rate,  $q_0$  represents the undisturbed stagnation point heat transfer rate, and  $\theta$  represents the angular distance from the undisturbed stagnation point (negative  $\theta$  is counterclockwise). The peak heating rate is a factor of 20 higher than the no-shock case. Accurate definition of local heating loads such as these are essential for the design of safe minimum weight structures and active cooling systems for hypersonic vehicles.

(Allan R. Wieting, 3423)



Schlieren photograph of Type IV interference pattern.



Heat flux distribution.

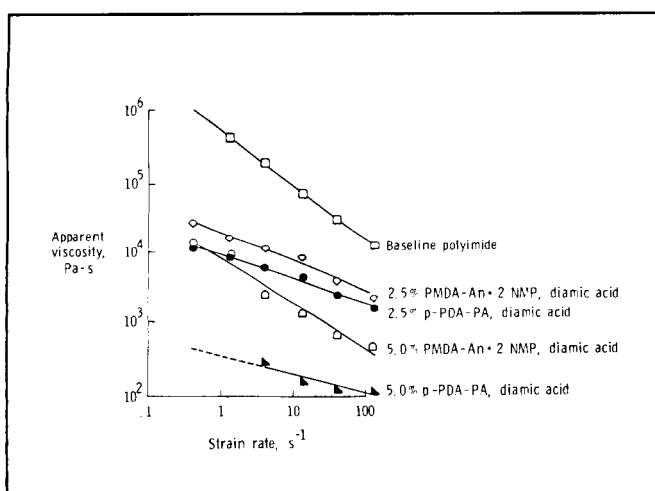
## Improved Processibility of Polyimides Through Use of Diamic Acid Additives

Conventional polyimides are tough, flexible, thermooxidatively stable, and solvent resistant, but they are very difficult to process. LARC-TPI and copolyimide 422 are two polyimides developed at Langley Research Center which possess somewhat improved processibility; however, further improvements were needed to expand their use as high-performance matrix resins. Low molecular weight diamic acid additives were synthesized and added at varying concentrations to the polyamic acid resins of LARC-TPI and copolyimide 422 as a means of improving their processibility.

Polyimide films containing the diamic acid additives were screened by thermomechanical analysis (TMA) and compared to LARC-TPI and copolyimide 422 control films. The TMA results indicated improved processibility with the addition of the diamic acids. This effect was quantified on the capillary rheometer by running copolyimide 422 molding powders containing various additives. There was a several orders of magnitude difference in the apparent

viscosities of the copolyimide 422 control and copolyimide 422 with 2.5 or 5.0 weight percent of selected additives (as shown in the figure). When composites were prepared from the LARC-TPI system containing a diamic acid additive, the increased melt flow resulted in better consolidation. This consolidation translated into improved room temperature and elevated temperature mechanical properties.

(Diane M. Stoakley and Harold D. Burks, 3041)



Capillary rheometry study of additives in copolyimide 422.

### Comparison of Simulated Low-Earth and Geosynchronous Orbit Exposure on Composite Materials

Graphite-fiber-reinforced polymer matrix composite materials are being considered for space applications because of their low density, high strength and stiffness, and high-dimensional stability. These materials have exhibited good environmental durability in short-term space applications. Since most future spacecraft will be designed for 10 years or longer, there is a concern that the space environment may interact with the polymer matrix to alter the properties of the composite and limit their usefulness.

MATERIAL	MATRIX DESCRIPTION	MICROCRACK DENSITY, CRACKS/CM		
		AS-FABRICATED	LEO SIMULATION <sup>1</sup>	GEO SIMULATION <sup>2</sup>
1500/954	177°C CURE, MY720 BASED EPOXY	0	7 <sup>A</sup>	17
1500/BP907	177°C CURE, SINGLE PHASE TOUGHENED EPOXY	0	0 <sup>A</sup>	>50 <sup>5</sup>
1500/CE539	121°C CURE, 2-PHASE ELASTOMER TOUGHENED EPOXY	0	8 <sup>B</sup>	25
C6000/P1700	POLYSULFONE, AMORPHOUS THERMOPLASTIC	5	21 <sup>A</sup>	24
AS4/PPS	POLYPHENYLENE SULFIDE, SEMICRYSTALLINE THERMOPLASTIC	0	19 <sup>B</sup>	22
AS4/PEEK	POLYETHERETHER KETONE, SEMICRYSTALLINE THERMOPLASTIC	0	1 <sup>A</sup>	5

1 500 THERMAL CYCLES: CYCLE A: 95°-150°C  
CYCLE B: 65°-150°C  
2 EXPOSED TO 1 MeV ELECTRONS FOR 10<sup>10</sup> RAD FOLLOWS BY 500 THERMAL CYCLES WITH SAME TEMPERATURE LIMITS  
AS LEO SIMULATION  
3 CRACKING AND DELAMINATION EXTENSIVE

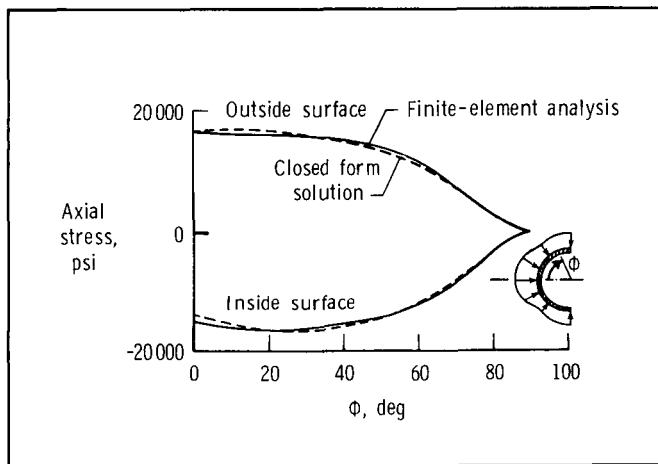
### Microdamage in composite materials.

The space durability of a variety of composite materials with matrices ranging from a brittle epoxy to a tough semicrystalline thermoplastic has been evaluated. The durability was determined by measuring the environmental-induced microcrack density resulting from simulated low-Earth orbit (LEO) and geosynchronous orbit (GEO) environments. The table summarizes the microdamage for six commercially available aerospace material systems. Only the C6000/P1700 composite exhibited microcracks in the as-fabricated condition. The simulated LEO environment produced major microdamage in all the composites except the T300/BP907 and the AS4/PEEK. Overall, the microcrack density for all materials exposed to the simulated GEO environment was greater than that found following the LEO simulation indicating that radiation affected the matrix in the composites and thus the thermal cycling response. The results show that the composite system that was not damaged during LEO simulated exposure was the most damaged by simulated GEO environment and that all of the materials were damaged by the GEO simulated environment. Thus, composite materials suitable for LEO spacecraft applications may not have the required durability for long-term GEO missions.

(J. G. Funk, 4582)

## New Direct Solution for Thermal Stresses in Spherical Nose Cap Under Arbitrary Temperature Distribution

The process to design a nose cap for a hypersonic vehicle begins with a trajectory analysis followed by a stagnation point heating rate analysis. The heating rate distribution is used in a transient thermal analysis to find the time-dependent temperatures throughout the structure. Thermally induced stresses are computed for the worst-case temperature profile and used to size the structure. Since the design process as outlined is iterated to arrive at a final design, it becomes essential to use a rapid, easy-to-use and accurate stress determination technique. If the nose cap structure is treated as a thin spherical shell with an axisymmetric temperature distribution and the stress solution to the thermoelastic equations is represented as a series of Legendre polynomials, the governing differential equations are readily solved.



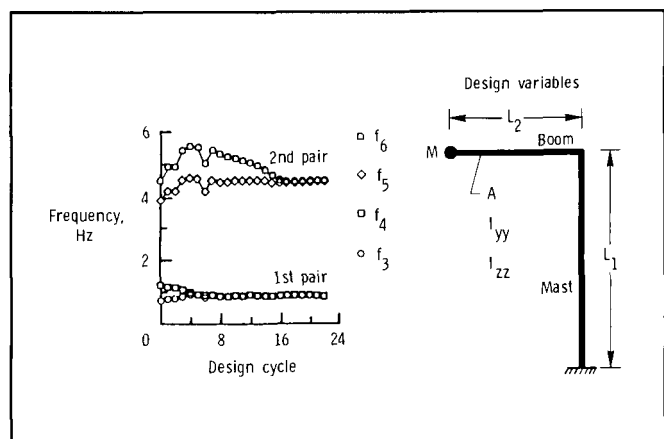
*Axial stress distribution.*

The solution technique has been developed and programmed on a personal computer. The program is user friendly such that the user need not be concerned with the solution technique. Other than specifying the temperature as a polynomial, the user's only concerns are computing the stresses and plotting the results of parameter studies for any material and spherical shell geometries specified. The re-

sults shown in the figure compare the direct solution technique with results from a detailed finite-element analysis. The stresses are representative of those in a ceramic nose cap with a typical temperature distribution. The solution technique significantly reduces the iteration time to arrive at an acceptable design. (Randall C. Davis, 2291)

## Optimization Procedure to Control Spacing of Vibration Frequencies for Flexible Space Structures

As spacecraft structural concepts increase in size and flexibility, the vibration frequencies become more closely spaced. The identification and control of structures having closely spaced frequencies present a significant challenge, and it is necessary to assess the performance of control and identification algorithms on such structures. The Control of Flexible Structures (COFS) Project is aimed at developing this technology and therefore requires a structure that has closely spaced vibration frequencies. Thus, a need exists to develop a systematic method to design such a structure.



*Frequency placement optimization study for COFS II.*

An optimization procedure has been developed which will systematically design a structure to have closely spaced frequencies and minimum mass. The procedure uses a general-purpose finite-element analysis program for the vibration and sensitivity analyses and a general-purpose optimization program. The optimization procedure has been applied to an equivalent beam model of a candidate COFS II configuration to obtain two pairs of closely spaced frequencies while avoiding an excessive mass penalty. Specifically, it is required to place the frequencies of the two pairs of modes indicated in the figure within 1 percent. Six quantities are allowed to vary in order to achieve the objective: the mast length  $L_1$ , the boom length  $L_2$ , the boom cross-sectional area  $A$ , the two boom area moments of inertia  $I_{yy}$  and  $I_{zz}$ , and a concentrated mass  $M$  at the tip of the beam. As shown in the figure, the first pair of frequencies are closely spaced after four design cycles. The second pair of frequencies require longer to become closely spaced; however, after 16 cycles, both pairs of frequencies have met the frequency-placement requirement.

(Joanne L. Walsh, 2887)

### Shape Control of Large Space Antenna Reflectors Based on Electromagnetic Performance

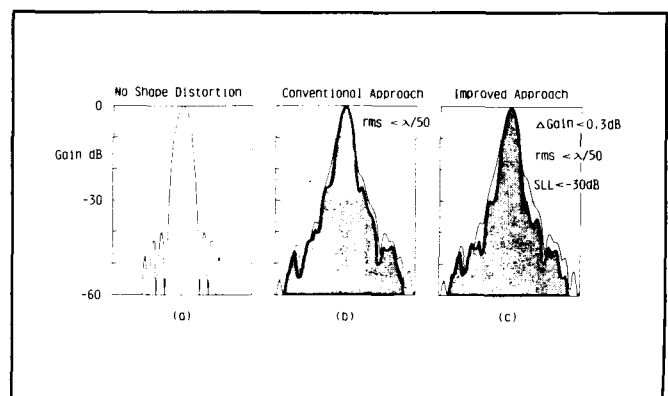
A key issue in design and operation of large space antenna reflectors is the precise shape control of the reflector surface. The present work integrates structural analysis, aperture integration electromagnetic (EM) analysis, and constrained optimization techniques such that shape control is driven by explicit measures of antenna performance rather than by estimates of root mean square (rms) surface distortion error (the conventional approach).

The procedure has been applied to a tetrahedral truss antenna. The reflector surface shape is controlled by 48 actuators, which can lengthen or shorten individual truss members of the backup structure. The best set of actuator inputs is the set that meets performance goals while minimizing the maximum change in the length of any element. The performance goals are to reduce side lobe lev-

els (SLL) ( $< -30$  dB) while limiting peak gain loss (loss  $< 0.3$  dB) and rms surface distortion error (rms  $< \lambda/50$ , where  $\lambda$  is the characteristic wavelength). Side lobe level is the most critical factor in many large space antenna applications (e.g., it controls the remote-sensing accuracy for a radiometer, the tracking accuracy for a radar antenna, and the interference between communications satellites).

The effectiveness of the present approach is shown in the figure. Relative power levels (gain) are plotted against an angle measured from the antenna axis. The ideal antenna with no shape distortion (as shown in part (a) of the figure) has a very high main beam surrounded by low side lobes. In actual antennas, manufacturing errors and thermal expansion cause significant distortion of the reflector. The next two graphs (parts (b) and (c) of the figure) compare expected power level patterns with (gray) and without (white) shape control. Notice that very little improvement is made in SLL by the conventional approach of reducing rms surface distortion error. However, all side lobe levels meet or exceed the  $-30$  dB limit when shape control is driven by explicit measures of EM performance. The new approach is important because it guarantees acceptable antenna performance using the least amount of control effort possible.

(S. L. Padula, 2887)



*Integrated electromagnetic/shape control optimization.*

## Tapered Ends for Space Shuttle Solid Rocket Booster/External Tank Attachment Ring

Three struts attach the Space Shuttle external tank (ET) to a partial ring structure on the aft end of the solid rocket booster (SRB). The existing ring design, which extends about 270° around the circumference of the SRB case wall, provides insufficient tapering of the cross section at the ring ends. Consequently, shear failure has occurred in the bolts that attach the ring to tangs on the SRB case walls in both recovered flight boosters and ground test boosters. A cooperative activity has been established between Langley Research Center and Marshall Space Flight Center to modify the design for the tapered partial ring so that all margins of safety, as verified through test and analysis, are positive.

A one-dimensional linear representation of the ring, tang bolts, and case wall has been developed to efficiently calculate an initial taper profile for the ring area. Preliminary drawings were prepared for this design, and detailed finite-element analysis was conducted which led to modifications of the design. Numerous iterations on the ring area profile led to a final design that exhibited all positive margins of safety in bolt loads and ring web stresses.

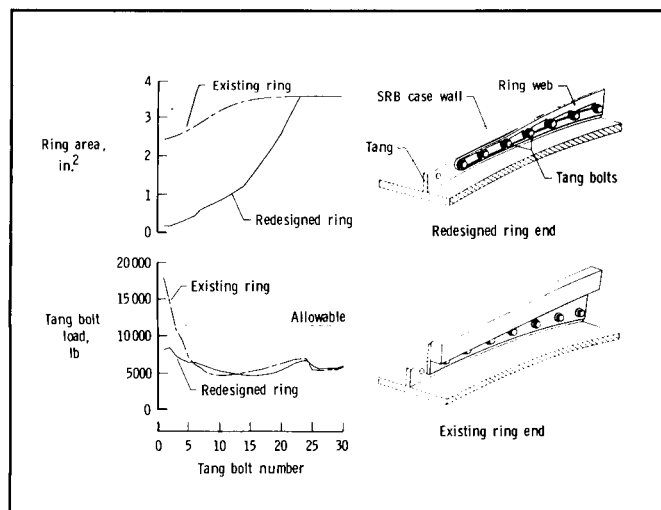
The figure compares the geometry of the tapered end of the existing ring (lower right) to the end of the redesigned ring (upper right). The graph in the upper left compares the cross-sectional area profiles of the two rings for the first 30 tang bolts. The area at the end of the ring had to be significantly reduced to prevent tang bolt failures. The effect of this area reduction is seen in the lower left-hand plot, which shows the tang bolt load distributions for both designs during the worst-case flight loading condition. Analysis of the existing design shows negative margins of safety on the first few bolts, which is consistent with the failures that have occurred. Improved area tapering in the redesigned ring leads to greatly reduced end bolt loads and all positive margins of safety. Thus, the redesigned ring shows substantial improvement in performance over the existing design and, as a result, is being further developed for flight qualification testing.

(M. S. Lake, 2414)

## Weight Efficient In-Line Bolted Joint for Space Shuttle Solid Rocket Motor Case Segments

An in-line bolted-joint concept, which can be used to join Space Shuttle solid rocket motor (SRM) case segments, has been designed at Langley Research Center. The proposed concept (shown on the left side of the figure) uses studs and nuts to hold opposing flanges together and to seat the two polymeric O-rings. The studs are recessed into the shell wall, and bearing plates are used to transfer the compressive loads from the nuts into the flanges. Gussets, which are located between the alcoves, provide a path to transfer the axial load from the shell wall to the flanges. An advantage of the in-line bolted design is that it uses a static face seal between two precompressed flanges to eliminate the reliability issue associated with using gas pressure to seat the O-rings.

The objectives of the research were to evaluate the joint structural performance as major design parameters were varied and to assure that the primary design criteria were met. The primary requirement



Comparison of existing and redesigned SRB/ET attachment ring.



for the joint design was that the joint must remain closed in the vicinity of the O-rings during SRM firing so that the O-rings were never required to track moving surfaces. Another objective was to improve on an initial joint design that had excessive weight.

Finite-element models of the joint were constructed using three-dimensional solid elements, and the contact problem between mating joint surfaces was investigated using nonlinear contact elements. Parametric studies were performed to assess the changes in joint structural performance resulting from changes in design variables.

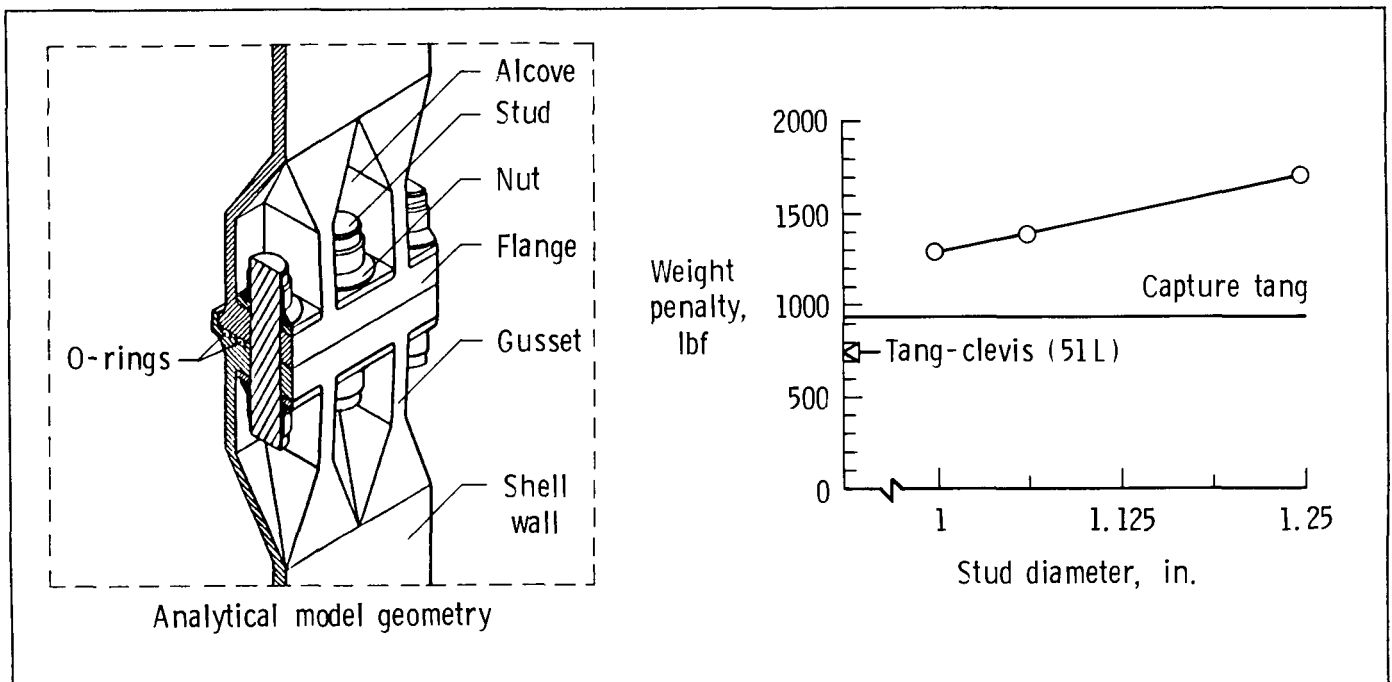
A design for the in-line bolted joint concept has been developed which meets the primary objective of keeping the joint closed at the O-rings, while maintaining acceptable stress levels and minimizing weight. Parametric studies indicate that, in general, weight is minimized by using the smallest stud size practical (right side of figure); the smallest offset between the stud centerline and shell wall centerline; and the smallest practical values of flange and gusset thickness. The design with 180 1-in. studs (shown in the figure) has a weight penalty that is only 346 lbf

(per joint) greater than the proposed capture tang fix. The weight penalty is defined as the mass of the joint minus the mass of an equivalent length of straight booster shell.

(John T. Dorsey, 2892)

### New Developments in Model Parameter Determination for System Identification

In developing aerospace structures for dynamic operating environments, considerable effort is expended to determine the structures modal parameters, such as damping, natural frequencies, mode shapes, and modal participation factors. Many methods have been developed and are currently in use; however, Langley Research Center has combined technology from both the controls and structural dynamics fields in an effort to unify the diverse field of modal parameter identification. A common basis,



Weight penalty calculated for in-line bolted joint model.

via system realization theory, has been developed to explain and to select from a myriad of possible techniques. The basic development of the state-space-model realization from noise-free data, attributed to Ho and Kalman (who introduced the important principles of minimum realization theory), has been recently modified and substantially extended to develop the Eigensystem Realization Algorithm (ERA) for identifying modal parameters from noisy measurement data.

Several variations of the ERA method for modal parameter identification, shown in the figure, have been derived using a system realization theory. Transfer functions are the basic elements for the frequency-domain ERA, whereas the other methods use the free-decay responses. The choice of methods can be made largely on the basis of the final purpose of the identification (such as mathematical model improvement or on-line control of flexible structures).

All methods have been shown to work well on simulated and test data, and a number of different important features exist for each method. The relations between different techniques have been explained and well correlated using system realization theory, thus providing a basis and insight for comparison and evaluation.

(Jer-Nan Juang, 2881)

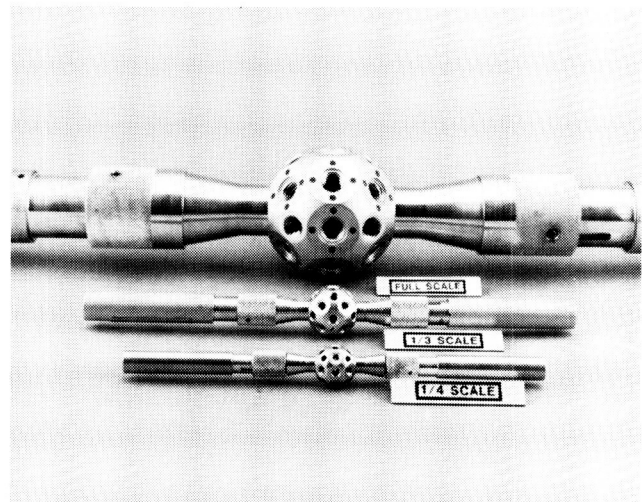
Application* Algorithm	Free Decay	Forced Response	Small Computer	On-line	Rapid Analysis	High Accuracy
Original ERA	X				X	X
Frequency domain ERA		X	X			X
Recursive ERA	X			X	X	
Data correlation ERA	X		X			X

\*Assumes noisy data

*Variations of ERA that apply in diverse modal parameter identification situations.*

## Feasibility of Scaled Models for Dynamic Tests of Erectable Space Station

In ground tests to verify structural dynamic analyses of very large spacecraft, such as the Space Station, scaled models offer attractive possibilities for reducing gravity effects in tests on large assemblies. Langley Research Center, in a combined in-house and contractual effort, has shown the feasibility of manufacturing truss-type space structures of the class expected to be used in an erectable Space Station. Test data on composite tubes scaled by reducing the number of fiber lay-ups showed excellent correlation with full-scale tubes. Analytical studies at the Massachusetts Institute of Technology and Carnegie-Mellon University showed that joint behavior can be replicated at subscale as long as manufacturing tolerances can be scaled.



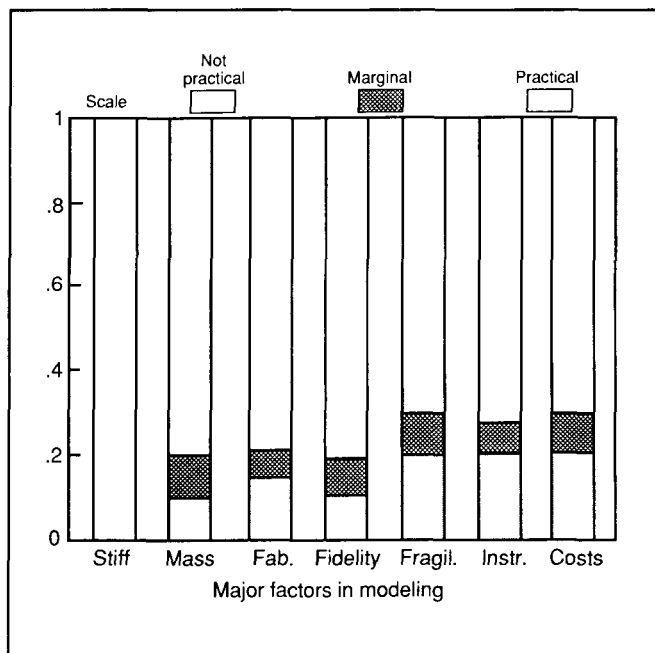
L-86-10,501

*Scaled erectable-space-truss joints used in test program.*

Tests at Langley Research Center on scaled joints, which were manufactured by Star-Net Structures, Incorporated (as shown in the first figure) verified those findings. Studies by Lockheed Missiles

and Space Company, AEC-Able Engineering Company, and Langley Research Center evaluated several additional factors in scaling, including fabrication limits, fragility, and costs (as shown in the second figure). The conclusion was that currently envisioned erectable Space Station structures can be accurately and affordably scaled down to approximately 1/5 size.

(Paul E. McGowan, 3615)



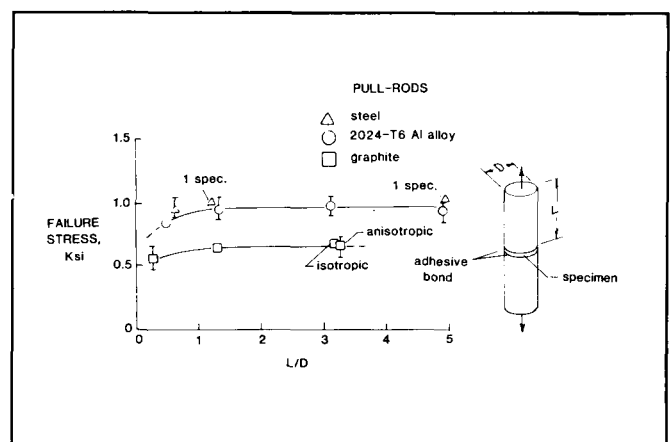
Assessment of scaling factors for Space Station model.

### Test Methodology for Carbon-Carbon Composites

Carbon-carbon composites are attractive materials for thermal protection systems and hot structures on advanced space transportation systems because of their strength retention at high temperature (above 2500°F). In conventional two-directional lay-ups, however, strength in the thickness direction is much lower than desirable and can be further degraded by application of oxidation protective coat-

ings. It is therefore very important to be able to accurately measure the interlaminar tensile strength for design purposes and in order to delineate the effects of efforts to improve this property.

The experimentally observed failure stress is plotted (as shown in the figure) versus the pull-rod length-to-diameter ( $L/D$ ) ratio for circular cross-sectional specimens bonded to pull-rods made of materials having different elastic moduli. A minimum  $L/D$  of about 1.3 is indicated for which specimens can be tested without reducing the observed failure stress due to pull-rod deflections. These data are generally supported by finite-element analyses that show that stress concentrations are significant for lesser  $L/D$  values. Of special interest is the fact that specimens bonded to graphite pull-rods failed at about 30 percent lower stress than those bonded to metal pull-rods. Graphite happens to be the material used by a reputable testing laboratory for interlaminar tensile testing of carbon-carbon.



Measured interlaminar tensile stress versus length-to-diameter ratio for steel, aluminum, and graphite pull-rods.

Two types of graphite were evaluated in this investigation. As shown in the figure, the results were the same, even though one material is elastically isotropic while the other is not. A finite-element analysis predicts conditions leading to the observed behavior for anisotropic graphite; however, no plausible explanation has been found to date for the similar behavior observed for isotropic graphite. In lieu

**ORIGINAL PAGE IS****OF POOR QUALITY**

of sufficient data on the behavior of the graphites, a recommendation is made that graphites not be used as pull-rod material in interlaminar tensile testing of carbon-carbon.

(P. O. Ransone, 4412)

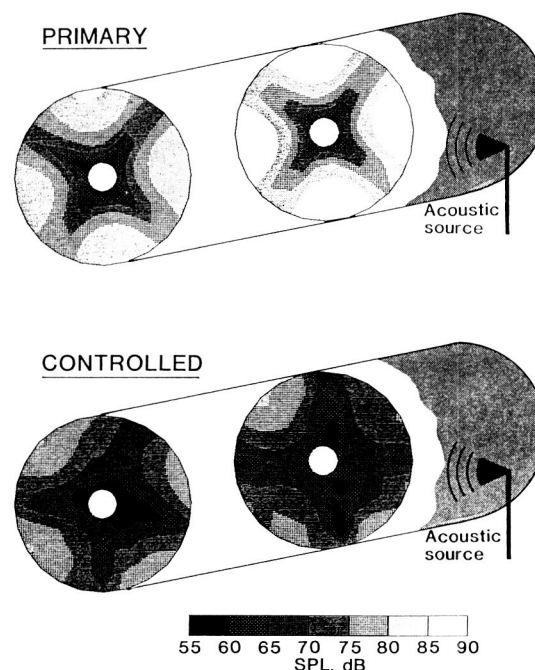
a much more uniformly quieted interior environment results. Additionally, good agreement between these measurements and an analytical model have been obtained.

(Richard J. Silcox, 3561)

### Active Control of 3-D Acoustic Environments

The need for additional low-frequency noise attenuation in advanced turboprop aircraft has been emphasized by recent flight testing on these prototype systems. Although the design of turboprop aircraft makes possible a 25- to 30-percent increase in fuel efficiency, their exterior noise levels have been measured to be significantly higher than current-generation propeller aircraft. To attain acceptable cabin levels, sound transmission losses of 50 to 70 dB must be provided through the fuselage sidewall. Conventional construction techniques must be augmented with innovative techniques to provide enhanced sound isolation without an unacceptable weight penalty. One evolving technique is active noise control in which additional interior noise sources are used to provide control of the cabin acoustic environment.

In order to investigate the application of this technology, a finite-length, thin-walled, elastic cylinder was used to model a fuselage. As shown in the figure, exterior acoustic sources placed on opposite sides of the cylinder forced the cylinder into vibration and produced an interior noise field. The noise field due to these exterior sources is characterized at two cross sections as the primary field in the top portion of the figure. Sound pressure levels ranging from 60 to 90 dB (see the figure key) were measured with maximum levels at the source plane and somewhat reduced levels shown 0.75 radius forward. The electrical inputs to four interior acoustic control sources were then optimized so as to minimize the pressure measured over an interior array of microphones. The resulting controlled field is shown in the lower portion of the figure where peak sound pressure levels have been reduced by greater than 15 dB in the source plane. Somewhat reduced attenuations were measured out of the source plane, but, overall,



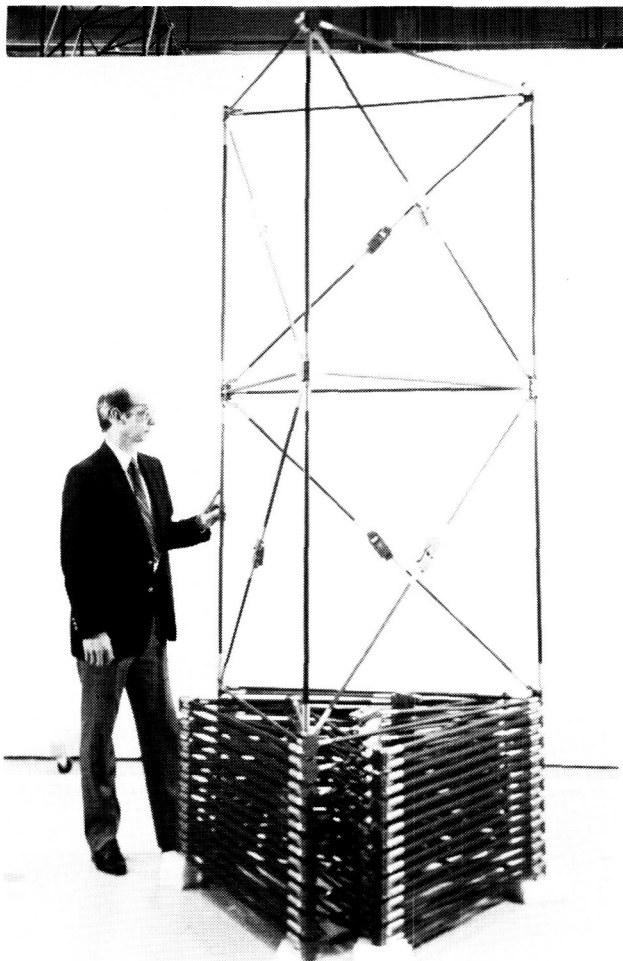
*Comparison of primary and controlled acoustic fields at two axial positions.*

### Deployable and Foldable Beam/Truss for Space Applications

A lightweight, deployable beam/truss for application to space structures, such as antennas and scientific instrument supports, has been developed through a contract with the Astro Aerospace Corporation. The triangular cross-sectional truss folds to a compact package that is approximately 5 percent of its deployed length and approximately the same diameter as when deployed. The concept is not

limited to ultimate length or diameter, except by design load and packaged-size considerations. The initial design is 20-m long, comprised of 18 truss bays, and has 1.2-m triangular sides. The beam/truss is made of graphite/epoxy tubes with machined titanium joints to yield a very low coefficient of thermal expansion. Precision manufacturing was employed to produce joints that do not have significant free play. Kinematic simplicity is maintained by using single-axis hinges combined with structural members that bend during the deployment and folding process.

(Marvin D. Rhodes, 3596)



L-86-11,557

18-bay beam truss model with two bays fully deployed.

## Cornering and Wear Behavior of Space Shuttle Orbiter Main Tire

Extensive testing has been completed at the recently upgraded Aircraft Landing Dynamics Facility to define and model the cornering characteristics of the Space Shuttle orbiter main tires. In addition, as a result of excessive tire wear produced by Space Shuttle orbiter landings at the Kennedy Space Center (KSC), tests have been conducted to determine the wear mechanisms associated with rough-runway operation in hopes of generating a mathematical model for inclusion into astronaut training simulators.

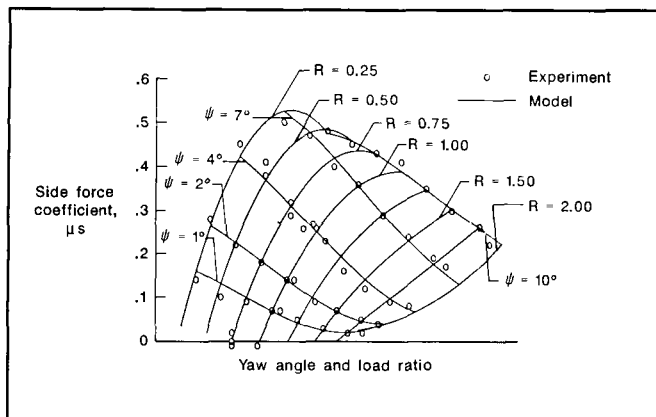
Cornering data were generated by conducting tests at speeds up to 220 kn for a variety of conditions on the tire including yaw angles up to  $10^\circ$  and loads up to 122,000 lbf. These values cover the full range of conditions expected during flight operations.

The first figure shows side force coefficient, which is a measurement of the cornering efficiency of the tire, plotted as a function of yaw angle  $\psi$  and the load ratio  $R$ . A load ratio of 1 equals about 61,000 lbf of vertical load on the tire. These data show that cornering efficiency increases as yaw angle increases but decreases as load is increased. The mathematical model shown plotted with the data was included in Space Shuttle orbiter rollout simulation programs and produces a realistic simulation of the handling behavior of the Space Shuttle orbiter during landing.

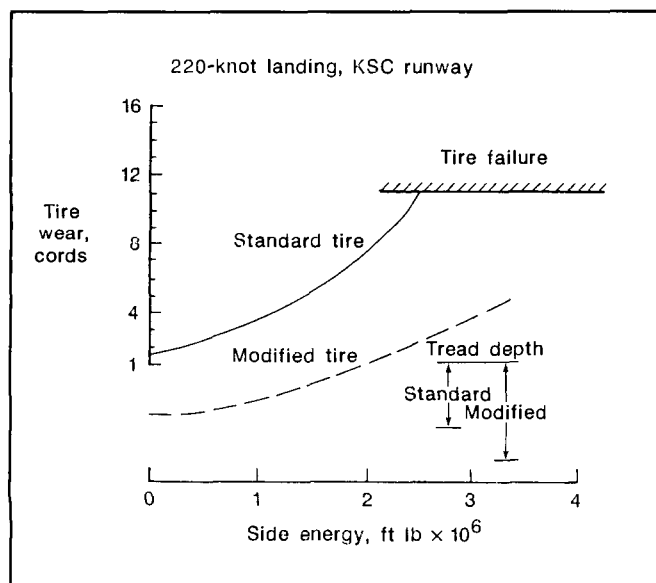
The second figure shows the result of tests to define the wear behavior of the tire on the extremely rough KSC surface. The plot shows tire wear, measured in cord layers, to be a function of the side energy. (Side energy is defined as the work produced laterally by the tire while rolling in a yawed attitude.) Typical flight tires wear through one cord layer during the spin-up process, hence the placement of the curve for the standard tire wear progression. This curve has also been installed on the Space Shuttle orbiter rollout computers so that after a simulated landing, pilots can receive feedback on how their piloting techniques have affected tire wear. A modified tire with a thicker tread that uses a different rubber compound has been tested to try to reduce the total wear likely to be experienced during crosswind landings. The curve for this tire is also shown. Since the cord layers of the tire are what dictate its strength, both wear curves are adjusted so that the first cord layers of each tire are coincident. Due to an interest

in the much-improved wear behavior of this tire, an investigation of possible flight qualification has begun.

(Robert H. Daugherty, 2796)



*Bi-cubic curve fit with experimental data showing side force coefficient, or cornering efficiency, as function of both yaw angle and load ratio.*



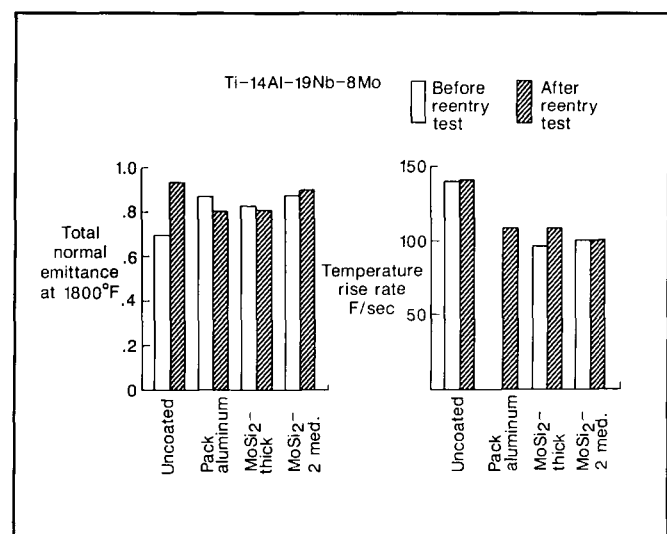
*Tire wear is modeled as function of side energy for both standard tire and one with modified tread compound.*

## Improved Performance of Titanium-Aluminides by Use of Thermal Control Coatings

The use of titanium-aluminide intermetallic alloys and composites will result in minimum structural weights of the National Aero-Space Plane (NASP) structures. Protective coatings that shield the materials from oxidation and have a low catalytic efficiency and a high emittance, however, can significantly extend the applicability of these materials by reducing the heating rate to the surfaces in hypersonic flight environments and by radiating a significant portion of the heat flux away from the surface.

Coatings are prepared using sputtering, physical vapor deposition, chemical vapor deposition, pack cementation, and slurry processes. Materials used in the coating process are selected on the basis of their potential to reduce the catalysis and increase the emittance of the surface and to provide oxidation protection of the substate material. Coated specimens are screened for performance by simulated-hypersonic-flight testing in the Hypersonic Materials Environmental Test System (HYMETS). The figure shows results for Ti-14Al-19Nb-8Mo with three different coatings before and after simulated-hypersonic-flight testing for 1 hr at 1800°F. All three coatings reduced catalytic heating by 30 percent and increased the emittance to a favorable level ( $> 0.8$ ).

(R. K. Clark, 4557)

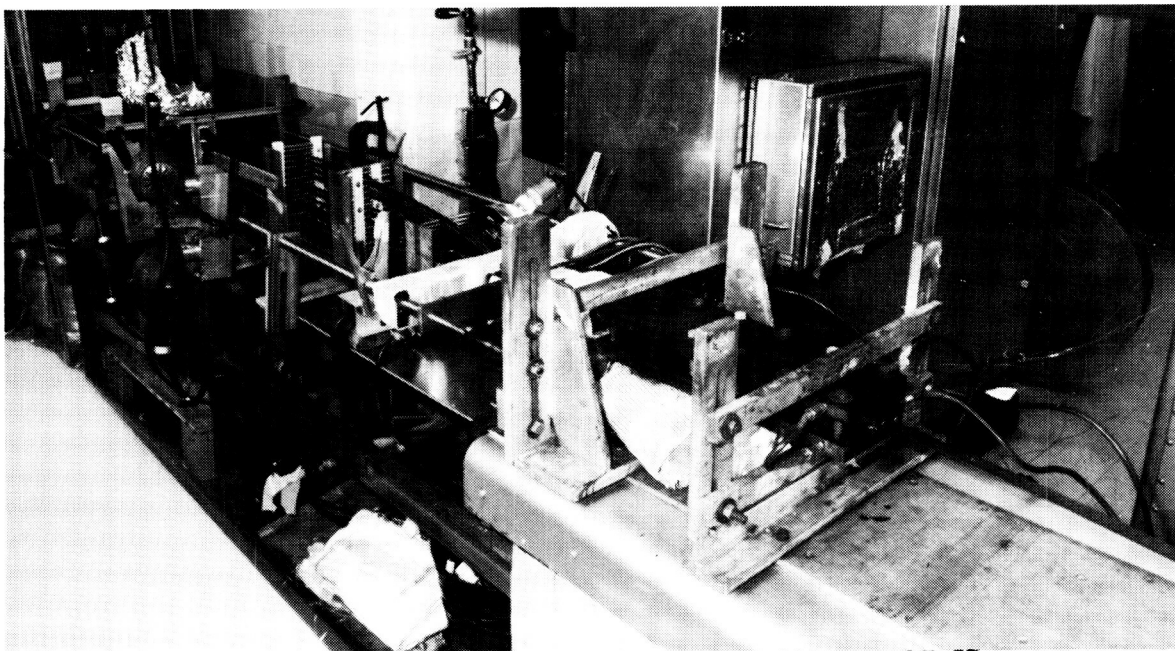
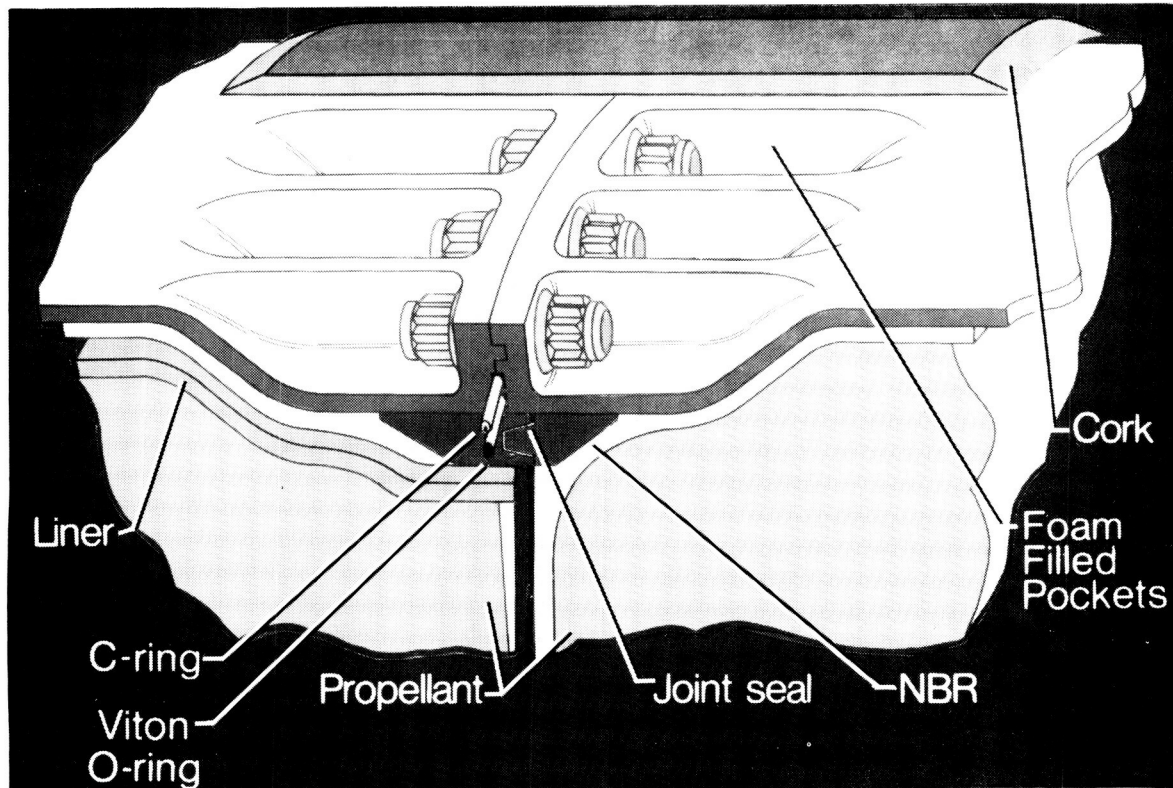


*Emittance/catalysis coatings improve performance of titanium-aluminide.*



# Systems Engineering and Operations Directorate

---



ORIGINAL PAGE IS  
OF POOR QUALITY



The function of the Systems Engineering and Operations Directorate is to support ongoing aeronautical and space research at Langley Research Center. This work force is divided into five divisions with specific support functions. The Systems Engineering Division is responsible for structural, mechanical, electrical, and aeronautical systems engineering functions required to provide research models and flight hardware for aerospace research applications and technology. The Facilities Engineering Division is responsible for engineering and design of aerospace research and development equipment and institutional facilities for aeronautical and space research, such as special handling equipment, model supports, and special test equipment. The Fabrication Division is responsible for developing and fabricating aeronautical and aerospace research hardware related to ground support equipment as well as research facilities test equipment. This division provides developmental manufacturing, technology and electronics technical support, including communications systems and instrumental hardware. The Operations Support Division is responsible for providing the technical, mechanical, electrical, and maintenance services for research and institutional facilities. This division operates laboratory equipment and wind tunnels and collects, records, and interprets test data. The Systems Safety, Quality, and Reliability Division has overall responsibility to insure the safety of operation of all aerospace and ground facilities as well as to insure that the aerospace hardware and ground research equipment meet all quality and reliability standards. This division also manages the environmental health program for the Center and inspects the construction of major modifications to the many unique research facilities. In addition to the five divisions, the Facilities Program Development Office is responsible to the directorate.

Because of the unique requirements of some of the aerospace research performed at the Center, both engineers and technicians are involved in applied research in solving engineering and fabrication problems. These problems relate to the support hardware and software necessary to provide the experimental systems requested by research. The following contributions represent typical engineering and fabrication research and technology development highlights in the Systems Engineering and Operations Directorate.

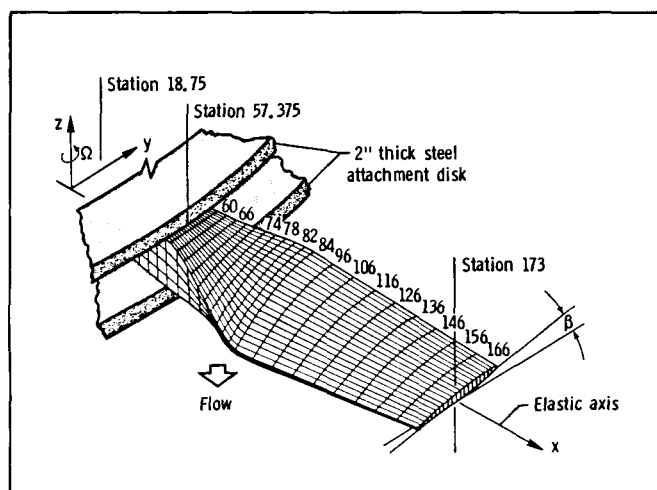
### **Coupled Bending-Torsion Steady-State Response of Pretwisted Nonuniform Rotating Beams Using Transfer-Matrix Method**

Numerous wind tunnels at Langley Research Center are driven by rotating propeller or fan blade systems, and nearly all of these tunnels have been in operation for several years. In order to insure safe and continued operation, fan blades require a thorough evaluation of the steady-state response under operating conditions. To determine this rotating blade steady-state response, effective and efficient analysis techniques are required which consider the unique features common to rotating systems.

An important consideration in the structural analysis of a rotating beam is the effect of the coupling between the centrifugal force and the elastic stiffness (deflections) of the beam. This effect provides a stiffer structural member in both the beamwise and chordwise directions. To solve this problem and to take advantage of the centrifugal-stiffening effect are difficult considerations due to the necessity of having to know the deformed state of the beam in order to apply the steady-state centrifugal loads.

Using the Newtonian method, the equations of motion are developed for the coupled bending-torsion steady-state response of beams rotating at constant angular velocity in a fixed plane. The resulting equations are valid to first-order strain-displacement relationships for a long beam with all other nonlinear terms retained. In addition, the equations are valid for beams with the mass centroidal axis offset (eccentric) from the elastic axis, nonuniform mass and section properties, and variable twist. The solution of these coupled, nonlinear, nonhomogeneous, differential equations is obtained by modifying a Hunter linear second-order transfer-matrix solution procedure to solve the nonlinear differential equations and by programming the solution for a desktop personal computer. The modified transfer-matrix method was verified by comparing the solution for a rotating beam with a geometric, nonlinear, finite-element computer code solution. For a simple rotating beam problem, the modified method demonstrated a significant advantage over the finite-element solution in accuracy, ease of solution, and actual computer processing time required to effect a solution.

(Carl E. Gray, Jr., 4508)



Langley 7- by 10-Foot High-Speed Wind Tunnel fan blade.

### Foam Fiberglass Used for Radio-Controlled Spin Model

Langley Research Center has used dynamically scaled, radio-controlled free-flight models for studies in the stall departure and spin characteristics of civilian general-aviation aircraft. The traditional methods for fabrication of these models require a great deal of time and manpower to make templates, patterns, and molds before any part of the model is actually constructed. The model components are then manufactured using complicated vacuum molding procedures from conventional materials such as fiberglass, balsa, and hardwood. The components are then assembled by hand.

Numerical control milling technology has been used to fabricate a dynamically scaled, free-flight radio-controlled spin research model. The model was constructed of closed-cell polyurethane foam covered with one to three layers of lightweight fiberglass and epoxy resin. The wing was machined in one piece and includes a lightweight I-beam spruce spar. The fuselage was machined in halves and was cored out to remove excess weight and to provide room for the radio control system and the research instrumentation. A firewall of aircraft plywood provided a sta-

ble mount for the single-cylinder, two-cycle engine and the forward landing gear strut. The horizontal and vertical stabilizers have been machined from lightweight balsa.

A time savings was realized by not having to make the templates, patterns, and molds of the more traditional procedure. Additionally, model symmetry is easier to maintain with this procedure than with more traditional fabrication methods.

(William C. Conkling, 2651)

### Radiographic Technique for Wooden Structures

A number of wind tunnels at Langley Research Center use fan blades made wholly or partly of laminated Sitka spruce (*Picea sitchensis*). The traditional method for inspecting these components has been a superficial visual review. This technique can locate surface defects but cannot detect in-depth flaws in the blades. Historically, the radiography of wooden structures has been hampered by the basic inhomogeneity of the material. Local discrete density changes in growth bands selectively attenuate penetrating radiation and cause corresponding density variations on the radiographic film image. These local density changes can best be described as a "zebra effect," and their presence makes interpretation of the radiographic image very difficult. In addition, these base material images tend to mask the presence of other latent defects such as cracks and delaminations.

A technique has been developed at Langley Research Center which has been employed to successfully enhance the image of latent wooden structure defects. This technique uses a commercial industrial cleaning solvent, Trichlorotrifluoroethane ( $\text{CCl}_2\text{FCClF}_2$ ), as a radiopaque penetrant. This solvent has a fairly high molecular weight and relatively safe toxicity threshold, especially when compared to more conventional radiopaque materials. The technique entails the radiography of the wooden parts before and after injection of the penetrant into surface cracks or delaminations. When the before and

after radiographs are reviewed simultaneously, latent internal defects are more readily discerned.

This technique has been successfully used on fan blades from the 16-Foot Transonic Tunnel.

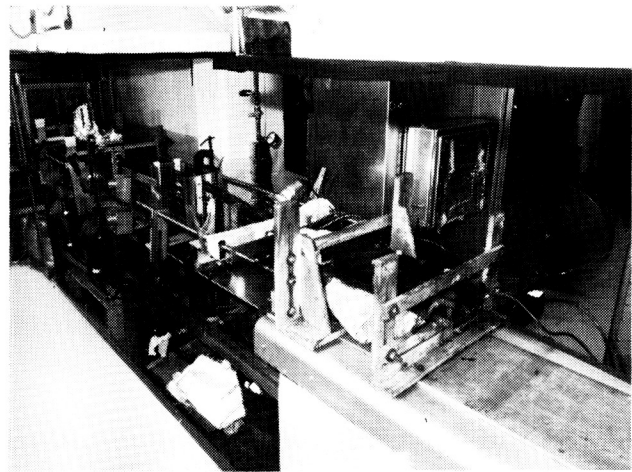
(M. L. Berry and R. F. Berry, Jr., 2781)

### **Pultrusion Process Development for Fabrication of High-Performance Thermoplastic/Graphite Composites**

Pultrusion research and development in fabrication technology for advanced composite materials is being conducted at the Langley Research Center Pultrusion Laboratory. Processes have been developed for pultruding two high-performance thermoplastic polymers, polyetherimide (PEI) and polyetheretherketone (PEEK). In these processes, continuous high-modulus graphite fiber is used as reinforcement. The PEI process includes in-line fiber impregnation. The PEEK process is designed for using multiple plies of commercially available solventless, prepregged materials. In both processes, consolidation of multiple plies, compaction, and polymerization is conducted in a continuous operation.

The development of pultrusion processing techniques for these high-temperature, high-strength thermoplastics is important to the aerospace community. The pultrusion process has the potential for manufacturing very long continuous lengths of structural profiles such as hat-sections, I-beams, channels, tubing, and many other shapes. The thermoplastic matrix materials can be postfabricated into various shapes and joined by welding in a manner similar to the postfabrication methods used with metal alloy sheet stock material. The solventless prepregged thermoplastic stock can be coiled on spools that will reduce storage volume and greatly increase packing density. Postfabrication of this type of material would not produce toxic fumes. Such characteristics would be advantageous for on-orbit manufacturing of large space structures, e.g., large antennas, long tethers, and space platforms.

(M. L. Wilson, 4615)



L-87-06208

*Pultrusion fabrication of high-performance thermoplastic matrix composites.*

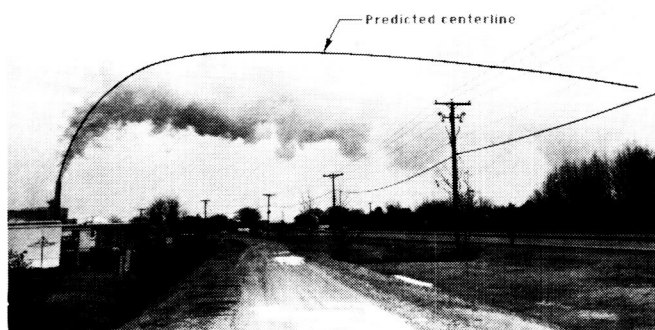
### **Plume Dispersion of Exhaust From Cryogenic Wind Tunnel**

As a result of concern for inadequate oxygen levels and fogging of roadways, an analytical model has been developed to predict the behavior of the plume that exhausts from the National Transonic Facility, a major cryogenic wind tunnel at Langley Research Center. The model consists of two stages. The first stage or ascent stage is analytically resolved by assuming a Gaussian distribution of the plume thermodynamic properties in the radial direction and numerically integrating the momentum and diffusion equations; the second stage describes the descent of the plume and is resolved by describing the crosswind displacements by vorticity and numerically integrating in the crosswind and downwind directions. Temperature, visibility, oxygen concentration, and flow characteristics of the plume have been calculated for distance downwind of the stack exhaust. Predictions have been compared with several photographic observations.

The model predicted the centerline trajectory of the plume fairly accurately, but underpredicted the extent of fogging. The model predicted descent of the plume, but at a lesser rate of change than observed. Second-stage diffusion terms in the model

were decreased in order to bring the predicted fog and descent data into better agreement with the observed data. The observed plume widths in the second stage spread in a vertical direction similar to that of a Gaussian plume. The model was used to predict dispersion characteristics of the National Transonic Facility exhaust over its operational envelope. Predictions indicate that oxygen levels are adequate and that some excessive fogging exists at high humidities. The results of this work are documented in NASA Technical Memorandum 89148, 1987.

(W. S. Lassiter, 4508)



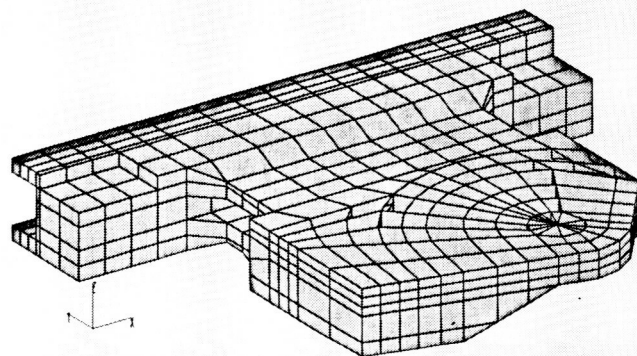
L-84-869

Vent stack plume for nitrogen mass flow of 458 lb/s and relative humidity of 94 percent.

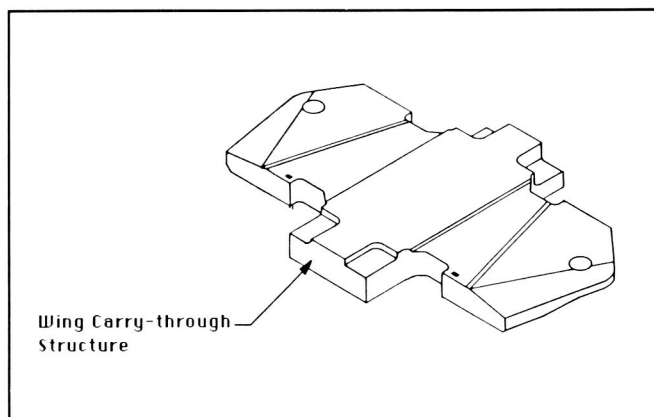
## FAVOR Model Carry-Through Fixture Test and Analysis Results

In order to evaluate the strength and stiffness of the FAVOR (Facility Aerodynamic Validation of Operations Research) F-111 model's carry-through structure, a detailed three-dimensional finite-element model of the most current configuration geometry was developed using the Patran-G modeling code. Stresses and deflections were then computed for several load cases and configurations using the Engineering Analysis Language (EAL) program. The finite-element model of the carry-through structure

solved a complex, preloaded, lapped joint problem that heretofore has defied solution by either closed-form or finite-element methods. The solution strategy was to iterate the contact forces and deflections until a compatible set of constraints was achieved at all mating interfaces.



Finite-element model of wing carry-through structure for FAVOR model.



Wing carry-through structure for FAVOR model.

The testing of the carry-through fixture validated the finite-element model. Although the model does tend to underpredict the stress at four strain-gauge locations, this underprediction is a result of the gauges being located in cutout regions and reading stress concentration effects. For the most part, in regions where the discontinuities are far removed from the gauges, there is excellent agreement between the

measured and calculated stresses. The demonstrated successful modeling and validation of the preloaded joint resulted in a design that met stringent requirements for testing in the National Transonic Facility. The success of this solution strategy demonstrated the capability for analyzing preloaded lapped joints, and the method can be used for analyzing other structures with similar joint connections.

(Clarence P. Young, Jr., 4508)

### Numerical Model of Unsteady, Subsonic Aeroelastic Behavior

A method for predicting unsteady, subsonic aeroelastic responses has been jointly developed by Virginia Polytechnic Institute and State University and Langley Research Center. The technique accounts for aerodynamic nonlinearities associated with angles of attack, vortex-dominated flow, static deformations, and unsteady behavior. The angle of attack is limited only by the occurrence of stall or vortex bursting near the wing. The fluid and the wing together are treated as a single dynamical system, and the equations of motion for the structure and flow field are integrated simultaneously and interactively in the time domain. The method

employs an iterative scheme based on a predictor-corrector technique. The aerodynamic loads are computed by the general Unsteady Vortex-Lattice Method (UVLM) and are determined simultaneously with the motion of the wing. The figure shows the flow field predicted by the UVLM. The wing tip vortex systems are fully developed. Because the unsteady vortex-lattice method predicts the wake as a part of the solution, the history of the motion is taken into account; hysteresis is predicted.

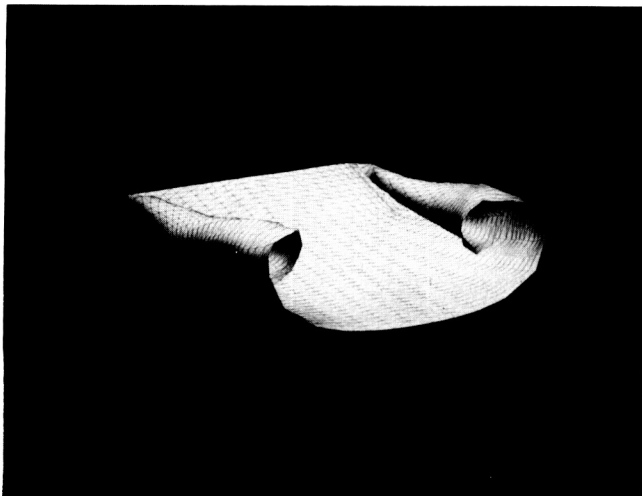
Two aeroelastic models are used to demonstrate the technique; these models are a rigid wing on an elastic support experiencing plunge and pitch about the elastic axis, and an elastic wing rigidly supported at the root chord experiencing spanwise bending and twisting. The method can readily account for structural nonlinearities and other methods of computing the aerodynamic loads. The time domain solution coupled with the UVLM provides the capability of graphically depicting wing and wake motion.

(Thomas W. Strganac, 4508)

### Use of Advanced Composites in Research Aircraft Models

With the introduction of highly loaded, high-speed general-aviation aircraft, new challenges have arisen in the fabrication of radio-controlled (R/C) research models. The higher structural loading and the demand for weight conservation during fabrication have limited the use of conventional construction materials typically used in research models. The most recent example of this problem occurred in the construction of an R/C model of the Swearingen SX300. It was discovered that due to high wing loading and landing abuse it would be necessary to use lighter, higher strength components, particularly in the wing and landing gear.

The typical construction materials of this aircraft would normally be spruce, fiberglass, plywood, balsa, and aluminum; however, because of structural demands, the wing spar was fabricated from laminated graphite/epoxy bonded to a spruce web. The graphite laminates and the spruce grain were oriented in order to dampen the torsional and bending



L-86-5197

*View of wing and wake vortex sheets.*



moments. The entire main landing gear was made from graphite/epoxy with discriminating ply orientation and titanium inserts for wheel-mounting accommodations.

This project was the first opportunity at Langley Research Center to fabricate and use advanced composites in the primary structure of an R/C model, and it will probably be a test bed of information for future research model construction.

(Tom Vranas, 2651)



Full-scale Swearingen SX300.

### Rotary Actuator for COFS Mini-Mast

The Control of Flexible Structures (COFS) project required rotary actuators as part of the ground testing of the Mini-Mast structure (a deployable, statically determinate, triangular truss-beam). The actuators were specified to have a torque output of 50 ft·lb while having minimum weight and occupying minimum space. The decision was made to build the actuators in-house because a commercial unit was not available to meet the specifications. A 50-ft·lb, frameless, torque motor was purchased from Magnetic Technology Division, Vernitron Corp., of Canoga Park, California, to drive the flywheel portion of the actuator. To minimize the weight, the housing and shaft were made of aluminum, but to reach the desired inertia, the flywheel was made of

steel. The flywheel was fabricated with the majority of the weight at the outer perimeter by machining the interior thinner than the outer circumference and by adding holes to lighten the flywheel.

The first completed actuator weighed approximately 85 lb with an inertia of about 0.7 ft·lb/s<sup>2</sup>, which was a considerable improvement over any commercially available unit. This actuator is presently being tested to verify the design torque and inertia. The actuators are driven by a PMI Motion Technologies pulse-width-modulated servo amplifier and power supply (Model AXA-90-10-20). This unit provides the current to drive the actuator in the forward and reverse directions.

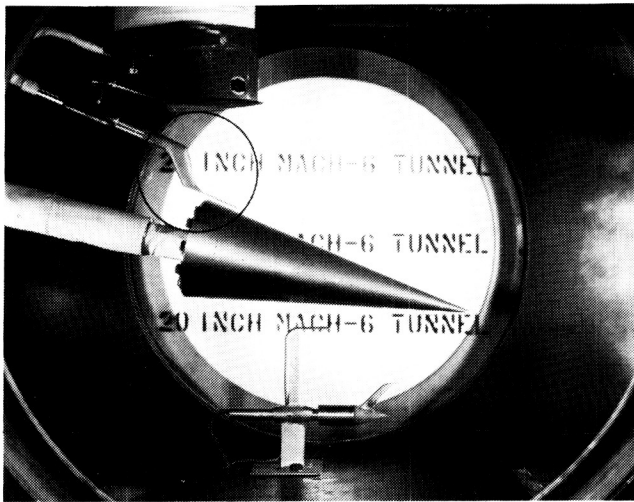
(Virgil S. Laney, 4621)

### Pitot-Static/Flow Direction Survey Probes

Some of the problems associated with wind tunnel testing involve the gathering of test data without producing erroneous information as a result of test equipment interference in the test stream. Langley Research Center has fabricated a micro-size survey probe capable of measuring pitot pressure (both static and dynamic flow) with minimal or no error because of the sensing equipment. Technicians at the Langley Research Center Foundry have developed a pressure-casting technique to encapsulate probe tubes and secure sensing instrumentation in one aerodynamic, high-strength package without destroying the delicate sensing instruments. This casting technique provided an inexpensive way of securing the instrumentation package while providing an aerodynamic, high-strength pylon survey probe cast of ZA-12 aluminum zinc alloy.

The results of this technique have been very successful. The micro-probe is being used in the 20-Inch Mach 6 facility. Seven instruments have been constructed using the same molds and techniques at a significant savings in time and machine costs. The near-surface survey probe is depicted by a circle on the photograph, which shows a typical wind tunnel test in the 20-Inch Mach 6 facility.

(P. Vasquez and J. Eves, 2651)



L-87-7629

*Near-surface probe (circled) being used under test conditions in 20-Inch Mach 6 facility.*

### Concept for Solid Rocket Booster In-Line Bolted Joint

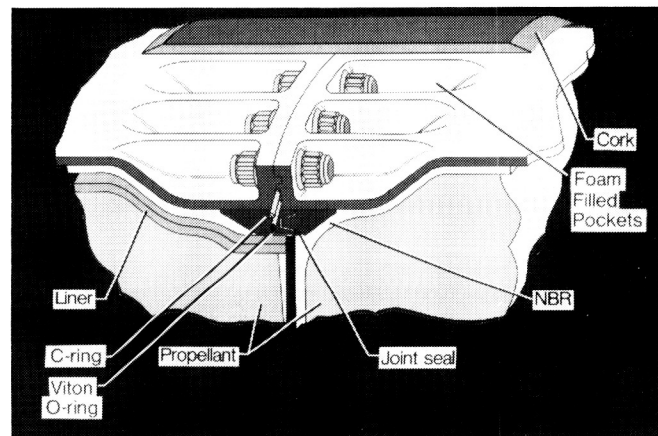
The Space Shuttle solid rocket booster (SRB) motor case sections are joined by a tang-and-clevis joint held together with 177 radial steel pins (see also p. 105). After being machined to close tolerances and fitted, the sections are assembled at the factory into four segments. These four segments are then cast with propellant and shipped to the John F. Kennedy Space Center for assembly. The joints assembled at the factory are called factory joints, and the joints between the four propellant cases are called field joints. The in-line joint is an alternate to the tang-and-clevis concept and is being studied for possible use.

The SRB joint concept (as shown in the figure), which has been developed by Langley Research Center, is a face-sealed in-line bolted joint. This concept was chosen because face seals are much less prone to leakage in a dynamic environment than the gland seals used in the existing design on the Space Transportation System (STS). The joint geometry minimizes the forces and moments that tend to reduce seal effectiveness. Integral flanges are stiffened by gussets located between 144 preloaded 1.25-in.-

diameter fasteners. The seal configuration consists of a Viton elastomer O-ring and an Inconel 718 metallic C-ring.

External thermal protection is provided by bonding a cork fairing over the in-line joint and part of the SRB cylindrical surface. A smooth bonding surface is formed by filling the void between the gussets with foam. Rigid molded phenolic-silica rings compressing a soft nitrile N rubber (NBR) elastomer seal (to fill manufacturing voids) protect the SRB case and face seals from internal heating. Thermal analysis results indicate that this concept will perform satisfactorily even if 50 percent of the rings are burned away and local gap openings to the steel case form. A feature of the rigid-ring concept is that the gap formed between the rings and soft seal, when exposed to a temperature drop, will be extremely small when compared to the current design. The rings will remain bonded during horizontal testing and allow for propellant venting.

(D. H. Butler, 4571)



L-86-6206

*SRB in-line bolted joint.*

### Alternate Design of Partial Solid Rocket Booster External Tank Attachment Ring for Space Transportation System

A full 360° ring to attach the SRB to the external tank is planned for the next STS flight, instead



of the 270° partial ring used in the past. A payload weight penalty is associated with the full ring because of increased structural weight and aerodynamic drag. Langley Research Center has designed a partial external tank attachment (ETA) ring with tapered ends which is being considered for use after the first STS reflight. The Langley Research Center ring will recover the lost payload weight.

The most significant change is to taper the webs and caps at each end of the ring to more evenly distribute the web-to-tang fastener loads and to fabricate the cap as an integral unit. The pockets between the first seven bolt holes are covered with a shear web. A 2024-T8 aluminum replaceable bushing anodized and coated with a polysulfide sealant is located in the first bolt hole to reduce the effective stiffness of the first bolt preventing excessive loading. The transition tunnel was also redesigned using more tunnel sections and incorporating elastomeric expansion joints to prevent excessive loading.

The tapered web design was analyzed extensively at Langley Research Center and Marshall Space Flight Center (MSFC). Langley Research Center performed linear and nonlinear finite-element and closed-form analyses of the ring ends, developed a ring area tapering analysis technique, and performed inelastic and fracture analyses. Marshall Space Flight Center performed the verification analysis with a large NASTRAN model.

Beneficial features of the partial SRB/ETA ring concept compared to the full-ring concept include easier installation on the vehicle, retention of the existing vehicle dynamic properties, web stresses that are insensitive to bolt stiffness, and capability of carrying limit load with several failed fasteners.

(D. H. Butler, 4571)

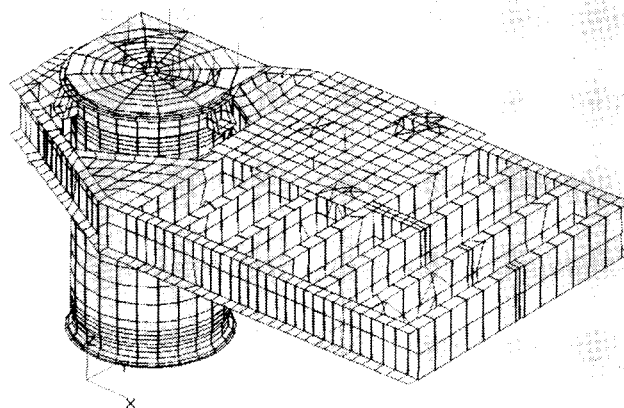
### **Low-Weight, High-Stiffness, Thermally Stable Equipment for High-Precision Optical Measurements**

The LIDAR (laser-radar) Atmospheric Sensing Experiment (LASE) will make high-altitude measurements of atmospheric gases using highly sensi-

tive optical instruments. The experiment will fly on the ER-2 aircraft and will be subject to an environment that is undesirable for precision optics. Weight limitations of the ER-2 aircraft dictate a lightweight design, whereas precise spacing and angular alignment requirements under in-flight mechanical and thermal loads necessitate the use of a high-stiffness, low-thermal-expansion material. A design has been developed for the equipment mounting deck and telescope barrel using lightweight graphite/epoxy laminates tailored to achieve high stiffness and near-zero coefficient of thermal expansion in directions of critical alignment. Test results on the graphite/epoxy laminates validated analytical predictions for both stiffness and thermal expansions.

A detailed finite-element model of the LASE equipment has been developed and analyzed for a variety of mechanical, thermal, and vibration loads. The analysis predicts that the deformations are minimal under all in-flight loads and that all critical alignment requirements are met.

(Michael C. Lindell, 4508)

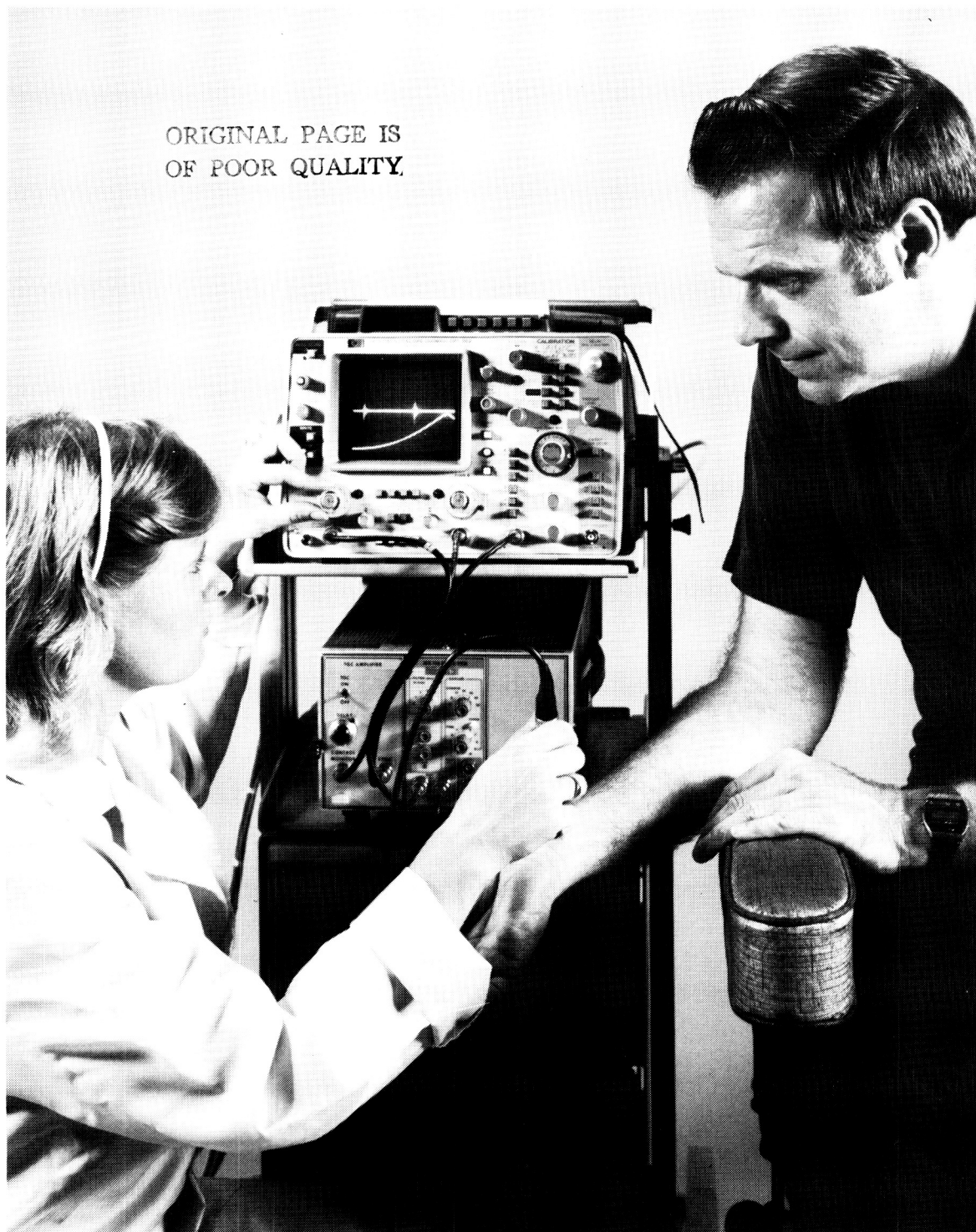


*LASE equipment mounting deck, receiver/telescope, and wavemeter.*

# Technology Utilization Program

---

ORIGINAL PAGE IS  
OF POOR QUALITY.



One of NASA's Congressionally mandated responsibilities is to promote economic and productivity benefits to the nation by facilitating the transfer of aerospace-generated technology to the public domain. NASA's means of meeting this objective is its Technology Utilization Program, which provides a link between the developers of aerospace technology and those in either the public or private sectors who might be able to employ the technology productively.

One important facet of NASA's Technology Utilization Program is its applications engineering projects, which involve the use of NASA expertise to redesign and/or re-engineer existing aerospace technology to solve problems encountered by federal agencies or other public sector institutions. Applications engineering projects originate in various ways. Some projects stem from requests for NASA assistance from other government agencies and some are generated by NASA engineers or scientists who perceive possible solutions to public-sector problems through the adaptation of NASA technology. In addition, NASA employs a multidisciplinary applications team that contacts public-sector agencies, medical and public-health institutions, and professional organizations to uncover significant problems in fields such as health care, public safety, transportation, and industrial processes which might be amenable to solution by the application of NASA technology. The projects reported on here are typical of the applications engineering efforts conducted at Langley Research Center in support of the Technology Utilization Program.

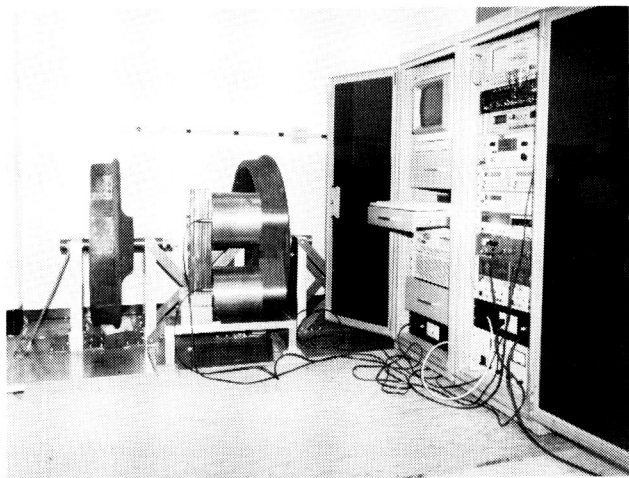
### Stress in Railcar Wheels

A collaborative interagency project between Langley Research Center and the Federal Railroad Administration (FRA) has resulted in the development of a prototype measurement system for characterizing the magnetoacoustic interaction in stressed railcar wheels. This system will enable the stress state of wheels to be determined nondestructively and thus will further the cause of preventing costly in-service railcar wheel failures. The photograph depicts the test system in use on railcar wheels.

This effort has capitalized on Langley Research Center's extensive research, conducted over the past several years, which has been directed toward measuring residual stress in steels using the low-field magnetoacoustic technique. In this technique, the magnetic domain structure in the steel is interrogated with an ultrasonic wave. As the magnetic domain structure is altered by internal stress, the resulting measurement identifies the internal stress state in the steel; this identification indicates the presence of dangerous tensile loads that could precipitate wheel failure.

The system takes advantage of Langley Research Center's patented pulsed-phase-locked loop ( $P^2L^2$ ) to resolve small changes in acoustic phase velocity which occur during magnetization. The prototype has been delivered to the Association of American Railroads Laboratory in Chicago. In its first practical test, the prototype correctly singled out a tensile wheel that subsequently failed under test.

(Min Namkung, 3036)



L-86-10,841

*Residual stress field testing unit.*

### Burn Depth Measurement System

Radically different medical treatments of a burn injury exist, depending upon whether the burn wound is a second-degree (dermal and deep dermal)



or a third-degree (full-thickness) wound. Presently, the assessment of the severity of a burn wound is estimated by visual inspection; however, it is often quite difficult, even for the experienced burn surgeon, to distinguish between deep dermal and full-thickness burns. This applications project addressed the need for a noninvasive, quantitative measurement technique to assist the burn surgeon in determining burn wound depth.

By combining theory with experiment, a technique has been developed to measure skin burn depth. Starting with an *in vivo* ultrasonics-based study of burn wounds in porcine skin, a theory of skin burn necrosis has been developed. Based on the porcine skin data, it has been determined that ultrasonic reflections occur at the interface between necrotic and viable skin. These reflections are caused by changes in the structure of collagen, a major component of skin. Because skin is very thin (typically 1 mm), the frequency response of the ultra-

sonic equipment must be substantially higher than that which is usually available on medical ultrasound instruments (up to 60 MHz); in addition, highly refined time-gain compensation and discrimination circuits are required.

The instrument shown in the photo is a Langley Research Center-developed unit that has been optimized for use in measuring skin burn depth. A specially manufactured high-frequency ultrasonic transducer is used with a high-frequency A-scan unit into which specially designed signal processing circuits are placed. This instrument is currently being evaluated in a clinical setting at the Medical College of Virginia (MCV). This evaluation is being directed by Dr. B. W. Haynes and his associates at MCV's Burn Center.

The initial results, although preliminary, are promising. To date the instrument has been used in the measurement of burn wound depths to ascertain the severity of the injury for victims of flame burns, scald burns, and chemical burns. The assessment of the severity of skin-burn wounds based on this technique has been correct in all cases attempted.

(John H. Cantrell and William T. Yost, 3036)



L-87-6198

*Ultrasonic burn depth analyzer.*

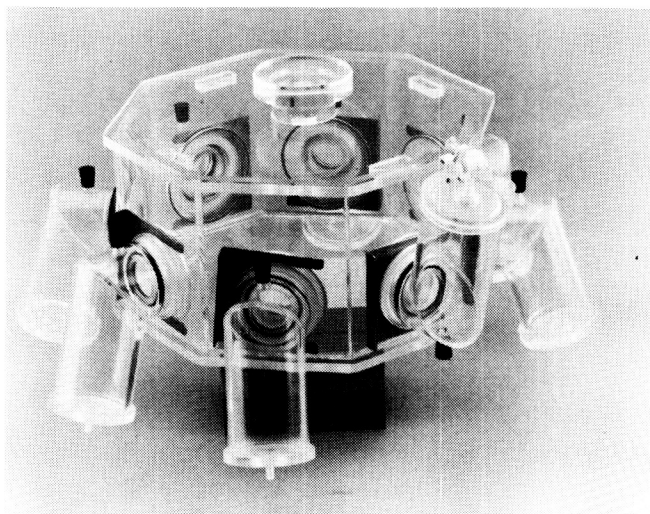
## Dialysis Chamber

Medical researchers at the Veterans Administration (VA) Medical Center, Hampton, Virginia, are investigating the permeability of parietal peritoneum (the lining of the intestinal cavity) to nutrients in a unique *in vitro* setting. This research will evaluate the efficacy of total peritoneal nutrition via the transperitoneal route for patients without renal failure.

To compare the permeability of artificial membranes with peritoneal membranes under controlled clinical conditions, a dialysis chamber was needed. The chamber design had to accommodate precise *in vitro* measurement of the migration of aqueous-aqueous or blood-aqueous phases simultaneously across different membranes. For design and fabrication of the dialysis chamber, the VA researchers requested support via NASA's Technology Utilization Program.

After assessing the project's requirements, an octagonal chamber with eight smaller chambers attached by spring-loaded clips and sealed by O-rings was designed and fabricated at Langley Research Center. The chamber, shown in the photograph, is simple, interchangeable, and time controllable, and it greatly enhances the research capability of the VA project.

(Bruce D. Little, 3141)



L-87-3033

*Nutrient migration chamber.*



## Report Documentation Page

1. Report No. NASA TM-4021	2. Government Accession No.	3. Recipient's Catalog No.	
4. Title and Subtitle Research and Technology 1987 Annual Report of the Langley Research Center		5. Report Date December 1987	
		6. Performing Organization Code	
7. Author(s)		8. Performing Organization Report No. L-16381	
		10. Work Unit No.	
9. Performing Organization Name and Address NASA Langley Research Center Hampton, VA 23665-5225		11. Contract or Grant No.	
		13. Type of Report and Period Covered Technical Memorandum	
12. Sponsoring Agency Name and Address National Aeronautics and Space Administration Washington, DC 20546-0001		14. Sponsoring Agency Code	
15. Supplementary Notes			
16. Abstract The mission of the NASA Langley Research Center is to increase the knowledge and capability of the United States in a full range of aeronautics disciplines and in selected space disciplines. This mission will be accomplished by performing innovative research relevant to national needs and Agency goals, transferring technology to users in a timely manner, and providing development support to other United States Government agencies, industry, and other NASA centers. This report contains highlights of the major accomplishments and applications that have been made during the past year. The highlights illustrate both the broad range of the research and technology activities at NASA Langley Research Center and the contributions of this work toward maintaining United States leadership in aeronautics and space research. For further information about the report, contact Dr. Richard W. Barnwell, Chief Scientist, Mail Stop 105-A, NASA Langley Research Center, Hampton, Virginia 23665, (804) 865-3316.			
17. Key Words (Suggested by Authors(s)) Research and technology		18. Distribution Statement Unclassified—Unlimited  Subject Category 99	
19. Security Classif.(of this report) Unclassified	20. Security Classif.(of this page) Unclassified	21. No. of Pages 154	22. Price A08